공학박사 학위논문

Mn-Based Olivine Cathode Materials for High-Performance Li-Ion Batteries

고성능 리튬 이온 전지를 위한 망간계 올리빈 양극물질 연구

2017년 2월

서울대학교 대학원
재료공학부

위 성 언

Mn-Based Olivine Cathode Materials for High-Performance Li-Ion Batteries

고성능 리튬 이온 전지를 위한 망간계 올리빈 양극물질 연구

지도교수 박 병 우

이 논문을 공학박사 학위논문으로 제출함

2017 년 2 월

서울대학교 대학원

재료공학부

위 성 언

위성언의 박사학위논문을 인준함

2017 년 2 월

위 원 장	강 기 석	(인)
부 위 원 장	박 병 우	(인)
위 원	김 천 중	(인)
위 원	엄 지 용	(인)
위 원	이 국 승	(인)

Ph.D. Thesis

Mn-Based Olivine Cathode Materials for High-Performance Li-Ion Batteries

Sungun Wi

February 2017

WCU Hybrid Materials Program,

Department of Materials Science and Engineering,

Seoul National University

Abstract

Energy sources are important for the way of life in modern society, but most of the energy demand now depends on the power of nuclear and fossil fuels. This will eventually accelerate global warming and seriously deplete natural resources. As a result, it is important to develop efficient, environmentally friendly, and safe energy sources such as fuel cells and solar cells, and the development of efficient energy storage systems for storing these eco-friendly energy sources is also becoming an important issue. Among the various energy storage systems, lithium-ion batteries are attracting attention as the most realistic energy source because they have the charm of high energy density and durability. Because the performance of a battery is usually determined by electrode materials, people have been looking for a breakthrough challenge to overcome the limitations of the known materials. Conventional cathode materials such as lithium transition metal oxides ($LiMO_2$, M = transition metals) possess intrinsic chemical instability at overcharged state. They release oxygen from the crystal structure or experience irreversible phase transformation at elevated temperature, which consequently raises safety concerns during operation. In this respect, numerous studies have been carried out in order to find a safe and stable cathode material. Among many candidates, phosphate materials have been considered as the best candidate of energy storage system for large-scale applications due to its high structural stability and safety by strong P-O covalent bonding, potentially low production cost, high energy density, and excellent cyclability. Olivine structured lithium iron phosphate ($LiFePO_4$) has been extensively studied as a promising candidate for cathode materials of lithium-ion batteries due to its high theoretical capacity, superior structural stability, environmental benignity, and low cost. However, the $LiFePO_4$ has relatively low redox potential (3.4 V vs. Li+/Li), which results in low energy density limiting its wider application to the market. For this

reason, isostructural $LiMnPO_4$ with higher redox potential (4.1 V vs. Li+/Li) has emerged as an alternative material for $LiFePO_4$.

Therefore, in my thesis, I focused on design of novel Mn-based olivine cathode materials ($LiMn_{0.8}Fe_{0.2}PO_4$) and comprehensive analysis of the reaction mechanism of Mn and Fe in $LiMn_{0.8}Fe_{0.2}PO_4$ electrodes during battery operation.

In Chapter 1, the issues to overcome the limitation of olivine cathode materials for practical application are briefly introduced, mainly dealing with the development of Mn-based olivine cathode materials.

In Chapter 2, electrochemically efficient micro/nano-structured $LiMn_{0.8}Fe_{0.2}PO_4$ electrodes were designed by controlling synthesis parameters. I demonstrated that control of the size and shape of the $LiMn_{0.8}Fe_{0.2}PO_4$ crystals as well as of the particles' tendency toward oriented agglomeration (mesocrystal) is possible by applying synthesis route. Furthermore, performance enhancement of $LiMn_{0.8}Fe_{0.2}PO_4$ has been realized by a morphology tailoring from ellipsoidal-shaped mesocrystals into flake-shaped mesocrystals. The origin of the enhanced electrochemical performance is investigated in terms of the primary particle size, porosity, anti-site defect concentration, and secondary particle shape. I believe that this work provides one of the routes to design electrochemically-favorable meso/nano-structures, which is of great potential for improving the battery performance by tuning the morphology of particles at the multi-length scale.

A thorough understanding on the electronic structure of $LiMn_{0.8}Fe_{0.2}PO_4$ can provide a guide to design high performance multi-transition-metal olivine materials, since the electronic structure comprises the electrochemical potential and structural stability of cathodes during battery operation. Thus, in Chapter 3, in order to investigate the electronic-structure effects of each transition metal (Mn and Fe) on the electrochemical performance, I performed synchrotron-based soft and hard x-ray absorption spectroscopy (sXAS and XAS), and quantitatively analyzed the changes of

the transition-metal redox states in the carbon-coated $LiMn_{0.8}Fe_{0.2}PO_4$ electrodes during the electrochemical reaction. I believe that our comprehensive as well as complementary analyses using *ex situ* sXAS and *in situ* XAS can provide clear experimental evidence on the reaction mechanism of $LiMn_{0.8}Fe_{0.2}PO_4$ electrodes during battery operation.

In chapter 4, the kinetic processes during lithiation/delithiation reaction of $Li_xMn_{0.8}Fe_{0.2}PO_4$ were investigated through *in situ* x-ray diffraction (XRD) and *in situ* electrochemical impedance spectroscopy (EIS) combined with galvanostatic intermittent titration technique (GITT), by which unprecedented insights on the phase propagation and sluggish kinetics of $LiMn_{0.8}Fe_{0.2}PO_4$ (LMFP) cathode materials are delivered. *In situ* analyses on the carbon-coated LMFP mesocrystal disclosed that the phase-propagation mechanism of LMFP differs during lithiation/delithiation process, and the sluggish kinetics of LMFP mesocrystal and resultant limitation of obtainable discharge capacity is featured from significant reduction of apparent Li^+ diffusivity during cycling through the region governed by Mn redox reaction. Being an in-depth characterization on the *in operando* kinetics of LMFP mesocrystal, I believe that this work provides fundamental understandings needed for proceeding to high-performance Mn-based olivine cathodes.

Finally, in Appendix 1, the graphene-wrapped $LiFePO_4$ ($LiFePO_4$/G) was introduced as a cathode material for Li-ion battery with an excellent rate capability. A straightforward solid-state reaction between graphene oxide-wrapped $FePO_4$ and a lithium precursor resulted in highly conducting $LiFePO_4$/G composites, which are featured by ~70-nm sized $LiFePO_4$ crystallites with robust connection to external graphene network. This unique morphology enables all $LiFePO_4$ particles to be readily accessed by electrons during battery operation, leading to remarkably enhanced rate capability. The *in situ* electrochemical impedance spectra were studied in detail throughout charge and discharge processes, by which enhanced electronic conductance

and thereby reduced charge transfer resistance was confirmed as the origin of the superior performance in the novel $LiFePO_4$/G.

Keywords: Li-ion battery, $LiMnPO_4$, $LiMn_{0.8}Fe_{0.2}PO_4$, Li^+ diffusivity, Electronic conductivity, Mesocrystal, Rate capability, Morphology control, Electronic structure, X-ray absorption spectroscopy, Electrochemical impedance spectroscopy, Galvanostatic intermittent titration technique, X-ray diffraction, First-order phase transition, Carbon coating, Graphene wrapping.

Student Number: 2010-22761

Table of Contents

List of Figures

Chapter 1.

Chapter 2.

Chapter 3.

Fig. 3-16. (Color) Partial electron yield (PEY) spectra of O *K*-edge sXAS at different depths of charge/discharge levels. The three-peak absorption edge features are marked by the asterisks.

Fig. 3-17. (Color) (a) The first charging process of the in situ cell at a rate of 0.05 C, and circles in the voltage profile indicate the intervals of x-ray absorption fine structure (XAFS) scans. (b-c) Normalized Fe and Mn *K*-edge XAFS spectra at different depths of charge levels. The insets show (b) Fe and (c) Mn *K*-edge XANES spectra during delithiation.

Fig. 3-18. (Color) FTIR spectra of the $LiMn_{0.8}Fe_{0.2}PO_4$ mesocrystal. The symmetric P-O stretching vibration of the $LiMn_{0.8}Fe_{0.2}PO_4$ mesocrystal is located at 977 cm^{-1}, which is similar to the previous report in which the vibration mode of defect-free $LiMn_{0.75}Fe_{0.25}PO_4$ was observed [26].

Fig. 3-19. (Color) *In situ* Fourier transformed Mn *K*-edge extended x-ray absorption fine structure (EXAFS) with different degrees of delithiation (*x* value), with a schematic representation of Jahn-Teller distortion.

Fig. 3-20. (Color) Schematic illustration of the substitution effect on the electronic structures in $Li_xMn_yFe_{1-y}PO_4$, indicating that the replacement of Mn^{3+} by Fe^{3+} alleviates the Jahn-Teller distortion and energy splitting of the Mn 3*d*-orbitals [28]. Note that the energy diagram is not to scale.

Chapter 4.

Appendix 1.

Fig. A.1-15. (Color) (a) Charge-transfer resistance and (b) apparent Li^+ diffusivity of graphene-wrapped $LiFePO_4$ and graphene-wrapped commercial $LiFePO_4$ at different state of charge (delithiation) and discharge (lithiation). Different scales on the axis should be noted for charge-transfer resistance. The red and green solid lines represent the voltage profiles of the graphene-wrapped $LiFePO_4$ and graphene-wrapped commercial $LiFePO_4$, respectively.

List of Tables

Chapter 2.

Appendix 1.

Chapter 1.

Mn-Based Olivine Materials as a Cathode Material

Lithium-ion battery (LIB) defines an electrical device that convert the chemical energy of certain reactions into electricity. Due to the best energy densities, no memory effect, and negligible loss of the charge while it is not in use, lithium-ion battery is one of the most important and greatly appealing power sources in the twenty-first century for energy storage [1-4]. The main usages for Li-ion batteries include cellular phones, digital cameras, laptops, and any other portable devices [4]. In addition, as the amount of fossil fuels gradually decreases, the importance of Li-ion batteries is further highlighted as an alternative power supply of plug-in hybrid electric vehicles (PHEVs) and hybrid electric vehicles (HEVs) [1-4].

Schematic operation mechanism and energy diagrams of Li-ion batteries are shown in Fig. 1-1. The open-circuit voltage is obtained by the electrochemical potential difference of Li between the cathode and anode. During charging, the Li ions migrate from the cathode to the anode through the electrolyte and the electrons flow through the external circuit from the cathode into the anode, with the increase of the cell voltage. On the contrary, the electron and Li ions are extracted from the anode and then inserted into the cathode with the decrease of the cell voltage during discharging. Therefore, the active materials used in both electrodes apparently play pivotal roles in determining the performance of the LIBs [1-4].

In the past decade, with significant advances in nanotechnology and materials science, numerous nanostructured materials have been applied as the electrode

materials. Among them, $LiMnPO_4$ has been regarded as a promising candidate for positive electrodes in LIBs because of its high theoretical capacity, higher redox potential, long cycle life, superior safety, environmental benignity, and low cost [5-7]. Despite several advantages, this material has inherent limitations to be commercialized, which accelerates extensive research on the material. In this respect, this chapter deals with several efforts that has been made to enhance the $LiMnPO_4$.

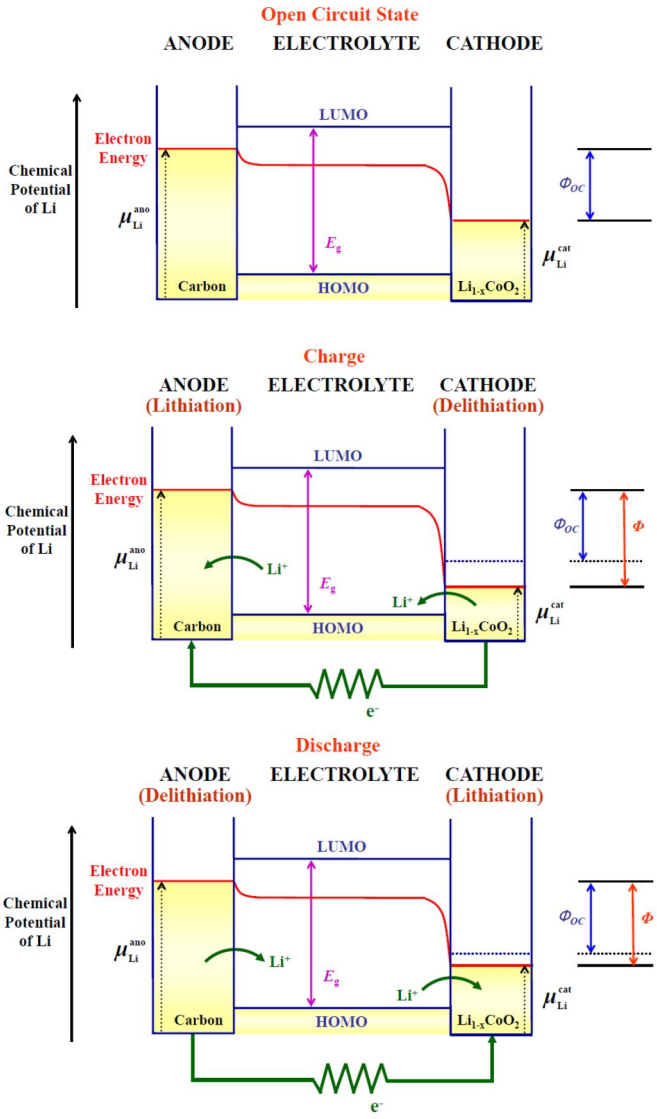

Fig. 1-1. (Color) Schematic energy diagram of Li-ion batteries at open-circuit, charged, and discharged state.

1.1. Olivine Structured $LiMnPO_4$ Cathode Materials

The lithium transition metal phosphate Li*M*PO_4 (*M* = Fe, Mn, Co, Ni) with olivine structure have attracted great attention as promising candidates for cathode materials of lithium-ion batteries due to their high theoretical capacity, long cycle life, superior safety, environmental benignity, and low cost [5-7].

Figure 1-2 shows the structure of olivine [8]. Transition metal ions exist at octahedral sites and these octahedra *M*O_6 are corner-sharing with three tetrahedra PO_4 and edgesharing with one PO_4. *M* ions in *M*O_6 are slightly shifted toward opposite side of edge-shared PO_4 because of the electrostatic repulsion between *M* ion and P ion. Li ions form linear chains of edge sharing octahedra along the b axis. Along the one-dimensional channel [010], Li ions diffuse from the octahedral site to adjacent octahedral site through intermediate tetrahedral site [9,10].

Among various olivine-structured materials, $LiFePO_4$ has been attracted as the best candidate of cathode material for large-scale application due to its intrinsic structural and chemical stability due to strong P-O covalent bonds that could lead to safe and long cycle life batteries [5-7]. Furthermore, olivine $LiFePO_4$ is composed of low cost and environmentally benign Fe and PO_4 moieties, which is an important merit for large scale applications. The discharge potential of $LiFePO_4$ is about ~3.4V vs. Li^+/Li and no obvious capacity fading was observed even after several hundred cycles. Its capacity approaches 170 mAh/g, higher than that obtained by $LiCoO_2$, and moreover, it is very stable during charge/discharge. One of the main obstacles for practical applications of $LiFePO_4$ is its poor rate capability, which can be attributed to slow kinetics of lithium-ion diffusion coefficient (10^{-14} to 10^{-16} cm^2/s) and the poor

electronic conductivity (<10^{-9} S/cm) [5-7]. Since its discovery by John Goodenough and coworkers, a number of intensive researches have been done to overcome these limitations via nanostructural engineering, such as particle size reduction, cation doping, and carbon coating. These strategies have advanced the electrochemical performances considerably.

However, due to the intrinsic problem of low energy density resulting from a low Fe^{2+}/Fe^{3+} redox potential of ca. ~3.4 V vs. Li^+/Li, $LiMnPO_4$ is considered to be the best candidate among all olivine cathode materials owing to its redox potential Mn^{2+}/Mn^{3+} of ~4.1 V vs. Li^+/Li, which is is similar to that of $LiCoO_2$, presently the most widely used cathode (Fig. 1-3) [11-13]. Also, the availability of Mn in nature corresponds with that of Fe. However, the use of $LiMnPO_4$ in electrochemical applications has been limited by its extremely poor electronic conductivity (<10^{-12} S/cm), low lithium diffusion rate (10^{-14} to 10^{-16} cm^2/s), and Jahn–Teller distortion during the charge/discharge process [11-13]. So far, considerable efforts have been made to overcome these limitations by improving the intrinsic properties of $LiMnPO_4$, including modifying surface with electronically conductive layers, reducing Li^+-diffusion lengths to the nanoscale dimension by morphological control, or substituting partial Mn ions with other cations to form a solid solution of $LiMn_{1-y}M_yPO_4$ (M = Fe, Co, Ni, Si, etc.) [14-20].

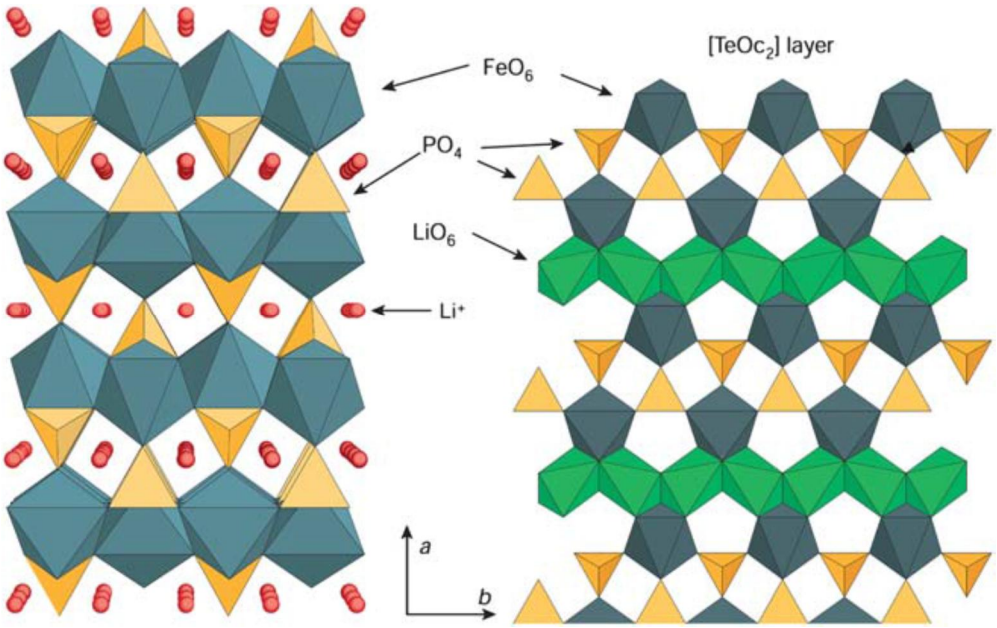

Fig. 1-2. (Color) The crystal structure of olivine $LiFePO_4$ in projection along [001]. From Ref. [8].

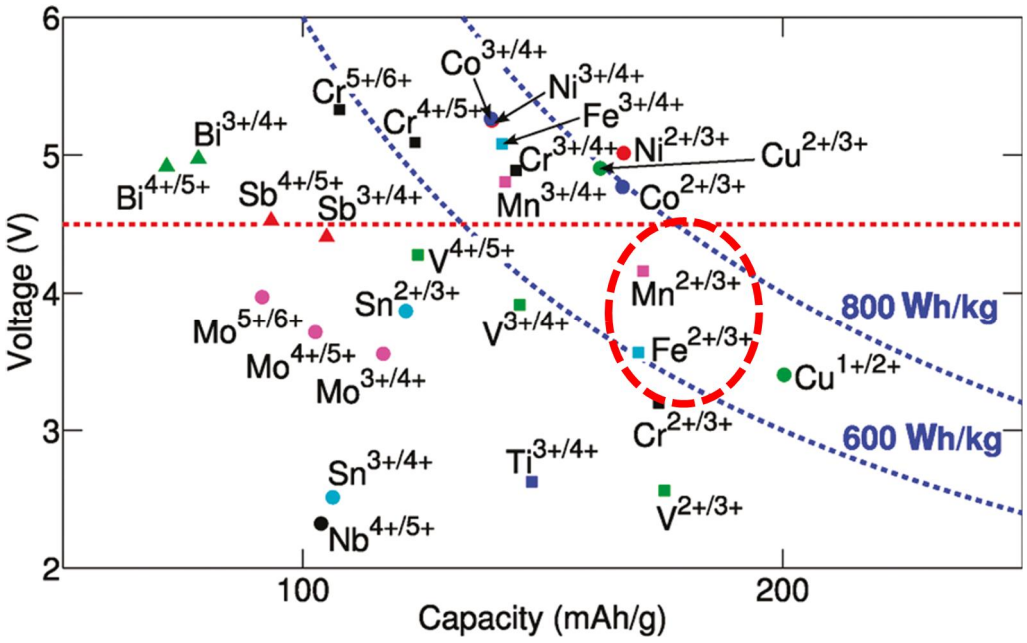

Fig. 1-3. (Color) Average voltage versus capacity for different redox couples in phosphates. From Ref. [11].

1.2. Nanosized $LiMnPO_4$

Size reduction to nanoscale dimension has been employed in a number of studies as an effective method to improve the high-rate capacity and cycling stability of $LiMPO_4$ (M = Fe or Mn). The capacities of $LiMPO_4$ at high current rates are believed by many to originate from its low ionic conductivity. Logically, the high-rate performance can be improved by reducing particle size because the transport distance for electrons and Li-ions is thus reduced [15,18,21]. Recent studies also show that ionic diffusion constant depends on particle size with diffusion in nanosized particles being much faster than in micrometre-sized particles or bulk (Fig. 1-4) [15,18,21]. Many other studies have been conducted to mitigate lithium diffusion limitations in $LiMPO_4$ via various nanostructure such as nanoparticle, nanorod, nanowire, and nanoplate (Fig. 1-5) [22-25].

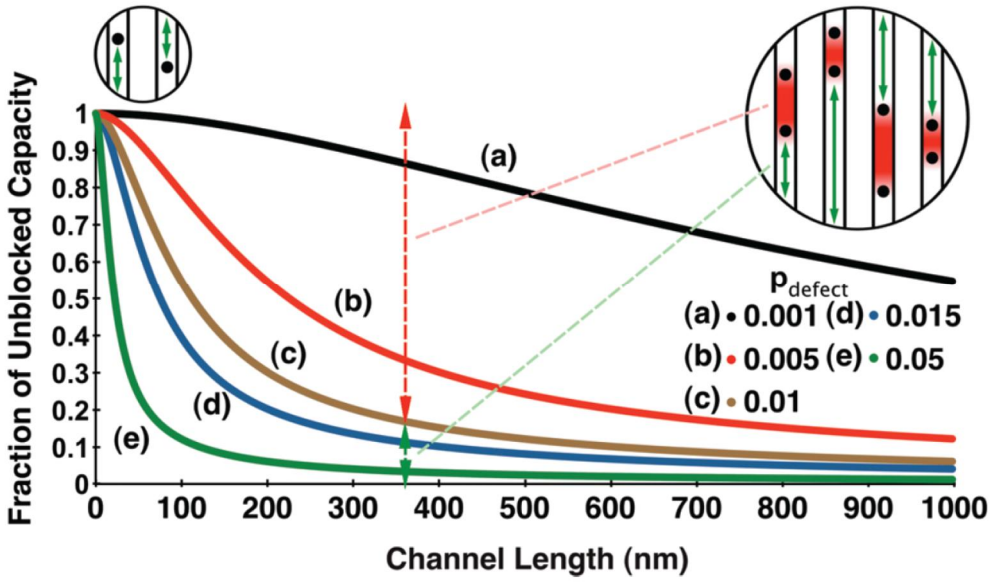

Fig. 1-4. (Color) Expected unblocked capacity vs channel length in $LiFePO_4$ for various defect concentrations. From Ref. [21].

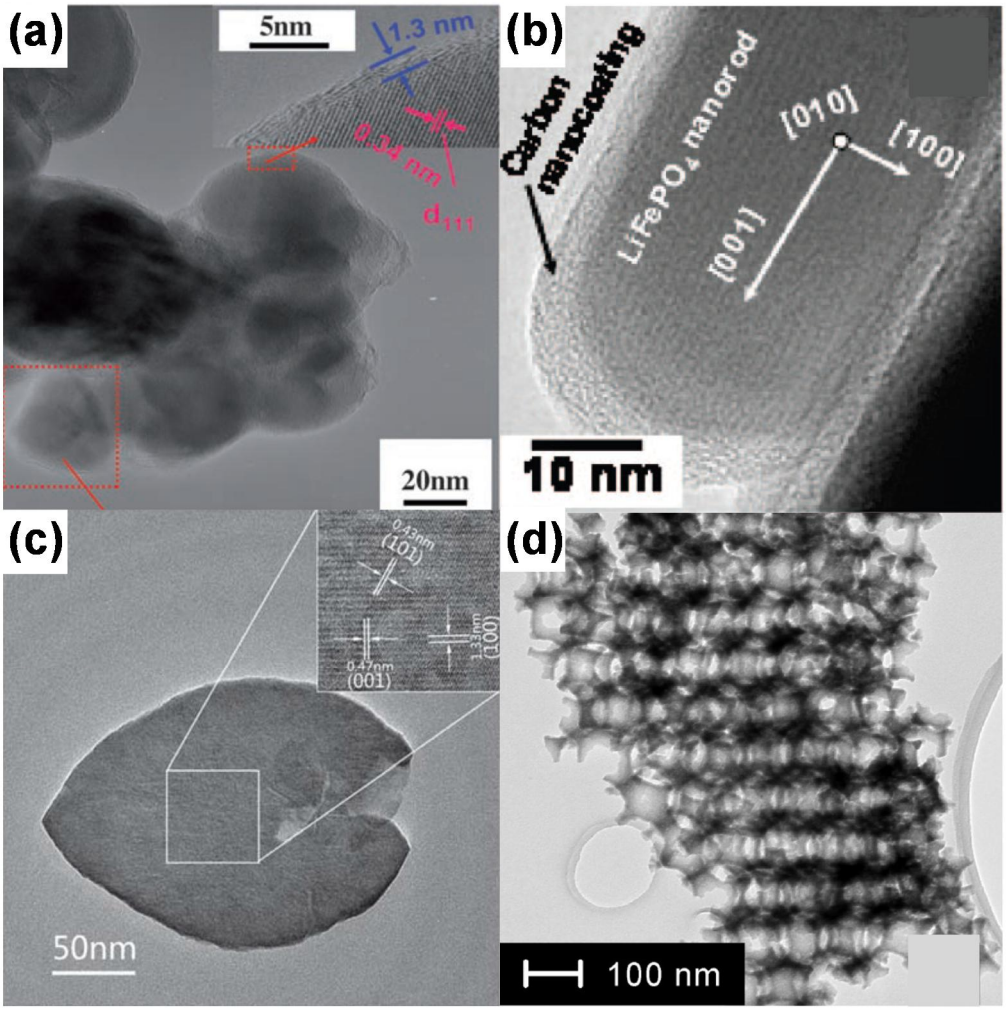

Fig. 1-5. Various nanostructured Li*M*PO$_4$ (*M* = Fe or Mn) such as (a) nanoparticles, (b) nanorods, (c) nanoplates, and (d) porous structures. From Refs. [22-25].

1.3. Coating with Electron-Conductive Materials

Carboneous material coating is one of the most important techniques used to improve the specific capacity, rate performance and cycling life of $LiMnPO_4$ [18,22-25]. The main role of carbon coating is to enhance the surface electronic conductivity of $LiMnPO_4$ particles so that the active materials can be fully utilized at high current rates. Carbon coating also reduces the particle size of $LiMnPO_4$ by inhibiting particle growth during sintering (Fig. 1-6(a)) [22]. Many reseachers have observed the beneficial effect of carbon coating to depend on the structure, uniformity, thickness, loading and precursor of the coating. Graphene, which has excellent conductivity and unique 2D sheet-like structure, has already widely used as functional additives to raise the conductivity of $LiMnPO_4$ (Fig. 1-6(b)) [18].

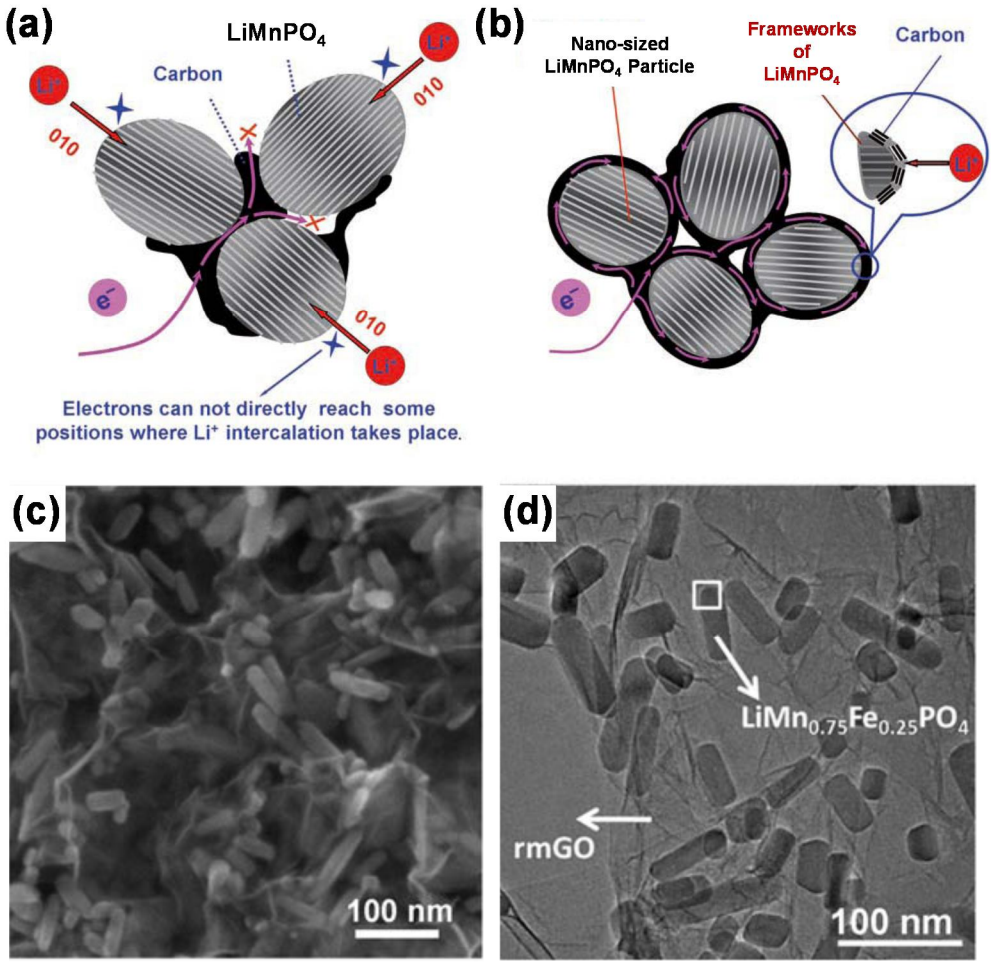

Fig. 1-6. (Color) (a) Electron-transfer pathway for $LiMnPO_4$ particles partially coated with carbon, and (b) designed ideal structure for $LiMnPO_4$ particles with typical nano-size and a complete carbon coating. (c) SEM and (d) TEM images of $LiMn_{0.75}Fe_{0.25}PO_4$/reduced graphene oxide nanocomposites. From Refs. [18,22].

1.4. Doping or Alloying with Other Transition Metals

Substituting partial Mn ions with other cations provides a practical way of enhancing the electrochemical performance particularly at higher rates [16-22]. One of the key limitations of $LiMnPO_4$ has been extremely low electronic conductivity, until now believed to be intrinsic to this family of compounds. S.-Y. Chung *et al*. reported that controlled cation nonstoichiometry combined with solid-solution doping by metals supervalent to Li^+ increases the electronic conductivity of $LiFePO_4$ (Fig. 1-7) [26]. Similarly, the small amount doping in $LiMnPO_4$ also enhances the electrochemical performance of $LiMnPO_4$, showing near-theoretical energy density at low charge/discharge rates and retaining significant capacity with little polarization at high rates.

J. Kim *et al*. demonstrated that the power capability of $LiFe_{0.05}Mg_{0.05}Mn_{0.9}PO_4$ can be significantly improved over pristine $LiMnPO_4$, in which small amounts of co-doping of Fe-Mg can serve as a nucleation enhancer in $LiMnPO_4$ framework [27]. Unfavorable Fe^{3+}-Mn^{2+} pairs during charging and unfavorable Mg^{2+}-Mn^{3+} pairs during discharging can make Mn^{2+}/Mn^{3+} transition more facile promoting the nucleation of the second phase (Fig. 1-8) [27].

Finally, the $LiMn_{1-x}Fe_xPO_4$ solid solution has been intensively studied. The $LiMn_{0.4}Fe_{0.6}PO_4$ exhibits even higher rate capability as a lithium battery cathode than $LiFePO_4$ of comparable particle size (Fig. 1-9) [19]. Instead of exhibiting binary lithiation states of pure $LiFePO_4$, the formations of metastable solid solutions covering a remarkable wide compositional range can reduce the misfit strain for the first-order phase transition and improve electrochemical kinetics [19].

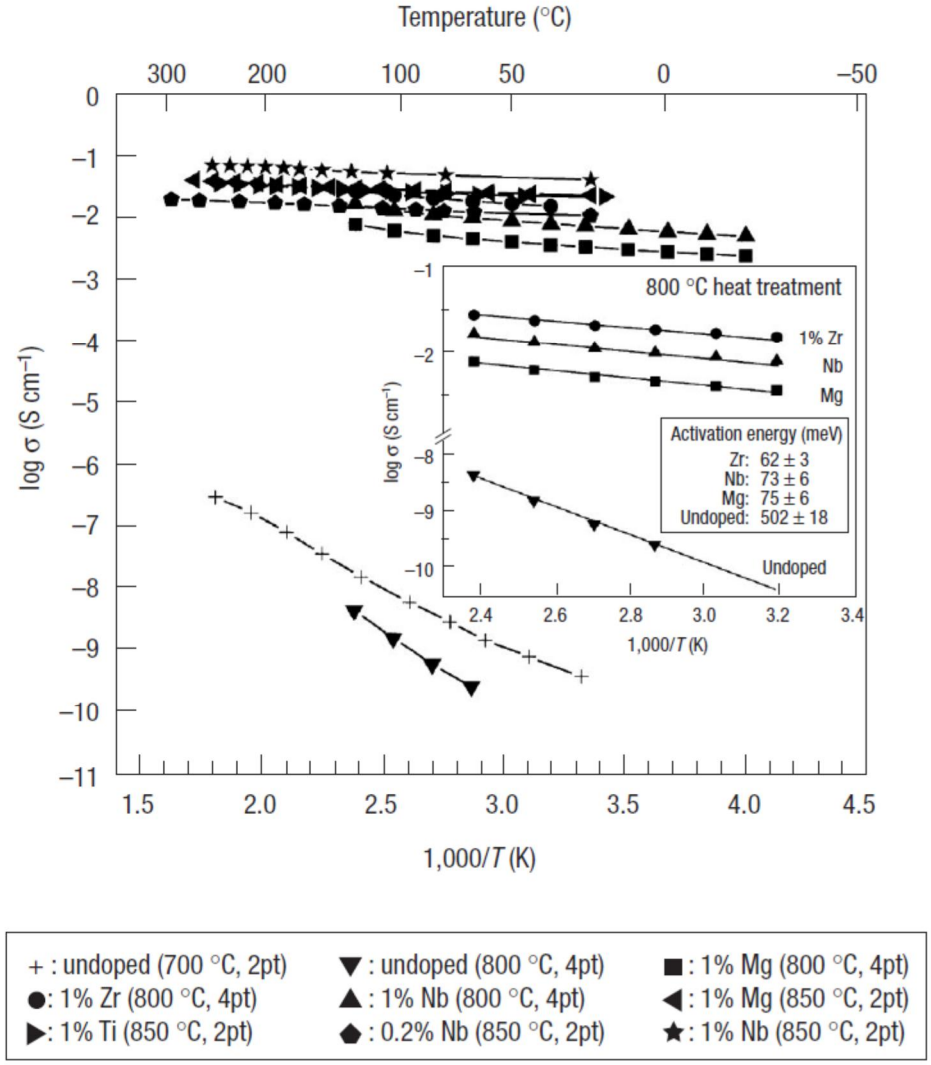

Fig. 1-7. Enhanced electrical conductivity of doped olivines of $Li_{1-x}M_xFePO_4$. From Ref. [26].

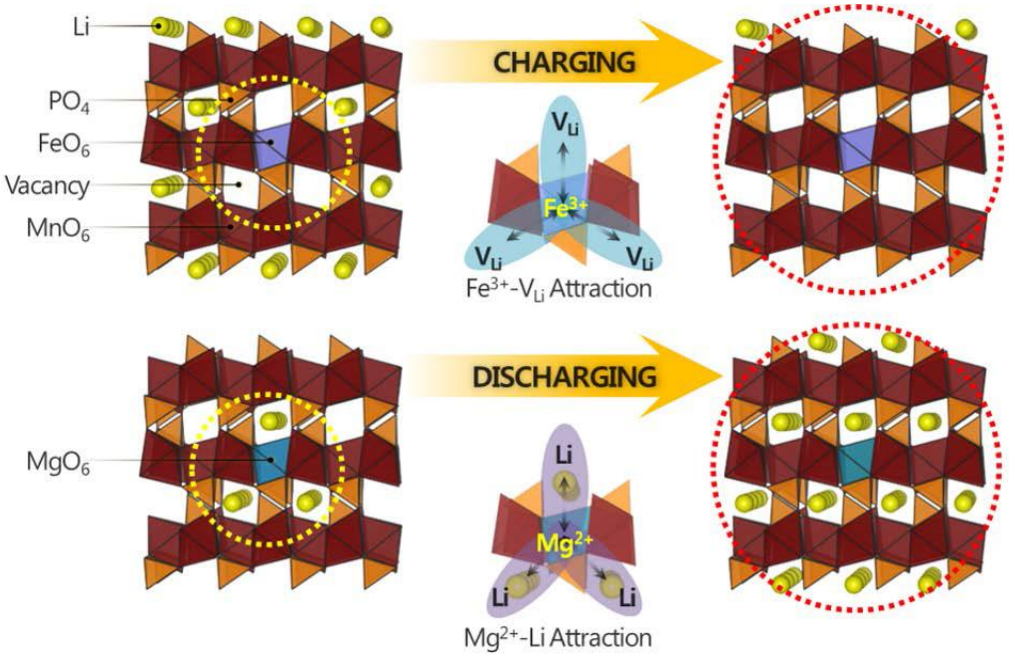

Fig. 1-8. (Color) Schematic illustration of the nucleation enhancing process in a multicomponent Mn based olivine cathode during charging and discharging (Yellow: Li, red: MnO_6, purple: FeO_6, blue: MgO_6, orange: PO_4, white: vacancy). Arrows are used to indicate the favorable interaction. From Ref. [27].

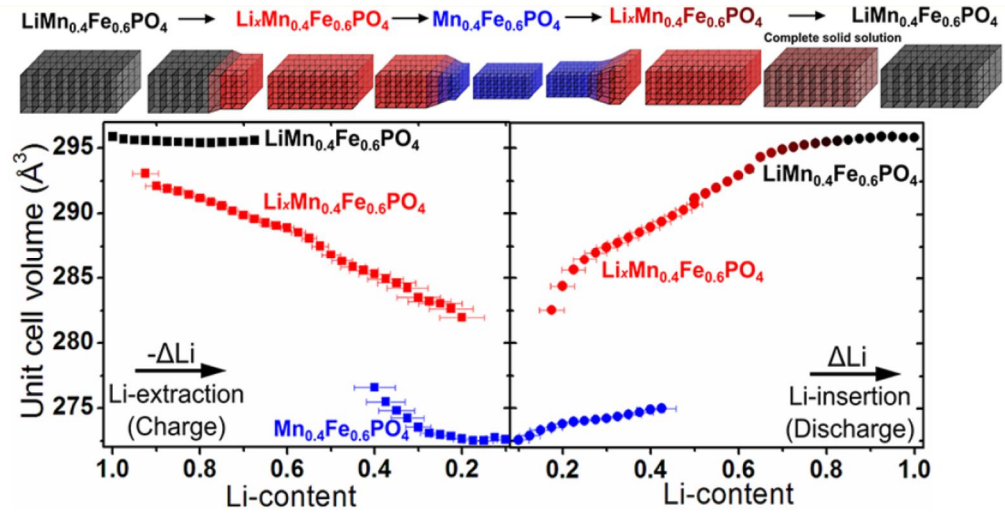

Fig. 1-9. (Color) Unit cell volumes determined by Rietveld refinement of operando XRD data measured during Li extraction (charge) and insertion (discharge), and schematic showing the coherent transformation model. The schematic corresponds to the observations during the first charge (Li extraction) and discharge (Li insertion) cycle showing hysteresis in the LMFP → L_xMFP step. From Ref. [19].

1.3. References

1. M. Winter and R. J. Brodd, What Are Batteries, Fuel Cells, and Supercapacitors?, *Chem. Rev*. 104 (2004) 4245.
2. M. S. Whittingham, Electrical Energy Storage and Intercalation Chemistry, *Science* 192 (1976) 1126.
3. K. Kang, Y. S. Meng, J. Breger, C. P. Grey, and G. Ceder, Electrodes with High Power and High Capacity for Rechargeable Lithium Batteries, *Science* 311 (2006) 977.
4. M. S. Whittingham, Lithium Batteries and Cathode Materials, *Chem. Rev*. 104 (2004) 4271..
5. A. K. Padhi, K. S. Nanjundaswamy, and J. B. Goodenough, Phospho-Olivines as Positive-Electrode Materials for Rechargeable Lithium Batteries, *J. Electrochem. Soc.* 144 (1997) 1188.
6. H. P. Subramanya, B. Ellis, N. Coombs, and L. F. Nazar, Nano-Network Electronic Conduction in Iron and Nickel Olivine Phosphates, *Nat. Mater*. 3 (2004) 147.
7. K. Amine, H. Yasuda, and M. Yamachi, Olivine $LiCoPO_4$ as 4.8 V Electrode Material for Lithium Batteries, Electrochem. *Solid-State Lett*. 3 (2000) 178.
8. J.-M. Tarascon and M. Armand, Issues and Challenges Facing Rechargeable Lithium Batteries, *Nature* 414 (2001) 359.
9. J. B. Goodenough and K.-S. Park, The Li-Ion Rechargeable Battery: A Perspective, *J. Am. Chem. Soc.* 135 (2013) 1167.
10. R. Malik, A. Abdellahi, and G. Ceder, A critical Review of the Li Insertion Mechanisms in $LiFePO_4$ Electrode, *J. Electrochem. Soc.* 160 (2013) A3179.

11. G. Hautier, A. Jain, T. Mueller, C. Moore, S. P. Ong, and G. Ceder, Designing Multielectron Lithium-Ion Phosphate Cathodes by Mixing Transition Metals, *Chem. Mater.* 25 (2013) 2064.
12. C. Delacourt, P. Poizot, M. Morcrette, J. M. Tarascon, and C. Masquelier, One-Step Low-Temperature Route for the Preparation of Electrochemically Active $LiMnPO_4$ Powders, *Chem. Mater.* 16 (2004) 93.
13. G. Li, H. Azuma, and M. Tohda, $LiMnPO_4$ as the Cathode for Lithium Batteries, *Electrochem. Solid-State Lett.* 5 (2002) A135.
14. G. Chen, A. K. Shukla, X. Song, and T. J. Richardson, Improved Kinetics and Stabilities in Mg-Substituted $LiMnPO_4$, *J. Mater. Chem.* 21 (2011) 10126.
15. M. Pivko, M. Bele, E. Tchernychova, N. Z. Logar, R. Dominko, and M. Gaberscek, Synthesis of Nanometric $LiMnPO_4$ via a Two-Step Technique, *Chem. Mater.* 24 (2012) 1041.
16. S. Wi, J. Kim, S. Lee, J. Kang, K. H. Kim, K. Park, K. Kim, S. Nam, C. Kim, and B. Park, Synthesis of $LiMn_{0.8}Fe_{0.2}PO_4$ Mesocrystals for High-Performance Li-Ion Cathode Materials. *Electrochim. Acta* 216 (2016) 203.
17. Y. K. Sun, S. M. Oh, H. K. Park, and B. Scrosati, Micrometer-Sized, Nanoporous, High-Volumetric-Capacity $LiMn_{0.85}Fe_{0.15}PO_4$ Cathode Material for Rechargeable Lithium-Ion Batteries, *Adv. Mater.* 23 (2011) 5050.
18. H. Wang, Y. Yang, Y. Liang, L. F. Cui, H. S. Casalongue, Y. Li, G. Hong, Y. Cui, and H. Dai, $LiMn_{1-x}Fe_xPO_4$ Nanorods Grown on Graphene Sheets for Ultrahigh-Rate-Performance Lithium Ion Batteries, *Angew. Chem. Int. Ed.* 123 (2011) 7502.
19. D. B. Ravnsbæk, K. Xiang, W. Xing, O. J. Borkiewicz, K. M. Wiaderek, P. Gionet, K. W. Chapman, P. J. Chupas, and Y. M. Chiang, Extended Solid

Solutions and Coherent Transformations in Nanoscale Olivine Cathodes, *Nano Lett.* 14 (2014) 1484.

20. M. S. Kim, J. P. Jegal, K. C. Roh, and K. B. Kim, Synthesis of $LiMn_{0.75}Fe_{0.25}PO_4/C$ Microspheres Using a Microwave-Assisted Process with a Complexing Agent for High-Rate Lithium Ion Batteries, *J. Mater. Chem. A* 2 (2014) 10607.
21. R. Malik, D. Burch, M. Bazant, and G. Ceder Particle Size Dependence of the Ionic Diffusivity, *Nano Lett.* 10 (2010) 4123.
22. Y. Yang, Y. Wang, E. Hosono, K. Wang, and H. Zhou, The Design of a $LiFePO_4$/Carbon Nanocomposite With a Core-Shell Structure and Its Synthesis by an In Situ Polymerization Restriction Method, *Angew. Chem. Int. Ed.* 47 (2008) 7461.
23. A. Vadivel Murugan, T. Muraliganth, and A. Manthiram, Comparison of Microwave Assisted Solvothermal and Hydrothermal Syntheses of $LiFePO_4/C$ Nanocomposite Cathodes for Lithium Ion Batteries, *J. Phys. Chem. C* 112 (2008) 14665.
24. C. Nan, J. Lu, C. Chen, Q. Peng, and Y. Li, Solvothermal Synthesis of Lithium Iron Phosphate Nanoplates, *J. Mater. Chem.* 21 (2011) 9994.
25. C. M. Doherty, R. A. Caruso, B. M. Smarsly, and C. J. Drummond, Colloidal Crystal Templating to Produce Hierarchically Porous $LiFePO_4$ Electrode Materials for High Power Lithium Ion Batteries, *Chem. Mater.* 21 (2009) 2895.
26. S.-Y. Chung, J. T. Bloking, and Y.-M. Chiang, Electronically Conductive Phospho-Olivines as Lithium Storage Electrodes, *Nat. Mater.* 1 (2002) 123.

27. J. Kim, Y.-U. Park, D.-H. Seo, J. Kim, S.-U. Kim, and K. Kang, Mg and Fe Co-doped Mn Based Olivine Cathode Material for High Power Capability, *J. Electrochem. Soc.* 158 (2011) A250.

Chapter 2.

Morphology Evolution of $LiMn_{0.8}Fe_{0.2}PO_4$ Mesocrystal for Advanced Cathode Materials in Lithium-Ion Batteries

2.1. Introduction

Construction of the advanced lithium-ion batteries which guarantee high energy density, long-term stability and lower costs has long been one of the most important topic due to their versatile use in various devices, such as portable electronic and electric/hybrid vehicles [1-3]. In order to serve as cathode materials for superior lithium-ion batteries, olivine-structured $LiFePO_4$ has been extensively studied due to their promising properties including high theoretical capacity, superior safety which derives from low volume change during lithium (de)intercalation, and low cost [4-6]. Even though the $LiFePO_4$ cathodes exhibited low energy density which results from their relatively low redox potential (3.4 V vs. Li^+/Li), continued studies on this field led to a solution with the introduction of Mn. Namely, the low redox potential of $LiFePO_4$ is complemented by higher redox potential of $LiMnPO_4$ (4.1 V vs. Li^+/Li), while the poor electronic/ionic conductivity of $LiMnPO_4$ is also compensated by alloying with $LiFePO_4$ [7,8]. Furthermore, it is now accepted that the kinetics inside the electrode can be enhanced by utilizing or extending solid-solution phase of $LiMn_{1-y}Fe_yPO_4$ over a certain composition ranges [9,10].

With binary transition metal phosphate $LiMn_{1-y}Fe_yPO_4$ being a robust chemistry to realize superior lithium-ion battery cathodes, various attempts have been made to

fabricate those materials with electrochemically favorable morphologies [11-21]. A typical approach is reducing the particle size down to several tens of nanometers, since the synthesis of the nanosized particles has the merit of improving the rate performance due to the enhanced conductance by reducing Li^+-transport paths and increasing the interfacial area between the electrolyte and active materials [22,23]. However, despite the dramatic enhancement of battery performance, nanosizing is not yet practical due to its low tap density (0.3 - 0.5 g/cm^3) compared with the commercial cathode materials (> 1.0 g/cm^3), leading to the poor volumetric energy density [2,24].

In this perspective, fabrication of $LiMn_{1-y}Fe_yPO_4$ with mesocrystalline structure is an attractive choice among possible alternative morphologies [26-30]. Mesocrystals, which represent crystallographically-oriented nanoparticle superstructures, guarantee both the inherent and uniform distribution of porosity associated with the well-defined orientation of each nanoparticle and the high tap density (also high volumetric energy density) associated with the micron-sized secondary particles [27-28]. However, fabrication of olivine-type transition metal phosphate mesocrystals has been explored only for single transition metal chemistry of $LiFePO_4$ or $LiMnPO_4$.

Herein, such hierarchical $LiMn_{0.8}Fe_{0.2}PO_4$ mesocrystals have successfully been synthesized, by controlling precursor ratio and pH of precursor solutions. Accordingly, the correlation between macro/microstructural features (secondary particle shape, primary particle size, porosity, anti-site defect concentration, and charge-transfer resistance) and electrochemical performance was thoroughly examined. Some interesting relations between the electrochemical performance and secondary-particle morphologies of the mesocrystals were observed and identified as for $LiMn_{0.8}Fe_{0.2}PO_4$, which sheds an insight to the rule of designs for the

electrochemically-favorable structure of an electrode.

2.2. Experimental Section

Materials Preparation: The $LiMn_{0.8}Fe_{0.2}PO_4$ (LMFP) mesocrystals were synthesized by the solvothermal method. At first, manganese acetate tetrahydrate ($Mn(CH_3COO)_2 \cdot 4H_2O$: 0.008 mol) and iron nitrate nonahydrate ($Fe(NO_3)_3 \cdot 9H_2O$: 0.002 mol) were dissolved in 10 ml of deionized (DI) water. The precursor aqueous solution was mixed with N,N-dimethylformamide (DMF) (C_3H_7NO: 140 ml) at 80°C. For the formation of the solid solution of Mn and Fe, the mixed solution was stirred for 1 h at 80°C, and cooled down to room temperature. Subsequently, the controlled amount of phosphoric acid (H_3PO_4), lithium hydroxide monohydrate ($LiOH \cdot H_2O$), and ascorbic acid ($C_6H_8O_6$) were introduced to the resulting solution to adjust the molar ratio of Li:transition metal (*TM*):PO_4 in precursor solution to be $3x$:1:x ($1 \leq x \leq 1.3$). Since the formation of LMFP is sensitive to the pH value during solvothermal reaction, a different amount of HNO_3 (1.6 ml - 3.2 ml) were injected to control the pH of the solution [19,20]. The mixed solution was transferred to a Teflon-lined autoclave, and heated at 180°C for 12 h. The resulting solution was centrifuged, and thoroughly washed with deionized water and acetone, followed by drying at 60°C overnight. The obtained mesocrystals were labelled as LMFP_3*x*_*y* (*x*: relative amount of PO_4^{3-} compared with transition metal, *y*: amount of HNO_3). The obtained LMFP mesocrystals were carbon-coated by mixing the as-synthesized LMFP powders and sucrose dissolved in ethanol (LMFP:sucrose = 7:3 by weight), followed by drying and calcination them at 700°C for 3 h under H_2/Ar (4 vol. % H_2) atmosphere.

Chemical delithiation of the LMFP was performed by reacting carbon-coated LMFP mesocrystals with nitronium tetrafluoroborate (NO_2BF_4) in acetonitrile. At

first, 500 mg of NO_2BF_4 was dissolved into 200 ml acetonitrile with vigorous stirring. Then, 300 mg of carbon-coated LMFP samples were added into the mixture. The reaction was performed in an argon-filled glove box. The resultant was washed with acetonitrile several times to remove unwanted sub-products.

Materials Characteriazation: The crystal structure and the grain size of the samples were characterized by x-ray diffraction (XRD, D8 Advance: Bruker). The morphology of the samples was observed by a field-emission scanning electron microscopy (FE-SEM, Merlin Compact: Zeiss) and a high-resolution transmission electron microscopy (HRTEM, JEM-3000F: JEOL, Japan). The pH values of the precursor solution were recorded using a pH meter (CR-10: Denver Instrument). The nitrogen adsorption-desorption isotherms (Micromeritics ASAP 2020) were measured at 77 K, and the specific surface area and pore size distribution of the samples were calculated using the Brunauer-Emmet-Teller (BET) and the Barret-Joyner-Halenda (BJH) methods, respectively. FTIR spectra (Tensor27, Bruker) were obtained using KBr pellets. An elemental analyzer (Flash EA 1112: Thermo Electron Corp.) was employed to determine the amount of carbon.

Electrochemical Measurements: All electrochemical tests were carried out using 2016 coin-type half cells with a Li counter electrode. The active materials, super P carbon black, and a polyvinylidene fluoride binder were mixed at a weight ratio of 7:2:1. The active material was spread on an Al current collector with a loading level of ~1 mg/cm^2. The electrolyte contained 1 M $LiPF_6$ in ethylene carbonate and diethyl carbonate (EC:DEC = 1/1 vol. %) (Panax Etec). In the case of 0.1 M $LiPF_6$ electrolyte, ordinary 1 M $LiPF_6$ electrolyte was diluted to one tenth of the concentration with an EC/DEC solution. The cycling tests were performed by a

constant current-constant voltage (CC-CV) and a constant current (CC) mode during the charge and discharge, respectively. The electrodes were charged to 4.5 V at a C/20 rate, then further charged at 4.5 V until the current decays to C/50, and discharged to 2 V at various current rates. The cyclic voltammetry (CV) and electrochemical impedance spectra (EIS) were obtained using a potentiostat (CHI 608C: CH Instrument Inc). The CV curve was obtained with the scan rate of 10 mV/s, in the voltage range from 2.5 V to 4.7V. The EIS measurements were carried out by applying a 5 mV harmonic perturbation signal in the frequency range from 10 mHz to 100 kHz at the open circuit voltage (OCV).

2.3. Results and Discussion

Figure 2-1 shows an overview on the morphologies of $LiMn_{0.8}Fe_{0.2}PO_4$ (LMFP) mesocrystals synthesized via a solvothermal method. As shown in Fig. 2-1, the micron-sized aggregated particles were observed within the whole range of our synthetic conditions, exhibiting characteristic features (ellipsoidal or flake shape). The SEM images were arranged by 4 different ratios of Li:transition metal (*TM*):PO_4, and placed at the *y* axis with respect to the pH value of the precursor solution. Figure 2-1 clearly shows that the size and shape (ellipsoidal or flake) of the LMFP mesocrystals are highly dependent upon the pH value and Li:*TM*:PO_4 ratio in the initial suspension. The secondary particles became larger when the amount of HNO_3 in the solution was increased, and the tendency toward the size enlargement becomes stronger at relatively low pH ranges. Even dumbbell-shaped particles were included in low pH condition, which is known as a result of further growth of the platelet- or ellipsoidal-shaped mesocrystals [31,32]. The effect of pH value of the initial solution on the size of secondary particles is quite obvious, and is consistent with the previous studies reported that the mesocrystals synthesized at high pH values finally developed into smaller primary/secondary particles since the highly acidic condition can increase the solubility of the LMFP particles during the solvothermal reaction [20,21,27,33,34]. This increased solubility accelerates the dissolution-crystallization (so-called Ostwald ripening) of the LMFP particles [17]. The morphology evolution from LMFP_3.9_1.8 to LMFP_3.9_3.2 provide an evidence for the dominating crystal growth mechanism.

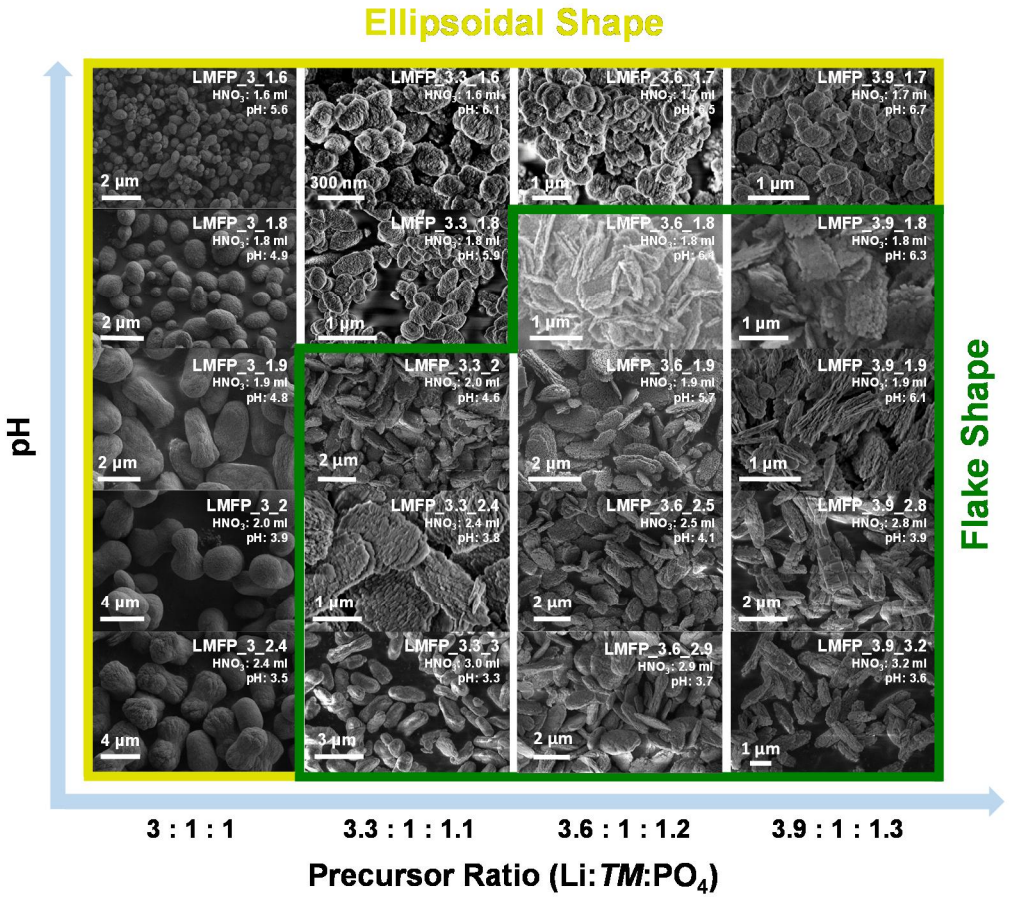

Fig. 2-1. (Color) SEM images of $LiMn_{0.8}Fe_{0.2}PO_4$ mesocrystal samples prepared with different precursor ratios (Li:*TM*:PO_4) and various pH-values.

The shape of the particles was also susceptible to pH values and Li:*TM*:PO_4 ratios in the initial precursor solutions. When the precursor solution contained higher content of proton, lithium, phosphate, and transition metal ions, shape of the synthesized secondary particles were generally evolved into flake shape, while the secondary particles synthesized from lower content of such ions were ellipsoidal shape. In short, shape and size of the mesocrystals were greatly changed by pH and the precursor ratio of the reactant solution in the solvothermal synthesis, and it might be attributed to the different nucleation conditions and adsorption tendency of chelating agents (ascorbic acid) [26,27,38]. The results were schematically summarized in Fig. 2-2.

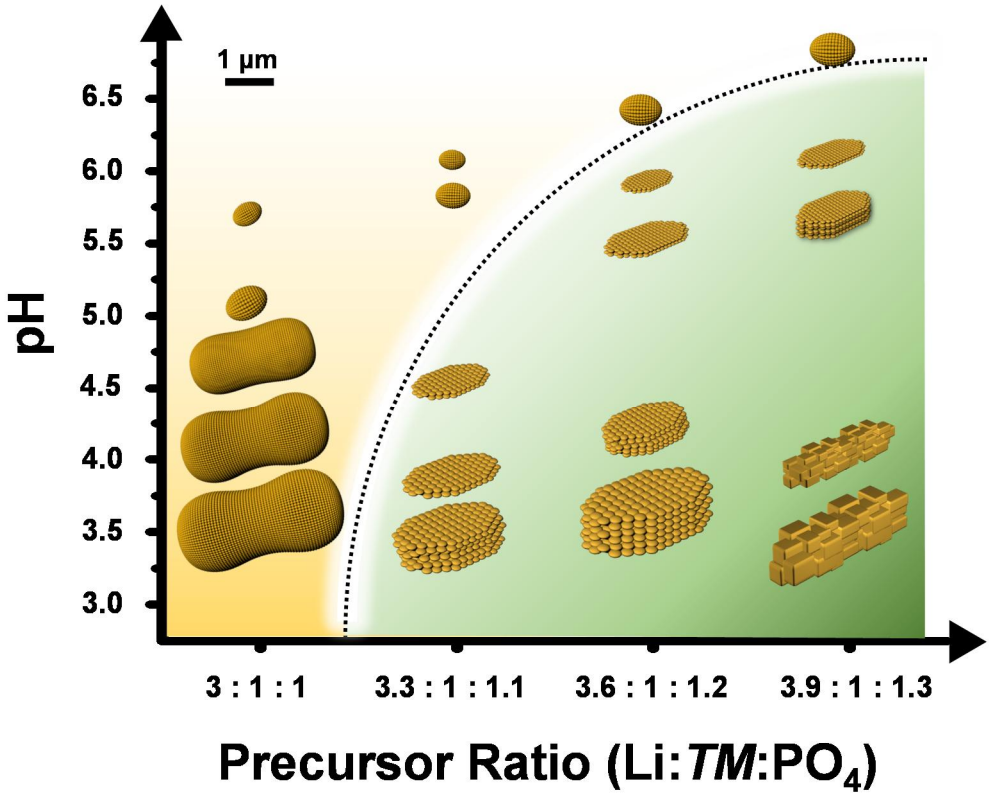

Fig. 2-2. (Color) Schematic diagram exhibiting the morphological changes in $LiMn_{0.8}Fe_{0.2}PO_4$ mesocrystals synthesized with different precursor ratios (Li:*TM*:PO_4) and various pH-values.

In order to study the effects of the synthetic condition on the electrochemical properties, 6 characteristic samples were selected as model compounds. X-ray diffraction of the selected LMFP mesocrystals corresponds to the orthorhombic olivine structure (Fig. 2-3), small fraction of Li_3PO_4 was found in the high precursor concentration samples, such as LMFP_3.6_1.7, LMFP_3.6_1.8, and LMFP_3.9_1.8, though. This small amount of Li_3PO_4 may come from the excess supply of precursor ions and high pH value. Such assumption can be explained by the previous studies showing that the solubility of Li_3PO_4 in high pH solution is insufficiently low [17,35-36]. However, small fraction of Li_3PO_4 in cathode samples aren't expected to seriously degrade the whole battery performance, since Li_3PO_4 is known to enhance lithium-ion conduction when small amount of Li_3PO_4 exists on the active material surface due to its high lithium-ion conductivity [37]. Although excess amount of Li_3PO_4 on cathode surface can act as an inactive part of the cathode materials which reduces the effective weight of the cathode [38], the amount of Li_3PO_4 in our case doesn't seem to possess major portion.

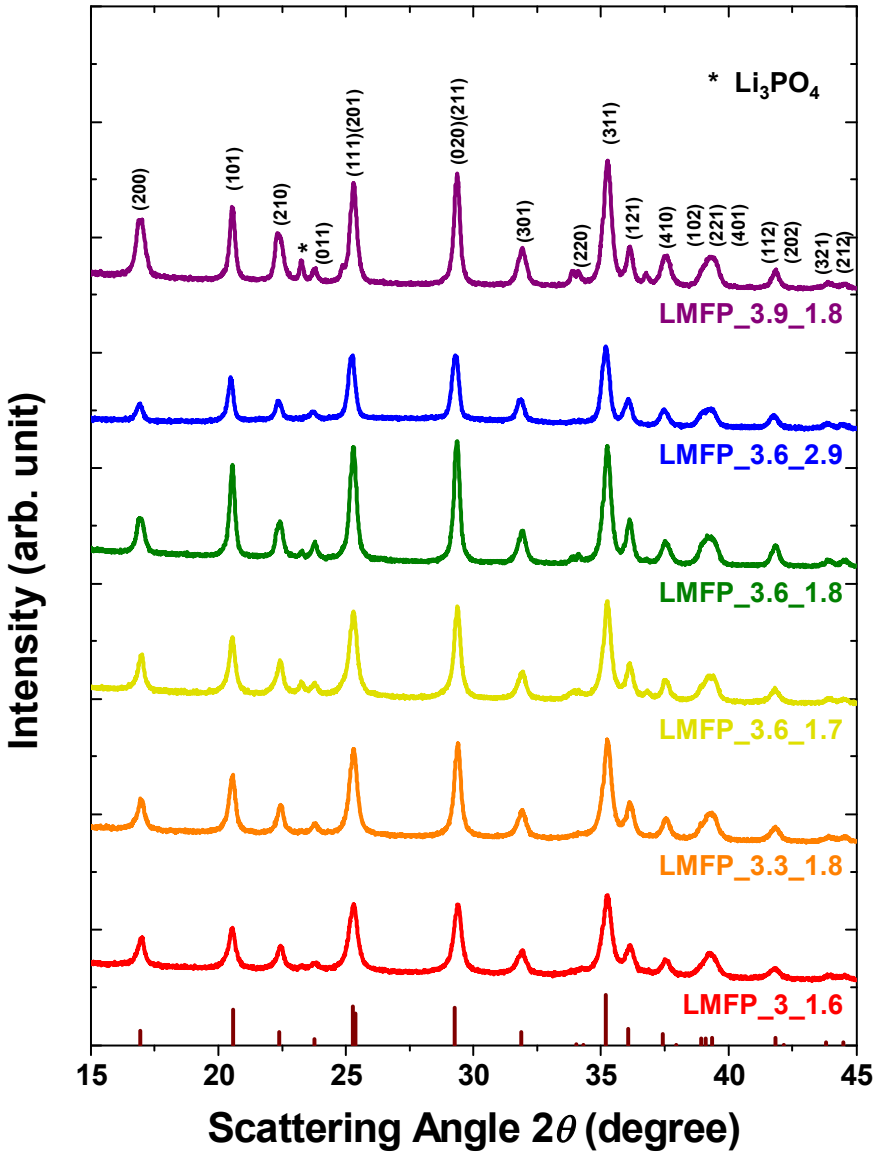

Fig. 2-3. (Color) XRD patterns of the selected $LiMn_{0.8}Fe_{0.2}PO_4$ mesocrystal samples.

The mesocrystalline feature (i.e., existence of crystallographic alignment among primary particles comprising of each secondary particle) of the selected LMFP samples were identified by TEM analysis (Fig. 2-4). The selected area electron diffraction (SAED) and the Fast Fourier Transform (FFT) pattern throughout the broad range of the LMFP particles exhibits spot patterns, which indicates that primary particles are highly oriented within the mesocrystals (Fig. 2-5). Such mesocrystalline characteristics and shape of the secondary particle are known to be determined by primary particles' stabilization and selective docking between crystal surfaces of stabilized primary particle [32].

Based on the TEM results, both ellipsoidal- and flake-shaped LMFP mesocrystals are elongated in the [001] direction. Meanwhile, the primary particles of the flake-shaped LMFP mesocrystals are mainly aligned in the [010] and [001] directions, and terminated by (200) plane as the primary exposed surface. These orientated attachments can be attributed to the different surface energies of the LMFP primary particles and the selective adhesion of crystal surface stabilized by ascorbic acid and mixed solvent [39]. Ceder's group reported that the relative low-energy surfaces of the olivine structured $LiMPO_4$ (M = Fe and Mn) are (100), (010), (011), (101), and (201) [40]. Islam's group also confirmed that the (100) and (010) planes have the lowest attachment energies in the olivine $LiFePO_4$, which is consistent with our observations of the mesocrystals that are elongated along the [001] direction [41].

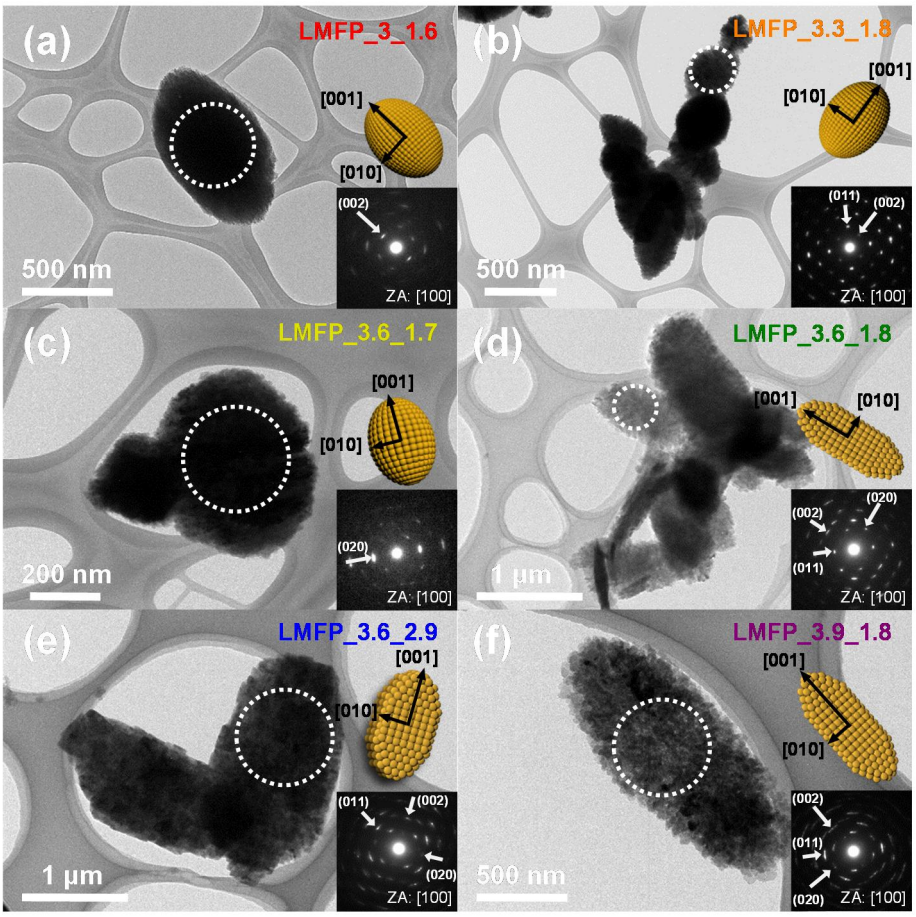

Fig. 2-4. (Color) HRTEM images and related SAED patterns of (a) LMFP_3_1.6, (b) LMFP_3.3_1.8, (c) LMFP_3.6_1.7, (d) LMFP_3.6_1.8, (e) LMFP_3.6_2.9, and (f) LMFP_3.9_1.8.

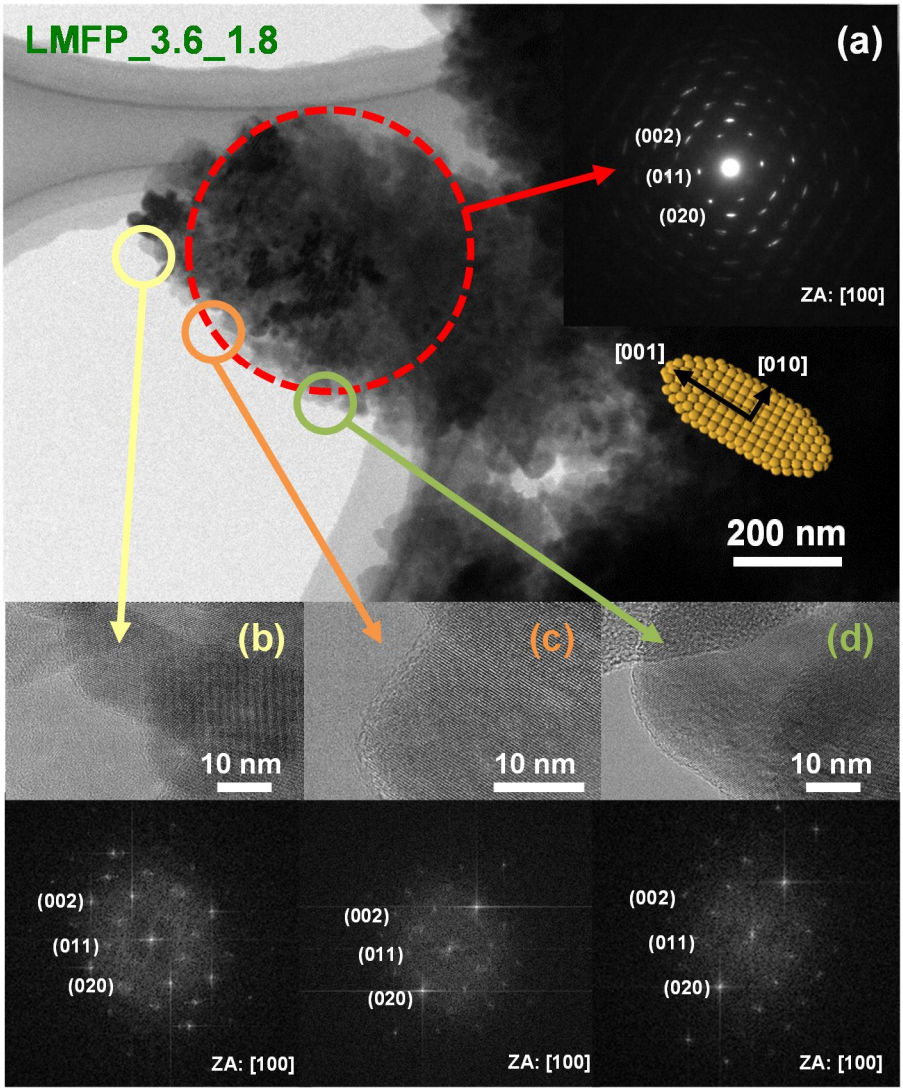

Fig. 2-5. (Color) (a) TEM image of a $LiMn_{0.8}Fe_{0.2}PO_4$ mesocrystal (LMFP_3.6_1.8) and a selected area electron diffraction pattern of the particle along the [100] zone axis. (b-d) HRTEM images of local areas in the $LiMn_{0.8}Fe_{0.2}PO_4$ nanoparticles as marked in (a), with the corresponding Fast-Fourier-Transform (FFT) images along the [100] zone axis.

In order to investigate the formation process of LMFP mesocrystals (flake shape: LMFP_3.6_1.8), time dependent XRD and SEM analysis were carried out (Figs. 2-6 and 2-7). The formation mechanisms of flake-shaped LMFP mesocrystals can be divided into the three-step solution processes. The first step is the nucleation of Mn/Fe-oxide nanoparticles as a precursor phase. The formation of amorphous Mn/Fe-oxide nanoparticles has been confirmed in our previous work [15]. In the second step, the formation of plate-like metal phosphate hydrate (M = Fe and Mn) occurs after mixing with LiOH, H_3PO_4, ascorbic acid, and HNO_3. In the third step, when the precursor-based solution is subsequently heated at 180°C, the plate-like metal phosphate hydrate particles begin to dissolve only after 5 min. With the gradual dissolution of metal phosphate hydrate phase, the nucleation of LMFP occurs within 30 min (Fig. 2-6). In this stage, the solvothermal reaction produces ~40-nm-sized LMFP nanoparticles which, afterwards, aggregate to minimize their surface free energies with the adsorption of the ascorbic acid ($C_6H_8O_6$) onto the preferential surface of the LMFP nanocrystals (Fig. 2-7) [39].

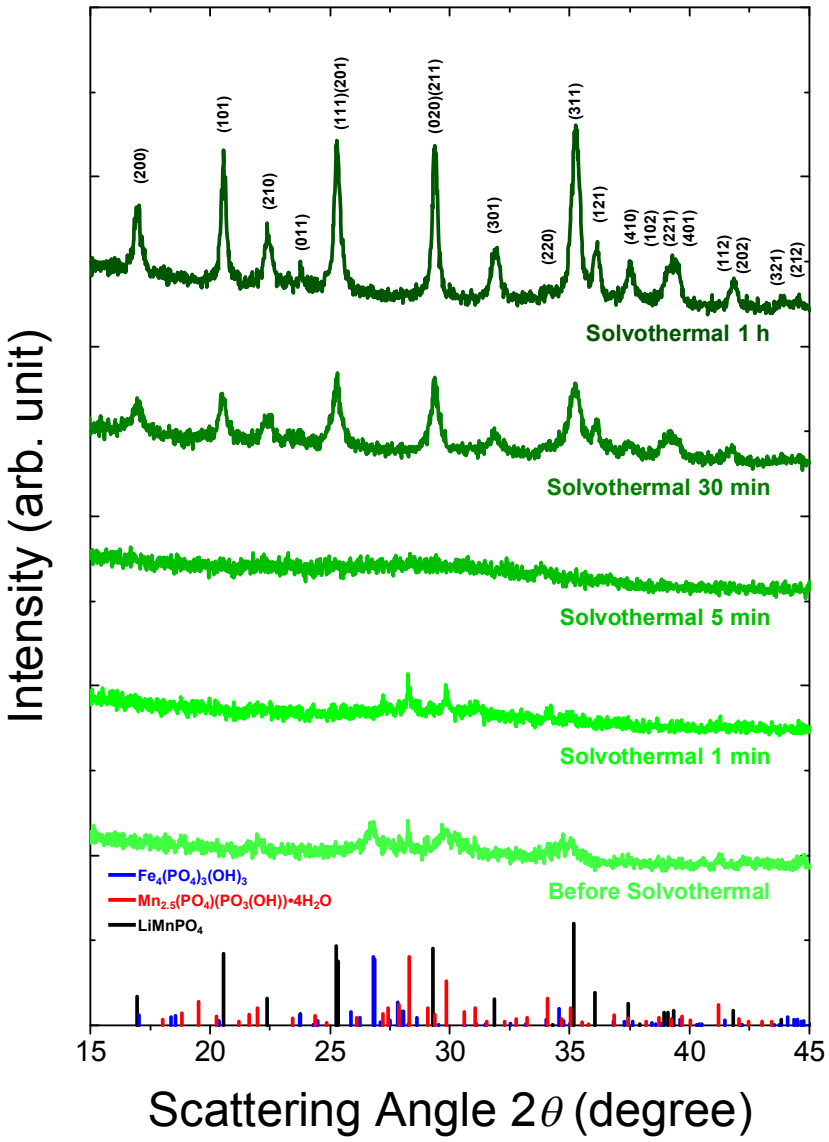

Fig. 2-6. (Color) XRD patterns of LMFP_3.6_1.8 samples obtained at different reaction times.

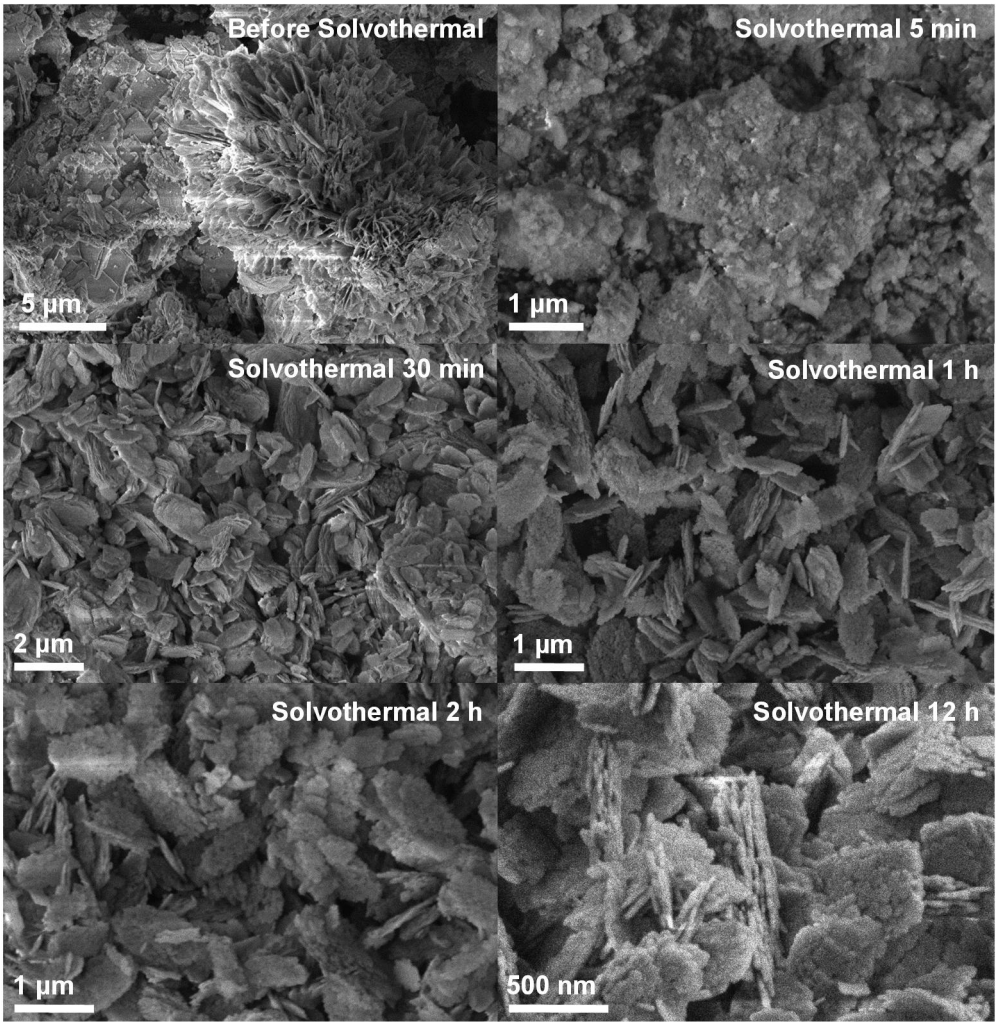

Fig. 2-7. SEM images of LMFP_3.6_1.8 samples obtained at different reaction times.

It is well known that a self-assembly process is controlled by the size of the nanocrystals, since the driving force for the self-assembly is reducing the surface free energy of the particles [42]. In this work, DMF solvent and ascorbic acid stabilize the nanocrystals and inhibit the growth of the nanocrystals, which plays an important role in the formation of the LMFP mesocrystals (Figs. 2-8, 2-9, and 2-10). Under such environment, primary particle cannot freely grow to larger sized particles. Therefore, further reduction of surface free energy is most likely to be accomplished by collisions between crystal surfaces. This selective collision in this case seems to be managed by attachment energies of different surfaces, as stated above [42]. Since such attachment energy is reported to be converted by pH [36], shape of the secondary particle is likely to be modified by pH for such reason. As the pH of the total solution goes up (100) surface with the reaction time increased to 1 h, the diffraction intensities became stronger, indicating the enhanced crystallinity of the LMFP (Fig. 2-6).

The summarized morphological evolution of the flake-shaped LMFP mesocrystals is schematically illustrated in Fig. 2-11. The formation process of the ellipsoidal-shaped LMFP mesocrystals (LMFP_3.6_1.7) was investigated in a same manner (Figs. 2-12 and 2-13). The formation process of flake- and ellipsoidal-shaped LMFP mesocrystals seems identical with each other, while the resultant particle shape was quite different. Since the initially formed phases in each condition were different, such distinction of the shape evolution of the secondary particles might be attributed to the different intermediate phase in the initial step of the solvothermal reaction. Since the initial dissolution phenomena should have some influence the composition of ionic species in precursor solution when dissolved into the solution, which results in the different adsorption of ascorbic acid on the LMFP primary particles [14,25].

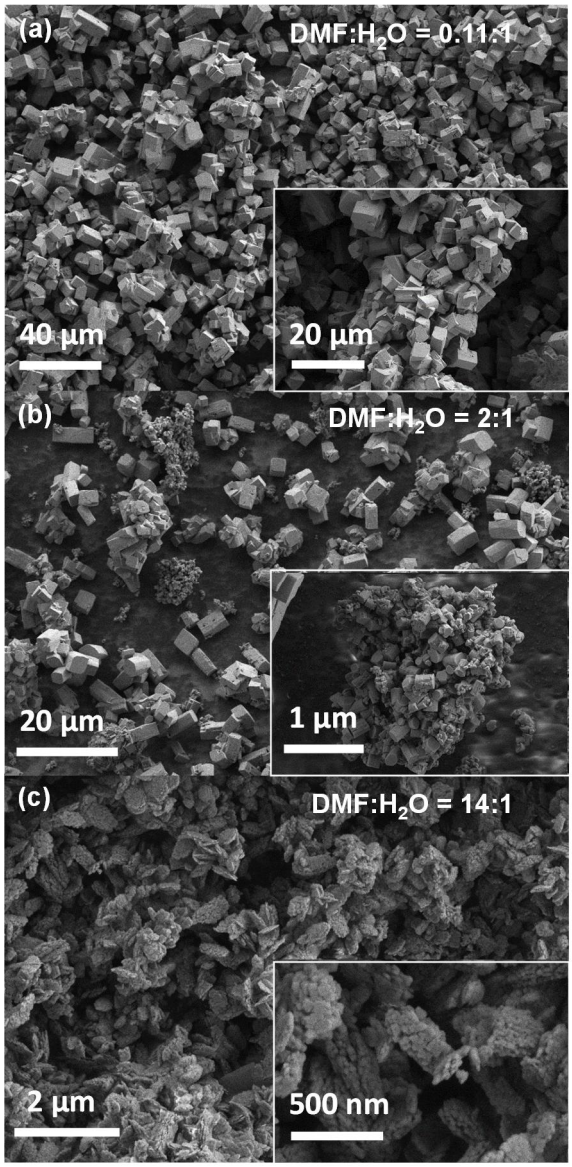

Fig. 2-8. SEM images of the $LiMn_{0.8}Fe_{0.2}PO_4$ synthesized with different solvent ratios of (a) DMF:H_2O = 0.11:1, (b) DMF:H_2O = 2:1, and (c) DMF:H_2O = 14:1.

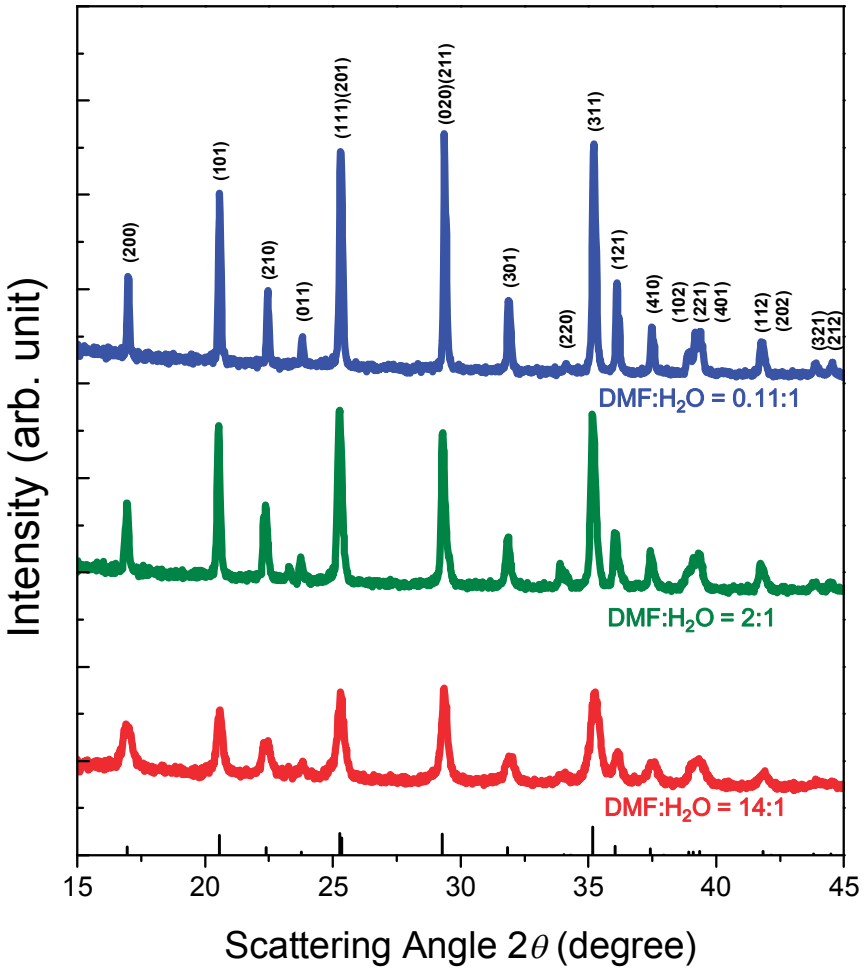

Fig. 2-9. (Color) XRD patterns of the $LiMn_{0.8}Fe_{0.2}PO_4$ synthesized with different solvent ratios of DMF:H_2O = 0.11:1, DMF:H_2O = 2:1 and DMF:H_2O = 14:1.

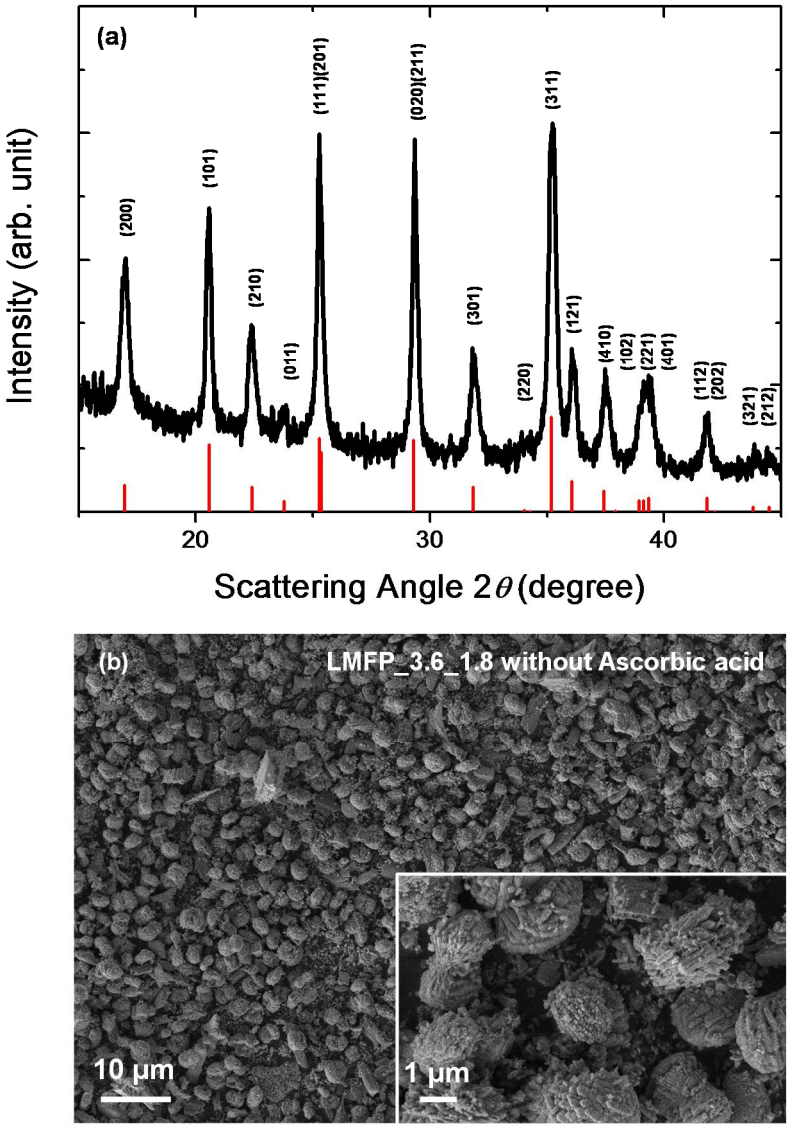

Fig. 2-10. (a) XRD patterns and (b) SEM images of LMFP_3.6_1.8 sample synthesized without ascorbic acid.

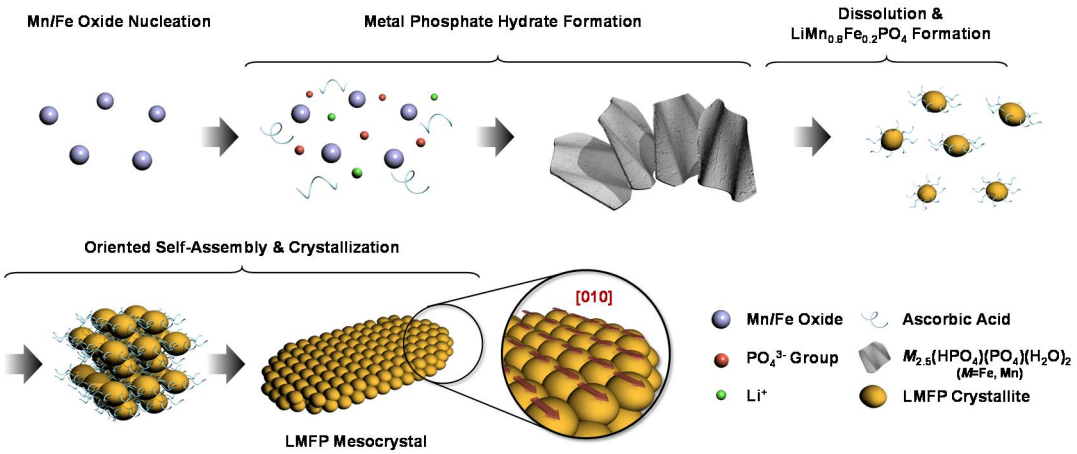

Fig. 2-11. (Color) Schematic illustration of the morphological evolution of the $LiMn_{0.8}Fe_{0.2}PO_4$ mesocrystals.

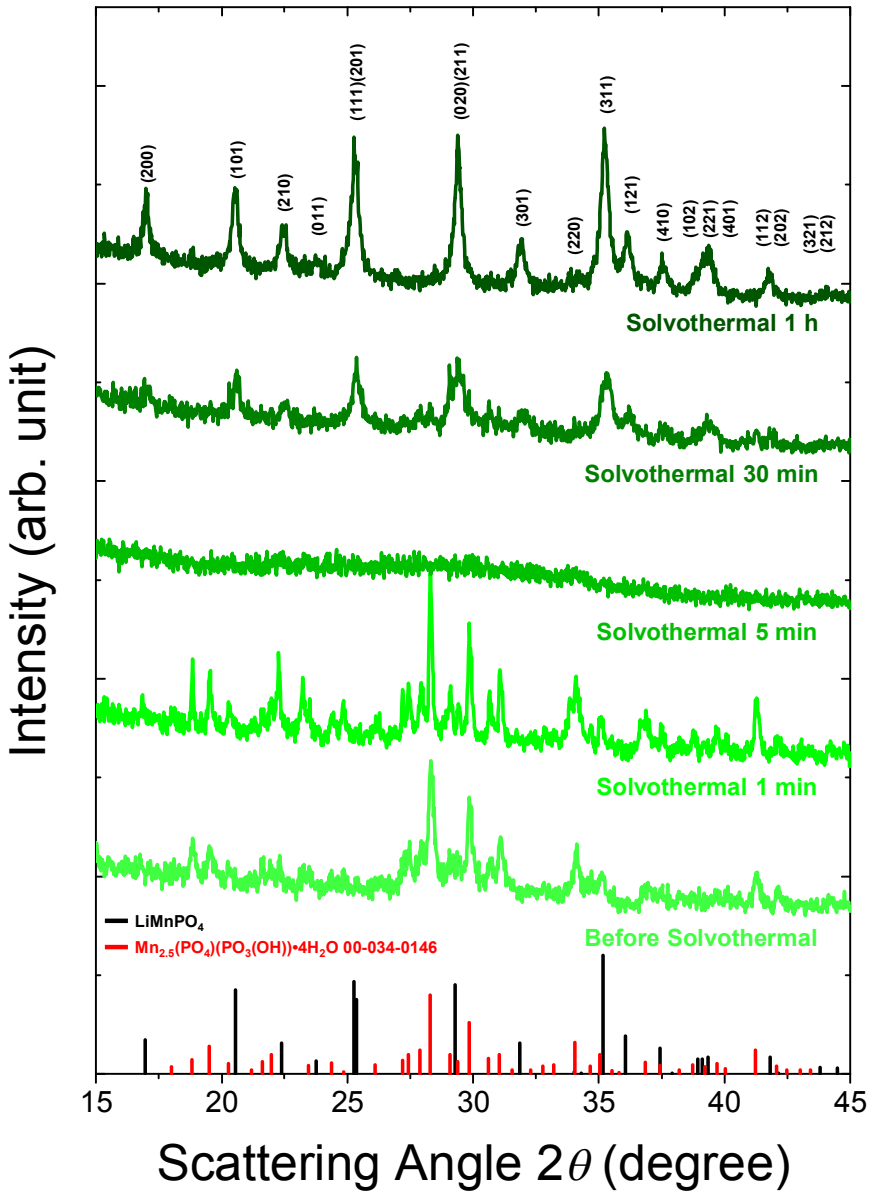

Fig. 2-12. (Color) XRD patterns of LMFP_3.6_1.7 samples obtained at different reaction times.

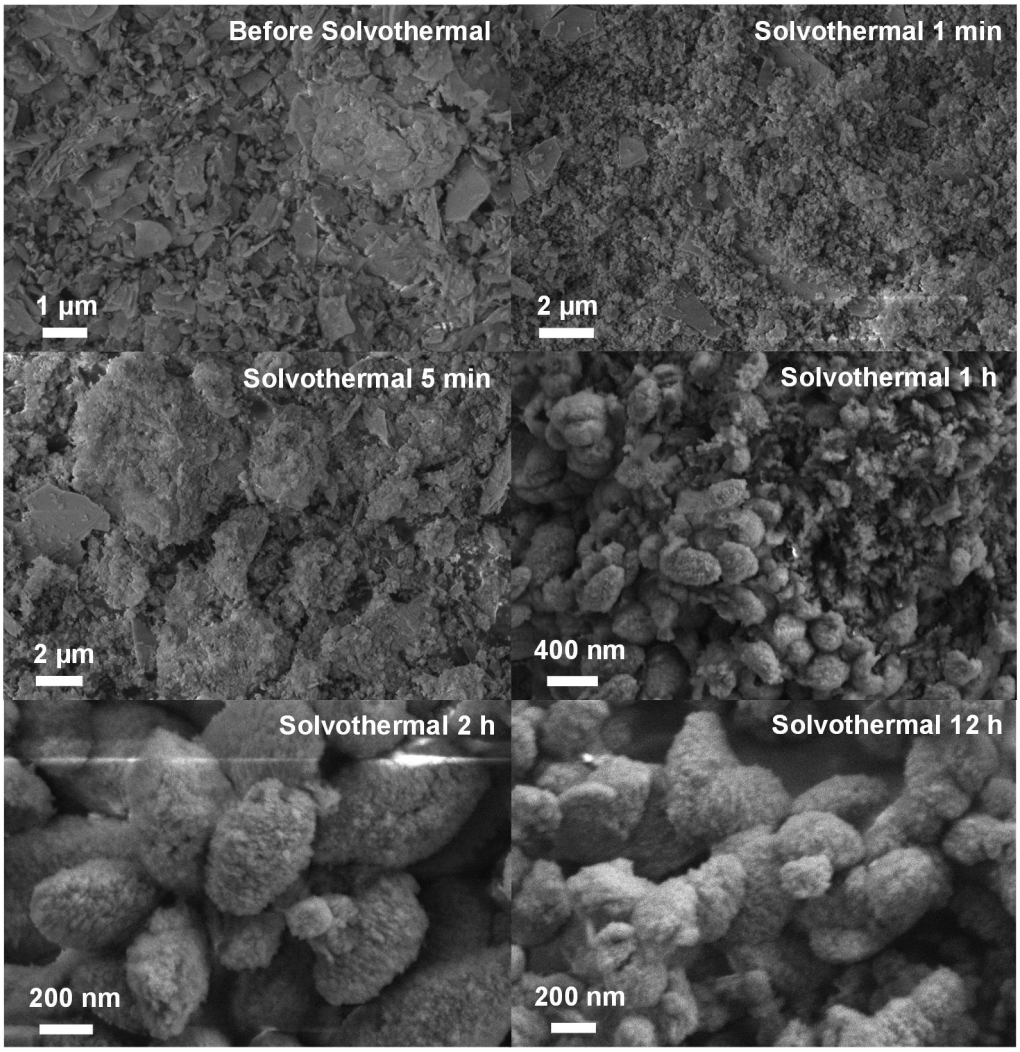

Fig. 2-13. SEM images of LMFP_3.6_1.7 samples obtained at different reaction times.

In order to investigate the battery performance of the LMFP mesocrystals and the effect of the synthesis condition, the selected LMFP samples were cycled at various current densities (sequentially from 0.05 C to 10 C) (Fig. 2-14). Among the 6 samples, the carbon-coated LMFP_3.6_1.8 (LMFPC_3.6_1.8) exhibited the highest discharge capacity of ~135 mAh/g (~80% of theoretical capacity) at a rate of 0.05 C. Compared with the LMFP_3.6_1.8 sample, the rest of the samples revealed capacities less than ~50% of the theoretical one, which is consistant with CV data (Fig. 2-15). Considering that the electrochemical properties of $LiMn_{0.8}Fe_{0.2}PO_4$ can be stated as a complicated function of particle size, morphology, electronic conduction, and anti-site defect concentration, the origin of the enhanced electrochemical properties for the LMFP_3.6_1.8 was identified by taking those factors into account.

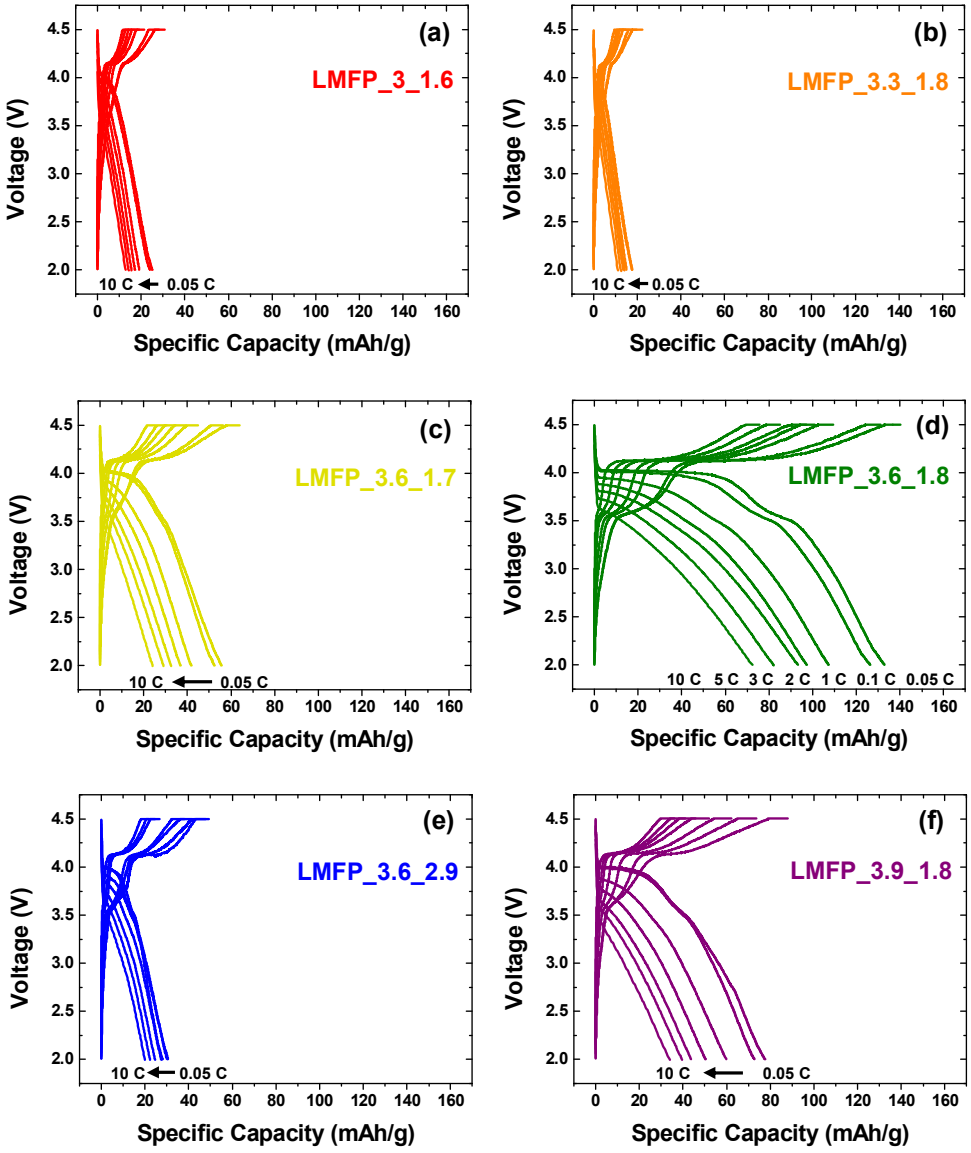

Fig. 2-14. (Color) Charge and discharge profiles of the (a) LMFPC_3_1.6, (b) LMFPC_3.3_1.8, (c) LMFPC_3.6_1.7, (d) LMFPC 3.6_1.8, (e) LMFPC_3.6_2.9, and (f) LMFPC_3.9_1.8 samples at various C rates from 0.05 C to 10 C (1 C = 170 mA/g).

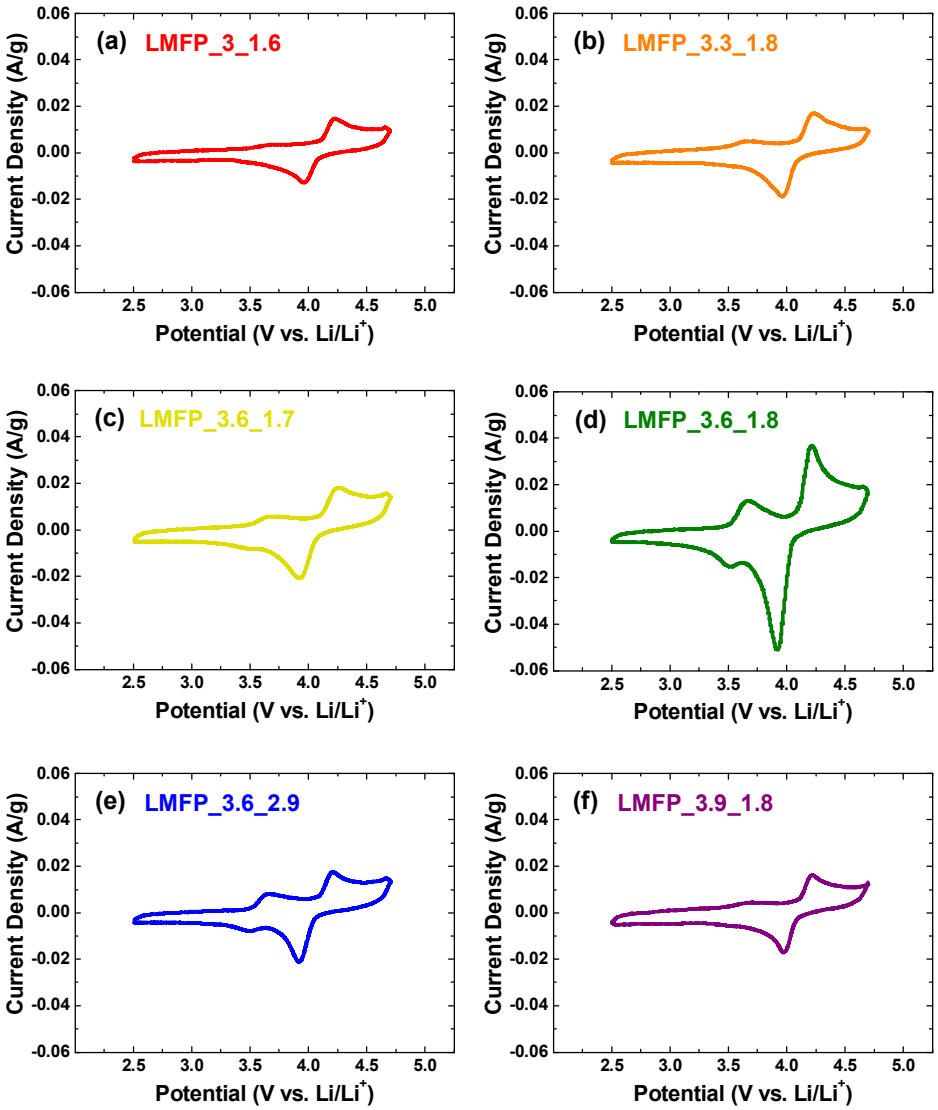

Fig. 2-15. (Color) CV curves of the (a) LMFPC_3.0_1.6, (b) LMFPC_3.3_1.8, (c) LMFPC_3.6_1.7, (d) LMFPC_3.6_1.8, (e) LMFPC_3.6_2.9, and (f) LMFPC_3.9_1.8.

In order to elucidate the limiting factor of electrochemical performance of the other LMFP mesocrystals, grain size, anti-site defect concentration, charge-transfer resistance, and discharge capacity of the samples are graphically plotted along (Fig. 2-16 and Table 2-1). The primary particle size and distributions of LMFP mesocrystals, estimated by the Williamson-Hall method and SEM images were indicated as a red rhombus. (Figs. 2-16 and 2-17) [22]. As shown in Fig. 2-16, the size of the primary particle of selected LMFP samples were quite similar to each other (30 - 50 nm) except the LMFP_3.6_2.9 sample (~150 nm). It is well known that shorter Li^+ diffusion length is beneficial for utilizing full capacity of $LiMnPO_4$. The primary particle size of the LMFP mesocrystals seems fairly small enough for the good electrochemical properties except the LMFP_3.6_2.9 sample. It is plausible to say that the poor electrochemical properties of the LMFP_3.6_2.9 sample might be attributed to the large size of primary particles. However, considering the negligible size difference between other samples, it seems that the origin of enhanced battery performance of the LMFP_3.6_1.8 cannot be simply explained by size issue of the LMFP mesocrystals.

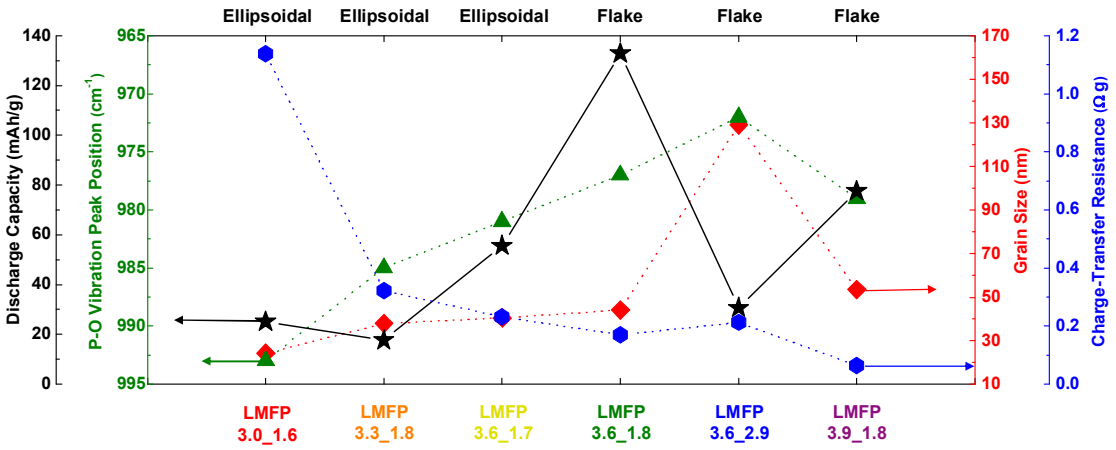

Fig. 2-16. (Color) Discharge capacity, P-O vibration peak position, grain size, charge-transfer resistance, and secondary particle shape for the selected $LiMn_{0.8}Fe_{0.2}PO_4$ mesocrystals samples.

Sample	Grain Size by XRD (nm)	Primary Particle Size by SEM (nm)	BET Surface Area (m^2/g)	Average Pore Size (nm)	Charge-Transfer Resistance (Ω g)
LMFP_3.0_1.6	40.5 ± 1.4	29.6 ± 15.1	49.2	4.7	1.14
LMFP_3.3_1.8	43.6 ± 1.1	40.4 ± 15.5	36.1	5.9	0.32
LMFP_3.6_1.7	41.3 ± 1.2	40.6 ± 16.2	42.4	6.1	0.23
LMFP_3.6_1.8	44.3 ± 1.6	44.2 ± 18.4	25.6	8.8	0.17
LMFP_3.6_2.9	-	130.5 ± 62.3	12.6	7.2	0.21
LMFP_3.9_1.8	50.6 ± 3.7	53.9 ± 20.4	41.5	7.1	0.06

Table 2-1. (Color) Grain size (XRD), primary particle size (SEM), BET surface area, average pore size, and charge-transfer resistance of the $LiMn_{0.8}Fe_{0.2}PO_4$ mesocrystals, synthesized with different precursor ratios and various pH-values.

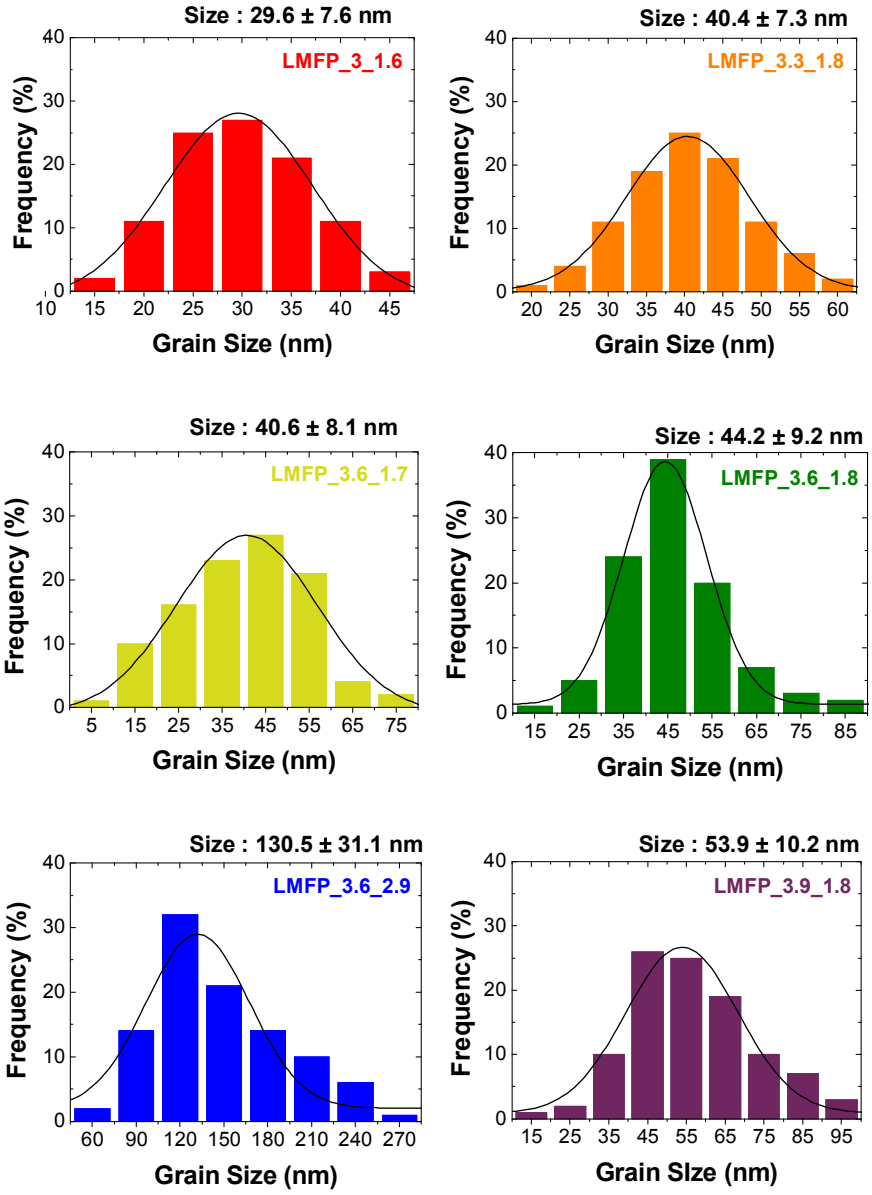

Fig. 2-17. (Color) Primary particle size distribution of LMFP_3_1.6, LMFP_3.3_1.8, LMFP_3.6_1.7, LMFP_3.6_1.8, LMFP_3.6_2.9, and LMFP_3.9_1.8.

The anti-site defect, replacement of lithium with transition metal in its original site, can seriously degrade the battery performance by blocking the lithium diffusion channel. Since the pH or precursor concentration of solvothermal treatment have strong influence in anti-site defect formation in $LiMPO_4$ [43], above major difference in electrochemical performance between selected samples can be caused by different anti-site defect concentration. Since the P-O bond length shifts by the changes of surrounding MnO_6 and LiO_6 octahedron environment in olivine materials, various groups determined the anti-site defect concentrations in olivine-structured $LiMnPO_4$ by tracking the shifts in P-O symmetric stretching vibration peaks in FT-IR spectra [30,44,45]. From those studies, the red-shifts of the P-O symmetric stretching vibration peak around ~980 cm^{-1} is known to reflect an increase in the anti-site defect concentration for $LiMnPO_4$ [12]. According to the FT-IR spectra in Fig. 2-18, it is reasonable to say that the LMFP mesocrystals synthesized at higher concentration of Li^+ and PO_4^{3-} ions in precursor usually contains less anti-site defect in their matrix than lower ones such as LMFP_3.0_1.6 and LMFP_3.3_1.8. As expected, the LMFP_3.0_1.6 and LMFP_3.3_1.8 exhibited lower discharge capacities than other similar-sized samples. Although it is not rational to say that the inferior capacities of LMFP_3.0_1.6 and LMFP_3.3_1.8 are entirely caused by the higher defect concentration of the samples, disparity in vibrational peak positions between those samples unambiguously indicates the decrease of site-change events caused by higher concentration of Li^+ and PO_4^3 enhances the discharge capacity considering similar-sized LMFP samples.

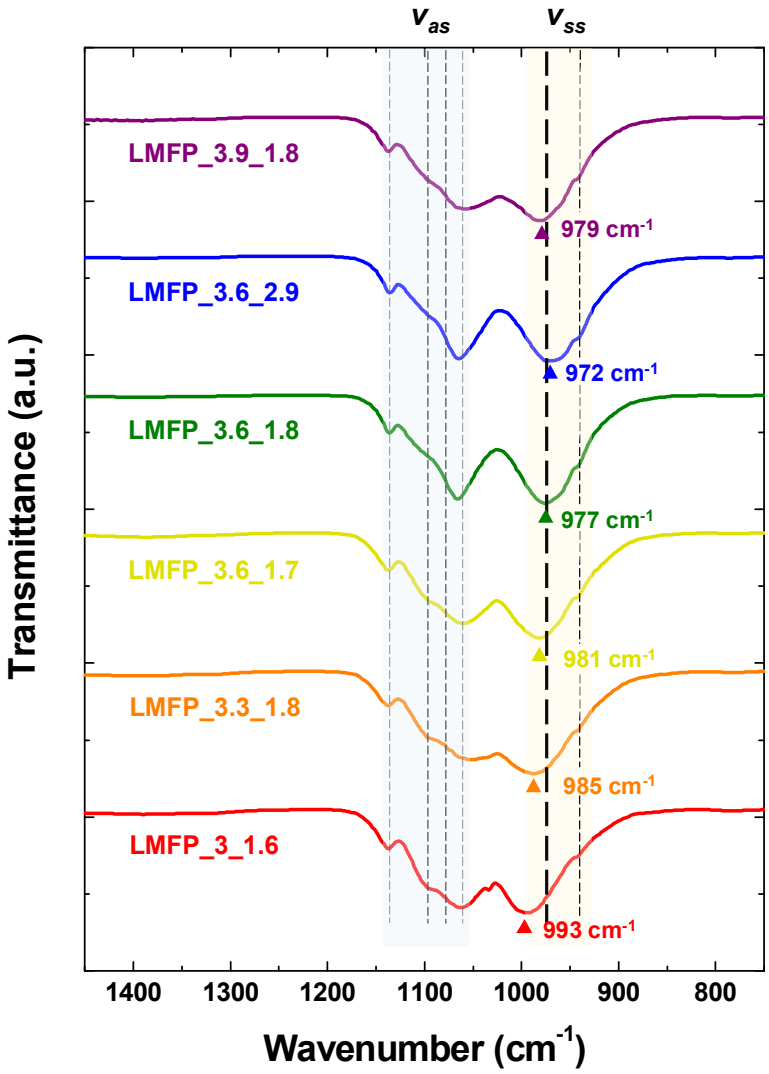

Fig. 2-18. (Color) FT-IR spectra of selected $LiMn_{0.8}Fe_{0.2}PO_4$ mesocrystal samples. Peak positions of electrochemically optimized sample (LMFP_3.6_1.8) were marked by dashed lines. Blue region and yellow region correspond to asymmetric stretch modes and symmetric stretch modes of PO_4^{3-} tetrahedron, respectively.

Although the difference in size and anti-site defect concentration between those different samples explain the dramatic electrochemical degradation in some extent, more detailed explanation is needed to fully understand the electrochemical performance of the mesocrystals. Comparing LMFP_3.6_1.7 and LMFP_3.6_1.8 in Fig. 2-16, there is an appreciable difference in capacity utilization between two samples, in spite of both sample's having similar size and defect concentration. According to the surface area and pore-size-distribution of the selected LMFP samples (Fig. 2-19 and Table 2-1), flake-shaped mesocrystals possess similar average pore size with ellipsoidal ones. From the TEM images in Fig. 2-4, however, it can be said that the flake-shaped samples seem to be less thicker than the ellipsoidal samples. It can be assumed that the ellipsoidal-shaped LMFP mesocrystals are too dense and thick to be completely penetrated by the electrolyte throughout the interior of the secondary particles, although the nitrogen adsorption-desorption can occur inside the LMFP mesocrystals and thereby exhibit *type-IV* mesoporosity.

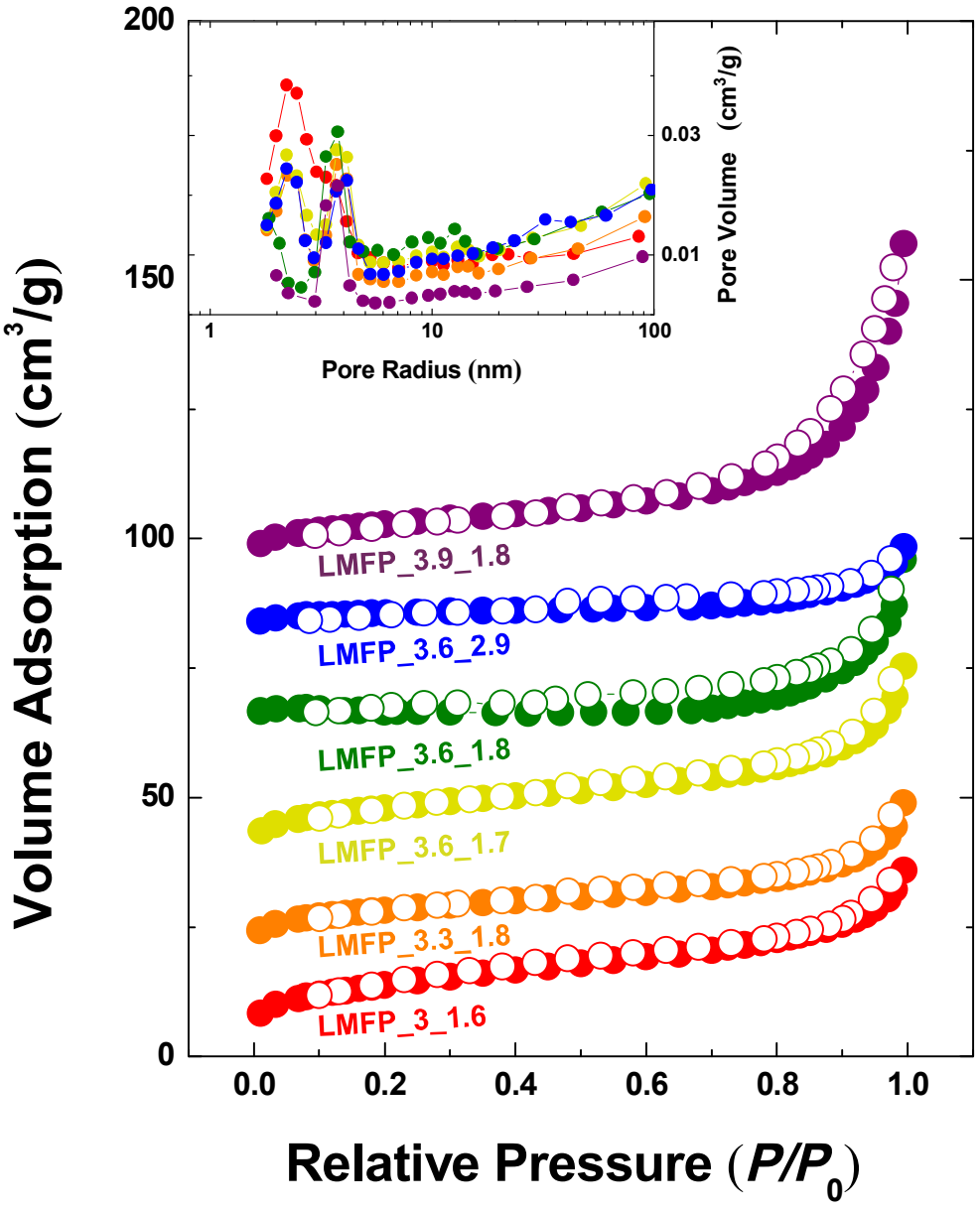

Fig. 2-19. (Color) Nitrogen adsorption-desorption isotherms for selected $LiMn_{0.8}Fe_{0.2}PO_4$ mesocrystal samples. The inset shows the pore-size distribution of these samples.

In order to identify whether the effective permeability of the electrolyte is the main contributor to the enhanced electrochemical performance of the LMFP_3.6_1.8 (flake shape) compared to that of the LMFP_3.6_1.7 (ellipsoidal shape), the electrochemical properties of the LMFP_3.6_1.8 and the LMFP_3.6_1.7 were investigated at various current densities (0.05 C to 10 C) using the diluted electrolyte ($LiPF_6$: 0.1 M) (Figs. 2-20 and 2-21). This experimental condition was designed from the viewpoint that the effect of the Li salt concentration in electrolyte might be more critical when the active surface area is large enough, because a short supply of Li ion can impede the electrochemical reaction, especially at high C rate. The LMFP_3.6_1.8 at 0.1 M electrolyte shows the similar discharge capacity of ~135 mAh/g with the normal electrolyte system at a rate of 0.05 C, however, this sample exhibited the dramatic capacity drop with the increasing C rates, and the negligible capacity is observed at 10 C (Fig. 2-21). Furthermore, the overpotential of the LMFP_3.6_1.8 at 1 M electrolyte significantly increased when tested in 0.1 M electrolyte. Such increase in *iR* drop is most likely to be originated from a decrease in salt concentration (Fig. 2-21) [46,47]. Compared to the flake-shaped LMFP_3.6_1.8, electrochemical performance of the LMFP_3.6_1.7 (ellipsoidal shape) seems less-affected by the reduction of lithium salt concentration, which indicates that the active surface area is limited to the surface of the secondary particles (Fig. 2-21).

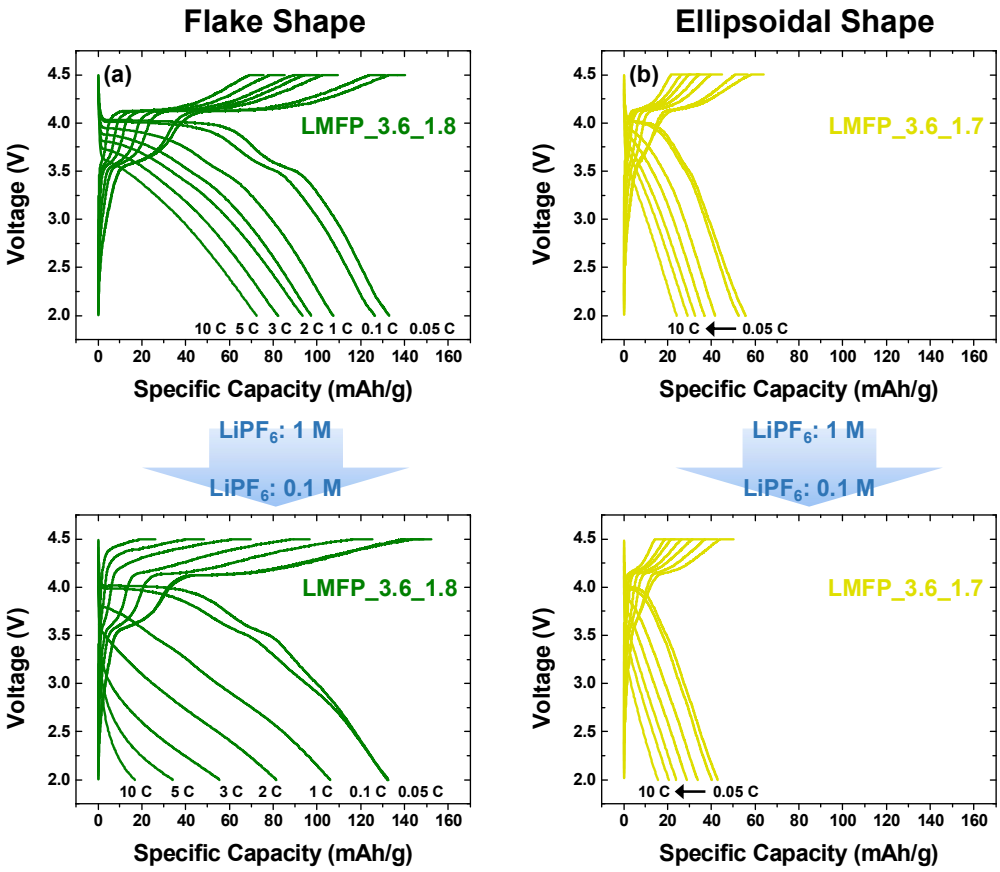

Fig. 2-20. (Color) Comparison of the morphological effects of the mesocrystals on electrolyte permeability. The voltage profiles of two different sets of (a) LMFP_3.6_1.8, and (b) LMFP_3.6_1.7, including two half-cell tests each containing ordinary ($LiPF_6$: 1 M) and dilute ($LiPF_6$: 0.1 M) concentration of lithium salt.

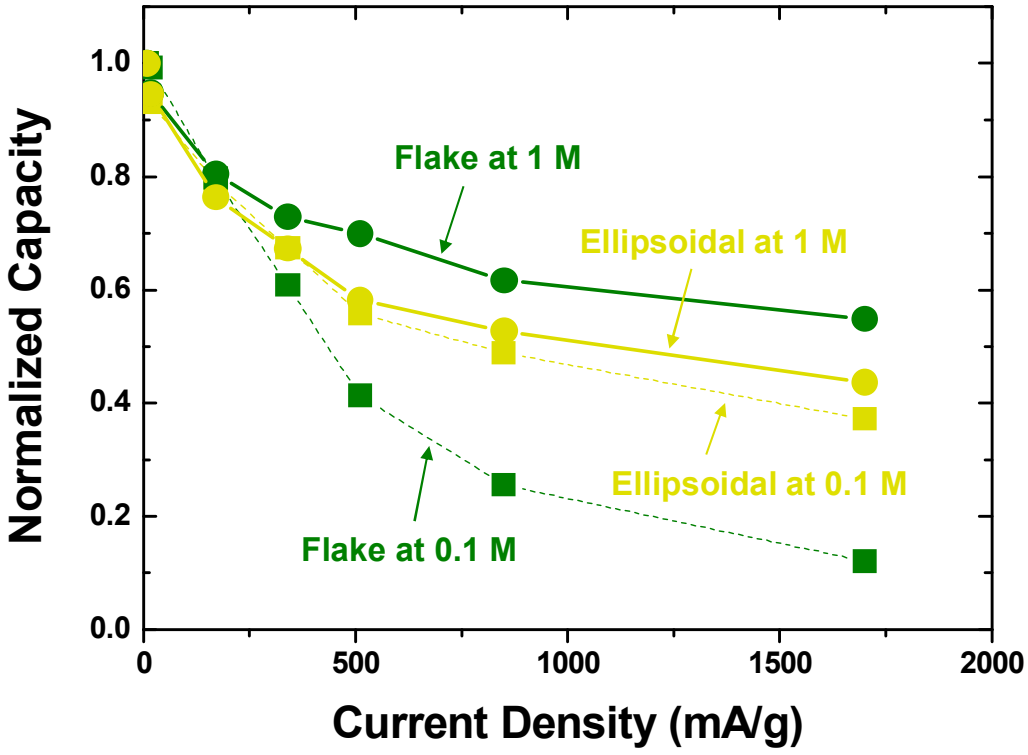

Fig. 2-21. (Color) Capacity ratios of two different sets of LMFP_3.6_1.8 (flake shape) and LMFP_3.6_1.7 (ellipsoidal shape) normalized by the capacities at a rate of 0.05 C (8.5 mA/g) with 1 M and 0.1 M $LiPF_6$ concentration electrolyte.

In order to reinforce our assumption that the capacity loss in ellipsoidal particles may be originated by insufficient electrolyte permeation, chemically delithiated samples of ellipsoidal (*D*-LMFP_3.6_1.7) and flake-shaped (*D*-LMFP_3.6_1.8) mesocrystals were prepared (Fig. 2-22). Since liquid penetration through nano-sized pores in our ellipsoidal samples is thought to much sluggish than the flake-shaped samples, chemical delithiation of our ellipsoidal samples via solution process has to be less effective than that of the flake-shaped samples. From the XRD results in Fig. 2-22, *D*-LMFP_3.6_1.7 seemed to experience much less phase transformation caused by chemical delithiation than *D*-LMFP_3.6_1.8 which corresponds well with our assumption. The newly occurred peaks of the *D*-LMFP_3.6_1.8 were fairly correspond to the peaks of chemically delithiated $LiMn_xFe_{1-x}PO_4$ phases in previous studies [9], which didn't seem to occur clearly in XRD patterns of chemically delithiated ellipsoidal samples. On the other hand, XRD pattern of chemically delithiated LMFP_3.6_1.7 indicates amorphorization of the powder. This might be caused by insufficient carbon-coating on ellipsoidal mesocrystal. Whittingham's group reported that insufficient carbon-coating on $LiMnPO_4$ surface can lead to Mn dissolution resulting amorphorization instead of selective extraction of lithium during the chemical delithiation process [48]. In our carbon-coating method, carbon precursor is provided to the cathode surface via liquid medium. Similar to electrolyte, percolation of carbon precursor into ellipsoidal samples' inner part is expected to sluggish due to its dense nature. The sluggish precursor transport into the internal side of ellipsoidal particles can cause the insufficiency of internal carbon-conducting layer through the secondary particle. Combined with the R_{ct} from the EIS result (Figs. 2-16 and 2-23), such results can be interpreted without losing any consistency, since insufficient carbon network in ellipsoidal mesocrystals can lead to the resistance

increase of the whole particle.

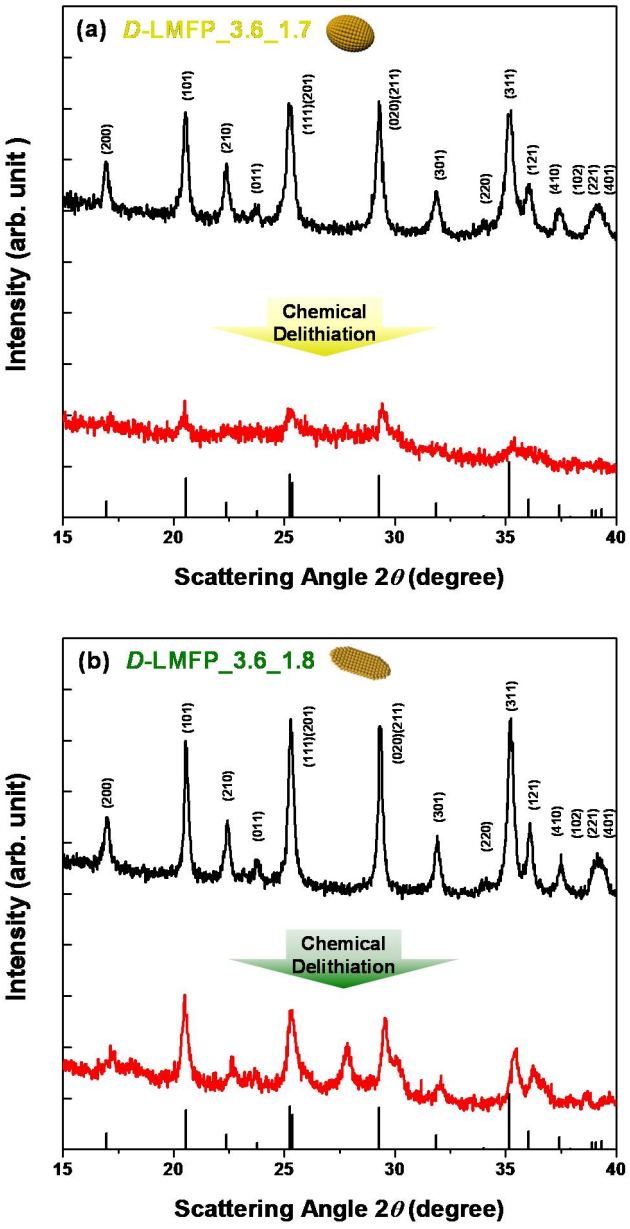

Fig. 2-22. (Color) XRD spectra of the carbon coated $LiMn_{0.8}Fe_{0.2}PO_4$ mesocrystals and their chemically-delithiated samples. (a) Ellipsoidal-shaped *D*-LMFP_3.6_1.7 and (b) flake-shaped *D*-LMFP_3.6_1.8.

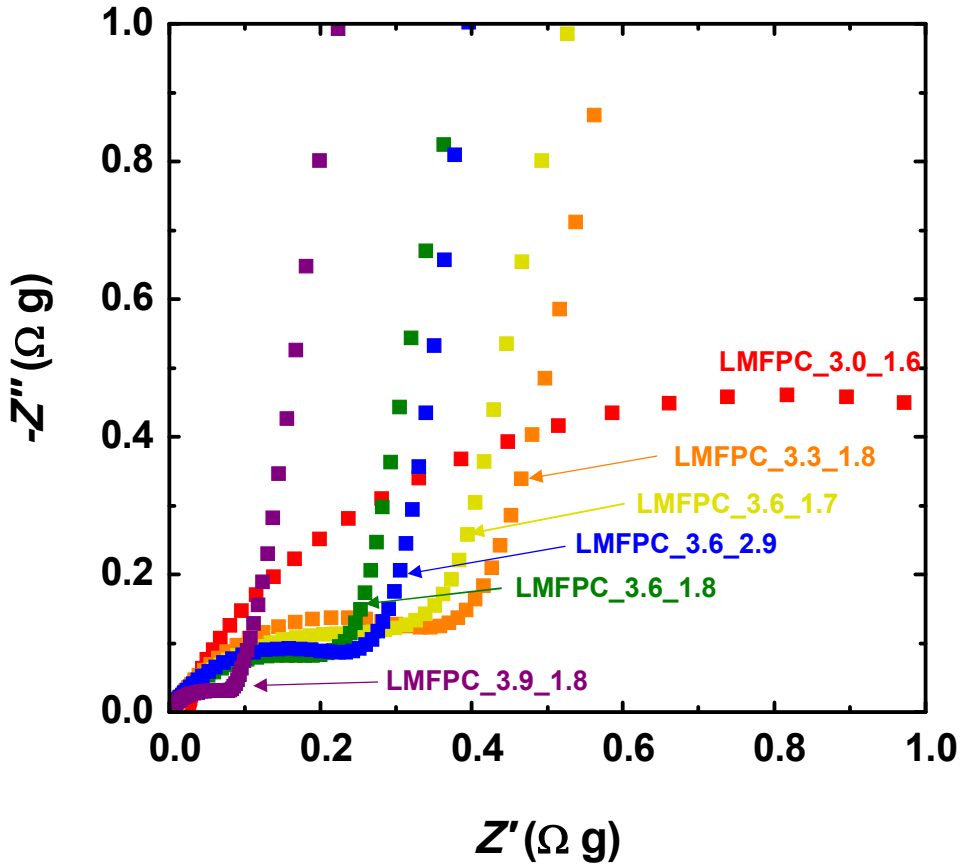

Fig. 2-23. (Color) Nyquist plots of the LMFPC_3.0_1.6, LMFPC_3.3_1.8, LMFPC_3.6_1.7, LMFPC_3.6_1.8, LMFPC_3.6_2.9, and LMFPC_3.9_1.8.

To summarize, shape of the secondary particle was revealed to be an important factor in designing the mesocrystalline cathode material. The flake-shaped LMFP mesocrystals' superior electrochemical properties seems to be originated by facile percolation of electrolyte and carbon precursor, ultimately facilitating Li^+ and electron access during the lithiation/delithiation processes. The origin of sluggish kinetics in the LMFP_3.6_1.7 (ellipsoidal shape) might be the insufficient porosity of the inner-structure. Schematic illustration depicts the morphological effects on electrolyte permeability of the flake shaped and ellipsoidal-shaped LMFP mesocrystals (Fig. 2-24).

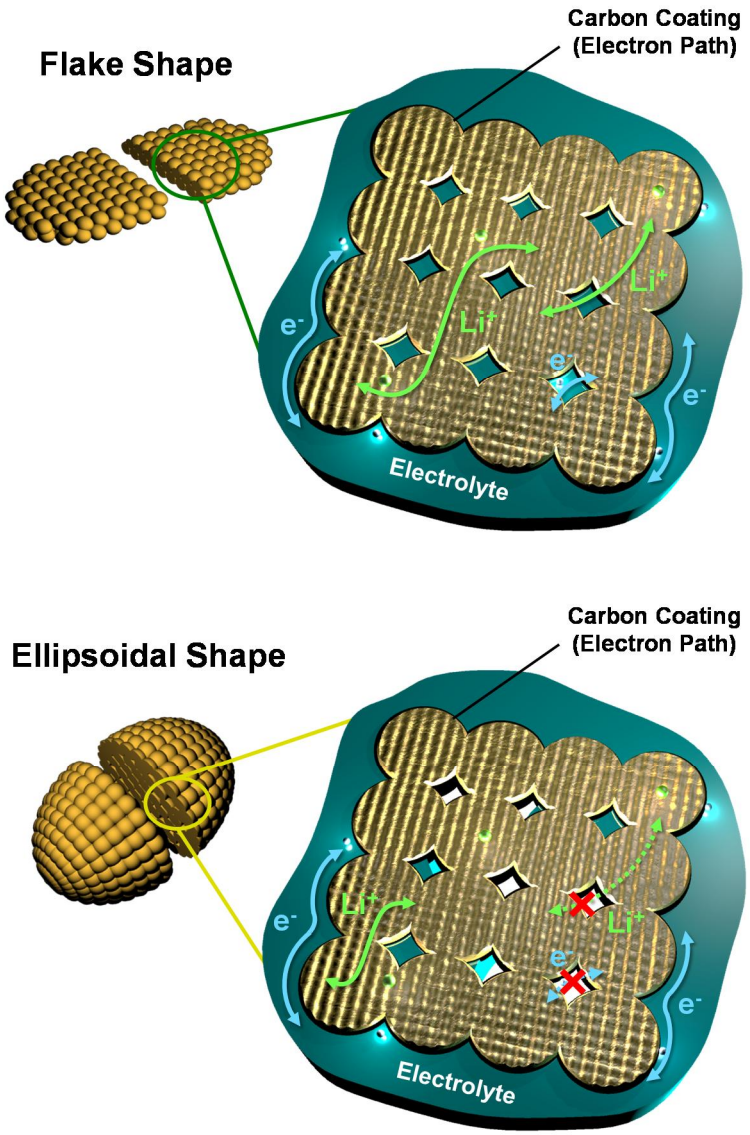

Fig. 2-24. (Color) Schematic illustration of the morphological effects on electrolyte permeability of the flake-shaped and ellipsoidal-shaped $LiMn_{0.8}Fe_{0.2}PO_4$ mesocrystals.

2.4. Conclusions

In this work, we synthesized $LiMn_{0.8}Fe_{0.2}PO_4$ mesocrystals exhibiting various shape and size by controlling the precursor ratio and pH of precursor solution. There is a clear relation between the initial solution condition of solvothremal reaction and morphology of the mesocrystals. When the battery performance of the mesocrystals was assessed by galvanostatic cycling, advancement of the electrochemical performance was achieved among the flake-shaped LMFP mesocrystals. The origin of the enhanced electrochemical performance was investigated by analyzing the primary particle size, porosity, anti-site defect concentration, and secondary particle shape. Interestingly, along with the primary crystallite size and anti-site defect, the secondary particle shape was also shown to have significant effect on the battery performance. We believe that this work can provide a simple insight to design electrochemically-favorable meso/nano-structures, which is of great potential for improving the battery performance by tuning the morphology of particles at the multi-length scale.

2.5. References

1. M. S. Whittingham, Lithium Batteries and Cathode Materials, *Chem. Rev.* 104 (2004) 4271-4302.
2. M. Armand, and J. M. Tarascon, Building Better Batteries, *Nature* 451 (2008) 652-657.
3. B. Dunn, H. Kamath, J. M. Tarascon, Electrical Energy Strorage for the grid: A Battery of Choices. *Science* 334 (2011) 928-935.
4. A. K. Padhi, K. S. Nanjundaswamy, and J. B. Goodenough, Phospho-Olivines as Positive-Electrode Materials for Rechargeable Lithium Batteries, *J. Electrochem. Soc.* 144 (1997) 1188-1194.
5. H. P. Subramanya, B. Ellis, N. Coombs, and L. F. Nazar, Nano-Network Electronic Conduction in Iron and Nickel Olivine Phosphates, *Nat. Mater.* 3 (2004) 147-152.
6. C. Delacourt, L. Laffont, R. Bouchet, C. Wurm, J. B. Leriche, M. Morcrette, J. M. Tarascon, C. Masquelier, Toward Understanding of Electrical Limitations (Electronic, Ionic) in $LiMPO_4$ (M = Fe, Mn) Electrode Materials, *J. Electrochem. Soc*. 152 (5) (2005) A913-A921.
7. D. D. Lecce, and J. Hassoun, Lithium Transport Properties in $LiMn_{1-\alpha}Fe_{\alpha}PO_4$ Olivine Cathodes, *J. Phys. Chem. C* 115 (2015) 20855-20863.
8. H. Wang, Y. Yang, Y. Liang, L. F. Cui, H. S. Casalongue, Y. Li, G. Hong, Y. Cui, and H. Dai, LiMn1−*x*Fe*x*PO4 Nanorods Grown on Graphene Sheets for Ultrahigh-Rate- Performance Lithium Ion Batteries, *Angew. Chem. Int. Ed.* 123 (2011) 7502-7506.
9. A. Yamada, Y. Kudo, K. Y. Liu, Reaction Mechanism of the Olivine Type

$Li_x(Mn_{0.6}Fe_{0.4})PO_4$ ($0 \leq x \leq 1$), *J. Electrochem. Soc.* 148 (7) (2001) A747-A754.

10. G. Li, H. Azuma, and M. Tohda, Optimized $LiMn_yFe_{1-y}PO_4$ as the Cathode for Lithium Batteries, *J. Electrochem. Soc.* 149 (6) (2002) A743-A747.
11. S. W. Oh, S. T. Myung, S. M. Oh, K. H. Oh, K. Amine, B. Scrosati, and Y. K. Sun, Double Carbon Coating of $LiFePO_4$ as High Rate Electrode for Rechargeable Lithium Batteries, *Adv. Mater*. 22 (2010) 4842-4845.
12. M. S. Kim, J. P. Jegal, K. C. Roh, and K. B. Kim, Synthesis of $LiMn_{0.75}Fe_{0.25}PO_4$/C Microspheres Using a Microwave-Assisted Process with a Complexing Agent for High-Rate Lithium Ion Batteries, *J. Mater. Chem. A* 2 (2014) 10607-10613.
13. L. Wang, X. He, W. Sun, J. Wang, Y. Li, and S. Fan, Crystal Orientation Tuning of $LiFePO_4$ Nanoplates for High-Rate Lithium Battery Cathode Materials, *Nano Lett*. 12 (2012) 5632-5636
14. Y. Oh, S. Nam, S. Wi, S. Hong, and B. Park, Nanoscale Interface Control for High- Performance Li-Ion Batteries, *Electron. Mater. Lett.* 8 (2012) 91-105.
15. S. Wi, J. Kim, S. Lee, J. Kang, K. H. Kim, K. Park, K. Kim, S. Nam, C. Kim, and B. Park, Synthesis of $LiMn_{0.8}Fe_{0.2}PO_4$ Mesocrystals for High-Performance Li-Ion Cathode Materials, *Electrochim. Acta* 216 (2016) 203-210.
16. S. Wi, S. Nam, Y. Oh, J. Kim, H. Choi, S. Hong, S. Byun, S. Kang, D. J. Choi, K. O. Ahn, Y. H. Kim, and B. Park, Facile Synthesis of Porous-Carbon/$LiFePO_4$ Nanocomposites, *J. Nanopart. Res.* 14 (2012) 1327-1335.
17. C. Neef, C. Jähne, H. P. Meyer, and R. Klingeler, Morphology and Agglomeration Control of $LiMnPO_4$ Micro- and Nanocrystals, *Langmuir* 29 (2013) 8054-8060.
18. S. Wi, J. Kim, S. Nam, J. Kang, S. Lee, H. Woo, M. Lee, C. H. Sonu, T. Moon, and B. Park, Enhanced Rate Capability of $LiMn_{0.9}Mg_{0.1}PO_4$ Nanoplates by

Reduced Graphene Oxide/Carbon Double Coating for Li-Ion Batteries, *Curr. Appl. Phys*. 14 (2014) 725-730.

19. Z. Dai, L. Wang, X. He, F. Ye, C. Huang, J. Li, J. Cao, J. Wang, G. Tian, and M. Ouyang, Morphology Regulation of Nano $LiMn_{0.9}Fe_{0.1}PO_4$ by Solvothermal Synthesis for Lithium Ion Batteries, *Electrochim. Acta* 112 (2013) 144-148.
20. H. Guo, C. Wu, L. Liao, J. Xie, S. Zhang, P. Zhu, G. Cao, and X. Zhao, Performance Improvement of Lithium Manganese Phosphate by Controllable Morphology Tailoring with Acid-Engaged Nano Engineering, *Inorg. Chem.* 54 (2015) 667-674.
21. G. Xu, Y. Yang, L. Li, F. Li, J. Wang, L. Bao, X. Li, G. Shen, and G. Han, Ethylene Glycol (EG) Solvothermal synthesis of flower-like $LiMnPO_4$ Nanostructures Self-Assembled with (010) Nanobelts for Li-Ion Battery Positive Cathodes, *CrystEngComm*, 18 (2016) 3282-3288.
22. Y. Oh, S. Nam, S. Wi, J. Kang, T. Hwang, S. Lee, H. H. Park, J. Cabana, C. Kim, and B. Park, Effective Wrapping of Graphene on Individual $Li_4Ti_5O_{12}$ Grains for High-Rate Li-Ion Batteries, *J. Mater. Chem. A* 2 (2014) 2023-2027.
23. T. Drezen, N. H. Kwon, P. Bowen, I. Teerlinck, M. Isono, I. Exnar, Effect of Particle Size on $LiMnPO_4$ Cathodes, *Journal of Power Sources*, 6 (2007) 949-953.
24. Y. Sun, N. Liu, and Y. Cui, Promises and Challenges of Nanomaterials for Lithium-Based Rechargeable Batteries, *Nat. Energy*, 1 (2016) 16071-16082.
25. Z. Zhang, G. Hu, Y. Cao, J. Duan, K. Du, and Z. Peng, Hierarchical $LiMnPO_4$ Assembled from Nanosheets Via a Solvothermal Method as a High Performance Cathode Material, *RSC. Adv*. 5 (2015) 81461-81467.
26. M. Y. Cho, K. B. Kim, J. W. Lee, H. Kim, H. Kim, K. Kang, and K. C. Roh, Defect-Free Solvothermally Assisted Synthesis of Microspherical Mesoporous

$LiFePO_4$/C, *RSC Adv.* 3 (2012) 3421-3427.

27. P. Voepel, C. Suchomski, A. Hofmann, S. Gross, P. Dolcet, and B. M Smarsly, In-Depth Mesocrystal Formation analysis of Microwave Assisted Synthesis of $LiMnPO_4$ Nanostructures in Organic Solution, *CrystEngComm* 18 (2016) 316-327.
28. E. Uchaker, and G. Cao, Mesocrystals as Electrode Materials for Lithium Ion Batteries, *Nano Today* 9 (2014) 499-524.
29. J. Popovic, R. Demir-Cakan, J. Tornow, M. Morcrette, D. S. Su, R. Schlögl, M. Antonietti, and M. M. Titirici, $LiFePO_4$ Mesocrystals for Lithium Ion Batteries, *Small* 7 (2011) 1127-1135.
30. C. Liu, C. Zhang, H. Song, C. Zhang, Y. Liu, X. Nan, and G. Cao, Mesocrystal MnO Cubes as Anode for Li-Ion Capacitors, *Nano Energy* 22 (2016) 290-300.
31. H. Yang, X. L. Wu, M. H. Cao, and Y. G. Guo. Solvothermal Synthesis of $LiFePO_4$ Hierarchically Dumbbell-Like Microstructures by Nanoplate Self-Assembly and Their Application as a Cathode Material in Lithium-Ion Batteries, *J. Phys. Chem. C* 113 (2009) 3345-3351
32. M. Niederberger, and H. Cölfen, Oriented Attachment and Mesocrystals: Non-Classical Crystallization Mechanisms Based on Nanoparticle Assembly, *Phys. Chem. Chem. Phys.* 8 (2006) 3271-3287.
33. L. Hu, B. Qiu, Y. Xia, Z. Qin, L.Qin, X. Zhou, and Z. Liu, Solvothermal Synthesis of Fe-Doping $LiMnPO_4$ Nanomaterials for Li-Ion Batteries, *Journal of Power Sources*, 248 (2014) 246-252.
34. L. Bao, G. Xu, J. Wang, H. Zong, L. Li, R. Zhao, S. Zhou, G. Shen, and G. Han, Hydrothermal Synthesis of Flower-Like $LiMnPO_4$ Nanostructures Self-Assembled with (010) Nanosheets and Their Application in Li-Ion Batteries, *CrystEngComm*. 17 (2016) 6399-6405.
35. C. Delacourt, P. Poizot, M. Morcrette, J. M. Tarascon, and C. Masquelier,One-

Step Low-Temperature Route for the Preparation of Electrochemically Active $LiMnPO_4$ Powders, *Chem. Mater.* 16 (2004) 93-99.

36. K. Dokko, S. Koizumi, H. Nakano, and K. Kanamura, Particle Morphology, Crystal Orientation, and Electrochemical Reactivity of $LiFePO_4$ Synthesized by the Hydrothermal Method at 443 K, *J. Mater. Chem*. 17 (2007) 4803-4810.
37. B. Kang, and G. Ceder, Battery Materials for ultrafast charging and discharging, *Nature* 458 (2009) 190-193.
38. Y. W. Denis, K. Donoue, T. Kadohata, T. Murata, S. Matsuda, and S. Fujitani, Impurities in $LiFePO_4$ and Their Influence on Material Characteristics, *J. Electrochem. Soc*. 155 (2008) A526-A530.
39. Z. Wu, S. Yang, and W. Wu, Shape Control of Inorganic Nanoparticles from Solution, *Nanoscale*, 8 (2016) 1237-1259.
40. L. Wang, F. Zhou, and G. Ceder, Ab Initio Study of the Surface Properties and Nanoscale Effects of $LiMnPO_4$ *Electrochem. Solid-State Lett*. 11 (2008) A94-A96.
41. C. A. Fisher, and M. S. Islam, Surface Structures and Crystal Morphologies of $LiFePO_4$: Relevance to Electrochemical Behavior *J. Mater. Chem*. 18 (2008) 1209-1215.
42. R. Q. Song, and H. Cölfen, Mesocrystals - Ordered Nanoparticle Superstructures, *Adv. Mater*. 22 (2010) 1301-1330.
43. J. Liu, R. Jiang, X. Wang, T. Huang, and A. Yu, The Defect Chemistry of $LiFePO_4$ Prepared by Hydrothermal Method at Different pH Values, J. Power Sources 194 (2009) 536-540.
44. K. Y. Park, I. Park, H. Kim, H. D. Lim, J. Hong, J. Kim, and K. Kang, Anti-Site Reordering in $LiFePO_4$: Defect Annihilation on Charge Carrier Injection, *Chem. Mater* 26 (2014) 5345-5351.
45. N. Ravet, M. Gautier, K. Zaghib, J. B. Goodenough, A. Mauger, F. Gendron, and

C. M. Julien, Mechanism of the Fe^{3+} Reduction at Low Temperature for $LiFePO_4$ Synthesis from a Polymeric Additive, *Chem. Mater.* 19 (2007) 2595-2602.

46. B. Lee, J. I. Kim, S. Lee, T. Hwang, S. Nam, H. Choi, K. Kim, J. Kim, and B. Park, Oriented Hierarchical Porous TiO_2 Nanowires on Ti Substrate: Evolution of Nanostructures for Dye-Sensitized Solar Cells, *Electrochim. Acta* 145 (2014) 231-236.
47. J. G. Limon-Petersen, I. Streeter, N. V. Rees, and R. G. Compton, Quantitative Voltammetry in Weakly Supported Media: Effects of the Applied Overpotential and Supporting Electrolyte Concentration on the One Electron Oxidation of Ferrocene in Acetonitrile, *J. Phys. Chem. C* 113 (2009) 333-337.
48. Y. Huang, N. A. Chernova, Q. Yin, Q. Wang, N. F. Quackenbush, M. Leskes, J. Fang, F. Omenya, R. Zhang, M. J Wahila, L. F. J. Piper, G. Zhou, C. P. Grey, and M. S. Whittingham, What Happens to $LiMnPO_4$ upon Chemical Delithiation, *Inorg. Chem.* 55 (2016) 4335-4343.

Chapter 3.

*Synchrotron-Based X-Ray Absorption Spectroscopy for the Electronic Structure of $Li_xMn_{0.8}Fe_{0.2}PO_4$ Mesocrystal in Li^+ Batteries

3.1. Introduction

The ever-growing market of portable electronics and electric vehicles demands advanced lithium-ion batteries with high energy density, long-term stability, safety, and low cost [1-5]. Olivine structured lithium iron phosphate ($LiFePO_4$) is considered as a promising candidate for cathode materials of lithium-ion batteries due to its high theoretical capacity, superior structural stability, environmental benignity, and low cost [6-8]. However, the $LiFePO_4$ has relatively low redox potential (3.4 V vs. Li^+/Li) compared with that of other commercialized cathode materials ($LiCoO_2$ (~4.0 V) and $LiMn_2O_4$ (~4.0 V)), which results in the low energy density that limits its wider applications to the market [9-10]. Isostructural lithium manganese phosphate, $LiMnPO_4$, has emerged as an alternative material to $LiFePO_4$ due to its higher redox potential (4.1 V vs. Li^+/Li) [12-13]. Since the poor electronic/ionic conductivity of $LiMnPO_4$ complicated their use as high-performance cathode materials, surface

*The work presented in Chapter 3 was accepted for *Nano Energy* (2017) entitled,
"Synchrotron-Based X-Ray Absorption Spectroscopy for the Electronic Structure of $Li_xMn_{0.8}Fe_{0.2}PO_4$ Mesocrystal in Li^+ Batteries"
Sungun Wi,[+] Jungjin Park,[+] Sangheon Lee, Joonhyeon Kang, Taehyun Hwang, Kug-Seung Lee, Han-Koo Lee, Seunghoon Nam, Chunjoong Kim,* Yung-Eun Sung,* and Byungwoo Park*

modification with electronically conductive layers and/or nanoscale morphological control for the shortened Li^+-diffusion path have been attempted in the earlier studies [14-22].

A notable success could be achieved by the solid-solution phase of $LiMn_{1-y}M_yPO_4$ (M = Fe, Co, Ni, etc.) via substitutional replacement of Mn by different cations [18-23]. Among them, $LiMn_{1-y}Fe_yPO_4$ turned out to be one of the most promising solid solution phases, mitigating the shortcomings but retaining the advantages of $LiMnPO_4$ parent counterpart [23-28].

A thorough understanding on the electronic structure of $LiMn_{1-y}Fe_yPO_4$ can provide a guide to design high performance multi-transition-metal olivine materials, since the electronic structure governs the electrochemical potential and structural stability of cathodes during battery operation. Tremendous efforts have been made to study the detailed electronic structure of $LiMn_{1-y}Fe_yPO_4$ electrode by electron energy loss spectroscopy (EELS) [24-25], x-ray photoelectron spectroscopy (XPS) [27], hard x-ray absorption spectroscopy (XAS) [27,29-35], and soft x-ray absorption and emission spectroscopy [36-38]. Although transition metal (*TM*) *K*-edge XAS has been extensively employed to investigate the electronic structure (such as the Mn/Fe valence evolution), the oxidation states cannot be clearly fingerprinted because transition metal (*TM*)-3*d* states are dipole forbidden in the *TM K*-edge spectra, and only exhibit some weak pre-edge features through the 1*s*-to-3*d* quadrupole transitions [37-39]. In contrast, soft x-ray absorption (sXAS) across the Mn/Fe *L*-edges provides a direct probe of the *TM*-3*d* states through dipole-allowed 2*p*-to-3*d* transitions ($L_{2,3}$-edges), which allows a quantitative determination of the redox evolution upon the electrochemical cycling [38-42]. However, the previous sXAS studies showed that

oxidation states of Mn did not change during the (de)lithiation of $LiMn_{1-y}Fe_yPO_4$ although it is generally accepted that the (de)lithiation of $LiMn_{1-y}Fe_yPO_4$ is accompanied by the change of the oxidation states in both Mn and Fe [36,43]. Meanwhile, Mn *K*-edge XAS can trace the change in the Mn local nearest-neighbor distance associated with the local structural change, since *TM K*-edge extended x-ray absorption fine structure (EXAFS) clearly reveals detailed structural information with short-to-medium ranges [33,34,37].

Herein, we synthesized carbon-coated $LiMn_{0.8}Fe_{0.2}PO_4$ mesocrystal, composed of ~40-nm-sized nanocrystallites, as a model compound to study the effect of each transition metal on the changes of the electronic structure and electrochemical performance in multi-transition-metal phosphates. The morphology-controlled $LiMn_{0.8}Fe_{0.2}PO_4$ mesocrystal exhibited good electrochemical properties (i.e., high specific capacity and good rate capability), which is prerequisite to investigate the evolution of Mn and Fe redox centers upon battery cycling. Our combined analysis of *ex situ* soft x-ray absorption spectroscopy (sXAS) and *in situ* hard x-ray absorption spectroscopy (XAS) provided clear experimental evidence on the reversible redox reaction of Mn and Fe in $LiMn_{0.8}Fe_{0.2}PO_4$.

3.2. Experimental Section

Materials Preparation: The micron-sized porous $LiMn_{0.8}Fe_{0.2}PO_4$ (LMFP) mesocrystal was synthesized by a solvothermal method. A mixture (10 ml) of manganese acetate tetrahydrate ($Mn(CH_3COO)_2 \cdot 4H_2O$: 0.008 mol) and iron nitrate nonahydrate ($Fe(NO_3)_3 \cdot 9H_2O$: 0.002 mol) aqueous solution was injected into *n*,*n*-dimethylformamide (DMF) (C_3H_7NO: 140 ml) at 80°C, and it was stirred for 1 h. Then, lithium hydroxide monohydrate ($LiOH \cdot H_2O$: 0.036 mol), phosphoric acid (H_3PO_4: 0.012 mol), ascorbic acid ($C_6H_8O_6$: 0.006 mol), and nitric acid (HNO_3: 0.04 mol) were added with the additional stirring for 6 h at 24°C. The mixed solution was transferred to a Teflon-lined autoclave and heated at 180°C for 12 h. Then, the resulting solution was centrifuged, and the precipitates were thoroughly washed with a deionized water followed by drying at 60°C overnight.

The carbon-coated LMFP mesocrystal (LMFP/C) was synthesized by impregnating the as-synthesized LMFP powders in sucrose solution (sucrose:LMFP = 3:7 by weight) followed by drying and calcining them at 700°C for 3 h under H_2/Ar (4 vol. % H_2) atmosphere.

Materials Characterization: The crystal structure and grain size of the LMFP mesocrystal were characterized by x-ray diffraction (XRD, D8 Advance: Bruker). The morphology and crystal structure were analyzed using field-emission scanning electron microscopy (FE-SEM, Merlin Compact: Zeiss) and high-resolution transmission electron microscopy (HRTEM, JEM-3000F: JEOL, Japan). An inductively coupled plasma-atomic emission spectrometer (ICP-AES, Optima-4300 DV: Perkin-Elmer) was used to measure the ratio of Mn and Fe in the LMFP

mesocrystal. Carbon concentration was measured by a CHNS analyzer (Flash EA 1112: Thermo Electron Corp.). The nitrogen adsorption and desorption isotherms were obtained at 77 K (Micromeritics ASAP 2020), and the specific surface area and the pore size distribution were calculated by the Brunauer-Emmet-Teller (BET) and the Barret-Joyner-Halenda (BJH) methods, respectively.

For the electrochemical characterization, the active materials were tested using coin-type half cells (2016 type) with a Li counter electrode. The composition of the electrode was set to be the same for all of the samples, which consisted of an active material, super P carbon black, and a polyvinylidene fluoride (PVDF) binder with a weight ratio of 7:2:1. Loading level of active materials was ~1 mg/cm^2. The electrolyte contained 1 M $LiPF_6$ in ethylene carbonate and diethyl carbonate (1/1 vol. %) (Panax Etec).

X-Ray Absorption Spectroscopy: The *ex situ* sXAS measurements were performed by carefully disassembling $Li_xMn_{0.8}Fe_{0.2}PO_4$ cells with different states of charge/discharge in an argon-filled glovebox. The electrodes were soaked in anhydrous dimethyl carbonate for 1 h to remove Li salts and/or thick SEI layer that prohibits the detailed analysis of sXAS, and dried in a vacuum chamber inside the glovebox, as reported elsewhere [37,38]. The samples were transferred to the ultra-high vacuum chamber at the end station for the synchrotron x-ray measurements. The Mn/Fe *L*-edge and O *K*-edge sXAS spectroscopy were performed at room temperature and at the beamline 4D of Pohang Light Source II (PLS II), Korea. We used the total electron yield (TEY) and partial electron yield (PEY) detection mode for sXAS spectra by recording the sample current normalized to a signal current, which was measured simultaneously using a gold mesh in ultrahigh vacuum (< 10^{-9} Torr). In this case, a *p*-

polarized (≅ 85%) synchrotron photon beam, with a spectral energy resolution of ΔE = 150 meV, had a probing depth of several nanometers and ~1 nm, respectively, for TEY and PEY modes [38,44]. The *in situ* XAS across the Mn and Fe *K*-edges were obtained at the 8C nano-probe XAFS beamline (BL8C) of Pohang Light Source (PLS-II) in the 3.0 GeV storage ring, with a ring current of 300 mA. The radiation source of BL8C is tapered in-vacuum-undulator. The XAS spectra were collected in transmission mode, and processed using Demeter software. Extended x-ray absorption fine structure (EXAFS) spectra were plotted in *r*-space with a Fourier-transform range of 3 - 11 $Å^{-1}$ and a k^2-weight [45].

3.3. Results and Discussion

Electrochemically favorable meso/nano-structures were designed to systematically investigate the effects of Mn and Fe on the electronic structure changes of $Li_xMn_{0.8}Fe_{0.2}PO_4$ during battery cycling. The $LiMn_{0.8}Fe_{0.2}PO_4$ mesocrystal (Figs. 3-1 and 3-2(a)) clearly exhibits porous plate-shaped morphology that consists of ~40-nm-sized nanoparticles, which enables facile transport of electrons and Li^+ during battery operation. Furthermore, such mesocrystal is highly adequate to perform synchrotron-based sXAS and XAS due to their good electrochemical performance and ease of handling [46,47]. Transmission electron microscopy (TEM) and electron diffraction from a single aggregate are presented in Fig. 3-2(a). The selected area electron diffraction (SAED) exhibits spot patterns, which indicate that ~40-nm-sized primary particles are highly oriented in the mesocrystal. The EDS elemental mapping for LMFP mesocrystal exhibits homogeneous distribution of Mn, Fe, P, and O elements (Fig. 3-2(b)). The Mn/Fe atomic ratio in the mesocrystal was confirmed to be ~4 by inductively coupled plasma-atomic emission spectroscopy (ICP-AES) analysis. X-ray diffraction of the bare LMFP mesocrystal corresponds to the orthorhombic olivine structure (Fig. 3-3), and the complete solid solution of $LiMn_{0.8}Fe_{0.2}PO_4$ is confirmed by comparing XRD pattern of LMFP with $LiMnPO_4$ (JCPDS #97-009-7763) and $LiFePO_4$ (JCPDS #40-1499). The scattering angle of LMFP shifts slightly to higher than that of $LiMnPO_4$ due to smaller ionic radius of Fe^{2+} than Mn^{2+}. The carbon content was measured to be ~5.2 wt. % by CHNS analysis.

The porous nanostructures of the bare and carbon-coated LMFP mesocrystal were also confirmed by BET and BJH of which isotherms showed a typical *type-IV* mesoporous structure (Fig. 3-4) [48]. The BET surface areas of the bare and carbon-coated LMFP mesocrystal were ~28 and ~61 m^2/g, respectively. The increase of BET surface area after carbon coating can be attributed to the porosity of carbon.

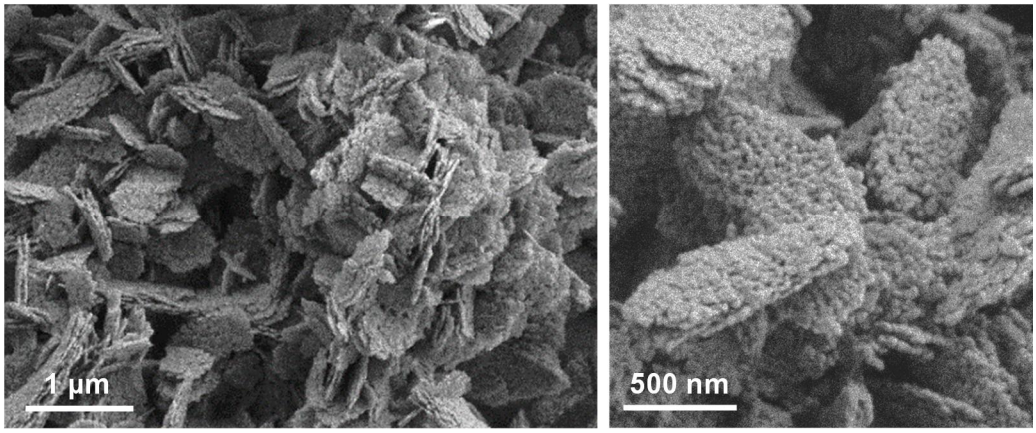

Fig. 3-1. SEM images of the $LiMn_{0.8}Fe_{0.2}PO_4$ mesocrystal.

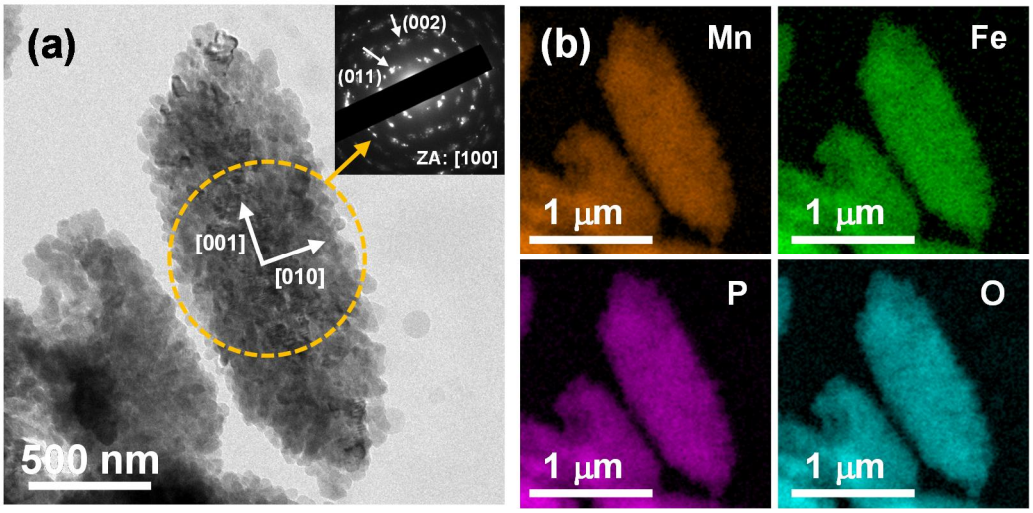

Fig. 3-2. (Color) (a) TEM image of the $LiMn_{0.8}Fe_{0.2}PO_4$ mesocrystal with a selected area electron diffraction pattern of the primary particles (along the [100] zone axis). (b) EDS mapping of Mn, Fe, P, and O, respectively.

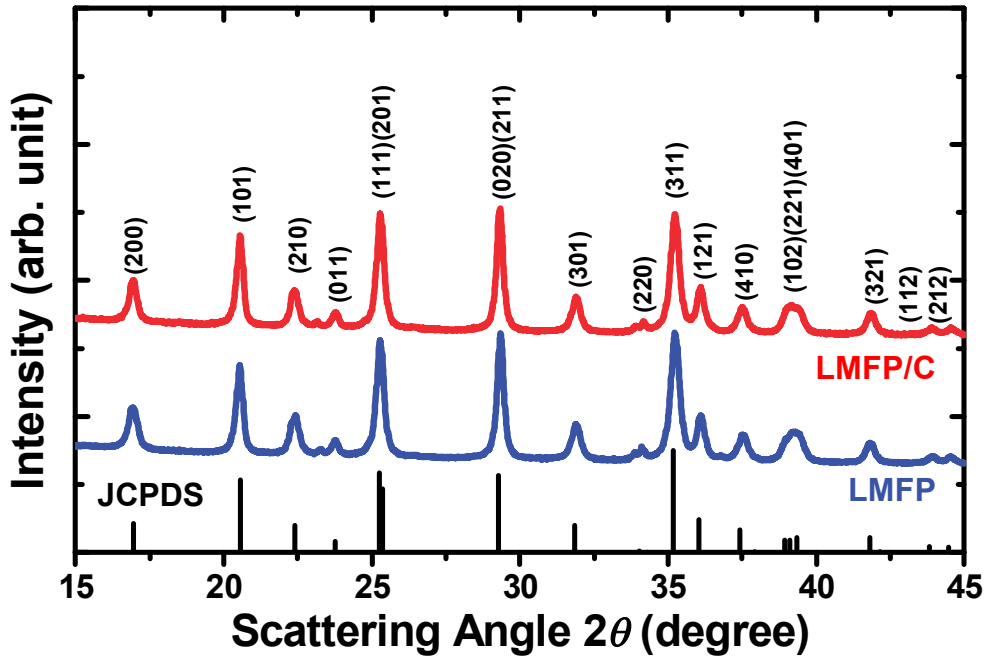

Fig. 3-3. (Color) XRD patterns for the bare and carbon-coated $LiMn_{0.8}Fe_{0.2}PO_4$ mesocrystal.

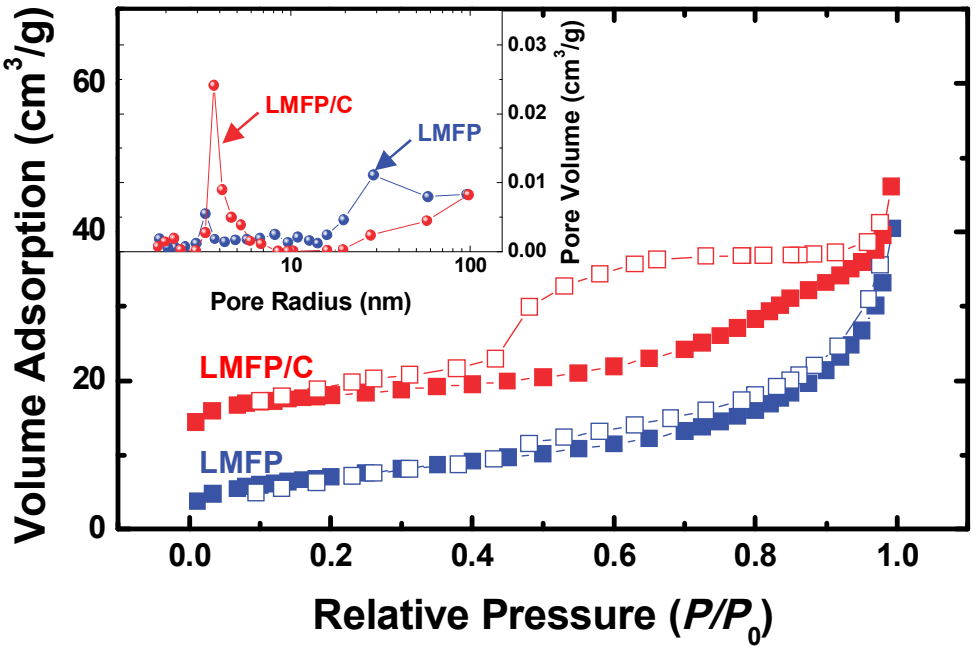

Fig. 3-4. (Color) N_2 adsorption/desorption isotherms with the pore-size distribution for the bare and carbon-coated $LiMn_{0.8}Fe_{0.2}PO_4$ mesocrystal.

The electrochemical performance of the carbon-coated LMFP mesocrystal was evaluated using galvanostatic charge/discharge tests and cyclic voltammetry (CV). The carbon-coated LMFP mesocrystal was cycled at various current densities (0.1 C to 10 C) (Figs. 3-5 and 3-6). The curves show a pseudo-flat potential profile with two redox potentials of ~3.5 V and ~4.1 V, which result from the redox reactions of Fe^{2+}/Fe^{3+} and Mn^{2+}/Mn^{3+}, respectively, implying that both transition metals in $LiMn_{0.8}Fe_{0.2}PO_4$ participate in the electrochemical reaction with concurrent (de)intercalation of Li^+. The carbon-coated LMFP mesocrystal showed a capacity of ~130 mAh/g (~75% of the theoretical capacity (= 171 mAh/g)), which is comparable with the previously reported carbon-coated $LiMn_{1-y}Fe_yPO_4$ nanoparticles [19-26]. The discharge capacity was ~80 mAh/g at a rate of 10 C, which is ~61% of the specific capacity at a rate of 0.05 C, indicating the high rate capability of the carbon-coated LMFP mesocrystal. Figure 3-7 shows CV profiles for the carbon-coated LMFP mesocrystal taken at the potential scan rates of 0.01, 0.05, 0.1, 0.15, and 0.2 mV/s (2.5 - 4.7 V). The CV data at 0.01 mV/s clearly show two sets of anodic/cathodic current peaks at ~4.1 V and ~3.5 V, which correspond to the two plateaus observed in the voltage profile. The shape of the CV was highly reversible even when the scan rate was increased up to 0.2 mV/s, indicative of the high rate capability of the carbon-coated LMFP mesocrystal [26]. The high rate performance of the carbon-coated LMFP mesocrystal is attributed to both the porous mesocrystal structure composed of ~40-nm-sized nanocrystallites and the conformal carbon coating on the surface of individual nanoparticles [22,49]. The cycling stability of the carbon-coated LMFP

mesocrystal is shown in Fig. 3-8. The cycling test was conducted for 100 cycles at a discharge rate of 0.1 C. Good electrochemical properties enable understanding of the electronic transitions and the corresponding structural changes in the LMFP phase, which provides fundamental and essential guides to design high performance batteries.

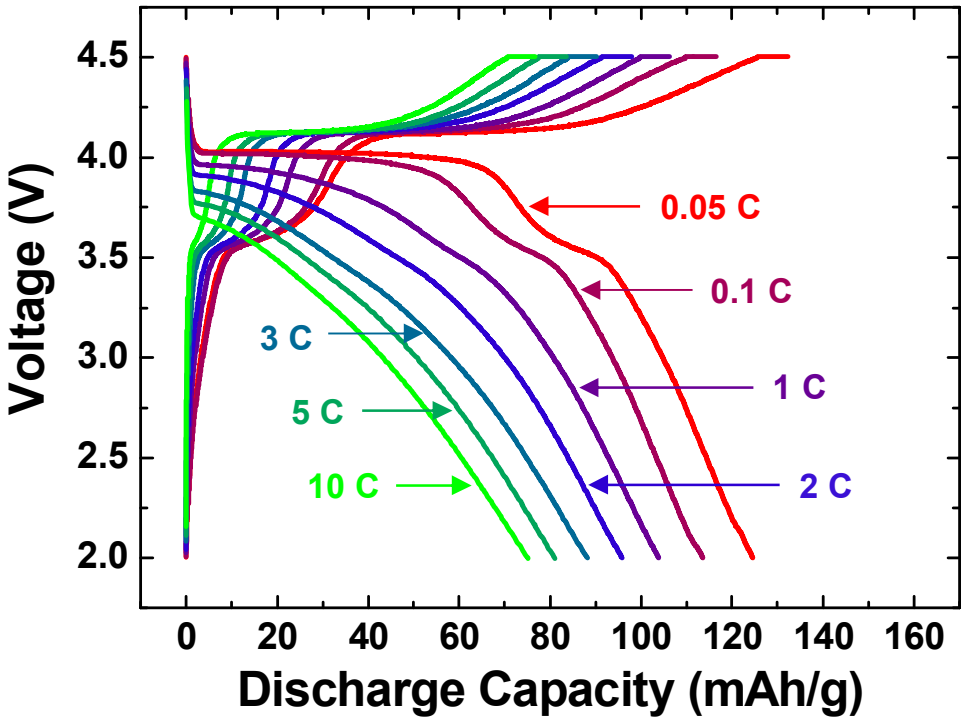

Fig. 3-5. (Color) Charge-discharge curves of the carbon-coated $LiMn_{0.8}Fe_{0.2}PO_4$ mesocrystal at various delithiation/lithiation rates.

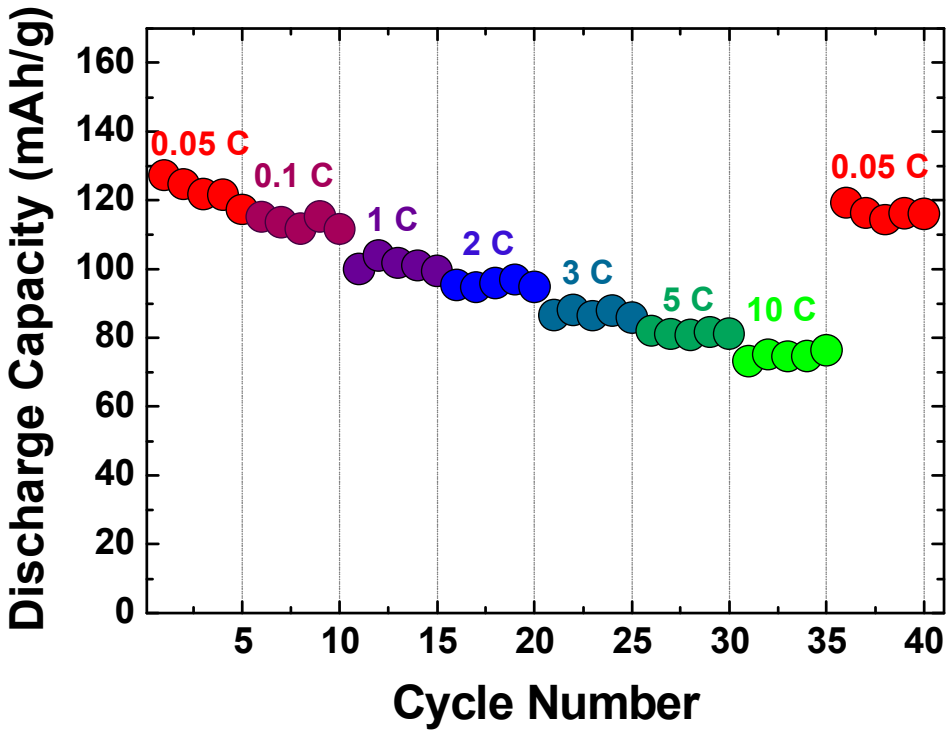

Fig. 3-6. (Color) Rate capability up to the rate of 10 C (1 C = 171 mA/g).

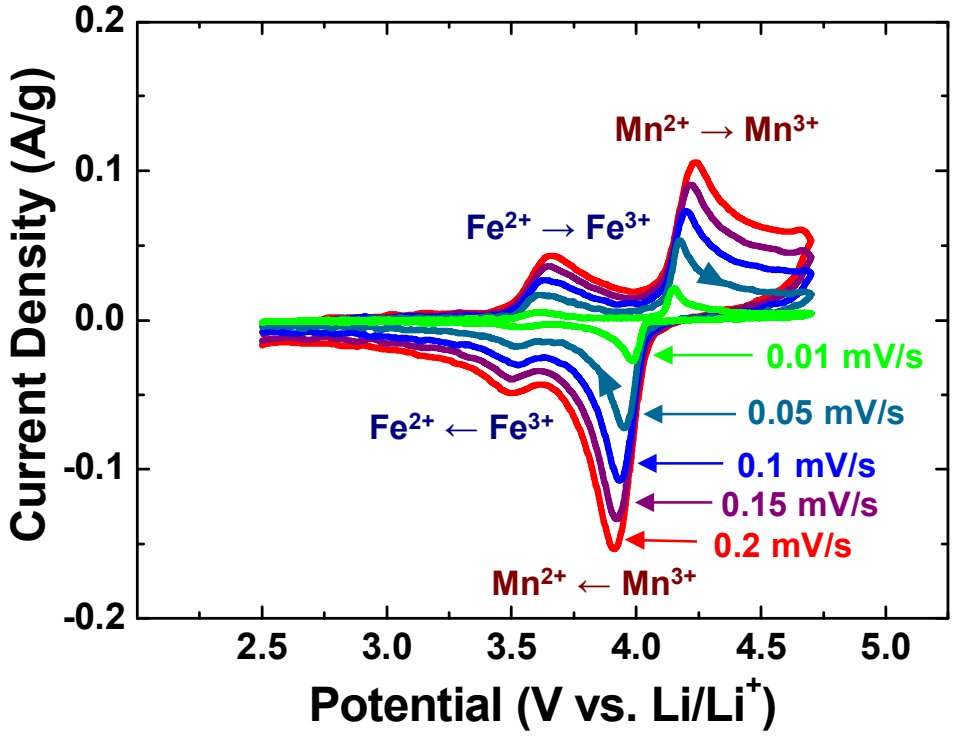

Fig. 3-7. (Color) Cyclic voltammetry profiles of the carbon-coated $LiMn_{0.8}Fe_{0.2}PO_4$ mesocrystal at various scan rates.

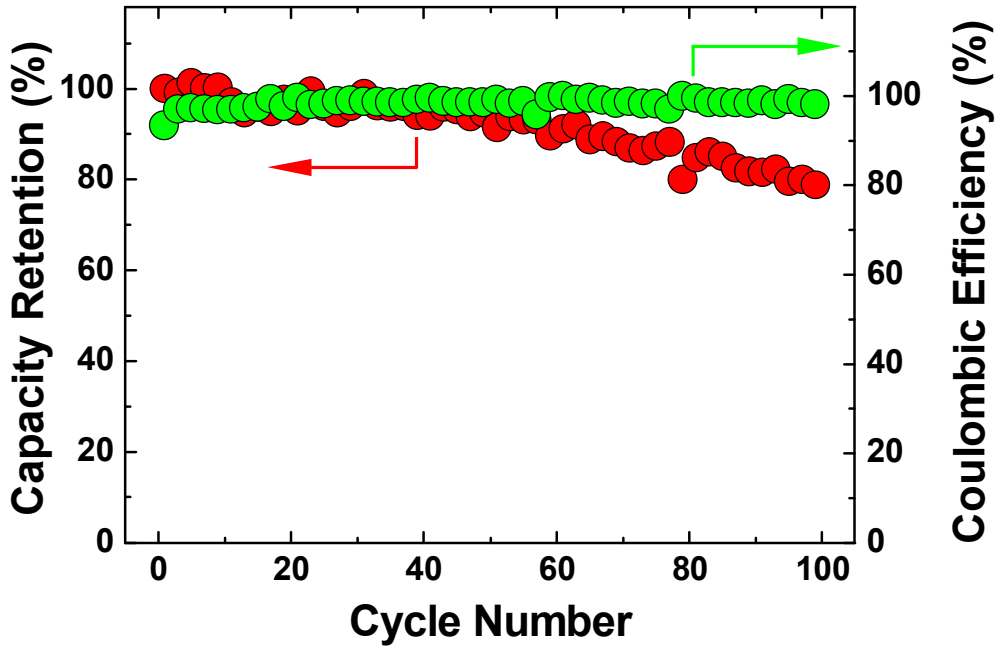

Fig. 3-8. (Color) Cycle-life performance of the carbon-coated $LiMn_{0.8}Fe_{0.2}PO_4$ mesocrystal at a rate of 0.1 C.

Compared with a hard x-ray (> 5 keV) technique, which is widely employed to investigate the electronic structural change in transition metals by x-ray absorption across the *K*-edge, sXAS has advantages on probing the key electronic states in the vicinity of the Fermi level, which are relevant to the battery performance, such as valence, spin states, and local structural changes on crystal field [37-40]. *Ex situ* sXAS measurements of Fe and Mn *L*-edges, and O *K*-edge were performed by carefully disassembling the partially-delithiated cells at different states of charge/discharge (Fig. 3-9).

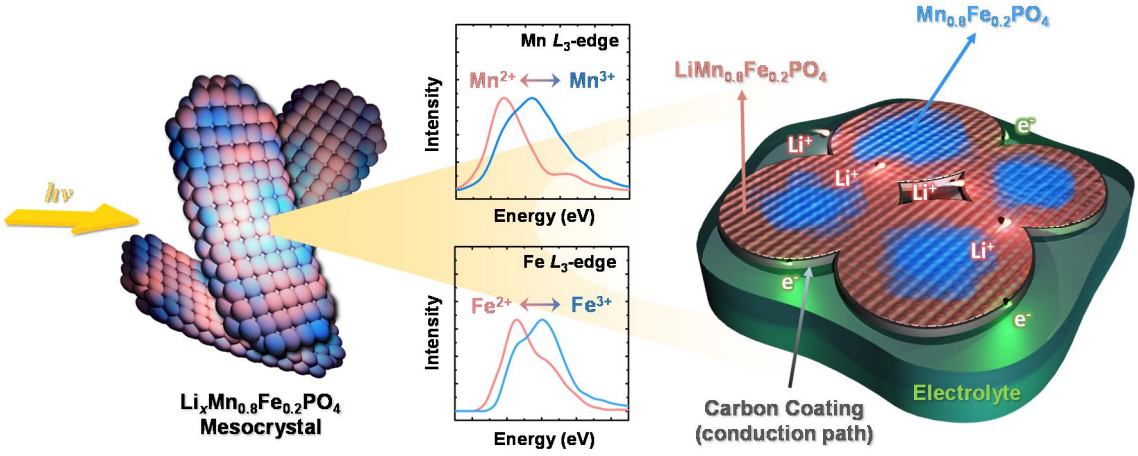

Fig. 3-9. (Color) Schematic illustration showing the carbon-coated $LiMn_{0.8}Fe_{0.2}PO_4$ mesocrystal and the soft x-ray absorption spectroscopy measurement.

The voltage profile of the $LiMn_{0.8}Fe_{0.2}PO_4$ cell for the *ex situ* sXAS was presented in Fig. 3-10(a), and the corresponding *L*-edge spectra of Fe and Mn in $Li_xMn_{0.8}Fe_{0.2}PO_4$ during a cycle are shown in Fig. 3-10(b). Total electron yield (TEY) signal of the Fe and Mn *L*-edge, with a probe depth of several nanometers, was collected from the different (dis)charged states of LMFP mesocrystal. The Fe and Mn *L*-edge spectra exhibit roughly two groups of peaks at ~706 and ~720 eV, and ~639 and ~652 eV, respectively, resulting from the core hole spin-orbital-coupling split [37-40]. Only L_3-edge spectra were analyzed because the L_2-edge in the *TM* spectra displays less distinct features than the L_3-edge due to the shorter lifetime of the $2p_{1/2}$ core hole (higher possibility of recombination, so-called Coster-Kronig Auger decay) [50]. The absorption profile of the double-peak features in the Fe L_3-region (at 706 and 708 eV) can be used to fingerprint the relative oxidation states of Fe between Fe^{2+} and Fe^{3+}. The double-peak features at 639 and 641 eV (Mn L_3-edge) represent the relative oxidation state of Mn between Mn^{2+} and Mn^{3+} (Fig. 3-10(b)).

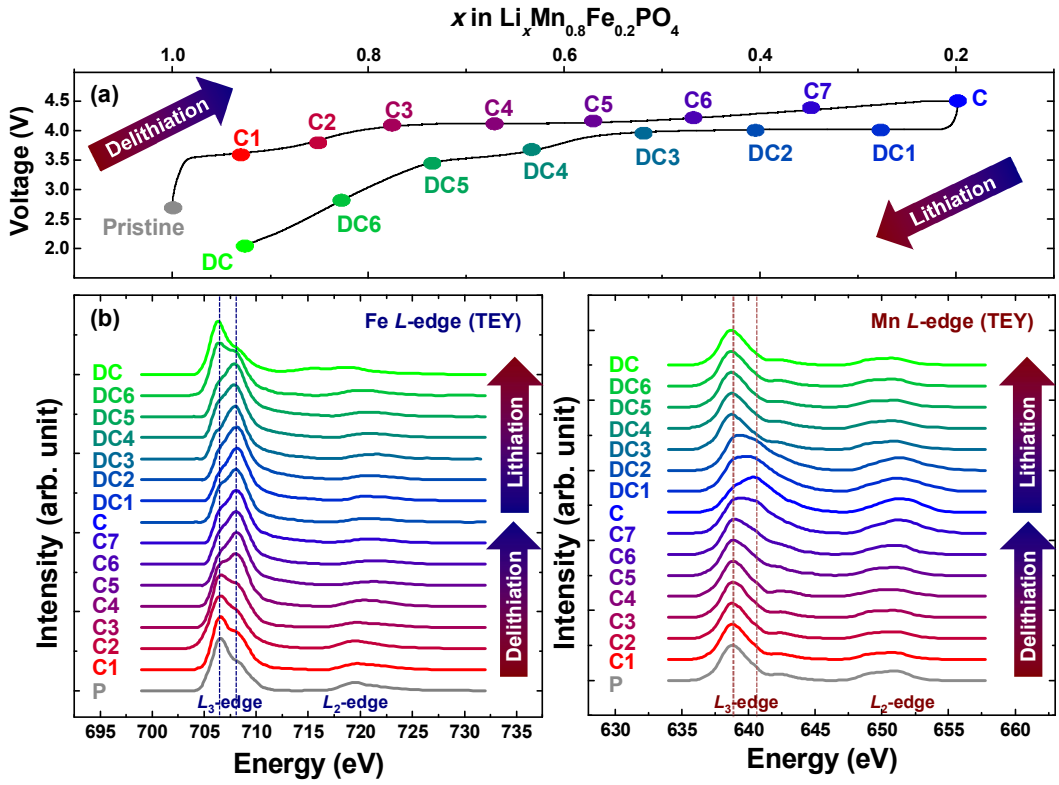

Fig. 3-10. (Color) (a) Charge-discharge curves for the carbon-coated $LiMn_{0.8}Fe_{0.2}PO_4$ mesocrystal showing cut-offs for the different cells at a rate of 0.05 C. (b) Fe and Mn *L*-edge soft x-ray absorption spectroscopy (sXAS) total electron yield (TEY) spectra at different depths of charge/discharge levels. Intensity ratio of the further L_3 splits (dotted lines) fingerprints the oxidation states of Fe and Mn.

The Fe L_3-edge spectra evolve with the electrochemical cycling, in which the intensity at 708 eV becomes stronger during delithiation process in the first plateau (~3.6 V) (Fig. 3-11). The 641 eV peak increases, indicating the oxidation of Mn^{2+} to Mn^{3+} proceeded in the second plateau (~4.2 V). Those spectral evolution of the *TM* L_3-edge during charge indicates the voltage plateaus at ~3.6 and ~4.2 V, originating from the redox reactions of Fe^{2+}/Fe^{3+} and Mn^{2+}/Mn^{3+} in the LMFP nanocrystallites, respectively [36-42,51]. The increase of the small peak at ~643 eV is associated with the oxidation reaction of Mn^{2+} to Mn^{3+} due to multiplet absorption process in sXAS, which results from the localized 3*d* states and strong overlap of core and valence wave functions [50,52,53]. The TEY spectra of Fe and Mn L_3-edge are reversibly recovered to the pristine state by discharge process (Fig. 3-11). Reduction of Mn^{3+} to Mn^{2+} occurs in the plateau at ~4.1 V, followed by that of Fe^{3+} to Fe^{2+} in the plateau at ~ 3.5 V. Partial electron yield (PEY) signal of sXAS (Fig. 3-12), with ~1-nm probe depth, shows similar behavior with TEY. Consistency of the change in Mn and Fe redox between two different probing depths is attributed to the homogeneous reaction throughout the LMFP mesocrystal, due to the nanometric size of primary particles, with the absence of any parasitic surface reaction [54].

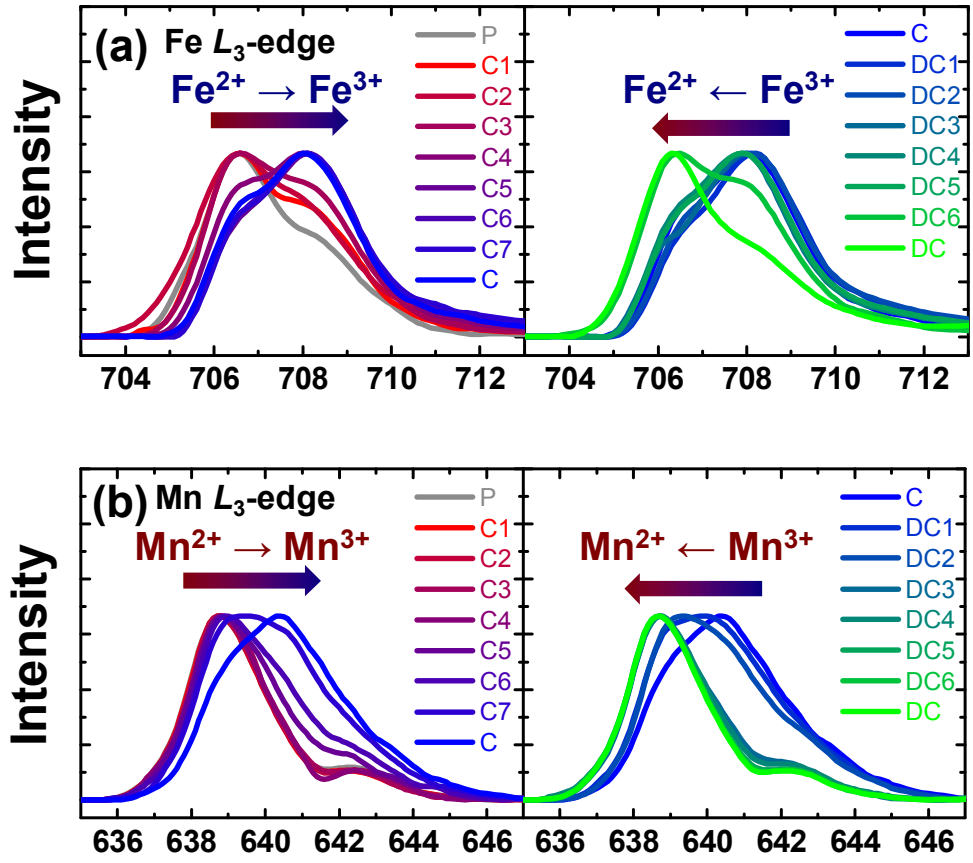

Fig. 3-11. (Color) Stacked (a) Fe and (b) Mn L_3-spectra with different degrees of charge/discharge.

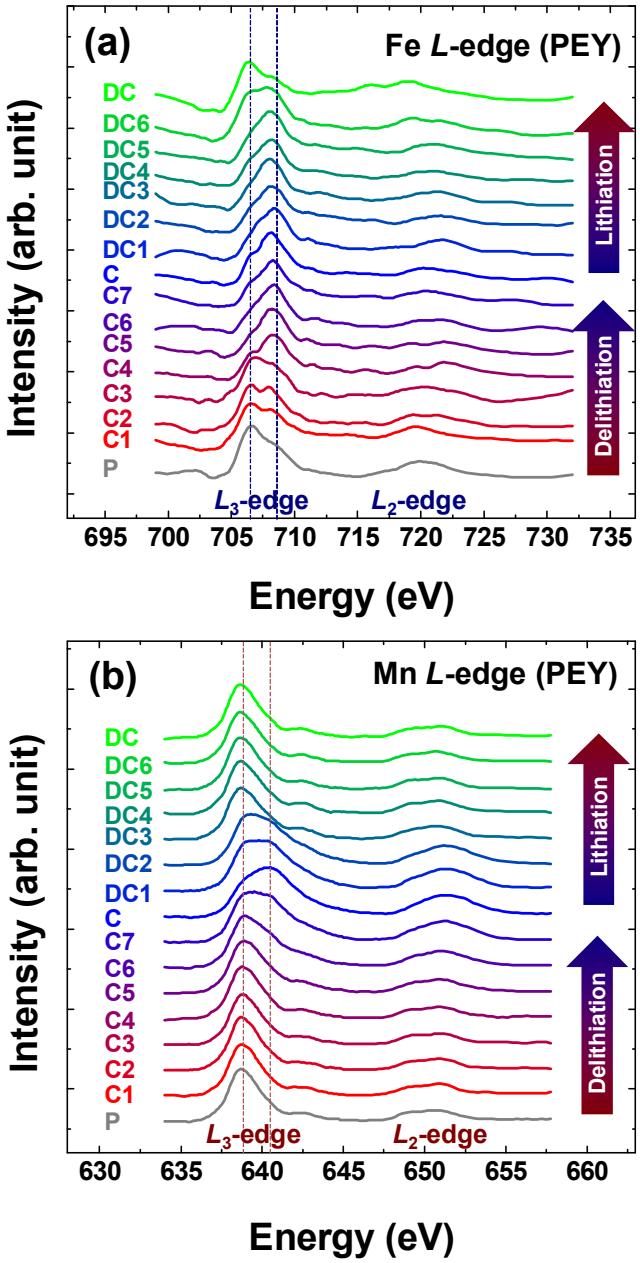

Fig. 3-12. (Color) Partial electron yield (PEY) spectra of (a) Fe *L*-edge, (b) Mn *L*-edge sXAS at different depths of charge/discharge levels.

In order to quantitatively estimate the oxidation states of each metal at different states of charge/discharge, fitting of the experimental data using a linear combination of reference states is generally employed [38,51]. In this work, however, the sXAS measurements were performed to trace the change of oxidation state of each transition metal during the battery operation. Therefore, the evolution of Fe and Mn oxidation states was estimated by fitting the experimental data using a linear combination of two reference spectra (pristine (Fe_{pri} or Mn_{pri}) and charged (Fe_{cha} or Mn_{cha}) states) in Figs. 3-13 and 3-14. It should be noted that such fitting method can be considered only in limited cases, where a two-phase reaction (first-order transition) proceeds [37-42]. The apparent fraction of Fe L_3-edge ($Fe_{cha}/(Fe_{pri} + Fe_{cha})$) increases during the initial stage of delithiation (i.e., charging up to ~3.6 V), indicating that Fe^{2+} oxidizes to Fe^{3+} in $Li_xMn_{0.8}Fe_{0.2}PO_4$. Meanwhile, the apparent fraction of Mn L_3-edge ($Mn_{cha}/(Mn_{pri} + Mn_{cha})$) is almost the same in this stage. The apparent fraction ($Fe_{cha}/(Fe_{pri} + Fe_{cha})$) of Fe L_3-edge spectra increase by delithiation of $Li_xMn_{0.8}Fe_{0.2}PO_4$ ($1 \geq x \geq \sim 0.7$). As the lithium content x decreases below ~0.7, the apparent fraction ($Mn_{cha}/(Mn_{pri} + Mn_{cha})$) of Mn L_3-edge starts to increase, which corresponds to the Mn^{2+} being oxidized to the Mn^{3+} state in $Li_xMn_{0.8}Fe_{0.2}PO_4$ during delithiation, whereas Fe L_3-edge spectra almost remain constant. This observation seems to deviate from the voltage profile which depicts that the redox reaction proceeds entirely by Fe^{2+}/Fe^{3+} in the early stage of delithiation ($1 \geq x \geq \sim 0.8$), followed by the oxidation of Mn ($\sim 0.8 \geq x \geq 0$) [37,38,42].

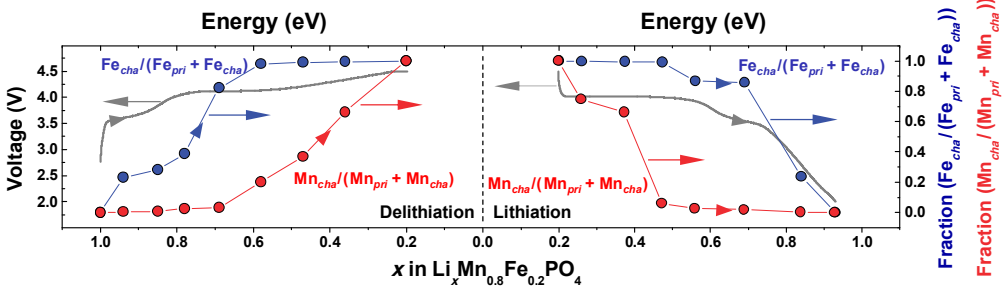

Fig. 3-13. (Color) Evolution of Fe or Mn oxidation states based on the linear combination of two reference spectra (pristine (Fe_{pri} or Mn_{pri}) and charged (Fe_{cha} or Mn_{cha}) states).

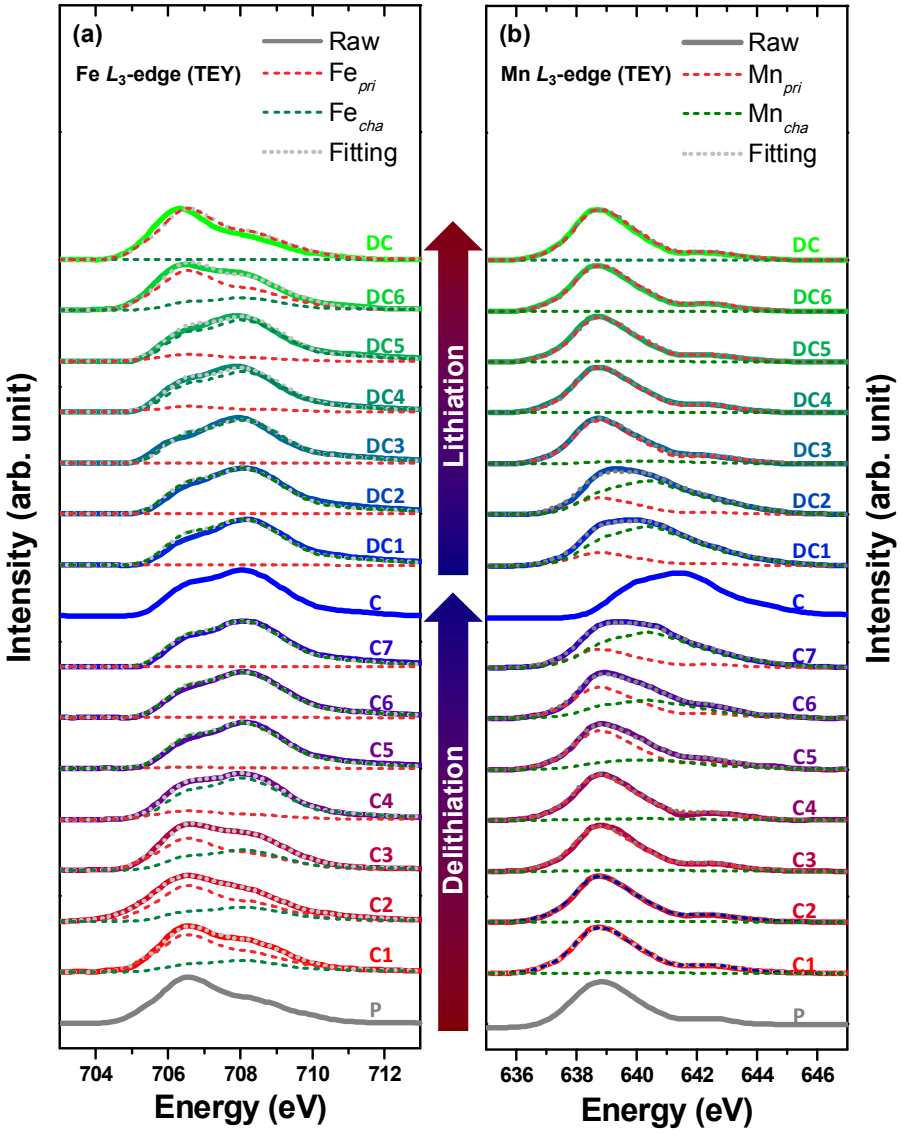

Fig. 3-14. (Color) The fitting results based on the linear combination of two reference spectra (pristine and charged samples). Comparison of the experimental (solid lines) and two- reference fitting spectra (dot lines) of (a) Fe and (b) Mn L_3-edge at different depths of charge/discharge levels.

To clarify the origin of discrepancy between the evolution of oxidation states of Fe/Mn and the electrochemical data, the O *K*-edge spectra were also investigated (Fig. 3-15). It has been established that, in the 3*d TM* compounds, the relatively sharp low-energy O *K*-edge features, so-called "pre-edge features," are of mainly *TM*-3*d* character, which is attributed to the O 2*p*-orbitals hybridized with the *TM* 3*d*-orbitals [36,37,55,56]. Figure 3-15 presents the XAS of the O *K*-edge collected on the partially-delithiated $Li_xMn_{0.8}Fe_{0.2}PO_4$ at different states of charge. Within the composition range of $1 \geq x \geq \sim 0.8$ in $Li_xMn_{0.8}Fe_{0.2}PO_4$, the pre-edge intensity at ~533 eV increases, where the oxidation reaction of Fe^{2+} occurs. (Fig. 3-15(b)). Possibly, the hybridization of the Fe-3*d* and O-2*p* states causes the transition of O 1*s*-orbitals to Fe 3*d*-orbitals, and contributes to the pre-edge intensity [37,38,57]. As the lithium content is further reduced to ~0.7, the oxidation of Mn is accompanied with the swelling of pre-edge features and appearance of additional peaks. Although the detailed assignment of each peak is not clear yet, these additional peaks are associated with the symmetry transition of Mn systems from O_h to D_{4h} by oxidation of Mn^{2+} to Mn^{3+}, which leads to the energy splitting of Mn 3*d*-orbitals, followed by the Jahn-Teller distortion [36,37,55]. During lithiation, the pre-edge features of O *K*-edge spectra reversibly change, finally returning back to that of the pristine state. PEY signal of O *K*-edge sXAS (Fig. 3-16), with ~1-nm probe depth, shows similar behavior with TEY, which is attributed to the homogeneous reaction throughout the LMFP mesocrystal.

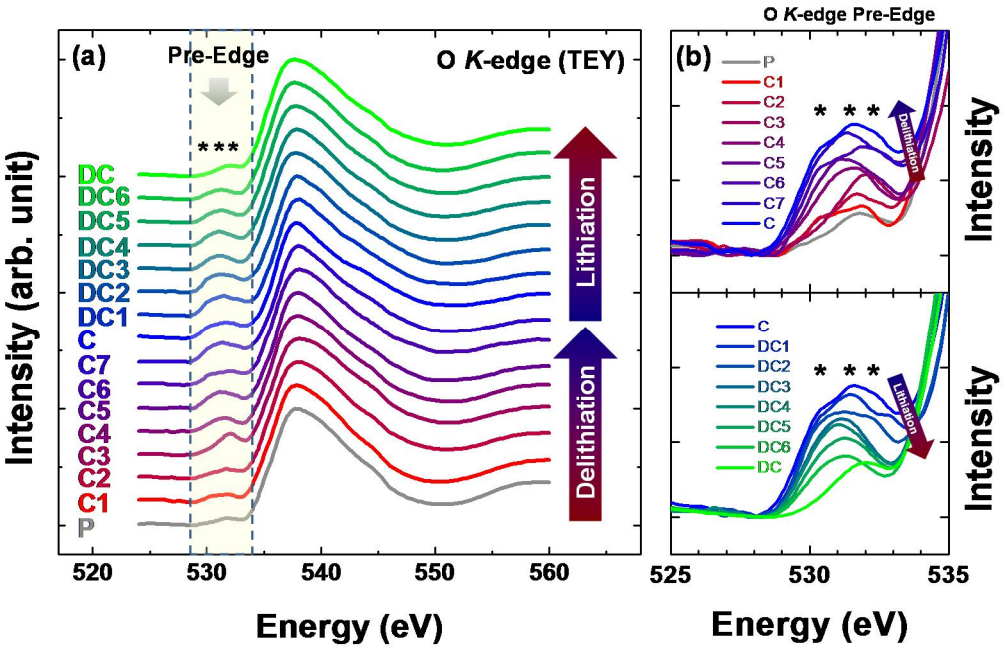

Fig. 3-15. (Color) (a) sXAS total electron yield (TEY) spectra of the O *K*-edge with different degrees of charge/discharge levels. (b) Stacked O *K*-pre-edge region with different degrees of charge and discharge, respectively. The three peak-absorption edges originate from the Jahn-Teller active Mn^{3+}, as marked by the asterisks.

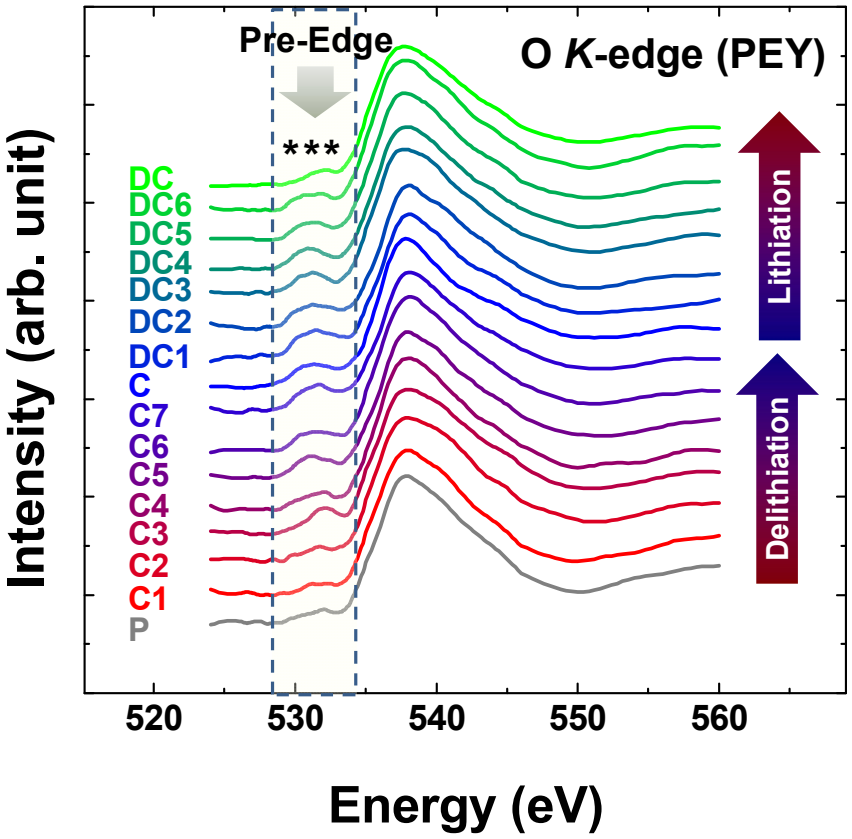

Fig. 3-16. (Color) Partial electron yield (PEY) spectra of O *K*-edge sXAS at different depths of charge/discharge levels. The three-peak absorption edge features are marked by the asterisks.

After careful investigation of the Fe L_3-edge, Mn L_3-edge, and O K-edge evolution with the electrochemical reaction, the swelling of pre-edge features at ~533 eV of O K-edge occurs although the Mn^{3+} concentration does not increase in the compositional range of ~0.8 ≥ x ≥ ~0.7 in $Li_xMn_{0.8}Fe_{0.2}PO_4$. Firstly, the expectation of the evolution of Fe/Mn oxidation states reveals error because the linear combination fitting using two reference spectra cannot reflect the real oxidation states, especially when the electrode materials are transformed by the solid solution reaction [39], and $LiMn_yFe_{1-y}PO_4$ materials show a mixed type of transformation (solid solution and two phase reaction) during (dis)charge process [33]. Secondly, it can be attributed to the charge compensation at the oxygen sites in the range of 1 ≥ x ≥ ~0.7 even in the olivine structure [36,43], which is similar to other cathode materials [58,59]. It has been reported that the redox reactions during delithiation/lithiation of $Li_xMn_{1-y}Fe_yPO_4$ are complex, and involve repopulation of charges for all the constituent elements [36,43]. If the oxygen participates in the charge compensation during electrochemical reaction, the redox reactions of the all components (i.e., Mn, Fe, and O) can occur at the same time, especially in the composition range of ~0.7 ≥ x ≥ ~0.6 in $Li_xMn_{0.8}Fe_{0.2}PO_4$. Theoretical predictions on the evolution of the electronic structures in Mn/Fe L-edge and O K-edge during (de)lithiation will be performed by DFT calculation for the future work.

In situ Fe/Mn K-edge XAS measurements were performed to investigate the overall trend of the Mn/Fe valence evolution during delithiation ((Fig. 3-17). According to the x-ray absorption near edge structure (XANES), the oxidation reaction

proceeds entirely by Fe^{2+}/Fe^{3+} in the early state of delithiation while oxidation of Mn sets in later, in good accordance with the trend shown in the sXAS results. In our XANES spectra across the Fe/Mn *K*-edge, there is no isosbestic point that is indicative of two-phase transformation upon delithiation [38]. These results look plausible since $LiMn_yFe_{1-y}PO_4$ suffers the solid solution reaction followed by two phase reaction during the charge process [33].

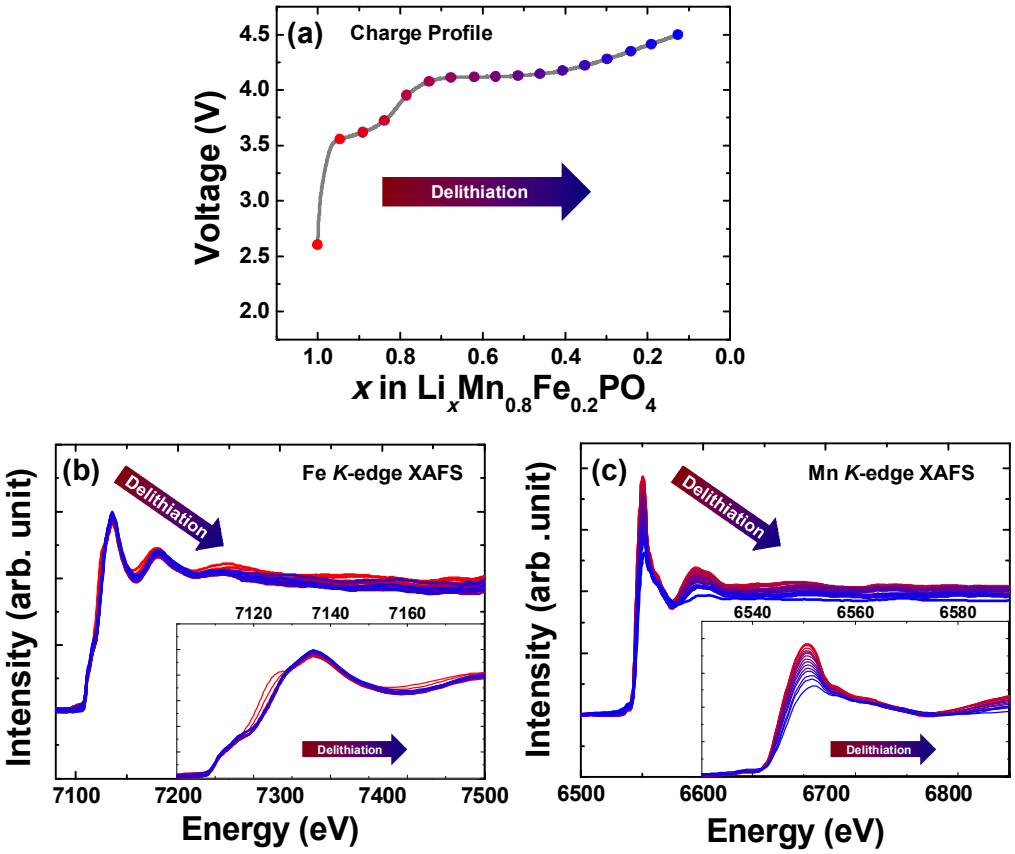

Fig. 3-17. (Color) (a) The first charging process of the in situ cell at a rate of 0.05 C, and circles in the voltage profile indicate the intervals of x-ray absorption fine structure (XAFS) scans. (b-c) Normalized Fe and Mn *K*-edge XAFS spectra at different depths of charge levels. The insets show (b) Fe and (c) Mn *K*-edge XANES spectra during delithiation.

It is noteworthy that the peak shapes of Fe L_3-edge agree well with Fe^{2+} and Fe^{3+}, at the fully charged and pristine (or discharged) states [38]. This indicates that Fe in the $LiMn_{0.8}Fe_{0.2}PO_4$ is fully redox-active during charge/discharge. Meanwhile, the peak shapes of Mn L_3-edge are consistent with Mn^{2+} before its oxidation ($x \geq \sim 0.8$ in $Li_xMn_{0.8}Fe_{0.2}PO_4$) [37], however, XAS spectra of Mn at fully charged state revealed mixed valence states of Mn^{2+} and Mn^{3+} [36,37,43]. Although the Mn L_3-edge absorption spectra became Mn^{3+}-rich upon the charge process, as confirmed by the increase of the peak ratio, the end of charged state did not reach the complete delithiated phase ($x \cong 0.2$ in $Li_xMn_{0.8}Fe_{0.2}PO_4$), which indicates that oxidation of Mn^{2+} to Mn^{3+} is incomplete [34,36]. Therefore, the incomplete oxidation of Mn^{2+} to Mn^{3+} led to the capacity less than the theoretical capacity. The incomplete oxidation of Mn^{2+} can be attributed to the sluggish transition to Mn^{3+} or antisite defects in $Li_xMn_{0.8}Fe_{0.2}PO_4$ [26,28,60]. The antisite defects (TM_{Li}) in the olivine framework block the Li^+ migration channel, and severely degrades the electrochemical performance [61,62]. The antisite defects (TM_{Li}) induce a change in the P-O bond in the PO_4 tetrahedrons, resulting in a shift in the vibration frequencies, thus the red shift of the P-O symmetric stretching peak (around 980 cm^{-1}) is an evidence for the reduced antisite-defect concentration [26]. According to FTIR in the as-prepared $LiMn_{0.8}Fe_{0.2}PO_4$, the P-O symmetric stretching peak position shows that the concentration of antisite defects is negligible compared to the previous studies [26], therefore, the $LiMn_{0.8}Fe_{0.2}PO_4$ mesocrystal is nearly antisite-defect free (Fig. 3-18). Considering the absence of antisite defects, the incomplete oxidation of Mn^{2+} is mostly

originated from the sluggish transition of Mn^{2+}/Mn^{3+}. Such a hypothesis is quite acceptable when comparing the battery performance of $LiFePO_4$ with that of $LiMnPO_4$ [54,63] which confirmed that the Jahn-Teller active Mn^{3+} ions mainly induce its poor kinetics [28,60,63]. Therefore, the Jahn-Teller behavior of Mn^{3+} was further studied to investigate the origin of sluggish Mn^{2+}/Mn^{3+} kinetics in the LMFP mesocrystal. X-ray absorption spectra across the O *K*-edge and Mn *K*-edge reveal that the neighboring oxygen and manganese core levels are influenced by the structural distortion, and thereby the origin of the sluggish transition of Mn can be understood [36,37,55].

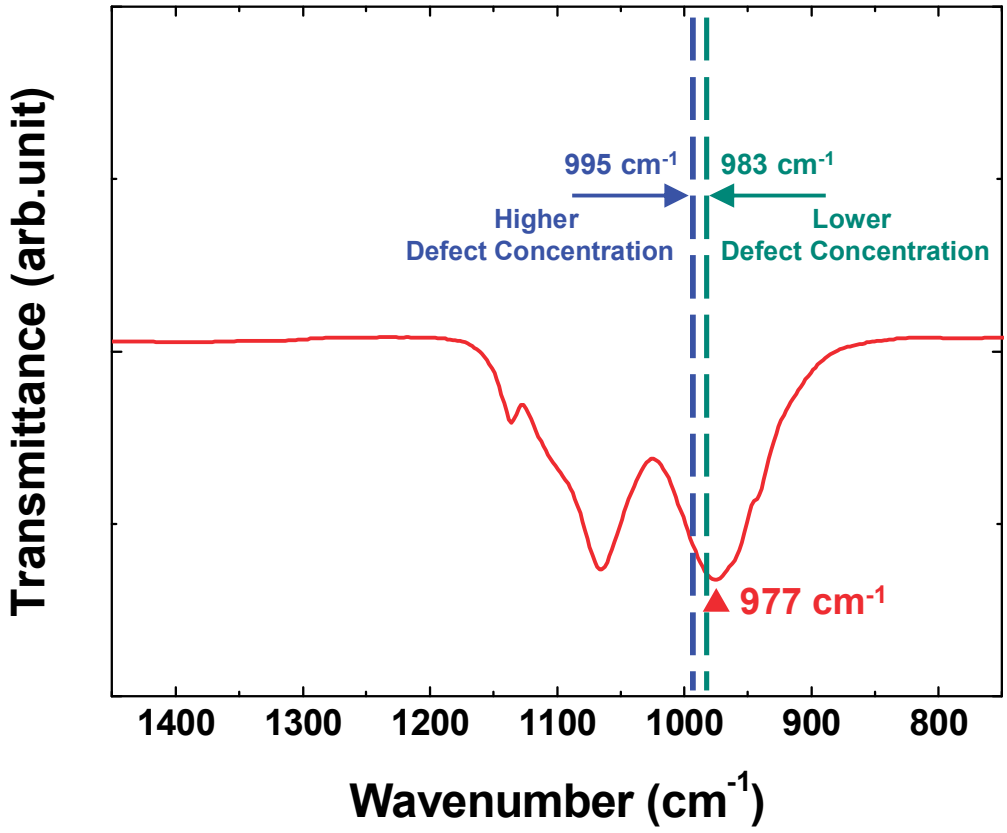

Fig. 3-18. (Color) FTIR spectra of the $LiMn_{0.8}Fe_{0.2}PO_4$ mesocrystal. The symmetric P-O stretching vibration of the $LiMn_{0.8}Fe_{0.2}PO_4$ mesocrystal is located at 977 cm^{-1}, which is similar to the previous report in which the vibration mode of defect-free $LiMn_{0.75}Fe_{0.25}PO_4$ was observed [26].

In addition to the sXAS spectra across the O *K*-edge spectra, direct information about the Jahn-Teller distortion can be extracted by XAS across the Mn *K*-edge. Extended x-ray absorption fine structure (EXAFS) (~6550 eV) of post edges in Mn *K*-edge are derived using Athena [64] to complement the XAS of the O *K*-edge (Figs. 3-17 and 3-19) [37,65]. The resultant Fourier transformed magnitude spectra in Fig. 3-19 are in agreement with other Mn *K*-edge EXAFS studies of $LiMnPO_4$ [37], which display both decrease in intensity and splitting of the first Mn-O shell into two peaks upon the oxidation of Mn^{2+} to Jahn-Teller active Mn^{3+} by delithiation. In olivine-structured $LiMn_{0.8}Fe_{0.2}PO_4$, the Mn^{2+} ions in MnO_6 are slightly shifted toward opposite side of edge-shared PO_4 due to the electrostatic repulsion between Mn^{2+} and P^{5+} ions, and therefore, the preferential elongation of PO_4 edge-sharing Mn-O bonds occurs rather than the typical *z*-axial elongation during delithiation [28,37]. These unusual distortions cause Mn^{3+} to become closer to the Li-diffusion pathway, which gives rise to the increase of the activation barrier for Li migration (Fig. 3-20) [28]. The observation about Jahn-Teller active Mn^{3+} provides the origin of the poor battery performance in $Li_xMn_{0.8}Fe_{0.2}PO_4$ as well as sluggish transition of Mn^{2+}/Mn^{3+}. As a result, our synchrotron-based x-ray absorption spectroscopy analyses help understand not only redox evolution of Fe and Mn in $LiMn_{0.8}Fe_{0.2}PO_4$ during battery operation but also the kinetics of redox change. We believe that the tailoring Jahn-Teller distortion in lithium manganese phosphate is a key to design advanced olivine cathode materials.

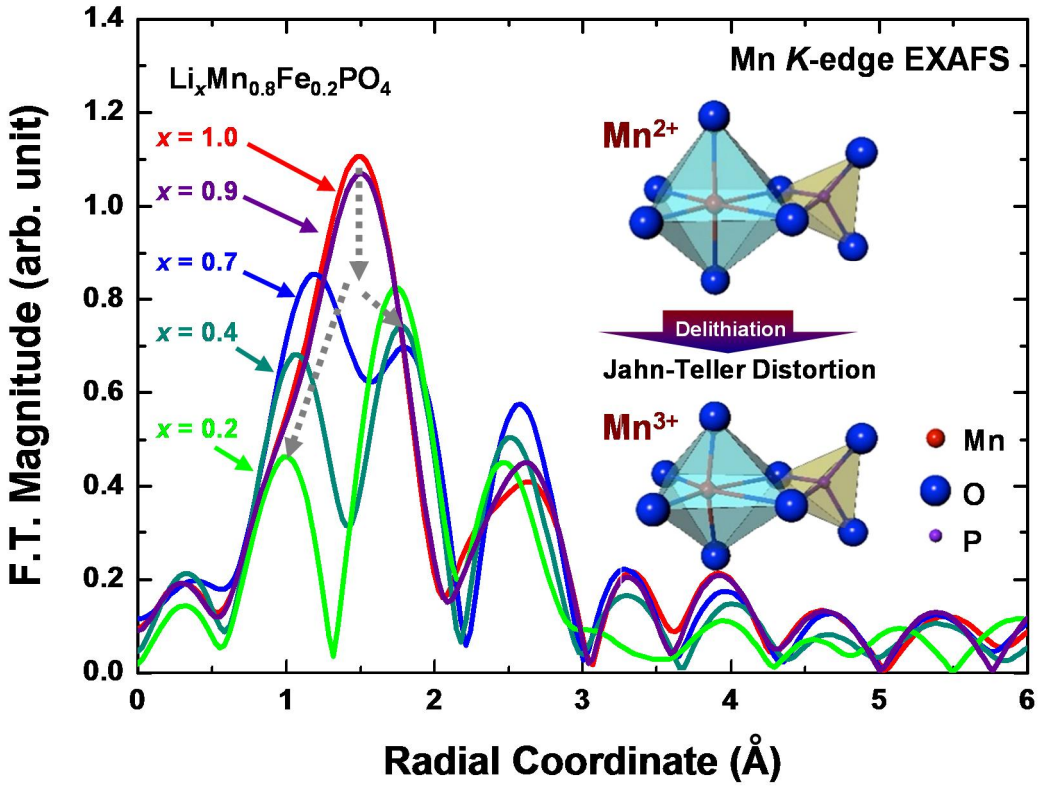

Fig. 3-19. (Color) *In situ* Fourier transformed Mn *K*-edge extended x-ray absorption fine structure (EXAFS) with different degrees of delithiation (*x* value), with a schematic representation of Jahn-Teller distortion.

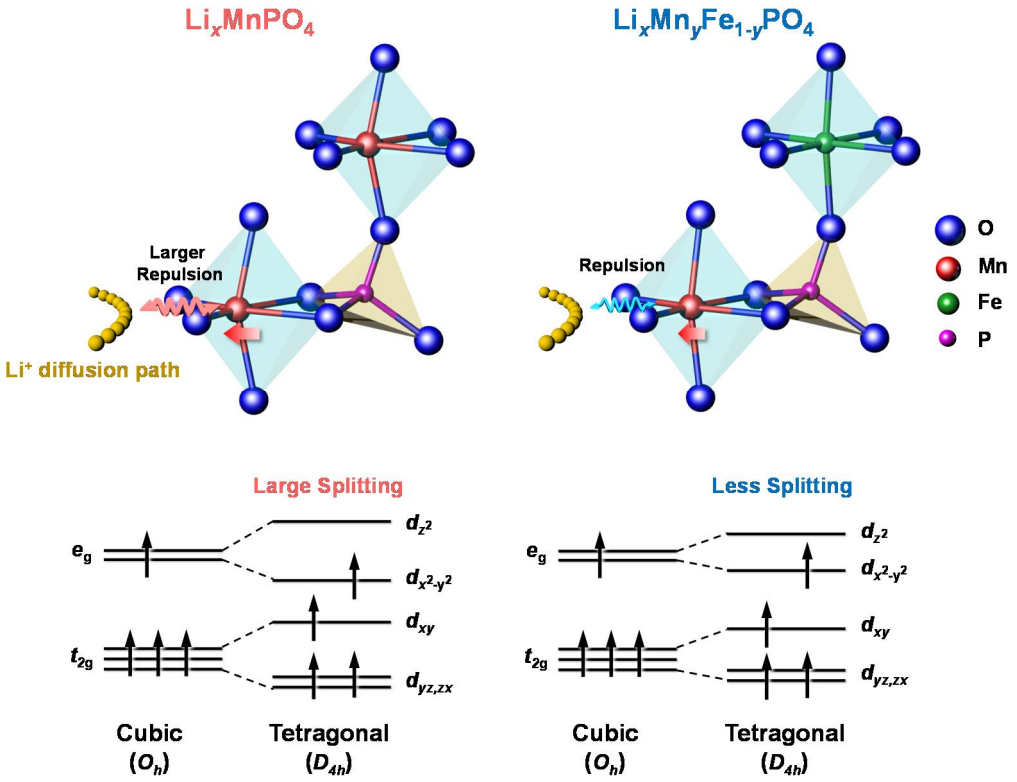

Fig. 3-20. (Color) Schematic illustration of the substitution effect on the electronic structures in $Li_xMn_yFe_{1-y}PO_4$, indicating that the replacement of Mn^{3+} by Fe^{3+} alleviates the Jahn-Teller distortion and energy splitting of the Mn 3*d*-orbitals [28]. Note that the energy diagram is not to scale.

3.4. Conclusions

In this work, we have designed the carbon-coated $LiMn_{0.8}Fe_{0.2}PO_4$ mesocrystal via a solvothermal method to improve the electronic conductivity and Li-ion mobility. This electrochemically favorable nanostructure which exhibited good electrochemical rate capability was used as a model compound for synchrotron-based x-ray absorption spectroscopy analyses to elucidate the changes of Mn and Fe redox centers and their effects on the electrochemical performance of the LMFP mesocrystal. Our combined analyses of *ex situ* sXAS and *in situ* XAS provided a clear understanding on the redox evolution of Mn and Fe in $LiMn_{0.8}Fe_{0.2}PO_4$ during battery operation. We believe that mitigation of concomitant Jahn-Teller behavior by Mn oxidation in $LiMn_{0.8}Fe_{0.2}PO_4$ is prerequisite to achieve the superior electrochemical properties. Further detailed studies about the kinetic bottleneck of $LiMn_{0.8}Fe_{0.2}PO_4$ are currently underway, including *in situ* x-ray diffraction, *in situ* electrochemical impedance spectra, as well as galvanostatic intermittent titration technique.

3.5 References

1. M. Winter and R. J. Brodd, What Are Batteries, Fuel Cells, and Supercapacitors?, *Chem. Rev.* 104 (2004) 4245.
2. M. S. Whittingham, Electrical Energy Storage and Intercalation Chemistry, *Science* 192 (1976) 1126.
3. K. Kang, Y. S. Meng, J. Breger, C. P. Grey, and G. Ceder, Electrodes with High Power and High Capacity for Rechargeable Lithium Batteries, *Science* 311 (2006) 977.
4. Y. Hwa, J. Zhao, and E. J. Cairns, Lithium Sulfide (Li_2S)/Graphene Oxide Nanospheres with Conformal Carbon Coating as a High-Rate, Long-Life Cathode for Li/S Cells. *Nano Lett.* 15 (2015) 34793.
5. L. Cheng, J. Yan, G. N. Zhu, J. Y. Luo, C. X. Wang, and Y. Y. Xia, General Synthesis of Carbon-Coated Nanostructure $Li_4Ti_5O_{12}$ as a High Rate Electrode Material for Li-Ion Intercalation. *J. Mater. Chem.* 20 (2010) 595.
6. A. K. Padhi, K. S. Nanjundaswamy, and J. B. Goodenough, Phospho-Olivines as Positive-Electrode Materials for Rechargeable Lithium Batteries, *J. Electrochem. Soc.* 144 (1997) 1188.
7. H. P. Subramanya, B. Ellis, N. Coombs, and L. F. Nazar, Nano-Network Electronic Conduction in Iron and Nickel Olivine Phosphates, *Nat. Mater.* 3 (2004) 147.
8. K. Amine, H. Yasuda, and M. Yamachi, Olivine $LiCoPO_4$ as 4.8 V Electrode Material for Lithium Batteries, *Electrochem. Solid-State Lett.* 3 (2000) 178.

9. Y. Wang, Y. Wang, E. Hosono, K. Wang, and H. Zhou, The Design of a $LiFePO_4$/Carbon Nanocomposite with a Core–Shell Structure and Its Synthesis by an *in situ* Polymerization Restriction Method, *Angew. Chem. Int. Ed.* 47 (2008) 7461.
10. S. Wi, S. Nam, Y. Oh, J. Kim, H. Choi, S. Hong, S. Byun, D. J. Choi, K. Ahn, Y. H. Kim, and B. Park, Facile Synthesis of Porous-Carbon/$LiFePO_4$ Nanocomposites, *J. Nanopart. Res.* 14 (2012) 1327.
11. K. F. Hsu, S. Y. Tsay, and B. J. Hwang, Synthesis and Characterization of Nano-Sized $LiFePO_4$ Cathode Materials Prepared by a Citric Acid-Based Sol–Gel Route, *J. Mater. Chem.* 14 (2004) 2690.
12. C. Delacourt, P. Poizot, M. Morcrette, J. M. Tarascon, and C. Masquelier, One-Step Low-Temperature Route for the Preparation of Electrochemically Active $LiMnPO_4$ Powders, *Chem. Mater.* 16 (2004) 93.
13. G. Li, H. Azuma, and M. Tohda, $LiMnPO_4$ as the Cathode for Lithium Batteries, *Electrochem. Solid-State Lett.* 5 (2002) A135.
14. Z. Qin, X. Zhou, Y. Xia, C. Tang, and Z. Liu, Morphology Controlled Synthesis and Modification of High-Performance $LiMnPO_4$ Cathode Materials for Li-Ion Batteries, *J. Mater. Chem.* 22 (2012) 21144.
15. S. M. Oh, S. W. Oh, C. S. Yoon, B. Scrosati, K. Amine, and Y. K. Sun, High-Performance Carbon-$LiMnPO_4$ Nanocomposite Cathode for Lithium Batteries, *Adv. Funct. Mater.* 20 (2010) 3260.
16. G. Chen, A. K. Shukla, X. Song, and T. J. Richardson, Improved Kinetics and Stabilities in Mg-Substituted $LiMnPO_4$, *J. Mater. Chem.* 21 (2011) 10126.

17. Y. Oh, S. Nam, S. Wi, S. Hong, and B. Park, Nanoscale Interface Control for High-Performance Li-Ion Batteries, *Electron. Mater. Lett.* 8 (2012) 91.
18. M. Pivko, M. Bele, E. Tchernychova, N. Z. Logar, R. Dominko, and M. Gaberscek, Synthesis of Nanometric $LiMnPO_4$ via a Two-Step Technique, *Chem. Mater.* 24 (2012) 1041.
19. J. S. Park, X. Meng, J. W. Elam, S. Hao, C. Wolverton, C. Kim, and J. Cabana, Ultrathin Lithium-Ion Conducting Coatings for Increased Interfacial Stability in High Voltage Lithium-Ion Batteries, *Chem. Mater.* 26 (2014) 3128.
20. H. H. Park, R. Heasley, L. Sun, V. Steinmann, R. Jaramillo, K. Hartman, R. Chakraborty, P. Sinsermsuksakul, D. Chua, T. Buonassisi, and R. G. Gordon, Co-Optimization of SnS Absorber and Zn(O,S) Buffer Materials for Improved Solar cells, *Prog. Photovolt.* 23 (2015) 901.
21. E. Lee, A. Murthy, and A. Manthiram, A. Carbon-Supported Pt Nanoparticles Prepared by a Modified Borohydride Reduction Method: Effect on the Particle Morphology and Catalytic Activity for CO_{ad} and Methanol Electro-Oxidation. *Electrochem. Commun.* 13 (2011) 480.
22. S. Wi, J. Kim, S. Lee, J. Kang, K. H. Kim, K. Park, K. Kim, S. Nam, C. Kim, and B. Park, Synthesis of $LiMn_{0.8}Fe_{0.2}PO_4$ Mesocrystals for High-Performance Li-Ion Cathode Materials. *Electrochim. Acta* 216 (2016) 203.
23. Y. K. Sun, S. M. Oh, H. K. Park, and B. Scrosati, Micrometer-Sized, Nanoporous, High-Volumetric-Capacity $LiMn_{0.85}Fe_{0.15}PO_4$ Cathode Material for Rechargeable Lithium-Ion Batteries, *Adv. Mater.* 23 (2011) 5050.

24. H. Wang, Y. Yang, Y. Liang, L. F. Cui, H. S. Casalongue, Y. Li, G. Hong, Y. Cui, and H. Dai, $LiMn_{1-x}Fe_xPO_4$ Nanorods Grown on Graphene Sheets for Ultrahigh-Rate-Performance Lithium Ion Batteries, *Angew. Chem. Int. Ed.* 123 (2011) 7502.
25. D. B. Ravnsbæk, K. Xiang, W. Xing, O. J. Borkiewicz, K. M. Wiaderek, P. Gionet, K. W. Chapman, P. J. Chupas, and Y. M. Chiang, Extended Solid Solutions and Coherent Transformations in Nanoscale Olivine Cathodes, *Nano Lett.* 14 (2014) 1484.
26. M. S. Kim, J. P. Jegal, K. C. Roh, and K. B. Kim, Synthesis of $LiMn_{0.75}Fe_{0.25}PO_4$/C Microspheres Using a Microwave-Assisted Process with a Complexing Agent for High-Rate Lithium Ion Batteries, *J. Mater. Chem. A* 2 (2014) 10607.
27. L. Laffont, C. Delacourt, P. Gibot, M. Yue Wu, P. Kooyman, C. Masquelier, and, J. Marie Tarascon, Study of the $LiFePO_4/FePO_4$ Two-Phase System by High-Resolution Electron Energy Loss Spectroscopy, *Chem. Mater.* 18 (2006) 5520.
28. D.-H. Seo, H. Gwon, S.-W. Kim, J. Kim, and K. Kang, Multicomponent Olivine Cathode for Lithium Rechargeable Batteries: A First-Principles Study, *Chem. Mater.* 22 (2010) 518.
29. A. Paolella, G. Bertoni, E. Dilena, S. Marras, A. Ansaldo, L. Manna, and C. George, Redox Centers Evolution in Phospho-Olivine Type ($LiFe_{0.5}Mn_{0.5}PO_4$) Nanoplatelets with Uniform Cation Distribution, *Nano Lett.* 14 (2014) 1477.
30. L. Castro, R. Dedryve`re, M. El Khalifi, P. E. Lippens, J. Bre´ger, C. Tessier, and D. Gonbeau, The Spin-Polarized Electronic Structure of $LiFePO_4$ and $FePO_4$ Evidenced by in-Lab XPS, *J. Phys. Chem. C* 114 (2010) 17995.

31. T. Nedoseykina, M. G. Kim, S. Park, H. S. Kim, S. B. Kim, J. Cho, and Y. Lee, In Situ X-ray Absorption Spectroscopic Study for the Electrochemical Delithiation of a Cathode $LiFe_{0.4}Mn_{0.6}PO_4$ material, *Electrochim. Acta* 55 (2010) 8876.
32. Y. C. Chen, J. M. Chen, C. H. Hsu, J. F. Lee, J. W. Yeh, and H. C. Shih, In-Situ Synchrotron X-ray Absorption Studies of $LiMn_{0.25}Fe_{0.75}PO_4$ as a Cathode Material for Lithium Ion Batteries, *Solid State Ionics* 180 (2009) 1215.
33. A. Yamada, Y. Kudo, and K. Y. Liu, Reaction Mechanism of the Olivine-Type $Li_x(Mn_{0.6}Fe_{0.4})PO_4$ ($0 < x < 1$), *J. Electrochem. Soc.* 148 (2001) A747.
34. G. Li, Y. Kudo, K. Y. Liu, H. Azuma, and M. Tohda, X-ray Absorption Study of $Li_xMn_yFe_{1-y}PO_4$ ($0 < x < 1$, $0 < y < 1$), *J. Electrochem. Soc.* 149 (2002) A1414.
35. I. Bezza, M. Kaus, R. Heinzmann, M. Yavuz, M. Knapp, S. Mangold, S. Doyle, C. P. Grey, H. Ehrenberg, S. Indris, and I. Saadoune, Mechanism of the Delithiation/Lithiation Process in $LiFe_{0.4}Mn_{0.6}PO_4$: In Situ and Ex Situ Investigations on Long-Range and Local Structures, *J. Phys. Chem. C* 119 (2015) 9016.
36. H. M. Hollmark, T. Gustafsson, K. Edstrom and L. C. Duda, Resonant Inelastic X-ray Scattering and X-ray Absorption Spectroscopy on the Cathode Materials $LiMnPO_4$ and $LiMn_{0.9}Fe_{0.1}PO_4$–a Comparative Study, *Phys. Chem. Chem. Phys.* 13 (2011) 20215.
37. L. F. J. Piper, N. F. Quackenbush, S. Sallis, D. O. Scanlon, G. W. Watson, K. W. Nam, X. Q. Yang, K. E. Smith, F. Omenya, N. A. Chernova, and M. S. Whittingham, Elucidating the Nature of Pseudo Jahn-Teller Distortions in Li_xMnPO_4: Combining Density Functional Theory with Soft and Hard X-ray Spectroscopy, *J. Phys. Chem. C* 117 (2013) 10383.

38. X. Liu, J. Liu, R. Qiao, Y. Yu, H. Li, L. Suo, Y. S. Hu, Y. D. Chuang, G. Shu, F. Chou, T. C. Weng, D. Nordlund, D. Sokaras, Y. J. Wang, H. Lin, B. Barbiellini, A. Bansil, X. Song, Z. Liu, S. Yan, G. Liu, S. Qiao, T. J. Richardson, D. Prendergast, Z. Hussain, F. M. F. de Groot, and W. Yang, Phase Transformation and Lithiation Effect on Electronic Structure of Li_xFePO_4: An In-Depth Study by Soft X-ray and Simulations, *J. Am. Chem. Soc.* 134 (2012) 13708.

39. W. Yang and R. Qiao, Soft X-Ray Spectroscopy for Probing Electronic and Chemical States of Battery Materials, *Chin. Phys. B* 25 (2016) 017104.

40. W. Yang, X. Liu, R. Qiao, P. O. Velasco, J. D. Spear, L. Roseguo, J. X. Pepper, Y. Chuang, J. D. Denlinger, and Z. Hussain, Key Electronic States in Lithium Battery Materials Probed by Soft X-ray Spectroscopy, *J. Electron. Spectrosc. Relat. Phenom.* 190 (2013) 64.

41. X. Liu, W. Yang, and Z. Liu, Recent Progress on Synchrotron-Based In-Situ Soft X-ray Spectroscopy for Energy Materials, *Adv. Mater.* 26 (2014) 7710.

42. X. Liu, D. Wang, G. Liu, V. Srinivasan, Z. Liu, Z. Hussain, and W. Yang, Distinct Charge Dynamics in Battery Electrodes Revealed by In Situ and Operando Soft X-ray Spectroscopy, *Nat. Commun.* 4 (2013) 2568.

43. S. Kurosumi, K. Horiba, N. Nagamura, S. Toyoda, H. Kumigashira, M. Oshima, S. Furutsuki, S. I. Nishimura, A. Yamada, and N. Mizuno, Resonant Photoemission Spectroscopy of the Cathode Material $Li_xMn_{0.5}Fe_{0.5}PO_4$ for Lithium-Ion Battery, *J. Power Sources* 226 (2013) 42.

44. M.-C. Jing, Y. M. Lee, H.-K. Lee, J. Park, S. R. Raga, L. K. Ono, S. Wang, M. R. Leyden, B. D. Yu, S. Hong, and Y. Qi, The Presence of CH_3NH_2 Neutral Species in Organometal Halide Perovskite Films, *Appl. Phys. Lett.* 108 (2016) 073901.

45. Y. G. Choi, K. H. Kim, K. S. Sohn, H. D. Park, and J. M. Lee, Mn *K*-Edge X-Ray Absorption Spectroscopic Study of Mn-Doped Zn_2SiO_4 Phosphors, *J. Mater. Sci. Lett.* 18 (1999) 621.

46. Y. Wang, P. He, and H. Zhou, Olivine $LiFePO_4$: Development and Future, *Energy Environ. Sci.* 4 (2011) 805.

47. C. Sun, S. Rajasekhara, J. B. Goodenough, and F. Zhou, Monodisperse Porous $LiFePO_4$ Microspheres for a High Power Li-Ion Battery Cathode, *J. Am. Chem. Soc.* 133 (2011) 2132.

48. S. Nam, S. J. Yang, S. Lee, J. Kim, J. Kang, J. Y. Oh, C. R. Park, T. Moon, K. T. Lee, and B. Park, Wrapping SnO_2 with Porosity-Tuned Graphene as a Strategy for High-Rate Performance in Lithium Battery Anodes, *Carbon* 85 (2015) 289.

49. S. Wi, J. Kim, K. Park, S. Lee, J. Kang, K. H. Kim, S. Nam, C. Kim, and B. Park, Evolution of Graphene-Wrapped $LiFePO_4$ as Novel Cathode Materials for Li-Ion Batteries. *RSC Adv.* 6 (2016) 105081.

50. F. M. F. de Groot, J. C. Fuggle, B. T. Thole, and G. A. Sawatzky, 2*p* X-Ray Absorption of 3*d* Transition-Metal Compounds: An Atomic Multiplet Description Including the Crystal Field, *Phys. Rev. B* 45 (1990) 5459.

51. Y. S. Yu, C. Kim, D. A. Shapiro, M. Farmand, D. Qian, T. Tyliszczak, A. L. D. Kilcoyne, R. Celestre, S. Marchesini, J. Joseph, P. Denes, T. Warwick, F. C. Strobridge, C. P. Grey, H. Padmore, Y. S. Meng, R. Kostecki, J. Cabana, Dependence on Crystal Size of the Nanoscale Chemical Phase Distribution and Fracture in Li_xFePO_4, *Nano Lett.* 15 (2015) 4282.

52. Z. Zhuo, J. Hu, Y. Duan, W. Yang, and F. Pan, Transition Metal Redox and Mn Disproportional Reaction in $LiMn_{0.5}Fe_{0.5}PO_4$ Electrodes Cycled with Aqueous Electrolyte, *Appl. Phys. Lett.* 109 (2016) 023901.

53. W. Yang and R. Qiao, Soft X-Ray Spectroscopy for Probing Electronic and Chemical States of Battery Materials, *Chin. Phys. B* 25 (2016) 017104.

54. W. S. Yoon, M. Balasubramanian, K. Y. Chung, X. Q. Yang, J. McBreen, C. P. Grey, and D. A. Fischer, Investigation of the Charge Compensation Mechanism on the Electrochemically Li-Ion Deintercalated $Li_{1-x}Co_{1/3}Ni_{1/3}Mn_{1/3}O_2$ Electrode System by Combination of Soft and Hard X-ray Absorption Spectroscopy, *J. Am. Chem. Soc.* 127 (2005) 17479.

55. H. J. Noh, S. Yeo, J. S. Kang, C. L. Zhang, S. W. Cheong, S. J. Oh, and P. D. Johnson, Jahn-Teller Effect in Spinel Manganites Probed by Soft X-Ray Absorption Spectroscopty, *Appl. Phys. Lett.* 88 (2006) 081911.

56. H. B. Li, W. H. Wang, X. Qian, Y. Cheng, X. Xie, J. Liu, S. Sung, J. Zhou, Y. Hu, J. Xu, L. Li, Y. Zhang, X. Du, K. Gao, Z. Li, C. Zhang, S. Wang, H. Chen, Y. Zhao, F. Lu, W. Wang, and H. Liu, Identifying the Descriptor Governing NO Oxidation on Mullite Sm (Y, Tb, Gd, Lu) Mn_2O_5 for Diesel Exhaust Cleaning, *Catal. Sci. Technol.* 6 (2016) 3971.

57. X. Liu, Y. J. Wang, B. Barbiellini, H. Hafiz, S. Basak, J. Liu, T. Richardson, G. Shu, F. Chou, T. C. Weng, D. Nordlund, D. Sokaras, B. Moritz, T. P. Devereaux, R. Qiao, Y. Chuang, A. Bansil, Z. Hussain, and W. Yang, Why $LiFePO_4$ is a Safe Battery Electrode: Coulomb Repulsion Induced Electron-State Reshuffling upon Lithiation, *Phys. Chem. Chem. Phys.* 17 (2015) 26369.

58. C. F. Petersburg, Z. Li, N. A. Chernova, M. S Whittingham, and F. M. Alamgir, Oxygen and Transition Metal Involvement in the Charge Compensation Mechanism of $LiNi_{1/3}Mn_{1/3}Co_{1/3}O_2$ Cathodes, *J. Mater. Chem.* 22 (2012) 19993.

59. H. M. Hollmark, L.-C. Duda, M. Dahbi, I. Saadoune, T. Gustafsson,c, and K. Edström, Resonant Soft X-Ray Emission Spectroscopy and X-Ray Absorption Spectroscopy on the Cathode Material $LiNi_{0.65}Co_{0.25}Mn_{0.1}O_2$, *J. Electrochem. Soc.* 158 (2010) A962.

60. H. Gwon, D. H. Seo, S. W. Kim, J. Kim, and K. Kang, Combined First-Principle Calculations and Experimental Study on Multi-Component Olivine Cathode for Lithium Rechargeable Batteries, *Adv. Funct. Mater.* 19 (2009) 3285.

61. R. Malik, D. Burch, M. Bazant, and G. Ceder, Particle Size Dependence of the Ionic Diffusivity, *Nano Lett.* 10 (2010) 4123.

62. K.-Y. Park, I. Park, H. Kim, G. Yoon, H. Gwon, Y. Cho, Y. S. Yun, J.-J. Kim, S. Lee, D. Ahn, Y. Kim, H. Kim, I. Hwang, W.-S. Yoon, and K. Kang, Lithium-Excess Olivine Electrode for Lithium Rechargeable Batteries, *Energy Environ. Sci.* 9 (2016) 2902.

63. C. Delacourt, L. Laffont, R. Bouchet, C. Wurm, J. B. Leriche, M. Morcrette, J. M. Tarascon, and C. Masquelier, Toward Understanding of Electrical Limitations (Electronic, Ionic) in $LiMPO_4$ (M = Fe, Mn) Electrode Materials, *J. Electrochem. Soc.* 152 (2005) A913.

64. B. Ravel and M. Newville, ATHENA, ARTEMIS, HEPHAESTUS: Data Analysis for X-Ray Absorption Spectroscopy Using IFEFFIT, *J. Synchrotron Radiat.* 12 (2005) 537.

65. H. Kim, G. Yoon, I. Park, K. Y. Park, B. Lee, J. Kim, Y. U. Park, S. K. Jung, H. D. Lim, D. Ahn, S. Lee, and K. Kang, Anomalous Jahn-Teller Behavior in a Manganese-Based Mixed-Phosphate Cathode for Sodium Ion Batteries, *Energy Environ. Sci.* 8 (2015) 3325.

Chapter 4.

Insights on the Delithiation/Lithiation Reactions of $Li_xMn_{0.8}Fe_{0.2}PO_4$ Mesocrystal in Li-Ion Batteries by *In Situ* Techniques

4.1. Introduction

Concern over the safety issue of commercial layered cathode materials is the main cause hindering utilization of the maximum capacity that materials can reveal [1-3]. Since the pioneering work by A. K. Padhi *et al.*, olivine structured lithium iron phosphate ($LiFePO_4$) has been studied intensively as a promising candidate for cathode materials of lithium-ion batteries due to its high theoretical capacity, good safety characteristic, high thermal and chemical stability, environmental benignity, and low cost [4-7]. However, the $LiFePO_4$ has relatively low redox potential (~3.4 V vs. Li^+/Li) compared with that of other commercialized cathode materials ($LiCoO_2$ (~4.0 V) and $LiMn_2O_4$ (~4.0 V)), which results in the low energy density that limits its wider applications in the market [8-10].

Among the members of olivine compounds, $LiMnPO_4$ is very attractive due to its high potential of ~4.1 V compared to ~3.4 V of $LiFePO_4$ [10,11]. However, the sluggish kinetics of $LiMnPO_4$ complicated its use as high-performance cathode materials [10-13]. Several issues related to the reaction kinetics such as the intrinsically poor ionic/electronic conductivity, the phase boundary mobility affected by the anisotropically large lattice mismatch between the lithiated and delithiated

phases, small polaronic conductivity of Jahn-Teller active Mn^{3+}, etc. are known as the possible origins of the sluggish kinetics [11-14]. Therefore, surface modification with electronically conductive layers and/or morphological control in the nanoscale regime for shortening Li^+-diffusion path have been attempted in earlier studies [11-15]. In addition, another effective strategy is the use of solid solution phases of olivine structures, such as in the case of $LiMn_{1-y}Fe_yPO_4$ solid solution [16-20]. Recently, several research groups have reported that Fe substitution could increase the solubility limit of $Li_xMn_{1-y}Fe_yPO_4$, narrowing miscibility gap between charged and discharged phases [20-23]. Since the delithiation/lithiation reactions in the first-order transition region are known to have the sluggish kinetics due to the nucleation and growth of a new phase followed by movement of the phase boundary when compared with those in the solid-solution reaction region, the wider immiscibility gap leads to improved electrochemical properties [20,23]. Recently, J. Kim *et al*. reported that a small amount doping of other transition metals in $LiMnPO_4$ matrix can significantly improve the battery performance, in which the dopant can act as a nucleation enhancer during both delithiation and lithiation process [24,25].

In our previous work, the redox evolution of Mn and Fe in $Li_xMn_{0.8}Fe_{0.2}PO_4$ during battery operation was investigated by combined analyses of *ex situ* soft x-ray absorption spectroscopy (sXAS) and *in situ* x-ray absorption spectroscopy (XAS) [26]. We suggested Jahn-Teller active Mn^{3+} led to the poor battery performance in $Li_xMn_{0.8}Fe_{0.2}PO_4$ as well as sluggish transition of Mn^{2+}/Mn^{3+} [26]. However, a clear understanding about the origin of the sluggish kinetics in $Li_xMn_{0.8}Fe_{0.2}PO_4$ has not been understood yet. In this work, we systematically investigate the delithiation/lithiation reactions of $Li_xMn_{0.8}Fe_{0.2}PO_4$ by *operando* x-ray diffraction and *in situ* electrochemical

impedance spectra with galvanostatic intermittent titration technique (GITT) to understand the charge/discharge mechanism and the origin of the sluggish kinetics of Mn-based olivine cathode materials. The study of mixed-composition olivine phosphates can provide better understanding of the electrochemical behavior of transition metal couples within the olivine structure, which shall be beneficial for efforts to further improvement of the Mn-based olivine cathode materials.

4.2. Experimental Section

Materials Preparation: The micron-sized porous $LiMn_{0.8}Fe_{0.2}PO_4$ (LMFP) mesocrystal was synthesized by a solvothermal method, as reported in our previous study [26]. A mixture (10 ml) of manganese acetate tetrahydrate ($Mn(CH_3COO)_2{\cdot}4H_2O$: 0.008 mol) and iron nitrate nonahydrate ($Fe(NO_3)_3{\cdot}9H_2O$: 0.002 mol) aqueous solution was injected into *n*,*n*-dimethylformamide (DMF) (C_3H_7NO: 140 ml) at 80°C, and the mixture was stirred for 1 h. Then, lithium hydroxide monohydrate ($LiOH{\cdot}H_2O$: 0.036 mol), phosphoric acid (H_3PO_4: 0.012 mol), ascorbic acid ($C_6H_8O_6$: 0.006 mol), and nitric acid (HNO_3: 0.04 mol) were added under the magnetic stirring at RT for 6 h. The mixed solution was transferred to a Teflon-lined autoclave and heated at 180°C for 12 h. Then, the resulting solution was centrifuged, and the precipitates were thoroughly washed with a deionized water followed by drying at 60°C overnight. Finally, the carbon-coated LMFP mesocrystal (LMFP/C) was synthesized by impregnating the as-synthesized LMFP powders in sucrose solution (sucrose:LMFP = 3:7 by weight) followed by drying and calcining them at 700°C for 3 h under H_2/Ar (4 vol. % H_2) atmosphere.

Materials Characteriazation: The crystal structure and grain size of the LMFP mesocrystal were characterized by x-ray diffraction (XRD, D8 Advance: Bruker). The morphology of the mesocrystal was analyzed using field-emission scanning electron microscopy (FE-SEM, Merlin Compact: Zeiss) and high-resolution transmission electron microscopy (HRTEM, JEM-3000F: JEOL, Japan) equipped with energy dispersive x-ray spectroscopy (EDS). An inductively coupled plasma-atomic emission spectrometer (ICP-AES, Optima-4300 DV: Perkin-Elmer) was used to

identify the ratio of Mn and Fe in the LMFP mesocrystal. Carbon concentration was measured by a CHNS analyzer (Flash EA 1112: Thermo Electron Corp.). *Operando* XRD experiments (Smartlab: Rigaku Corp.) are performed with a specially designed *in situ* cell that enables transmitted XRD acquisition through the polymer film window on the 2032 type coin cell (Fig. 4-1). The successive XRD data from 11° to 45° were acquired at 0.6°/min on C/20 rate (1 C = 171 mA/g).

Electrochemical Measurements: For the electrochemical characterization, the active materials were tested using coin-type half cells (2016 type) with a Li counter electrode. The composition of the electrode was set to be the same for all of the samples, which consisted of an active material (the LMFP mesocrystal), super P carbon black, and a polyvinylidene fluoride (PVDF) binder with a weight ratio of 7:2:1. Loading level of active materials was ~1 mg/cm^2. The electrolyte contained 1 M $LiPF_6$ in ethylene carbonate and diethyl carbonate (1/1 vol. %) (Panax Etec). Galvanostatic intermittent titration technique (GITT) measurement was performed by using a constant current of C/100. The electrochemical cells were charged and discharged for 30 min at C/100 rate with 30 min rest time in galvanostatic mode. *In situ* electrochemical impedance spectra (EIS) were measured from 10 mHz to 100 kHz with an AC amplitude of 5 mV at the end of each relaxation step of the GITT charge and discharge.

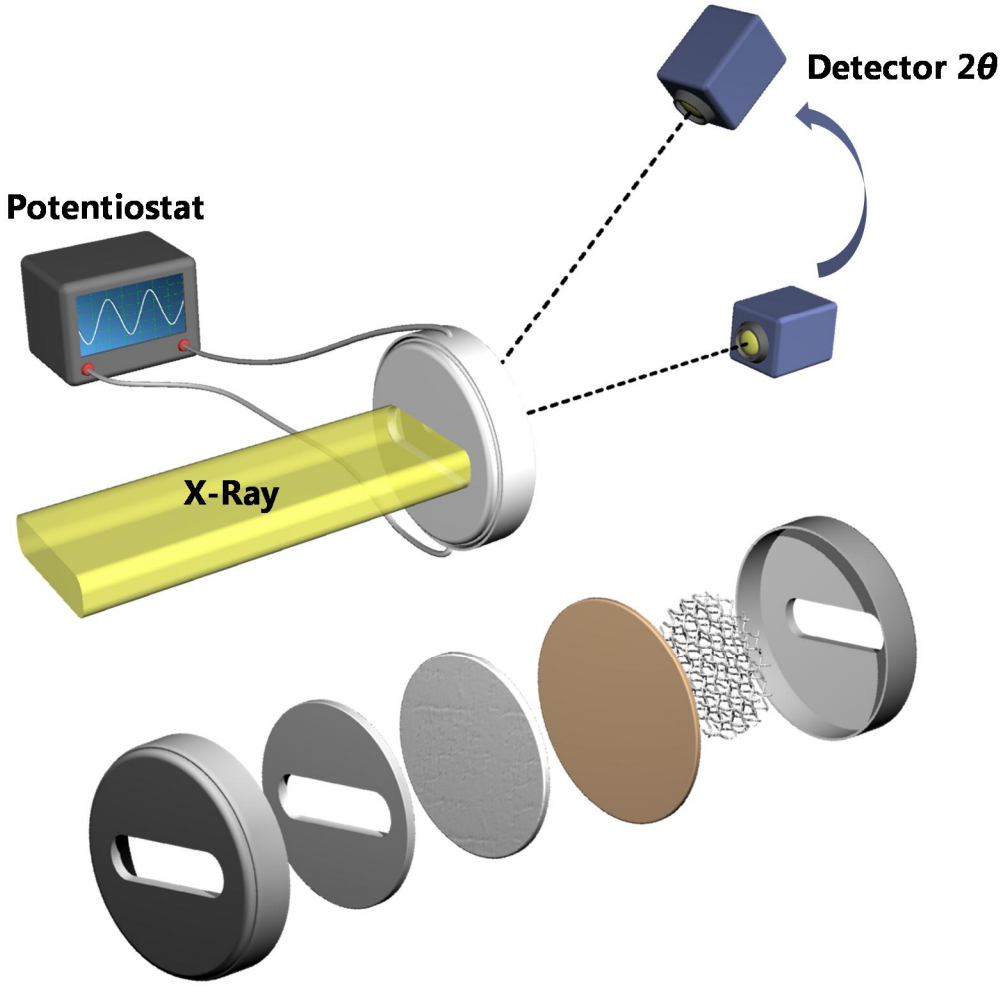

Fig. 4-1. (Color) The *in situ* cell configuration with interlocked potentiostat that enables acquisition of transmitted XRD data with simultaneously charge/discharge reaction.

4.3. Results and Discussion

The carbon-coated LMFP mesocrystal was synthesized based on our previous reports as a model compound that can reveals good electrochemical properties [16,26]. The $LiMn_{0.8}Fe_{0.2}PO_4$ mesocrystal clearly exhibits a porous plate-shaped morphology that consists of ~40-nm-sized nanoparticles, which enables facile transport of both electrons and Li^+ during electrochemical reaction (Fig. 4-2(a)). Transmission electron microscopy (TEM) image is presented in Fig. 4-2(b), in which ~40-nm-sized primary particles are highly oriented in the mesocrystal [26]. The EDS elemental mapping for LMFP mesocrystal was conducted, confirming that the synthesized mesocrystal is featured by homogeneous distribution of constituent elements (Mn, Fe, P, and O) (Fig. 4-2(c)). Inductively coupled plasma-atomic emission spectroscopy (ICP-AES) showed that the Mn/Fe atomic ratio to be ~4. The crystal structure of pristine LMFP mesocrystal matches the orthorhombic olivine structure. A complete solid-solution phase with individual single-transition metal phosphate of $LiMnPO_4$ (JCPDS #97-009-7763) and $LiFePO_4$ (JCPDS #40-1499) (Fig. 4-3) could be identified by XRD. Small ionic radius of Fe^{2+} compared with Mn^{2+} lead LMFP peaks shifted to higher scattering angles compared with that of $LiMnPO_4$ [16,26,27]. CHNS analysis on the carbon-coated LMFP mesocrystal shows that the carbon content of ~5.2 wt. %.

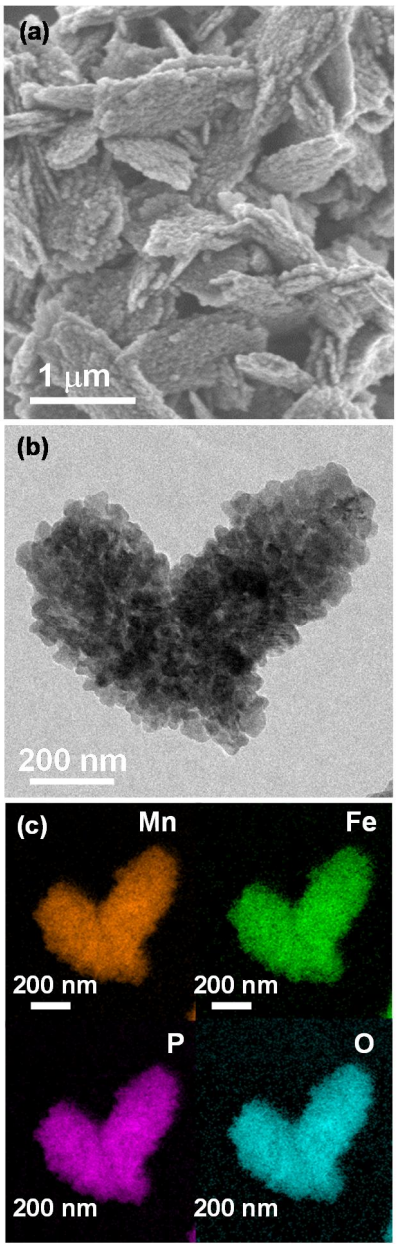

Fig. 4-2. (Color) (a) SEM and (b) TEM images of the $LiMn_{0.8}Fe_{0.2}PO_4$ mesocrystal. (c) EDS mapping of Mn, Fe, P, and O, respectively.

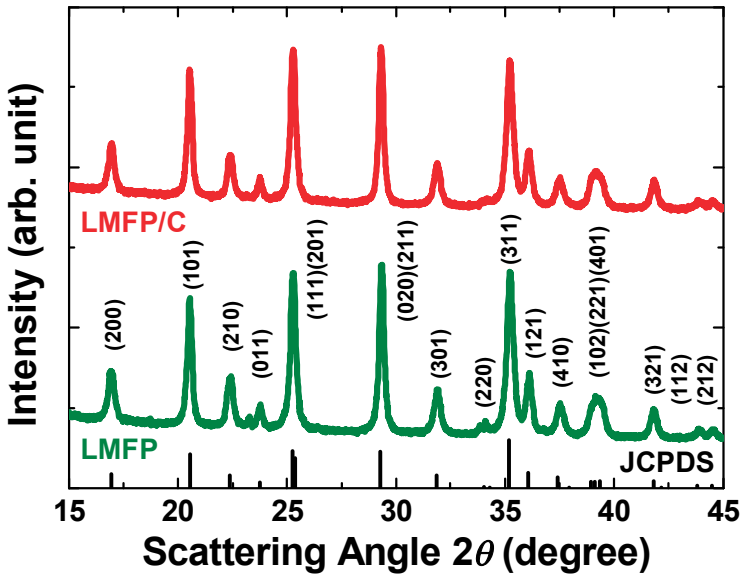

Fig. 4-3. (Color) XRD patterns for the bare and carbon-coated $LiMn_{0.8}Fe_{0.2}PO_4$ mesocrystal.

Cyclic voltammetry (CV) and galvanostatic charge-discharge cyclings are performed to investigate the electrochemical performance of the LMFP mesocrystal with conformal carbon coating (Figs. 4-4 and 4-5). In Fig. 4-4, the CV profiles of the carbon-coated LMFP mesocrystal at different potential scan rates (0.01, 0.05, 0.1, 0.15, and 0.2 mV/s) with the voltage window between 2.5 and 4.7 V are presented. Two cathodic peaks at ~3.99 V and ~3.55 V can be observed at 0.01 mV/s rate while two anodic peaks at ~4.15 V and ~3.59 V at the same sweep rate. The peaks at lower and higher voltage region result from the redox reactions of Fe^{2+}/Fe^{3+} and Mn^{2+}/Mn^{3+}, respectively, indicating that both Fe and Mn participate in the electrochemical reaction during the (de)intercalation of Li^{+}. The shape of the CV was highly reversible even when the scan rate was increased up to 0.2 mV/s, indicative of the high rate capability of the carbon-coated LMFP mesocrystal. The carbon-coated LMFP mesocrystal was cycled at various current densities (0.05 C to 10 C) as shown in Fig. 4-5. The capacity of ~133 mAh/g was achieved at 0.05 C (~78% of the theoretical capacity (= 171 mAh/g)), which is comparable with the previously reported carbon-coated $LiMn_{0.8}Fe_{0.2}PO_4$ nanoparticles. The discharge capacity was ~70 mAh/g at a rate of 10 C (~53% vs. that at 0.05 C), indicating the high rate capability of the carbon-coated LMFP mesocrystal. The high rate performance of the carbon-coated LMFP mesocrystal is attributed to both the porous mesocrystal structure composed of ~40-nm-sized nanocrystallites and the conformal carbon coating on the surface of individual nanoparticles.

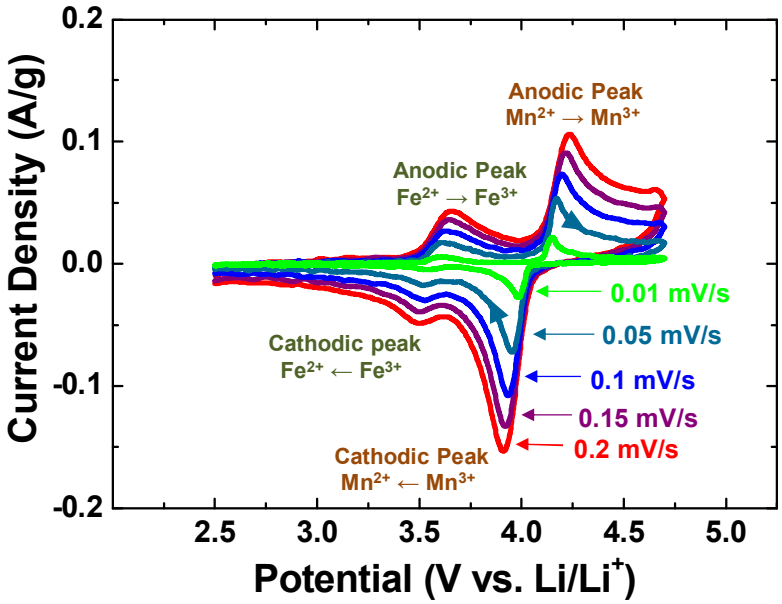

Fig. 4-4. (Color) Cyclic voltammetry profiles of the carbon-coated $LiMn_{0.8}Fe_{0.2}PO_4$ mesocrystal at various scan rates.

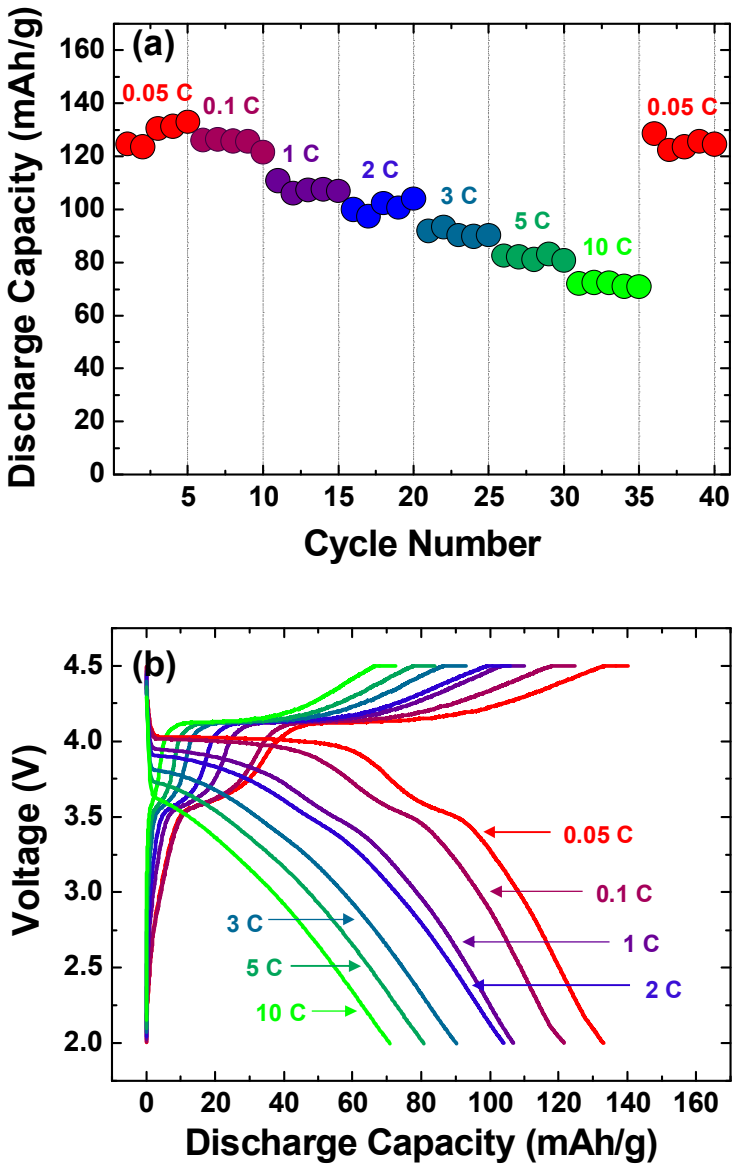

Fig. 4-5. (Color) (a) Rate capability up to the rate of 10 C (1 C = 171 mA/g), and (b) charge-discharge curves of the carbon-coated $LiMn_{0.8}Fe_{0.2}PO_4$ mesocrystal at various delithiation/lithiation rates.

Despite the superior rate capability, only ~78% of the theoretical capacity could be obtained from the LMFP mesocrystal. Although Jahn-Teller active Mn^{3+} and sluggish transition of Mn^{2+}/Mn^{3+} were reported to lead to the poor battery performance of LMFP [26], there exist unveiled factors that affect the kinetics of electrochemical reaction in $Li_xMn_{0.8}Fe_{0.2}PO_4$, such as slow polaronic conduction, slow Li^+ diffusion, or low mobility of phase boundary [24-28]. A deeper understanding of delithation/lithiation mechanism of $Li_xMn_{0.8}Fe_{0.2}PO_4$ would render the $LiMn_{0.8}Fe_{0.2}PO_4$ more electrochemically efficient.

First of all, the phase transformation mechanism of $Li_xMn_{0.8}Fe_{0.2}PO_4$ during delithation/lithiation was investigated for the deeper understanding about the origin of the sluggish kinetics in carbon-coated LMFP mesocrystal. The voltage curves show a pseudo-flat potential profile in Mn^{2+}/Mn^{3+} region (~4.1 V), which means a typical two-phase reaction (Fig. 4-5) occurs during redox reaction of Mn. The relatively inclined region can be observed in the Fe^{2+}/Fe^{3+} reaction region (~3.5 V) as a solid solution reaction proceeds. This result is consistent with earlier studies about $Li_xMn_{0.8}Fe_{0.2}PO_4$ [21,29]. Direct information about the phase transformation of $Li_xMn_{0.8}Fe_{0.2}PO_4$ mesocrystal during (de)lithaiation can be identified by the *operando* XRD measurements. The voltage profile of the $LiMn_{0.8}Fe_{0.2}PO_4$ during the *operando* XRD measurement is presented in Fig. 4-6(a) and corresponding *in situ* XRD patterns of $Li_xMn_{0.8}Fe_{0.2}PO_4$ are shown in Figs. 4-6(b) and 4-7. Starting from $LiMn_{0.8}Fe_{0.2}PO_4$ (β phase), continuous peak shift in the XRD pattern of delithiated $Li_xMn_{0.8}Fe_{0.2}PO_4$ ($1 \geq x \geq \sim 0.8$) is observed which is a clear indication of the solid solution behavior within the Fe^{2+}/Fe^{3+} redox region. The extraction of Li^+ induces continuous shrinkage of the *a* and *b* axes and elongation of the *c* axis during the oxidation reaction of Fe^{2+} in $Li_xMn_{0.8}Fe_{0.2}PO_4$ ($1 \geq x \geq \sim 0.8$) (Fig. 4-8). New peaks of $Mn_{0.8}Fe_{0.2}PO_4$ (α phase) appeared in the XRD patterns by further delithiation of $Li_xMn_{0.8}Fe_{0.2}PO_4$ ($\sim 0.8 \geq x \geq \sim 0.2$), which indicates that the two-phase reaction (first-order transition) occurs by the oxidation of Mn^{2+}. As a result, apparently, a solid solution phase transformation proceeds in the Fe^{2+}/Fe^{3+} reaction region (~3.5 V), followed by a typical two-phase reaction in the Mn^{2+}/Mn^{3+} reaction region (~4.1 V). The *operando* XRD patterns of subsequent discharge exhibit a reversible structural evolution from the α phase to the β phase. However, it should be noted that a small amount of α-phase remains at the

fully discharged state, which indicates that reduction of Mn^{3+} to Mn^{2+} is incomplete. This means the kinetics or the reaction pathway of Li^+ insertion reaction could be different with those of Li^+ extraction reaction in $Li_xMn_{0.8}Fe_{0.2}PO_4$, especially within the two phase reaction region (Mn^{2+}/Mn^{3+} reaction region of $\sim 0.8 \geq x \geq \sim 0.2$).

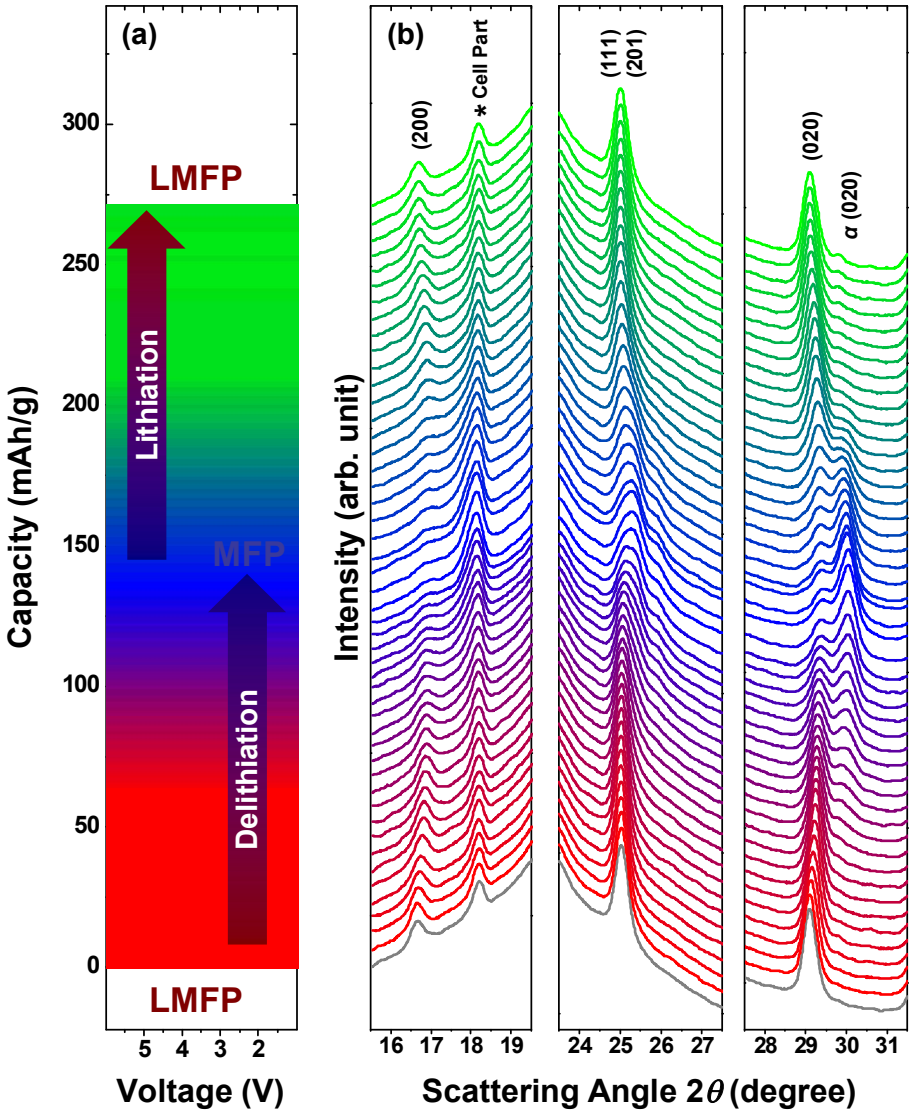

Fig. 4-6. (Color) (a) Galvanostatic charge/discharge profiles of $LiMn_{0.8}Fe_{0.2}PO_4$ mesocrystal at a rate of 0.05 C. (b) *Operando* XRD patterns of $LiMn_{0.8}Fe_{0.2}PO_4$ mesocrystal during delithiation/lithiation process. The peak marked by the asterisk is from the *in-situ* cell parts.

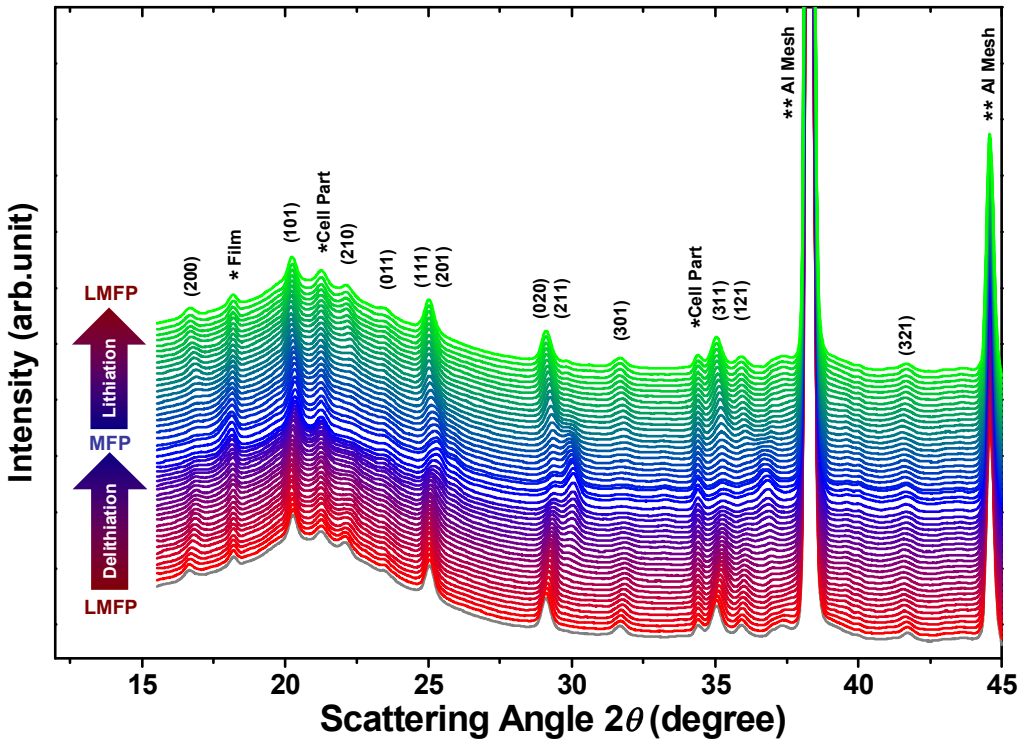

Fig. 4-7. (Color) The raw data of the *operando* XRD patterns from 16° to 45° during delithiation/lithiation process with corresponding phase information.

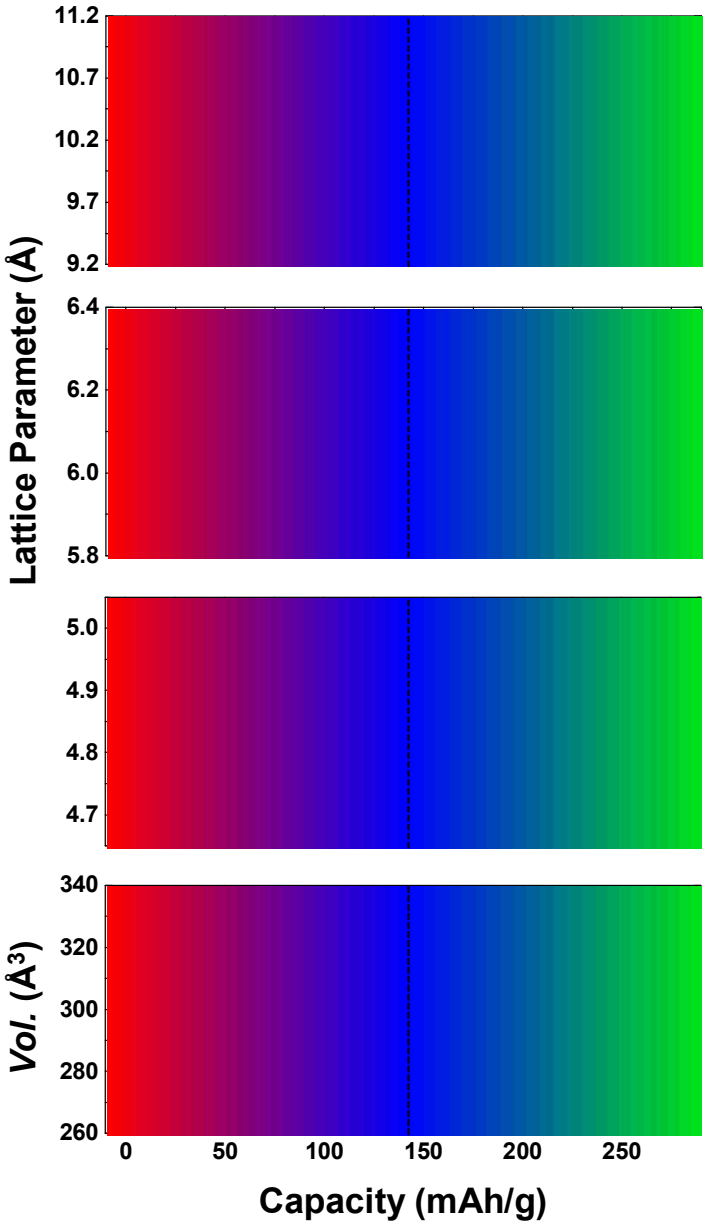

Fig. 4-8. (Color) (a) Lattice parameters and (d) cell volume changes upon delithiation/lithiation reactions.

Although our *operando* XRD results and the other previous studies about the phase transformation of $Li_xMn_yFe_{1-y}PO_4$ showed the apparent behavior, in which a solid solution phase transformation proceeds in the Fe^{2+}/Fe^{3+} reaction region ($1 \geq x \geq \sim y$), followed by a typical two-phase reaction in the Mn^{2+}/Mn^{3+} reaction region ($\sim y \geq x \geq 0$), the actual phase transformation mechanism appears to be more complicated [30,31]. It is well known that an intermediate phase ($Li_yMn_yFe_{1-y}PO_4$) between the β phase ($LiMn_yFe_{1-y}PO_4$) and α phase ($Mn_yFe_{1-y}PO_4$) (Fig. 4-9) exists, since the solid solution phase is stabilized at low temperature by substituting Mn on the Fe sublattice, and the phase diagram consists of two miscibility gaps at low temperature, the first between $LiMn_yFe_{1-y}PO_4$ (denoted β in Fig. 4-9) and $Li_yMn_yFe_{1-y}PO_4$ (denoted β' in Fig. 4-9) and the second between $Li_yMn_yFe_{1-y}PO_4$ (β') and $Mn_yFe_{1-y}PO_4$ (denoted α in Fig. 4-9) [22,32]. The peaks observed in the differential capacity, dQ/dV vs. V plot, can be attributed to the first-order phase transition of the $Li_xMn_{0.8}Fe_{0.2}PO_4$ during (de)lithiation (Fig. 4-10). The peaks observed at 3.55 and 4.11 V can be assigned to the coexistence of the $LiMn_yFe_{1-y}PO_4$ phase and $Li_yMn_yFe_{1-y}PO_4$ phase (β and β'), and the $Li_yMn_yFe_{1-y}PO_4$ phase and the $Mn_yFe_{1-y}PO_4$ phase (β' and α), respectively [22,32].

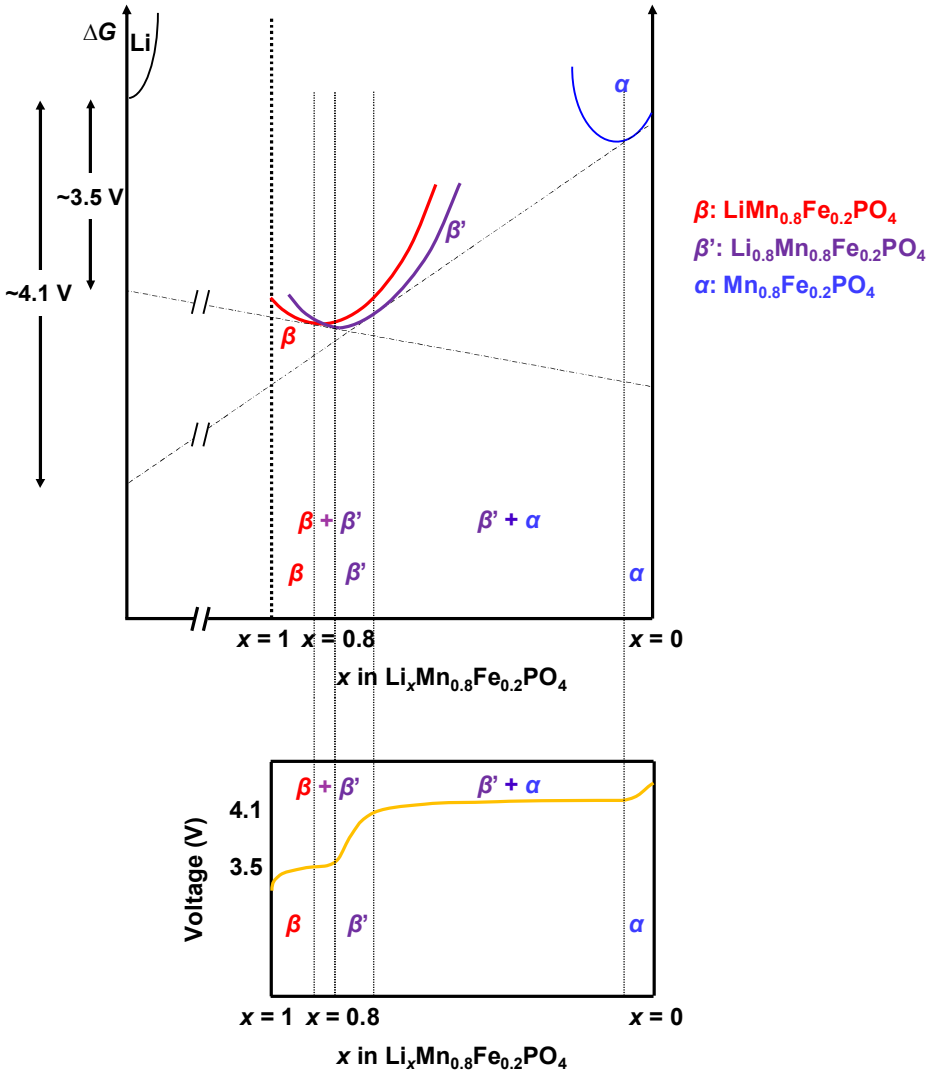

Fig. 4-9. (Color) The schematic illustration of the Gibbs free energy and voltage profile of $Li_xMn_{0.8}Fe_{0.2}PO_4$ mesocrystal upon (de)lithiation. Voltage curve is related to the intercept of tangent line drawn on the equilibrium ΔG curve of $Li_xMn_{0.8}Fe_{0.2}PO_4$ mesocrystal at the concentration coordinate corresponding to lithium.

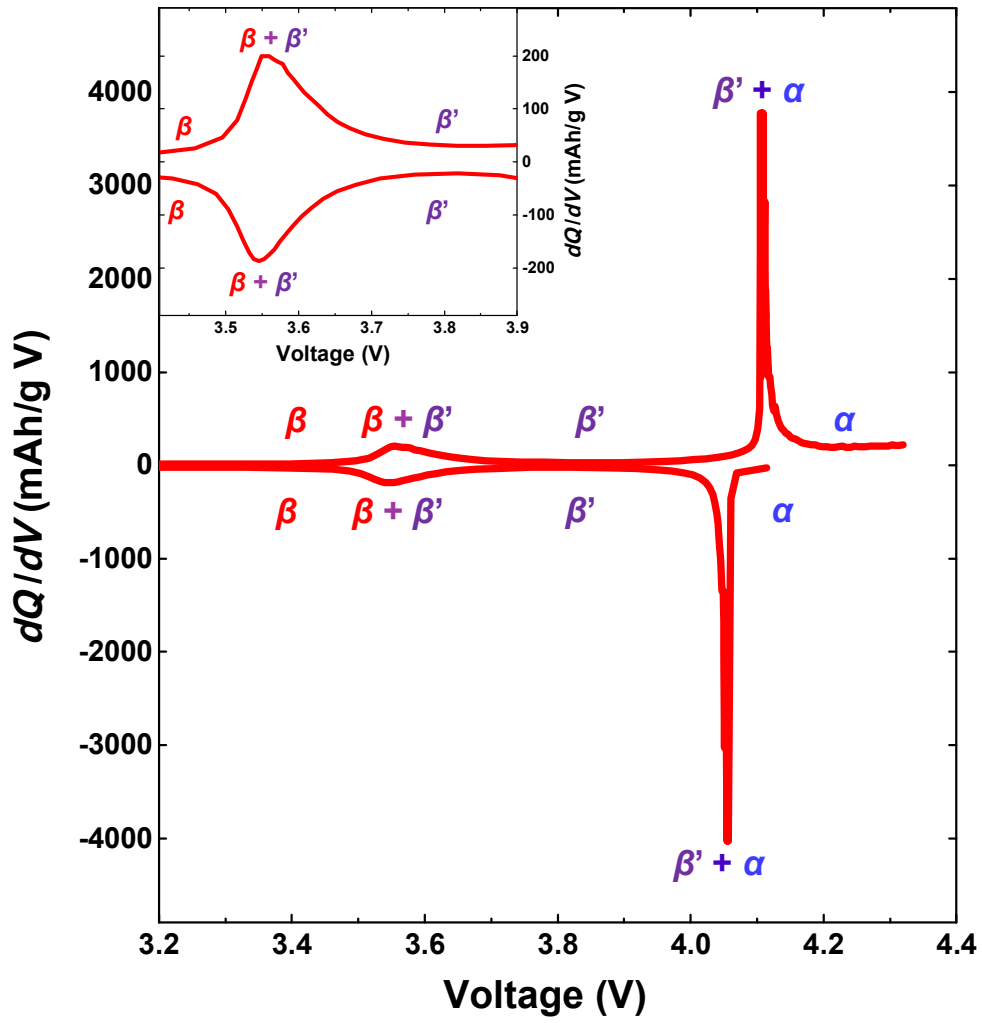

Fig. 4-10. (Color) Plot of the differential capacity (*dQ*/*dV*) vs. voltage for the open circuit voltage (OCV) curves from GITT curves in Fig. 3. The inset shows the magnified plot of the Fe^{2+}/Fe^{3+} redox reaction. Sharp peaks observed in the figure can be attributed to the characteristic first-order phase transition exhibited during cycling.

The *in situ* electrochemical impedance spectroscopy (EIS) with galvanostatic intermittent titration technique (GITT) was conducted to get insight of the electrochemical kinetics of $Li_xMn_{0.8}Fe_{0.2}PO_4$ (Fig. 4-11). GITT measurement was carried out to evaluate the overall trend of the overpotential, ohmic polarization, and apparent Li^+ diffusion coefficient at different states of charge/discharge [33-37]. The overpotential is the difference between the cutoff voltage and the open-circuit voltage after relaxation, i.e. the polarization of the electrode due to the slower Li-ion diffusivity than electron conductivity. Ohmic polarization is the voltage jump at the beginning of galvanostatic titration step, i.e. *iR* drop in the electrochemical circuit. The apparent chemical diffusion coefficient of Li^+ (D_{GITT}) was calculated according to Eq. (1), derived by Weppner and Huggins as follows [33]:

$$D_{GITT} = \frac{4}{\pi}\left(\frac{mV}{MS}\right)^2\left(\frac{\Delta E_S}{\tau(dE_\tau / d\sqrt{\tau}}\right)^2 \; ; \; \tau \ll L^2/D_{GITT} \qquad (1)$$

where V is the molar volume of the compound (cm^3/mol), τ is the duration of the current pulse (sec), and M and m are the molecular weight (g/mol) and the mass (g) of $LiMn_{0.8}Fe_{0.2}PO_4$, respectively. S is the interface area between the active material and electrolyte (cm^2), and L is the diffusion length (cm). ΔE_τ and ΔE_s are the transient voltage-change during the single titration current flux (after subtracting the *iR* drop) and the steady voltage-change after the relaxation period, respectively, as depicted in Fig. 4-11. The GITT curves, overpotential, ohmic polarization, and apparent Li^+ diffusion coefficient of LMFP mesocrystal during a cycle are shown in Fig. 4-12.

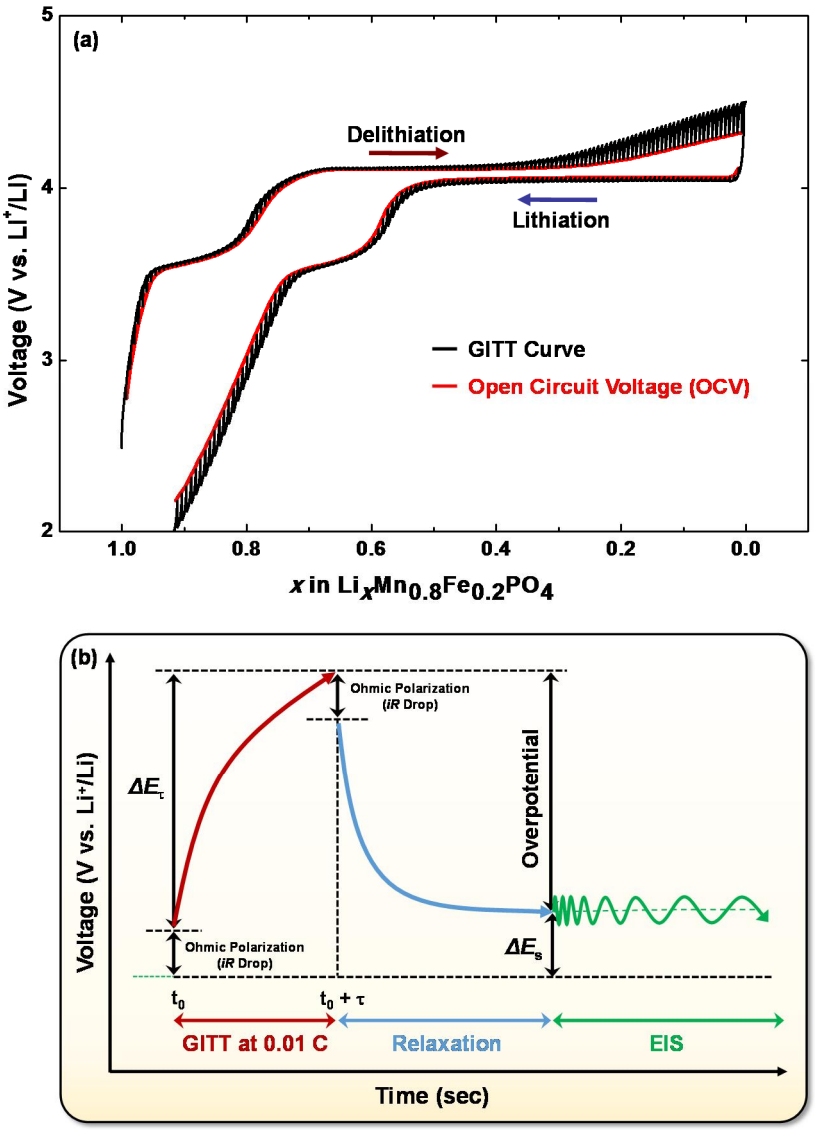

Fig. 4-11. (Color) (a) GITT curves of $LiMn_{0.8}Fe_{0.2}PO_4$ mesocrystal during delithiation/lithiation. (b) Schematic illustration of *E* vs. *t* profile for a single GITT titration during *in situ* EIS with GITT process.

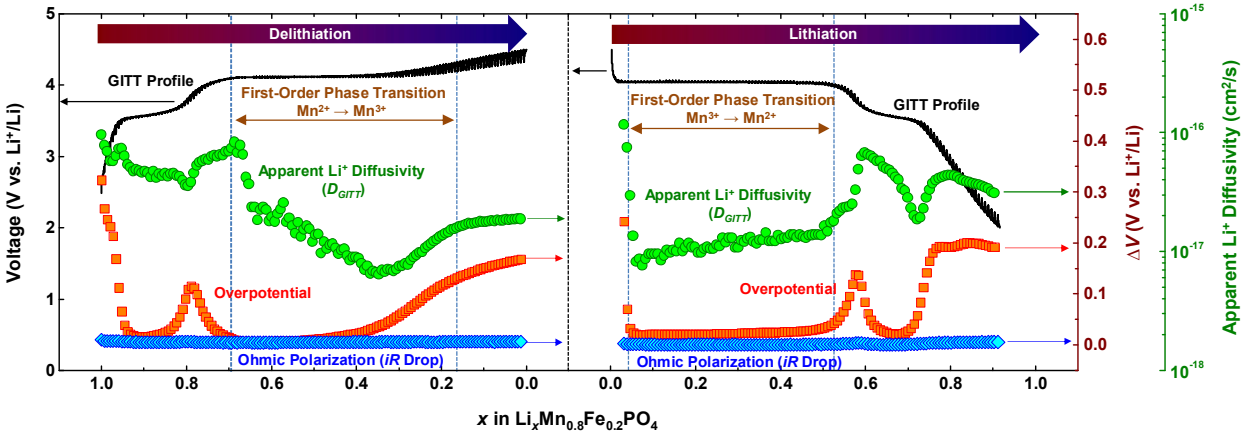

Fig. 4-12. (Color) GITT, overpotential, apparent Li^+ diffusivity (D_{GITT}), and ohmic polarization (*iR* drop) curves of carbon-coated $LiMn_{0.8}Fe_{0.2}PO_4$ mesocrystal during delithiation and lithiation process.

Because the ohmic polarization shows the negligible value compared to the overpotential, the overall trend of overpotential is highly dependent on the charge transfer and/or Li^+ diffusion process. The overpotential increases at the both beginning and end of (dis)charge process, but local maximum in the middle of the solid solution reaction regime of β'. The existence of local maximum in the overpotential is consistent with the previous results that were observed in $LiFe_{1/4}Mn_{1/4}Co_{1/4}Ni_{1/4}PO_4$, reported earlier by X. J. Wang *et al* [37]. Although the origin of this phenomenon is not understood yet [37-39], but it can be attributed to the change of Li^+ diffusivity [36-39]. In the solid solution reaction of β', Li^+ diffusivity that is affected by vacancy concentration, enthalpy of formation and migration, frequency, etc. reveals local minimum similarly to layered oxides with solid solution reaction, which results in the increase of overpotential [40,41]. Indeed, local maximum of overpotential is accompanied with local minimum of Li^+ diffusivity as discussed below. Afterward, the overpotential keeps increasing as the two-phase reaction proceeds, which result from increase in the portion of Mn^{3+}-rich phase that induces Jahn-Teller distortion of the structure [27,28]. The Jahn-Teller distortion causes Mn^{3+} to become closer to the Li^+-diffusion pathway, and it gives rise to the increase of the activation barrier for Li^+ migration [26-28]. The Jahn-Teller distortion in $Li_xMn_{0.8}Fe_{0.2}PO_4$ by delithiation was confirmed by *in situ* extended x-ray absorption fine structure (EXAFS) analysis in the previous study, and therefore, the sluggish transition of Mn^{2+}/Mn^{3+} by Jahn-Teller active Mn^{3+} could be the origin of the low specific capacity in $Li_xMn_{0.8}Fe_{0.2}PO_4$ [26]. The trend of overpotential is opposite during the discharge process. Of particular note is that the evolutions of overpotential are different at the two phase reaction region between charge and discharge process, which indicates the different reaction pathways

exist between them. While overpotential is increased by the formation of α phase during charge process, overpotential remains constant by the formation of β' phase upon discharge process. Such asymmetry is originated from the different reaction pathways between delithiation and lithiation process, which will be further discussed later.

Li^+ diffusivities during the electrochemical cycle are estimated by Eq. (1). While the overall trend of Li^+ diffusivity is opposite to that of overpotential, the apparent Li^+ diffusivities in the first-order phase transition regime are 1-2 orders of magnitude lower than those in the second-order phase transition regime [42,43]. The apparent diffusivity decreases during the two phase reaction, between β phase and β' phase (x = ~0.9 in $Li_xMn_{0.8}Fe_{0.2}PO_4$) and then between β' phase and α phase (~0.7 ≥ x), followed by the gradual increase at the end of charged state. The gradual increase of Li^+ diffusivity at the end of charged state results from the solid solution reaction at the end of charge ($Li_{\sim 0.1}Mn_{0.8}Fe_{0.2}PO_4$) [20,23]. It should be noted that the electroanalytical methods for measuring Li^+ transport, such as CV, EIS, GITT, and potentiostatic intermittent titration technique (PITT), rely on Fick's law of diffusion without considering the effect of interphase boundary movement on ion transport [42,43], thereby good estimation of Li^+ diffusivity via the electroanalytical methods is impossible. However, it is noteworthy that the value of the apparent Li^+ diffusivity at fully charged state is approximately one order of magnitude lower than that of the apparent Li^+ diffusivity at pristine state, which leads to the increase in the overpotential, and is associated with the evolution of Jahn-Teller active Mn^{3+} by delithiation. Although the overall trend of the apparent Li^+ diffusivities during discharge process, i.e. lithiation, is similar to that of the apparent Li^+ diffusivities during delithiation, there is a little difference between the delithiation and lithiation, especially in the two phase

reaction region. The apparent values of Li^+ diffusivities during delithiation seems to be higher than those of Li^+ diffusivities during lithiation in the first-order phase transition regime of the $Li_yMn_yFe_{1-y}PO_4$ phase and $Mn_yFe_{1-y}PO_4$ phase (β' and α). However, the precise comparison is difficult due to the consideration of the effect of interphase boundary movement on ion transport [42,43].

In situ EIS of $Li_xMn_{0.8}Fe_{0.2}PO_4$ during delithiation and lithiation were further analyzed to clarify the origin of the sluggish reduction of Mn^{3+}. While GITT is the DC perturbation technique to determine the diffusivity, EIS is an AC perturbation technique, in which impedance, the ratio of the perturbed voltage to current, is recorded in the given frequency window, thereby a resistance and a pseudocapacity of solution (R_s and C_{sol}), double layer capacitance (C_{dl}), a pure charge-transfer resistance (R_{ct}), and Warburg impedance (Z_w) can be estimated [6,43,44]. Figure 4-13 shows the Nyquist plots for $Li_xMn_{0.8}Fe_{0.2}PO_4$ during the charge and discharge processes, in which a high-frequency semicircle and low-frequency tails are observed [43,44]. The high-frequency semicircle is ascribed to R_{ct} in the electrode/electrolyte interface, and Z_w can be derived from the low-frequency tail, so called Warburg region, which accounts for a resistance to mass transfer (Fig. 4-14) [44-50]. By fitting trace of the spectra, the charge-transfer resistances and apparent Li^+ diffusivities were derived, and plotted in Figs. 4-15 and 4-16. As shown in Figs. 4-15, the overall tendency of R_{ct} shows apparently constant value during delithiation and lithiation processes, which means that the influence of charge (especially electron) transfer on the sluggish kinetics of the carbon-coated $Li_xMn_{0.8}Fe_{0.2}PO_4$ is negligible due to the well-percolated conductive carbon coating layer [6,51]. Instead, unexpectedly, overall trend of the apparent Li^+ diffusivity exactly follows that of the overpotential (Fig. 4-16). The origin of the same behavior of overpotential and D_{EIS} is not clear yet. However, it is reported that there is no true Li^+ diffusion coefficient in $Li_xMn_{0.8}Fe_{0.2}PO_4$ by EIS analysis, especially in the first-order phase transition region, because the diffusion length from EIS analysis is negligible, compared to the particle size [48,49]. Herein, the apparent diffusion length can be calculated as $L = (D_{EIS}/f)^{1/2} = \sim 3$ nm, where f = 10 mHz and

D_{EIS} = ~10^{-15} cm^2/s taken from the initial stage of the delithiation process shown in Fig. 4-16. Therefore, the EIS results exhibit the mass transfer information only at the interface between the surface of the $Li_xMn_{0.8}Fe_{0.2}PO_4$ particle and electrolyte.

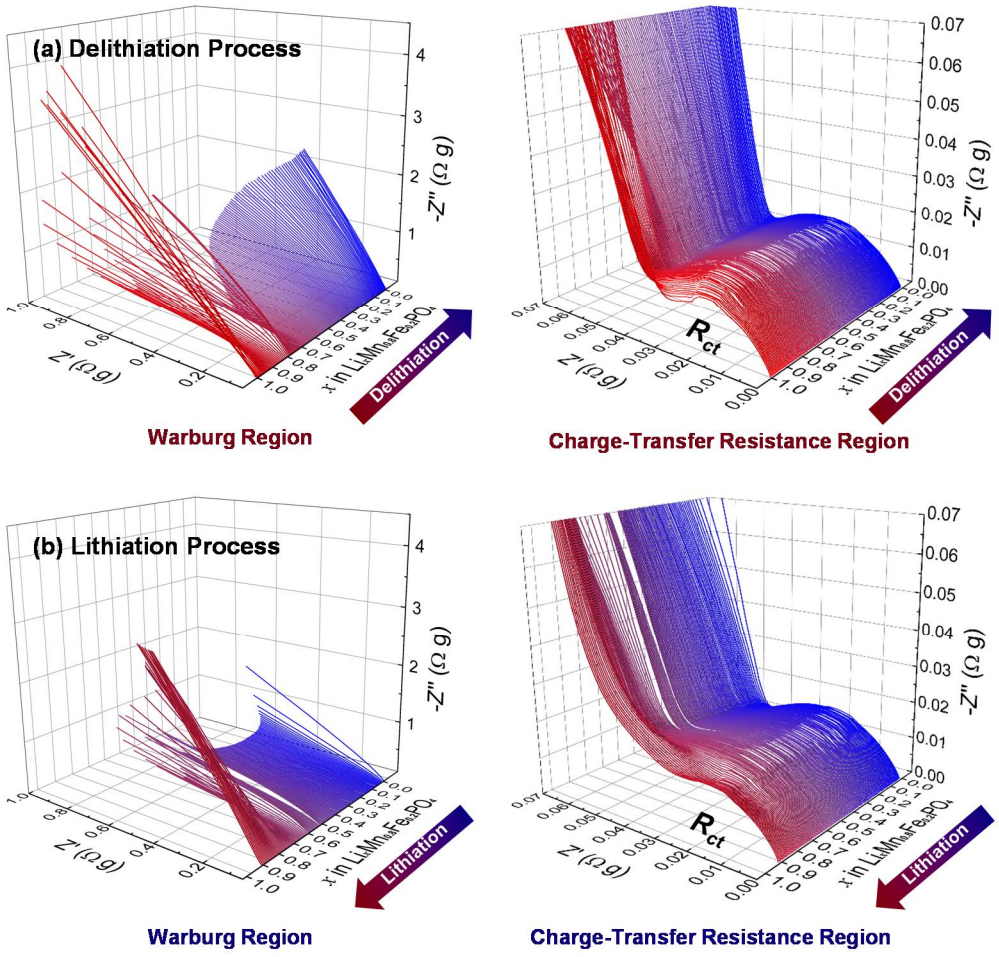

Fig. 4-13. (Color) Typical 3-dimentional Nyquist plots of carbon-coated $LiMn_{0.8}Fe_{0.2}PO_4$ mesocrystal, obtained by *in situ* EIS with GITT technique during (a) delithiation and (b) lithiation process. The Warburg regions in the low frequency (< 1 Hz) are plotted on the left, and the magnified plots are also presented on the right to manifest the characteristics of high-frequency region.

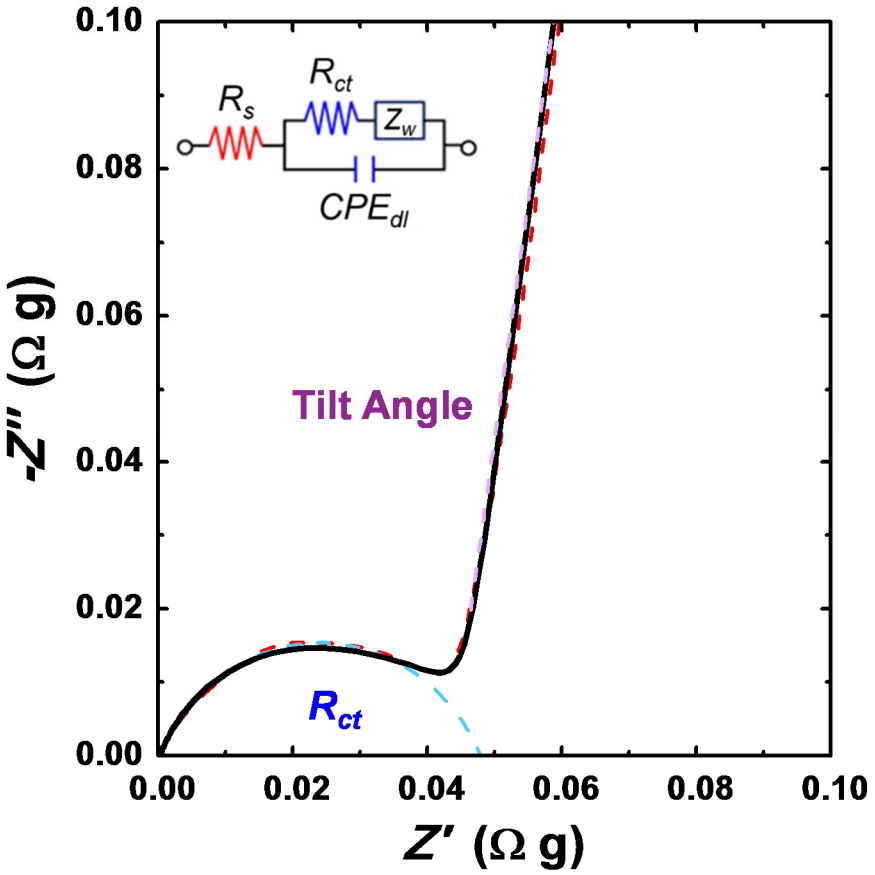

Fig. 4-14. (Color) Typical Nyquist plot of $Li_xMn_{0.8}Fe_{0.2}PO_4$ (x = 0), obtained by *in situ* EIS with GITT technique during delithiation. The blue-dashed, high-frequency arc arises from the charge-transfer resistance coupled with double-layer capacitance, and the purple dashed line is the linear fitting line for the tilt angle of Warburg region. The red dashed line is the fitting line obtained using the equivalent circuit in the inset.

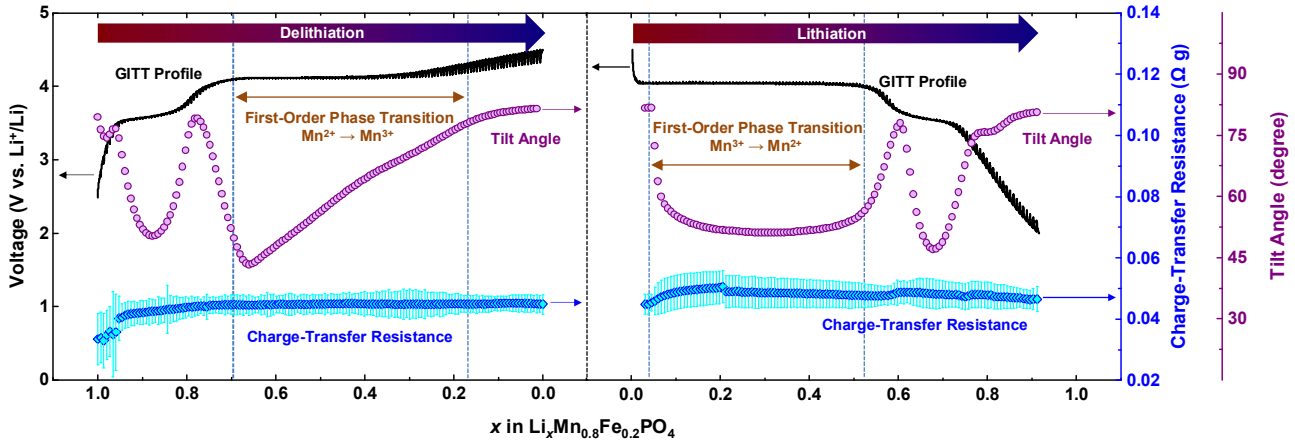

Fig. 4-15. (Color) *In situ* EIS with GITT technique results. GITT curves, charge-transfer resistance, and tilt angle of Warburg region in EIS spectra of the carbon-coated $LiMn_{0.8}Fe_{0.2}PO_4$ mesocrystal during delithiation and lithiation process.

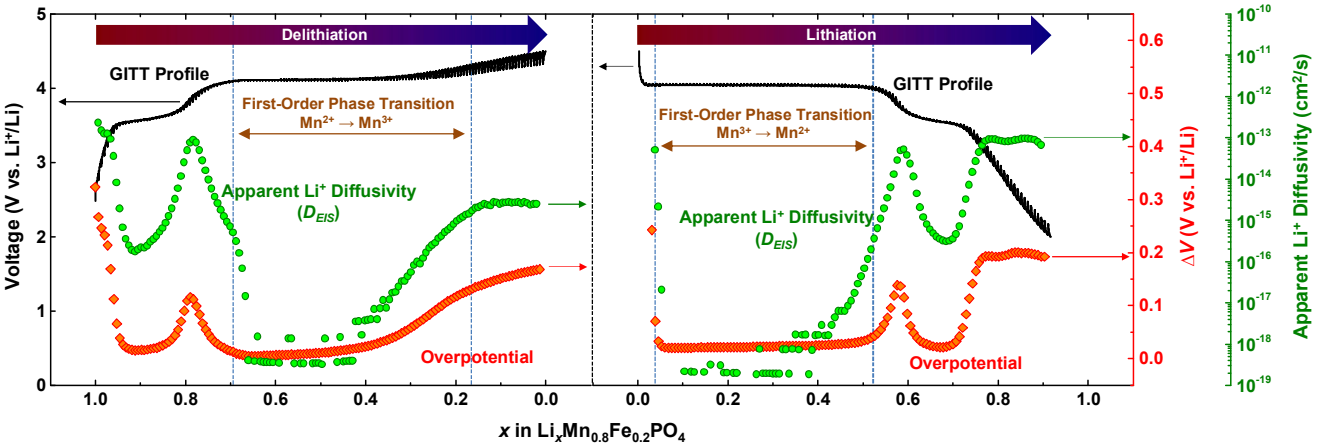

Fig. 4-16. (Color) *In situ* EIS with GITT technique results. GITT, overpotential (from GITT profiles), and apparent Li^+ diffusivity (D_{EIS}) curves of carbon-coated $LiMn_{0.8}Fe_{0.2}PO_4$ mesocrystal during delithiation and lithiation process.

For further information about the mass transport from the *in situ* EIS analysis, the tilt angle in the linear Warburg region was analyzed to get an insight about the reaction pathway in the first-order phase transition regime of the $Li_yMn_yFe_{1-y}PO_4$ phase and $Mn_yFe_{1-y}PO_4$ phase (β' and α) (Fig.4-15). Understanding of the reaction pathways during phase transformation in $LiMn_{0.8}Fe_{0.2}PO_4$ is important, because the reaction pathway and its kinetics directly comprise the electrochemical properties (i.e., specific capacity and rate capability). Although many research groups tried to model the reaction pathway during two-phase mechanism in olivine cathode materials, the specific model still remains controversial, including the shrinking core-shell, domino cascade, and mosaic model *etc.*, because strong entanglement of the chemical composition, particle size, and morphology of the studied olivine cathode materials hinders good understanding of (de)lithiation kinetics and reaction model [52-55]. D. Li *et al.* tried to confirm the two-phase reaction mechanism of $LiFePO_4$ and $Li_4Ti_5O_{12}$ by measuring the tilt angle in the linear Warburg region [48-50]. Although the confirmation of the reaction pathway during two-phase reaction in $Li_xMn_{0.8}Fe_{0.2}PO_4$ cannot be accurately elucidated by only the analysis of tilt angle in the linear Warburg region, the trend of tilt angle in the first-order phase transition regime of the $Li_yMn_yFe_{1-y}PO_4$ phase and $Mn_yFe_{1-y}PO_4$ phase (β' and α) during lithiation is quite different with that during delithiation, which means the reaction pathway of the two-phase reaction during lithiation could be different with that during delithiation. For the lithiation process, the tilt angle exhibits constant value in the reduction reaction region of Mn^{3+} (the first-order phase transition region), which means the surface of β' ($Li_yMn_{0.8}Fe_{0.2}PO_4$) does not change much during the two-phase reaction, in other words, the lithiated phase are formed on the surface in the initial stage of lithiation process,

then the lithiated-phase shell becomes thicker. Thereby, it can be concluded that the $Li_xMn_{0.8}Fe_{0.2}PO_4$ follow the core-shell model for the lithiation process. For the delithiation process, on the contrary, the tilt angle is gradually changed as the oxidation of Mn^{2+} to Mn^{3+} occurs, which means the surface of β' ($Li_yMn_{0.8}Fe_{0.2}PO_4$) changes continuously by the formation of α ($Mn_{0.8}Fe_{0.2}PO_4$) phase in the vicinity of the surface, which can be explained by the domino cascade or mosaic model (Fig. 4-17). Further investigation about the phase transformation mechanism during delithiation/lithiation of $LiMn_{0.8}Fe_{0.2}PO_4$ are currently underway via soft x-ray Fourier ptychographic microscopy combined with x-ray absorption spectroscopy and electron microscopy.

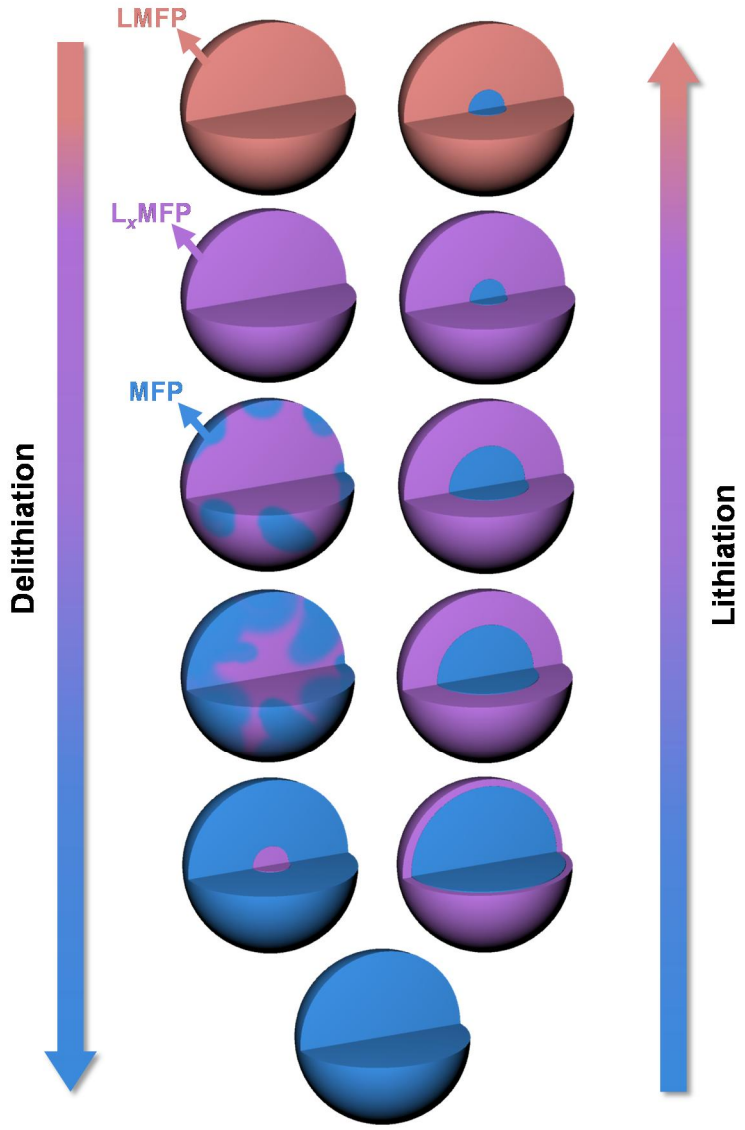

Fig. 4-17. (Color) The schematic illustration of the proposed mechanism of phase transformation of $Li_xMn_{0.8}Fe_{0.2}PO_4$ during delithiation and lithiation processes [53-56].

The difference of the two-phase reaction mechanism (β' and α) between the delithiation and lithiation process could be explained by the role of a nucleation enhancer. It is known that electrochemical properties of $LiMnPO_4$ can be significantly improved by co-doping of Fe and Co, because a small amount of Fe in $LiMnPO_4$ matrix will accelerate the delithiation kinetics due to both lower nucleation barrier and more nucleation sites during delithiation process, and similarly, the high-potential redox element, Co, in the $LiMnPO_4$ matrix can act as a nucleation enhancer during lithiation process, as reported by J. Kim *et al* [24,25]. In the case of $LiMn_{0.8}Fe_{0.2}PO_4$ mesocrystal, the oxidation reaction of Fe^{2+} can enhance the oxidation reaction kinetics of Mn^{2+} during delithiation. However, there exists no nucleation enhancer such as Co for the facile reduction reaction of Mn^{3+} during lithiation process. Therefore, it seems to be reasonable that the reaction kinetics of the $Li_xMn_{0.8}Fe_{0.2}PO_4$ during delithiation is different with those during lithiation process, and delithiation process is more electrochemically efficient than lithiation process in the first-order phase transition regime of the $Li_yMn_yFe_{1-y}PO_4$ phase and $Mn_yFe_{1-y}PO_4$ phase (β' and α) of the $Li_xMn_{0.8}Fe_{0.2}PO_4$ as can be seen in the difference of overpotential. As a result, our systematic studies for the kinetics in the $Li_xMn_{0.8}Fe_{0.2}PO_4$ not only help understand the origin of the sluggish kinetics in $Li_xMn_{0.8}Fe_{0.2}PO_4$ during battery operation but also provide the guide to achieve further improvement of the electrochemical properties of Mn-based olivine cathode materials. We believe that the carbon-coated ternary olivine mesocrystal containing Mn, Fe, and Co compounds can be a key for advanced Mn-based olivine cathode materials, and further systematic studies on the ternary olivine mesocrystal by soft x-ray absorption coupled with ptychography is currently undergoing to clarify the effects of the nucleation enhancer such as Fe or Co on the kinetics for Mn-based olivine cathode materials [55,56].

4.4. Conclusions

In this work, we systematically investigate the reaction kinetics of $Li_xMn_{0.8}Fe_{0.2}PO_4$ (LMFP) mesocrystal during battery operation through *operando* x-ray diffraction and *in situ* electrochemical impedance spectroscopy combined with galvanostatic intermittent titration technique (GITT), by which insights on the phase propagation and sluggish kinetics of LMFP mesocrystal could be elaborated. *In situ* analyses on the carbon-coated LMFP mesocrystal reveal that the reaction pathway of LMFP might differ during delithiation/lithiation process, and the sluggish kinetics of LMFP mesocrystal and resultant limitation of obtainable discharge capacity is attributed to the decrease of apparent Li^+ diffusivity triggered by Mn redox reaction. Considering the in-depth study about reaction kinetics of LMFP mesocrystal by combination of various *in situ* techniques, our work provides tools as well as fundamental understandings to design high-performance Mn-based olivine cathodes.

4.5 References

1. M. Winter and R. J. Brodd, What Are Batteries, Fuel Cells, and Supercapacitors?, *Chem. Rev.* 104 (2004) 4245.
2. M. S. Whittingham, Electrical Energy Storage and Intercalation Chemistry, *Science* 192 (1976) 1126.
3. K. Kang, Y. S. Meng, J. Breger, C. P. Grey, and G. Ceder, Electrodes with High Power and High Capacity for Rechargeable Lithium Batteries, *Science* 311 (2006) 977.
4. A. K. Padhi, K. S. Nanjundaswamy, and J. B. Goodenough, Phospho-Olivines as Positive-Electrode Materials for Rechargeable Lithium Batteries, *J. Electrochem. Soc.* 144 (1997) 1188.
5. S. Wi, S. Nam, Y. Oh, J. Kim, H. Choi, S. Hong, S. Byun, D. J. Choi, K. Ahn, Y. H. Kim, and B. Park, Facile Synthesis of Porous-Carbon/$LiFePO_4$ Nanocomposites, *J. Nanopart. Res.* 14 (2012) 1327.
6. S. Wi, J. Kim, K. Park, S. Lee, J. Kang, K. H. Kim, S. Nam, C. Kim, and B. Park, Evolution of Graphene-Wrapped $LiFePO_4$ as Novel Cathode Materials for Li-Ion Batteries. *RSC Adv.* 6 (2016) 105081.
7. K. F. Hsu, S. Y. Tsay, and B. J. Hwang, Synthesis and Characterization of Nano-Sized $LiFePO_4$ Cathode Materials Prepared by a Citric Acid-Based Sol-Gel Route, *J. Mater. Chem.* 14 (2004) 2690.
8. H. P. Subramanya, B. Ellis, N. Coombs, and L. F. Nazar, Nano-Network Electronic Conduction in Iron and Nickel Olivine Phosphates, *Nat. Mater.* 3 (2004) 147.
9. K. Amine, H. Yasuda, and M. Yamachi, Olivine $LiCoPO_4$ as 4.8 V Electrode Material for Lithium Batteries, *Electrochem. Solid-State Lett.* 3 (2000) 178.
10. G. Li, H. Azuma, and M. Tohda, $LiMnPO_4$ as the Cathode for Lithium Batteries, *Electrochem. Solid-State Lett.* 5 (2002) A135.

11. C. Delacourt, P. Poizot, M. Morcrette, J. M. Tarascon, and C. Masquelier, One-Step Low-Temperature Route for the Preparation of Electrochemically Active $LiMnPO_4$ Powders, *Chem. Mater.* 16 (2004) 93.
12. Z. Qin, X. Zhou, Y. Xia, C. Tang, and Z. Liu, Morphology Controlled Synthesis and Modification of High-Performance $LiMnPO_4$ Cathode Materials for Li-Ion Batteries, *J. Mater. Chem.* 22 (2012) 21144.
13. S. M. Oh, S. W. Oh, C. S. Yoon, B. Scrosati, K. Amine, and Y. K. Sun, High-Performance Carbon-$LiMnPO_4$ Nanocomposite Cathode for Lithium Batteries, *Adv. Funct. Mater.* 20 (2010) 3260.
14. G. Chen, A. K. Shukla, X. Song, and T. J. Richardson, Improved Kinetics and Stabilities in Mg-Substituted $LiMnPO_4$, *J. Mater. Chem.* 21 (2011) 10126.
15. M. Pivko, M. Bele, E. Tchernychova, N. Z. Logar, R. Dominko, and M. Gaberscek, Synthesis of Nanometric $LiMnPO_4$ via a Two-Step Technique, *Chem. Mater.* 24 (2012) 1041.
16. S. Wi, J. Kim, S. Lee, J. Kang, K. H. Kim, K. Park, K. Kim, S. Nam, C. Kim, and B. Park, Synthesis of $LiMn_{0.8}Fe_{0.2}PO_4$ Mesocrystals for High-Performance Li-Ion Cathode Materials. *Electrochim. Acta* 216 (2016) 203.
17. Y. K. Sun, S. M. Oh, H. K. Park, and B. Scrosati, Micrometer-Sized, Nanoporous, High-Volumetric-Capacity $LiMn_{0.85}Fe_{0.15}PO_4$ Cathode Material for Rechargeable Lithium-Ion Batteries, *Adv. Mater.* 23 (2011) 5050.
18. H. Wang, Y. Yang, Y. Liang, L. F. Cui, H. S. Casalongue, Y. Li, G. Hong, Y. Cui, and H. Dai, $LiMn_{1-x}Fe_xPO_4$ Nanorods Grown on Graphene Sheets for Ultrahigh-Rate-Performance Lithium Ion Batteries, *Angew. Chem. Int. Ed.* 123 (2011) 7502.
19. M. S. Kim, J. P. Jegal, K. C. Roh, and K. B. Kim, Synthesis of $LiMn_{0.75}Fe_{0.25}PO_4$/C Microspheres Using a Microwave-Assisted Process with a Complexing Agent for High-Rate Lithium Ion Batteries, *J. Mater. Chem. A* 2 (2014) 10607.
20. D. B. Ravnsbæk, K. Xiang, W. Xing, O. J. Borkiewicz, K. M. Wiaderek, P. Gionet, K. W. Chapman, P. J. Chupas, and Y. M. Chiang, Extended Solid Solutions and

Coherent Transformations in Nanoscale Olivine Cathodes, *Nano Lett.* 14 (2014) 1484.

21. A. Yamada, Y. Kudo, and K. Y. Liu, Reaction Mechanism of the Olivine-Type $Li_x(Mn_{0.6}Fe_{0.4})PO_4$ ($0 < x < 1$), *J. Electrochem. Soc.* 148 (2001) A747.
22. R. Malik, F. Zhou, and G. Ceder, Phase Diagram and Electrochemical Properties of Mixed Olivines from First-Principles Calculations, *Phy. Rev. B* 79 (2009) 214201.
23. D. B. Ravnsbæk, K. Xiang, W. Xing, O. J. Borkiewicz, K. M. Wiaderek, P. Gionet, K. W. Chapman, P. J. Chupas, M. Tang, and Y. M. Chiang, Engineering the Transformation Strain in $LiMn_yFe_{1-y}PO_4$ Olivines for Ultrahigh Rate Battery Cathodes, *Nano Lett.* 16 (2016) 2375.
24. J. Kim, D. H. Seo, S. W. Kim, Y. U. Park, and K. Kang, Mn Based Olivine Electrode Material with High Power and Energy, *Chem. Commun.* 46 (2010) 1305.
25. J. Kim, Y. U. Park, D. H. Seo, J. Kim, S. W. Kim, and K. Kang, Mg and Fe Co-doped Mn Based Olivine Cathode Material for High Power Capability, *J. Electrochem. Soc.* 158 (2011) A250.
26. S. Wi, J. Park, S. Lee, J. Kang, T. Hwang, K.-S. Lee, H.-K. Lee, S. Nam, C. Kim, Y.-E. Sung, and B. Park, Synchrotron-Based X-Ray Absorption Spectroscopy for the Electronic Structure of $Li_xMn_{0.8}Fe_{0.2}PO_4$ Mesocrystal in Li^+ Batteries, *Nano Energy* 31 (2017) 495.
27. H. Gwon, D. H. Seo, S. W. Kim, J. Kim, and K. Kang, Combined First-Principle Calculations and Experimental Study on Multi-Component Olivine Cathode for Lithium Rechargeable Batteries, *Adv. Funct. Mater.* 19 (2009) 3285.
28. D.-H. Seo, H. Gwon, S.-W. Kim, J. Kim, and K. Kang, Multicomponent Olivine Cathode for Lithium Rechargeable Batteries: A First-Principles Study, *Chem. Mater.* 22 (2010) 518.
29. A. Yamada, Y. Kudo, and K. Y. Liu, Phase Diagram of $Li_x(Mn_yFe_{1-y})PO_4$ ($0 \leq x, y \leq 1$), *J. Electrochem. Soc.* 148 (2001) A1153.

30. X. Zhang, M. Hulzen, D. P. Singh, A. Brownrigg, J. P. Wright, N. H. Dijk, and M. Wagemaker, Rate-Induced Solubility and Suppression of the First-Order Phase Transition in Olivine $LiFePO_4$, *Nano Lett.* 14 (2014) 2279.
31. Y. Orikasa, T. Maeda, Y. Koyama, H. Murayama, K. Fukuda, H. Tanida, H. Arai, E. Matsubara, Y. Uchimoto, and Z. Ogumi, Direct Observation of a Metastable Crystal Phase of Li_xFePO_4 under Electrochemical Phase Transition, *J. Am. Chem. Soc.* 135 (2013) 5497.
32. K.-W. Nam, W.-S. Yoon, K. Zaghib, K. Y. Chung, X.-Q. Yang, The phase transition behaviors of $Li_{1-x}Mn_{0.5}Fe_{0.5}PO_4$ during lithium extraction studied by in situ X-ray absorption and diffraction techniques, *Electrochem. Commun.* 11 (2009) 2023.
33. W. Weppner and R. A. Hugguns, Determination of the Kinetic Parameters of Mixed-Conducting Electrodes and Application to the System Li_3Sb, *J. Electrochem. Soc.* 124 (1977) 1569.
34. D. D. Lecce, R. Brescia, A. Scarpellini, M. Prato, and J. Hassoun, A High Voltage Olivine Cathode for Application in Lithium-Ion Batteries, *ChemSusChem* 9 (2016) 223.
35. A. M. Hashambhoy and J. F. Whitacre, Li Diffusivity and Phase Change in $LiFe_{0.5}Mn_{0.5}PO_4$: A Comparative Study using Galvanostatic Intermittent Titration and Cyclic Voltammetry, *J. Electrochem. Soc.* 158 (2011) A390.
36. B. Zhang, X. Wang, Z. Liu, H. Li, and X. Huang, Enhanced Electrochemical Performances of Carbon Coated Mesoporous $LiFe_{0.2}Mn_{0.8}PO_4$, *J. Electrochem. Soc.* 157 (2010) A285.
37. X. J. Wang, X. Q. Yu, H. Li, X. Q. Yang, J. McBreen, and X. Huang, Li-Storage in $LiFe_{1/4}Mn_{1/4}Co_{1/4}Ni_{1/4}PO_4$ Solid Solution, *Electrochem. Commun.* 10 (2008) 1347.
38. B. Ding, P. Xiao, G. Ji, Y. Ma, L. Lu, and J. Y. Lee, High-Performance Lithium-Ion Cathode $LiMn_{0.7}Fe_{0.3}PO_4$/C and the Mechanism of Performance Enhancements through Fe Substitution, *ACS Appl. Mater. Inter.* 5 (2013) 12120.
39. B. Zhang, X. Wang, H. Li, X. Huang, Electrochemical Performances of $LiFe_{1-x}Mn_xPO_4$ with High Mn Content, *J. Power Sources* 196 (2011) 6992.

40. R. Amin and Y.-M. Chiang, Characterization of Electronic and Ionic Transport in $Li_{1-x}Ni_{0.33}Mn_{0.33}Co_{0.33}O_2$ (NMC333) and $Li_{1-x}Ni_{0.50}Mn_{0.20}Co_{0.30}O_2$ (NMC523) as a Function of Li Content, *J. Electrochem. Soc.* 163 (2016) A1512.
41. R. Amin, D. B. Ravnsbaek, and Y.-M. Chiang, Characterization of Electronic and Ionic Transport in $Li_{1-x}Ni_{0.8}Co_{0.15}Al_{0.05}O_2$ (NCA), *J. Electrochem. Soc.* 162 (2015) A1163.
42. Y. Zhu and C. Wang, Galvanostatic Intermittent Titration Technique for Phase-Transformation Electrodes, *J. Phys. Chem. C* 114 (2010) 2830.
43. K. Tang, X. Yu, J. Sun, H. Li, X. Huang, Kinetic Analysis on $LiFePO_4$ Thin Films by CV, GITT, and EIS, *Electrochim. Acta* 56 (2011) 4869.
44. C. Ho, I. D. Raistrick, R. A. Huggins, Application of A-C Technique to the Study of Lithium Diffusion in Tungsten Trioxide Thin Film, *J. Electrochem. Soc.* 127 (1980) 345.
45. S.-I. Pyun and J.-S. Bae, The AC Impedance Study of Electrochemical Lithium Intercalation into Porous Vanadium Oxide Electrode, *Electrochim. Acta* 41 (1996) 919.
46. Y. Oh, S. Nam, S. Wi, J. Kang, T. Hwang, S. Lee, H. H. Park, J. Cabana, C. Kim, and B. Park, Effective Wrapping of Graphene on Individual $Li_4Ti_5O_{12}$ Grains for High-Rate Li-Ion Batteries, *J. Mater. Chem. A* 2 (2014) 2023.
47. J. Kim, K. E. Lee, K. H. Kim, S. Wi, S. Lee, S. Nam, C. Kim, S. O. Kim, and B. Park, Single-Layer Graphene-Wrapped $Li_4Ti_5O_{12}$ Anode with Superior Lithium Storage Capability, *Carbon* 114 (2017) 275.
48. D. Li, T. Zhang, X. Liu, P. He, R. Peng, M. Wang, M. Han, and H. Zhou, A Hybrid Phase-Transition Model of Olivine $LiFePO_4$ for the Charge and Discharge Processes, *J. Power Sources* 223 (2013) 299.
49. D. Li, X. Liu, and H. Zhou, The Size-Dependent Phase Transition of $LiFePO_4$ Particles during Charging and Discharging in Lithium-Ion Batteries, *Energy Technol.* 2 (2014) 542.

50. D. Li, P. He, H. Li, and H. Zhou, An Unsymmetrical Lithium-Ion Pathway between Charge and Discharge Processes in a Two-Phase Stage of $Li_4Ti_5O_{12}$, *Phys. Chem. Chem. Phys.* 14 (2012) 9086.
51. J. Yang, B. Yan, J. Ye, Y. Liu, and H. You, Carbon-Coated $LiCrTiO_4$ Electrode Material Promoting Phase Transition to Reduce Asymmetric Polarization for Lithium-Ion Batteries, *Phys. Chem. Chem. Phys.* 16 (2014) 2882.
52. A. S. Andersson and J. O. Thomas, The Source of First-Cycle Capacity Loss in $LiFePO_4$, *J. Power Sources* 97 (2001) 498.
53. C. Delmas, M. Maccario, L. Croguennec, F. Le Cras, and F. Weill, Lithium Deintercalation in $LiFePO_4$ Nanoparticles via a Domino-Cascade Model, *Nat. Mater.* 7 (2008) 665.
54. V. Srinivasan and J. Newman, Existence of Path-Dependence in the $LiFePO_4$ Electrode, *Electrochem. Solid-State Lett.* 9 (2006) A110.
55. Y.-S. Yu, C. Kim, D. A. Shapiro, M. Farmand, D. Qian, T. Tyliszczak, A. L. D. Kilcoyne, R. Celestre, S. Marchesini, J. Joseph, P. Denes, T. Warwick, F. C. Strobridge, C. P. Grey, H. Padmore, Y. S. Meng, R. Kostecki, J. Cabana, Dependence on Crystal Size of the Nanoscale Chemical Phase Distribution and Fracture in Li_xFePO_4, *Nano Lett.* 15 (2015) 4282.
56. J. Lim, Y. Li, D. H. Alsem, H. So, S. C. Lee, P. Bai, D. A. Cogswell, X. Liu, N. Jin, Y.-S. Yu, N. J. Salmon, D. A. Shapiro, M. Z. Bazant, T. Tyliszczak, W. C. Cueh, Origin and Hysteresis of Lithium Compositional Spatiodynamics within Battery Primary Particles, *Science* 353 (2016) 566.

Appendix

*A.1. Evaluation of Graphene-Wrapped $LiFePO_4$ as Novel Cathode Materials for Li-Ion Batteries

A.1.1. Introduction

Since the first study by Goodenough group in 1997, $LiFePO_4$ has been considered as one of the most promising cathode materials for lithium ion batteries due to its high theoretical capacity (170 mAh g^{-1}), moderate operating voltage (3.4 V vs. Li^+/Li), environmental benignity, long cycle life, superior safety, and low material cost [1-3]. However, there are several disadvantages in using $LiFePO_4$ for the wider use in the market. The main obstacles are the poor electronic conductivity (~10^{-9} S cm^{-1}) and low ion-transfer coefficient (~10^{-15} cm^2 s^{-1}), which result from a small polaron hoping and the one-dimensional (1D) lithium-ion diffusion channel, respectively [4-6]. Aiming to solve these problems, many efforts have been made to improve the electrochemical performance of $LiFePO_4$, by modifying surface with electronically conductive layers [7-14], reducing Li^+-diffusion lengths [15,16], or doping with supervalent ions [17]. Of these methods, coating with carbonaceous materials is the most common and effective way to enhance the electrical conductivity of $LiFePO_4$ [7-12]. Among derivatives of carbon, graphene has attracted tremendous interests due to

*The work presented in Appendix 1 was published in *RSC Adv.* **6**, 105081 (2016) entitled,
"Evaluation of Graphene-Wrapped $LiFePO_4$ as Novel Cathode Materials for Li-Ion Batteries"
Sungun Wi,+ Jaewon Kim,+ Kimin Park,+ Sangheon Lee, Joonhyeon Kang, Kyung Hwan Kim, Seunghoon Nam,* Chunjoong Kim,* and Byungwoo Park*

its intrinsic characteristics (superior electronic conductivity, high mechanical strength, structural flexibility, and large surface area), and therefore graphene can offer an improved interfacial contact to $LiFePO_4$ [18-27]. Of particular note is stacking graphene on the surface of target materials via electrostatic interaction to incorporate graphene [18,20,23,24]. In the case of directly attaching graphene on the surface of active materials via electrostatic interactions, $LiFePO_4$ nanoparticles easily becomes aggregated, which inhibits individual graphene from wrapping or coating around each $LiFePO_4$ nanoparticle. As a result, these aggregated active materials, which cannot be benefitted from the incorporated graphene, will be left electronically isolated, resulting in unsatisfactory electrochemical performances [22-24].

Herein, we report on an effective strategy to obtain graphene-wrapped $LiFePO_4$ from graphene oxide-wrapped metal phosphate and a Li precursor, instead of simple graphene wrapping on prepared $LiFePO_4$ particles. The subsequent solid-state reaction led to a composite of $LiFePO_4$ and three-dimensional (3D) conducting networks of graphene on the $LiFePO_4$ surface, and as such composite is electronically percolated via the graphene sheets. The method of precursor-incorporated graphene-wrapping proved to exhibit a faster electron transfer rate than the conventional graphene-wrapping [18]. The graphene-wrapped $LiFePO_4$ achieved a high capacity of ~165 mAh g^{-1} (theoretical capacity: 170 mAh g^{-1}) at a discharge rate of 0.1 C (1 C = 170 mA g^{-1}) and ~100 mAh g^{-1} even at a rate of 10 C. In addition, the origin of superior electrochemical performance of the graphene-wrapped $LiFePO_4$ was investigated by in-depth *in situ* analysis of the electrochemical impedance spectroscopy.

A.1.2. Experimental Section

Materials Preperation: $FePO_4$ nanoparticles were synthesized using $FeCl_3$ and $NH_4H_2PO_4$. 100 mL of a distilled water solution containing $FeCl_3$ (0.02 M) was slowly added to 200 mL of deionized (DI) water solution containing $NH_4H_2PO_4$ (0.02 M). The reaction mixture was stirred for 5 h at room temperature, then the resulting $FePO_4$ nanoparticles were centrifuged and washed several times with DI water. The obtained yellow precipitate was dried at 200°C under vacuum overnight with its change of color to dark green.

The modified Hummers' method was used to synthesize graphene oxide (GO), and the details are described elsewhere [11,18,28]. Prior to GO wrapping, the surface of $FePO_4$ was modified to be favourable for assembly with GO. In a typical process, the dried $FePO_4$ powder was dispersed in 100 ml of anhydrous ethanol by ultrasonication for 1 h. Then, aminopropyltriethoxysilane ($C_9H_{23}NO_3Si$: APTES, 1 ml) was injected into a $FePO_4$ ethanol dispersion, followed by being kept under constant stirring overnight. The APTES induces positive charges on the surface of the $FePO_4$ particles. The fabrication of graphene-oxide-wrapped $FePO_4$ was rendered by electrostatic interactions between positively-charged APTES-modified $FePO_4$ and negatively-charged graphene oxide [29-33]. For the self-assembly, an aqueous graphene-oxide suspension (100 ml, 1 mg ml^{-1}) was added into the APTES-modified $FePO_4$ dispersion (500 ml, 1 mg ml^{-1}) under stirring for 1 h. The $FePO_4$/GO powder was collected by centrifuge, and dried for 12 h. The resulting powder was mixed thoroughly with lithium acetate ($C_2H_3LiO_2$) as a lithium precursor at a Li:Fe molar ratio of 1.05:1, followed by annealing at 600°C for 10 h under H_2/Ar (5 vol. % H_2 in argon) atmosphere. After the pyrolysis, the graphene oxide turned into graphene

(reduced graphene oxide), and the graphene-wrapped $LiFePO_4$ ($LiFePO_4$/G) could be obtained. The terminology "graphene" was used throughout this article for the convenience's sake, although it is actually reduced graphene oxide.

For comparison, $LiFePO_4$ without graphene (bare $LiFePO_4$) and graphene-wrapped commercial $LiFePO_4$ (*c*-$LiFePO_4$/G) were also prepared in a similar manner. Bare $LiFePO_4$ was synthesized by the same method as above, except the use of graphene oxide. As for the *c*-$LiFePO_4$/G, the surface modification of commercial $LiFePO_4$ powder (Sigma-Aldrich) was performed by mixing APTES with commercial $LiFePO_4$ in ethanol dispersion for 12 h. The resulting well-dispersed solution was slowly added to GO solution, and gently stirred for 1 h. The obtained graphene-wrapped commercial $LiFePO_4$ powder was centrifuged, and dried for 12 h. Thermal reduction of GO was carried out under H_2/Ar (5 vol. % H_2 in argon) at 600°C for 3 h.

Materials Characterization: The crystal structures of the prepared samples were characterized by x-ray diffraction (XRD, D8 Advance: Bruker). The morphologies of synthesized materials were analyzed using a field-emission scanning electron microscopy (FE-SEM, Merlin Compact: Zeiss) and high-resolution transmission electron microscopy (HRTEM, JEM-3000F: JEOL, Japan). The graphene amount in the composites was measured using a CHNS analyzer (Flash EA 1112: Thermo Electron Corp.).

Electrochemical Measurement: For the electrochemical characterization, the active materials were tested by using coin-type half cells (2016 type) with a Li counter electrode. The composition of the electrode was set to be the same for all samples, which consisted of an active material, super P carbon black, and a polyvinylidene fluoride (PVDF) binder with a weight ratio of 7:2:1. Loading level of active materials was ~1 mg cm^{-2}. The electrolyte contained 1 M $LiPF_6$ in ethylene carbonate and

diethyl carbonate (1/1 vol. %) (Panax Etec). The cells were charged and discharged between 4.3 and 2 V by applying various current densities. The cycling tests were performed at a constant current density of 170 mA g^{-1} (1 C rate based on the theoretical capacity of $LiFePO_4$). The specific capacity was calculated based on the mass of only $LiFePO_4$. Electrochemical impedance spectra (EIS) were measured using a potentiostat (CHI 608C: CH Instrumental Inc.) from 10 mHz to 100 kHz with an AC amplitude of 5 mV.

A.1.3. Results and Discussion

A schematic depicts how graphene-wrapped $LiFePO_4$ ($LiFePO_4$/G) and graphene-wrapped commercial $LiFePO_4$ (*c*-$LiFePO_4$/G) are synthesized, as shown in Figs. A.1-1 and A.1-2. In the case of $LiFePO_4$/G (Fig. A.2-1), the positively-charged $FePO_4$ nanoparticles (Fig. A.1-3, prepared through the surface modification by APTES) attracted the negatively-charged graphene oxide (GO) to assemble themselves into GO-wrapped $FePO_4$ (GO/$FePO_4$) nanocomposites. After the electrostatic self-assembly, the GO/$FePO_4$ nanoparticles were thoroughly mixed with lithium acetate followed by annealing under a reducing atmosphere to obtain $LiFePO_4$/G. In this solid-state reaction, the graphene sheets became crimped, and connected to form a conducting 3D network, while the $LiFePO_4$ nanoparticles were confined, and wrapped by this graphene matrix. These well-connected graphene sheets not only act as a conductive network for $LiFePO_4$ particles, but also constrain the size of $LiFePO_4$ from getting larger during the heat treatment. For *c*-$LiFePO_4$/G, on the other hand, the likelihood that each $LiFePO_4$ particle is confined and connected by GO sheets is relatively small (Fig. A.1-2). Because of the non-uniform contact between $LiFePO_4$ and graphene, the electrons could reach only the $LiFePO_4$ particles that are directly attached to graphene during electrochemical cycling. As a result, the transport of electrons in *c*-$LiFePO_4$/G is limited, leading to low utilization of $LiFePO_4$ at a given charge/discharge rate.

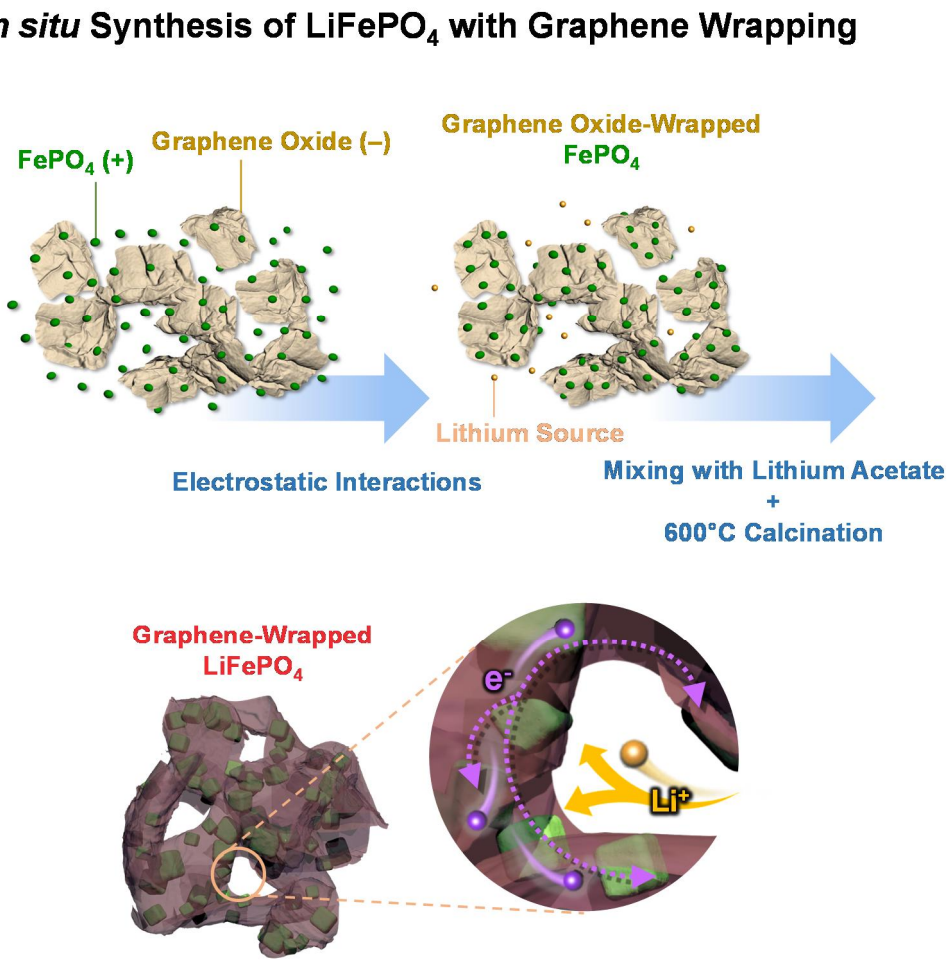

Fig. A.1-1. (Color) Schematic illustration showing the synthetic process for the graphene-wrapped $LiFePO_4$.

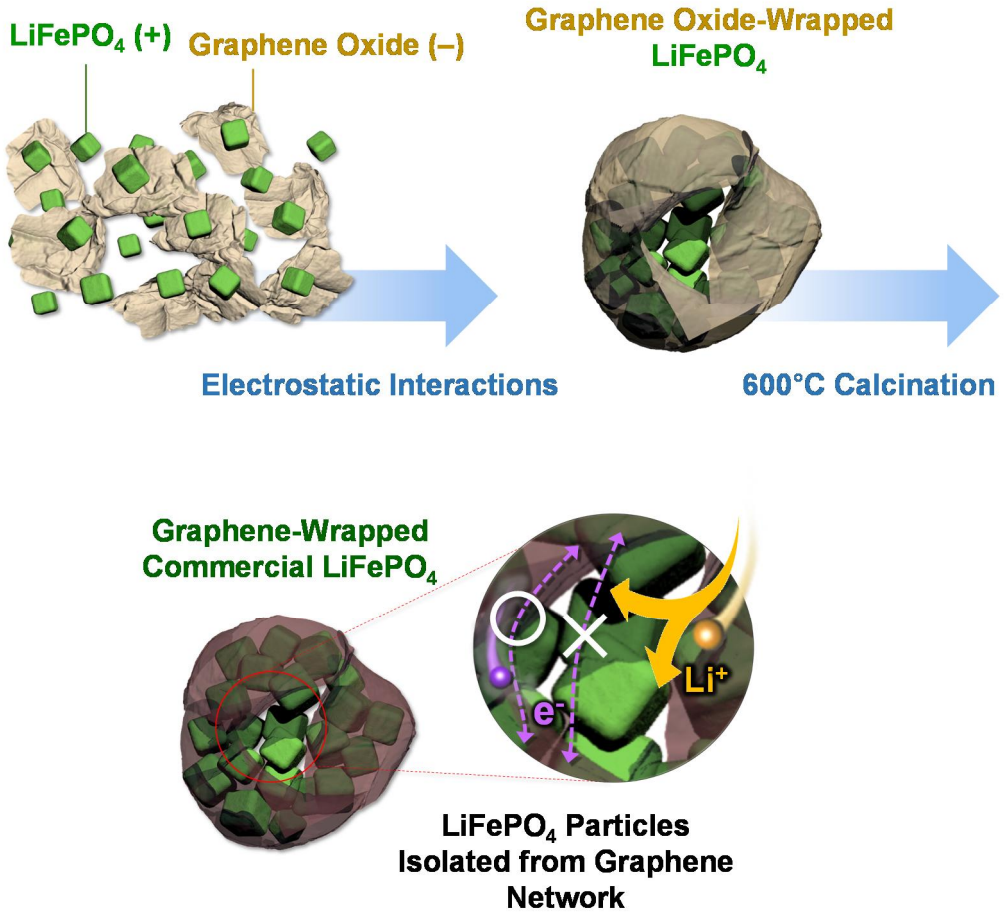

Fig. A.1-2. (Color) Schematic illustration showing the synthetic process for the graphene-wrapped commercial $LiFePO_4$.

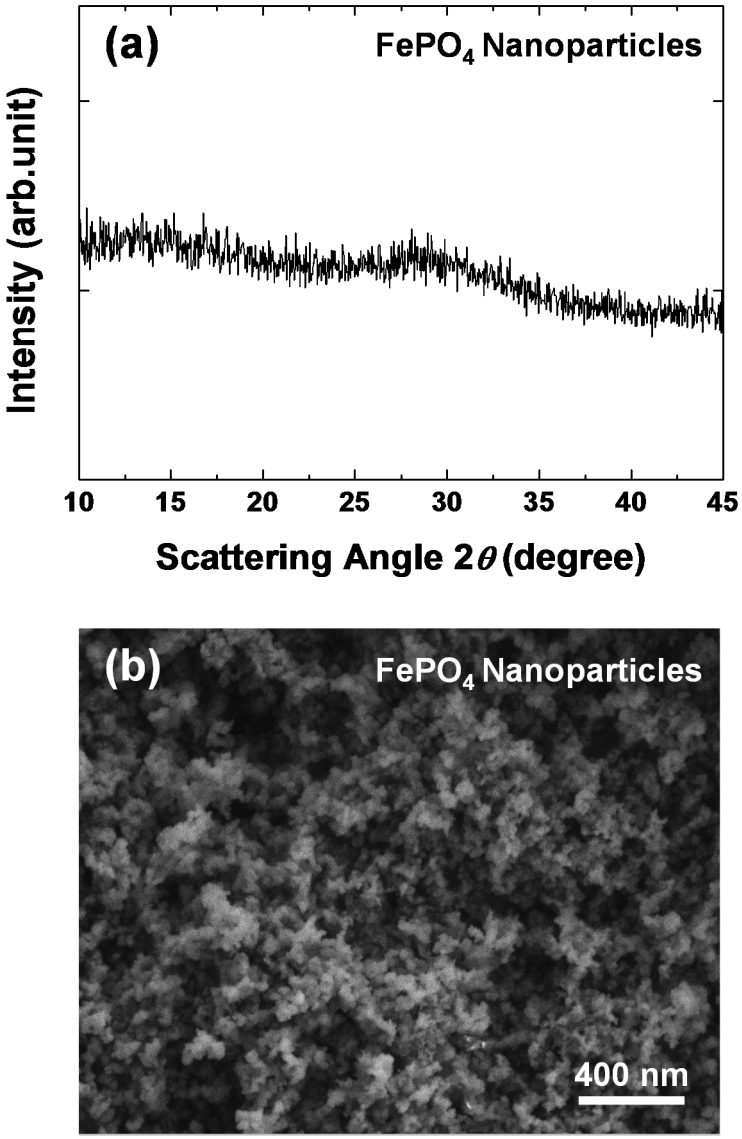

Fig. A.1-3. (a) XRD pattern and (b) SEM image of the amorphous $FePO_4$ nanoparticles.

Transmission electron microscopy (TEM) images in Fig. A.1-4 revealed that the $FePO_4$ nanoparticles were fully wrapped by the flexible GO. While the SEM images (Figs. A.1-5) could not visualize the crinkled textures associated with the presence of flexible graphene sheets, high magnification TEM clearly exhibited that most of the $LiFePO_4$ nanoparticles were well-wrapped by the 3D network of flexible graphene sheets (Figs. A.1-6(a-c)). The HRTEM image in Fig. A.1-6(d) clearly shows lattice fringes, corresponding to the (101) plane of $LiFePO_4$. On the contrary, for *c*-$LiFePO_4$/G, only a few $LiFePO_4$ particles were attached to the graphene sheets (Fig. A.1-7).

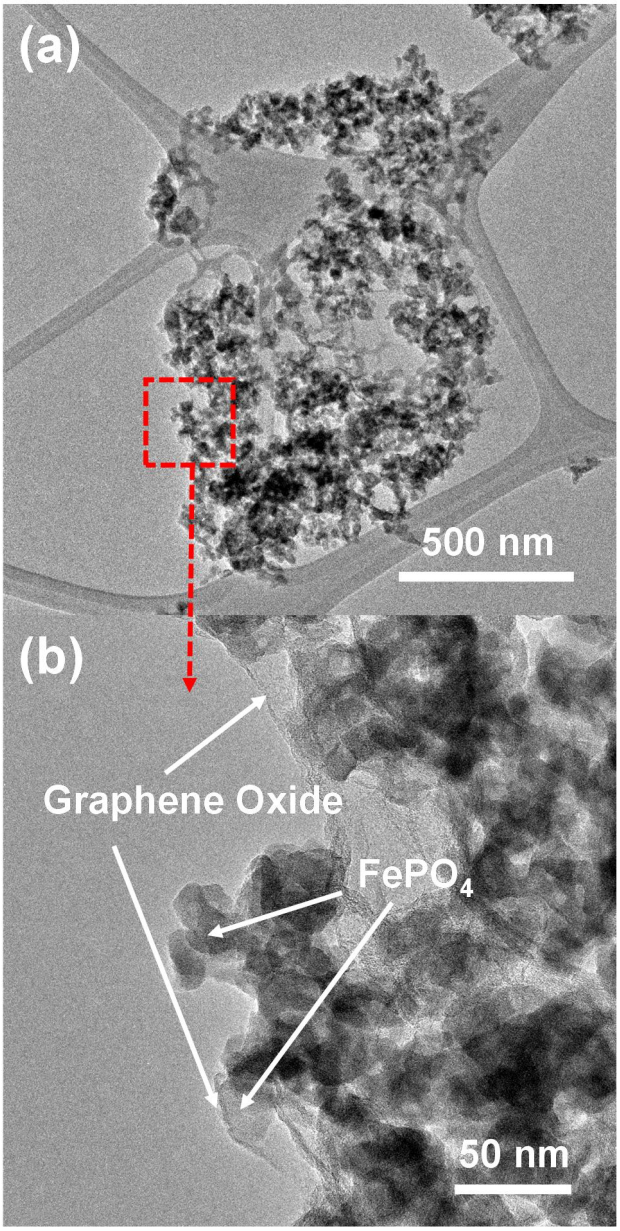

Fig. A.1-4. (a-b) TEM images of the graphene oxide-wrapped $FePO_4$.

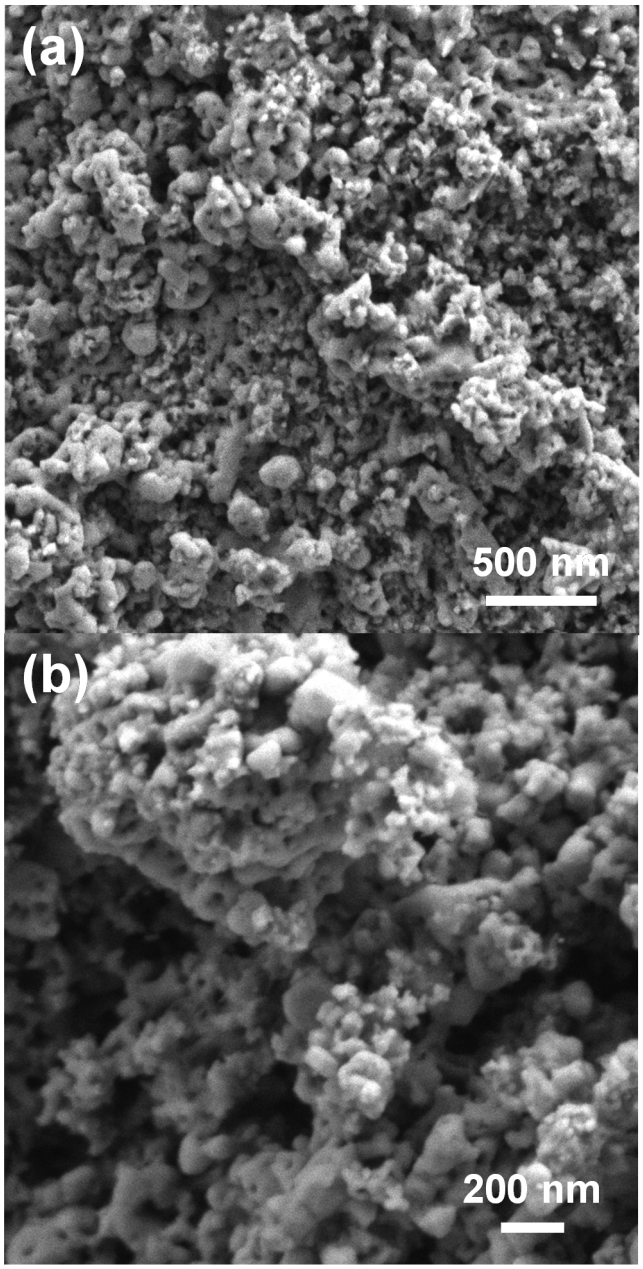

Fig. A.1-5. (a-b) SEM images of the graphene-wrapped $LiFePO_4$.

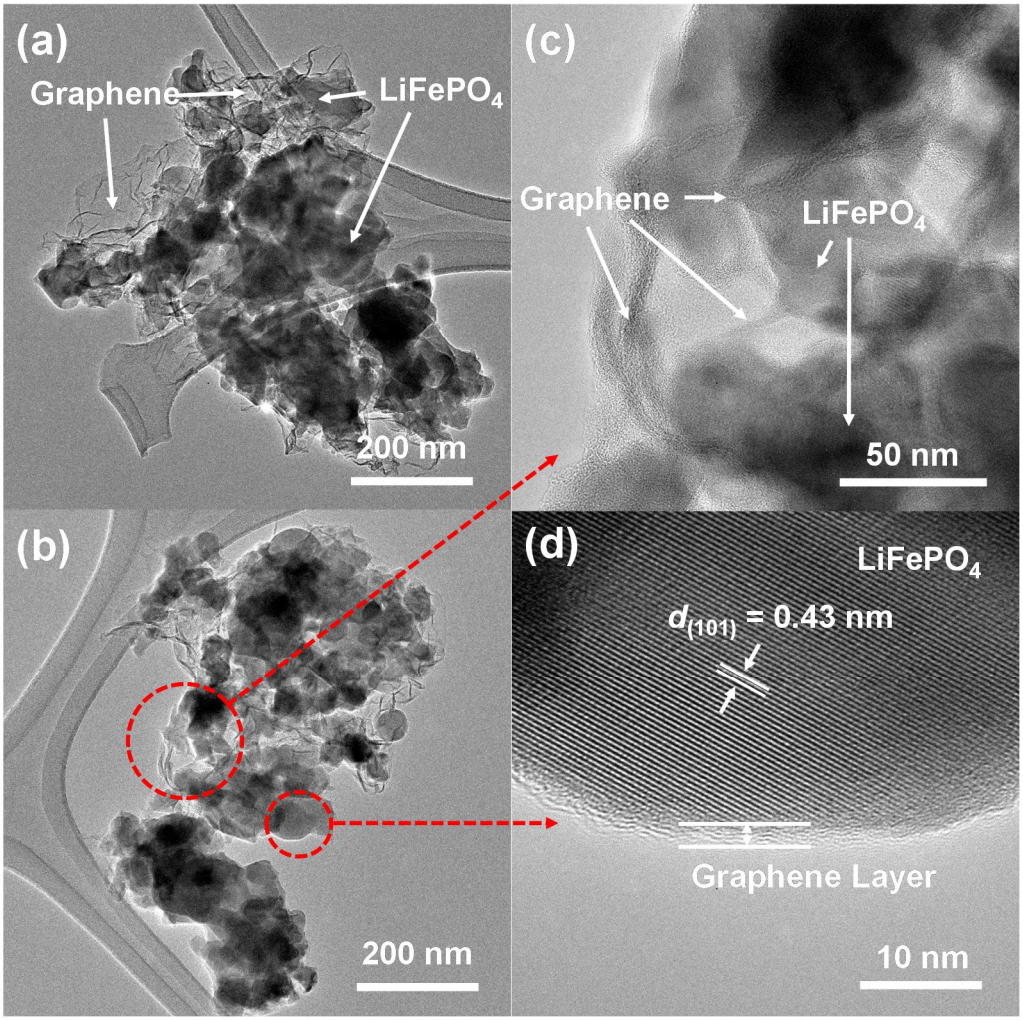

Fig. A.1-6. (a-b) TEM images of the graphene-wrapped $LiFePO_4$. (c-d) HRTEM images of local areas in the graphene-wrapped $LiFePO_4$ as marked in (b).

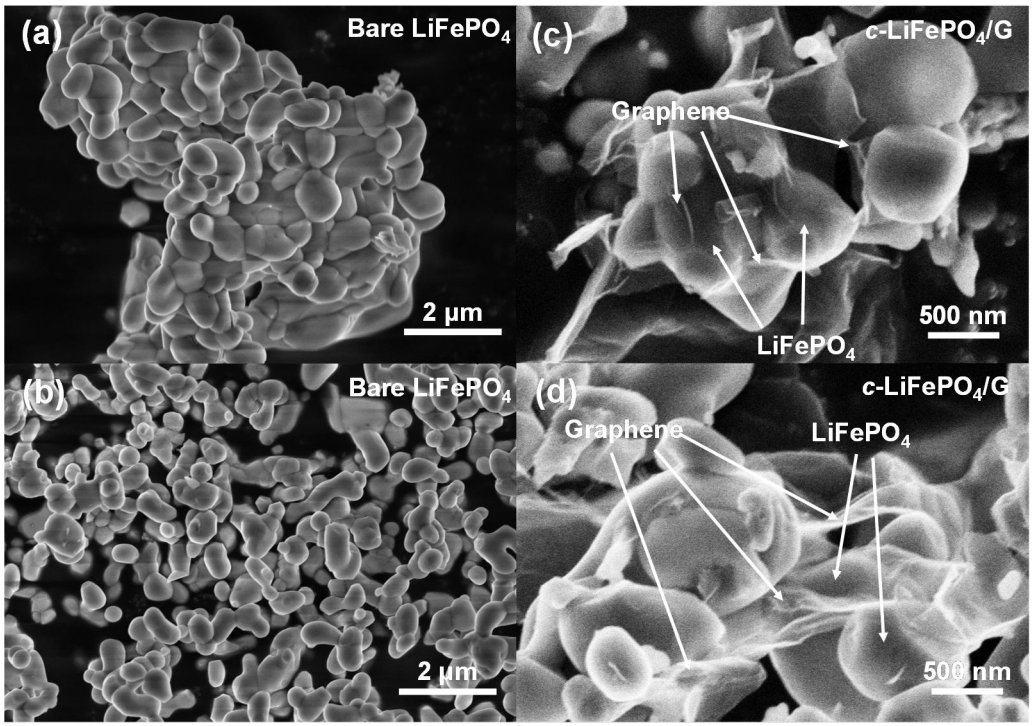

Fig. A.1-7. SEM images of the (a-b) bare $LiFePO_4$ and (c-d) graphene-wrapped commercial $LiFePO_4$.

The graphene content in $LiFePO_4$/G composite was 1.7 wt. % (from CHN analysis, Table A.1-1), which is lower than that of the conventional carbon-coated and/or graphene-wrapped active material having ~10 wt. % [11,15]. The average grain size of graphene-wrapped $LiFePO_4$ particles estimated from the Scherrer equation (Fig. A.1-8) was ~80 nm [11-13], which is consistent with the size distribution of graphene-wrapped $LiFePO_4$ grains from the SEM images, as shown in Fig. A.1-9. When compared with $LiFePO_4$ particles synthesized without GO (~400 nm), the size of graphene-wrapped $LiFePO_4$ particles was smaller (Fig. A.1-7 and Table A.1-1). These results confirm that even small amount of graphene layer (~1.7 wt. %) successfully prevent the growth of $LiFePO_4$ nanoparticles during the annealing process.

Sample	C [wt. %]	Grain Size [nm]
Bare $LiFePO_4$	-	~400 (from SEM)
***c*-$LiFePO_4$/G**	2.1	~400 (from SEM)
$LiFePO_4$/G	1.7	83 ± 10 (from XRD) 67 ± 25 (from SEM)

Table A.1-1 Carbon content and grain size of the bare $LiFePO_4$, graphene-wrapped commercial $LiFePO_4$, and graphene-wrapped $LiFePO_4$.

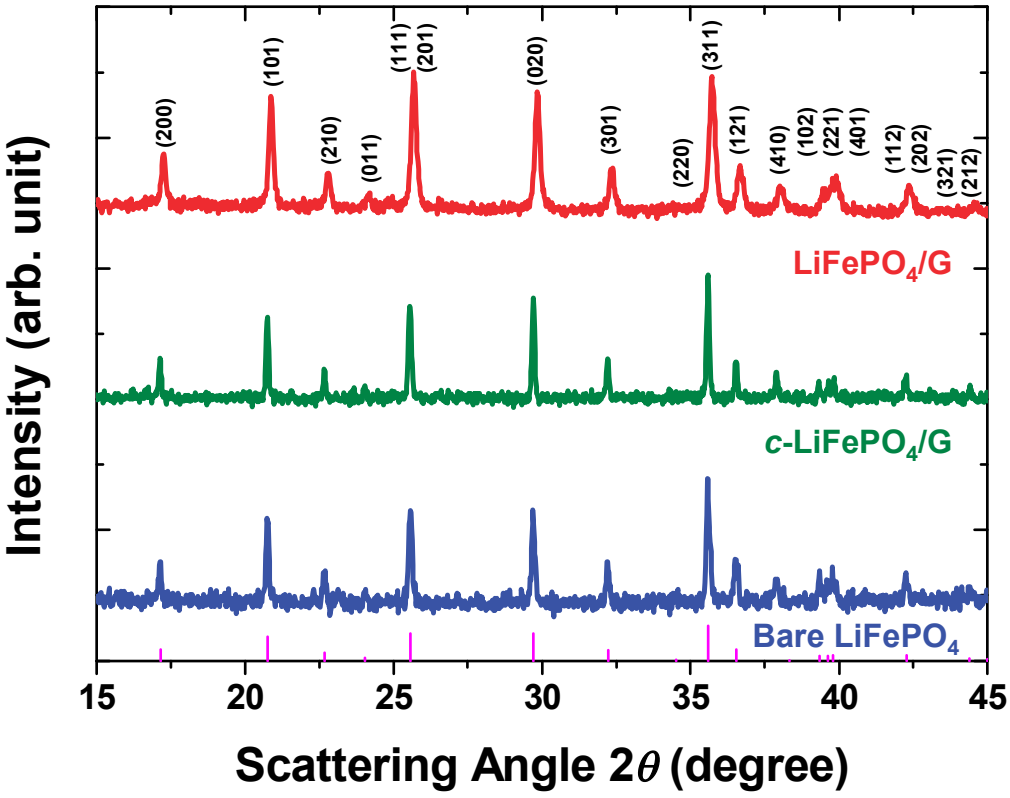

Fig. A.1-8. (Color) XRD patterns of the bare $LiFePO_4$, graphene-wrapped commercial $LiFePO_4$, and graphene-wrapped $LiFePO_4$. The ideal peak positions and intensities for $LiFePO_4$ (JCPDS #40-1499) are marked at the bottom.

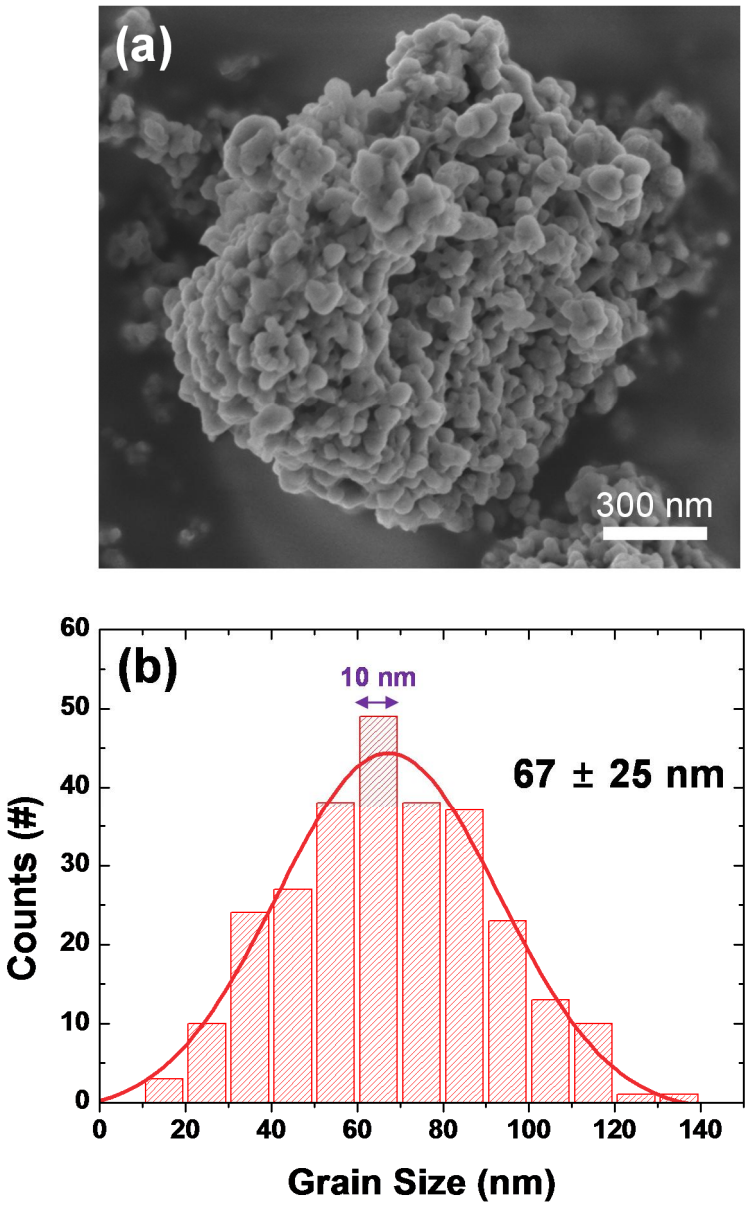

Fig. A.1-9. (a) SEM image of the graphene-eliminated $LiFePO_4$, and (b) grain-size distribution of the graphene-wrapped $LiFePO_4$.

In order to investigate the battery performance of the graphene-wrapped $LiFePO_4$ and the effect of the graphene layers, the bare $LiFePO_4$, graphene-wrapped commercial $LiFePO_4$ (*c*-$LiFePO_4$/G), and graphene-wrapped $LiFePO_4$ ($LiFePO_4$/G) were cycled at various current densities (sequentially from 0.1 C to 10 C) (Figs. A.1-10(a-c)). The battery performance of the bare $LiFePO_4$ was very poor due to the low electronic conductance and the large grain size (~400 nm), and the agglomeration of the active particles leading to reduction of the exposed surfaces to the liquid electrolyte (Figs. 1.2-7(a-b)). Even at a discharge rate of 0.1 C, the bare $LiFePO_4$ showed a low capacity less than 50 mAh g^{-1} (Fig. A.1-10(a)), which is consistent with previous studies [34-36]. On the contrary, the formation of the surface-conducting layer (graphene) dramatically improved the capacity of both the commercial and synthesized $LiFePO_4$. Particularly, the $LiFePO_4$/G samples showed much better rate capability than that of the *c*-$LiFePO_4$/G with distinguishable features between them, as seen in Fig. A.1-10(d). The discharge capacity of $LiFePO_4$/G at a discharge rate of 0.1 C was ~165 mAh g^{-1} (~97% of the theoretical capacity), and a specific capacity of ~100 mAh g^{-1} could be retained at a 10-C rate (~60% of the capacity at a rate of 0.1 C). In comparison with the excellent performance of $LiFePO_4$/G, the discharge capacity of *c*-$LiFePO_4$/G at a rate of 10 C was ~30 mAh g^{-1} (~30% of the initial capacity at a rate of 0.1 C). The degree of polarization in the voltage profile is much less significant for $LiFePO_4$/G whereas *c*-$LiFePO_4$/G shows high polarization resistance with a limited flat-potential region (Figs. A.1-10(b-c)). When the cycling performance of the $LiFePO_4$/G was investigated at a rate of 1 C (Fig. A.1-11), the $LiFePO_4$/G still delivered a discharge capacity of ~115 mAh g^{-1} after 500 cycles which is about 86% of the initial capacity. The $LiFePO_4$/G has high specific capacity and excellent rate

capability under fast discharging conditions, and this remarkable performance is attributed to the well-connected electron percolation among the $LiFePO_4$ nanoparticles via the graphene sheets. Comparison of this superior rate capability of the $LiFePO_4$/G with those of the previously-reported graphene-wrapped $LiFePO_4$ (Fig. A.1-12) [21-26] indicates that the $LiFePO_4$/G outperforms the others, or at least, it is competitive amongst other graphene-wrapped $LiFePO_4$.

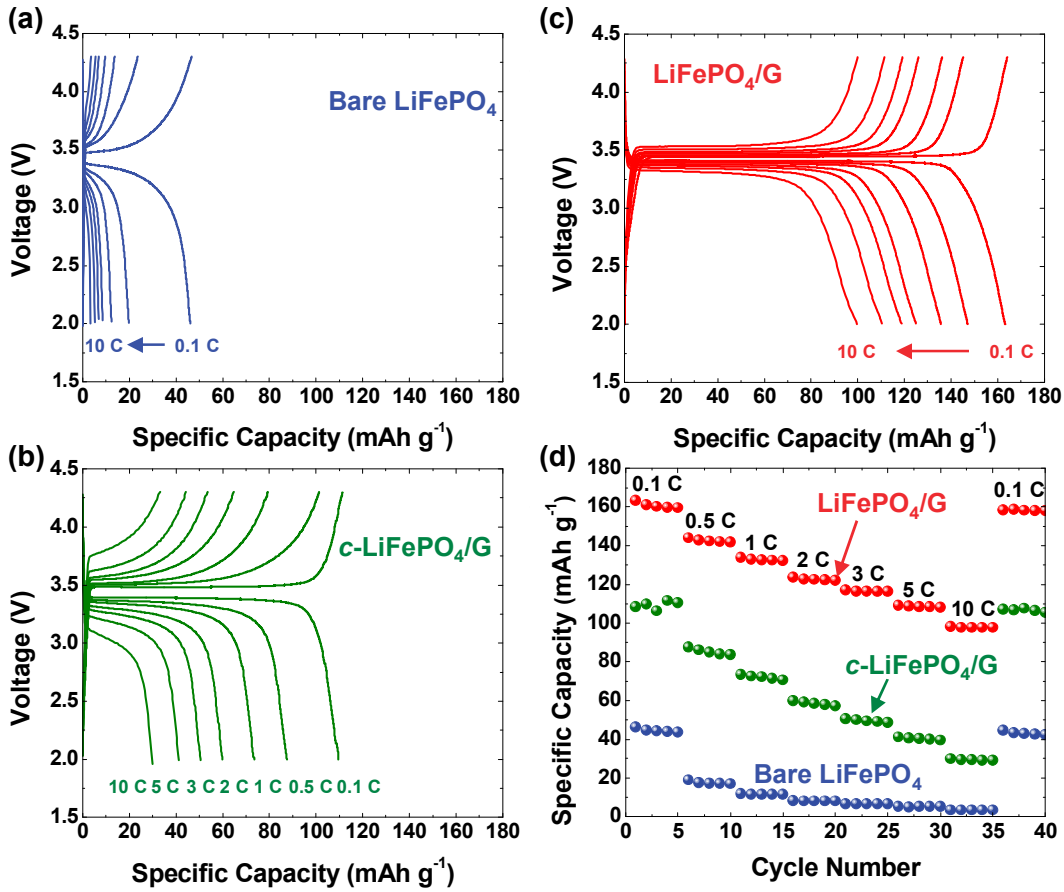

Fig. A.1-10. (Color) Charge-discharge curves of the (a) bare $LiFePO_4$, (b) graphene-wrapped commercial $LiFePO_4$, and (c) graphene-wrapped $LiFePO_4$. (d) Rate capability of the bare $LiFePO_4$, graphene-wrapped commercial $LiFePO_4$, and graphene-wrapped $LiFePO_4$ (1 C = 170 mA g^{-1}).

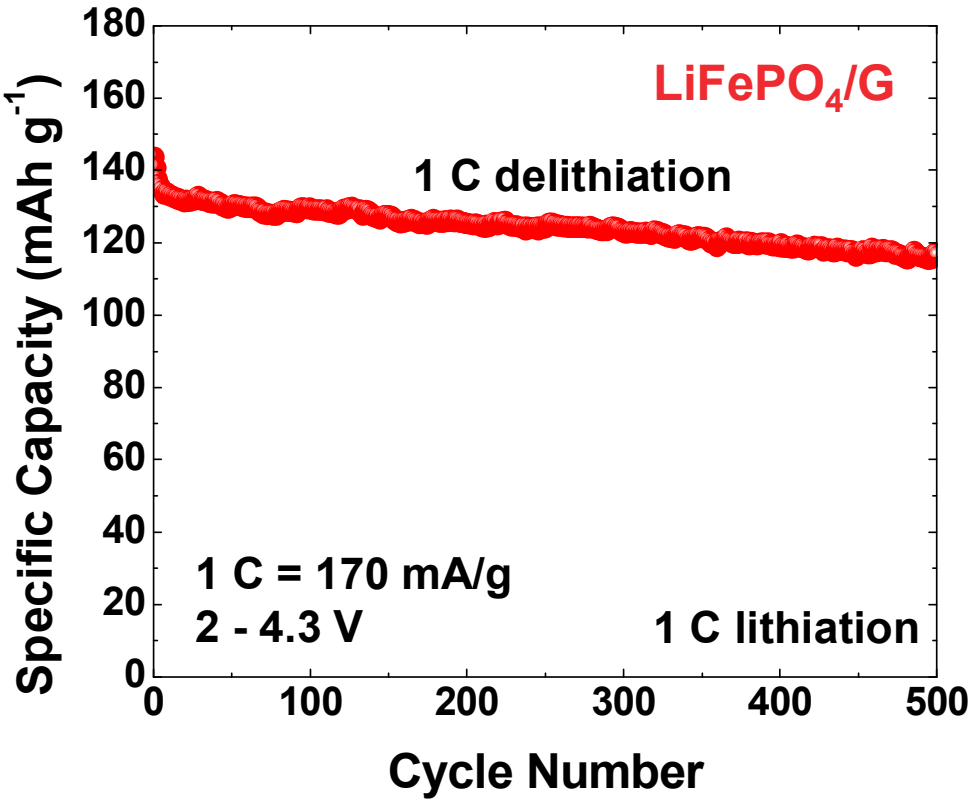

Fig. A.1-11. (Color) Cycling performance of graphene-wrapped $LiFePO_4$ at a rate of 1 C.

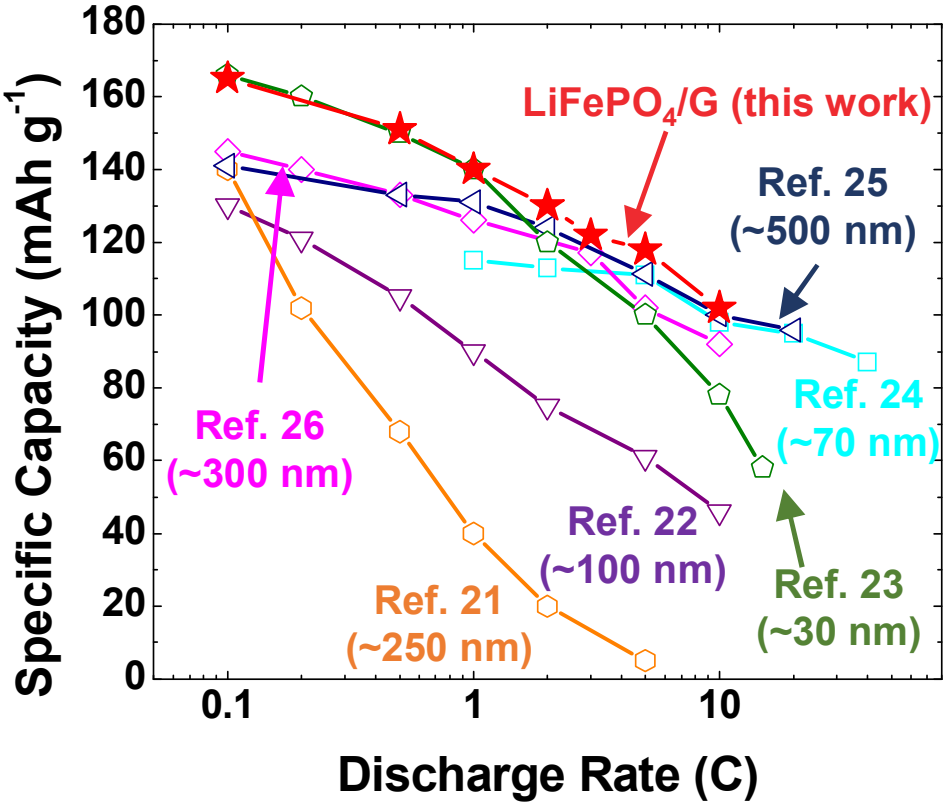

Fig. A.1-12. (Color) Comparison of the rate capability between this study and typical graphene-wrapped $LiFePO_4$.

The origin of the enhanced electrochemical properties for the $LiFePO_4$/G was identified by *in situ* electrochemical impedance spectroscopy (EIS). The EIS spectra were measured point by point at a rate of 0.1 C (Figs. A.1-13 and A.1-14). During lithiation/delithiation, the cell was switched off every hour to observe the EIS spectra at each open-circuit potential (OCP), in correspondence to the points marked by circles in the voltage profiles of Figs. A.1-13 and A.1-14. By fitting trace of the spectra, the charge-transfer resistances and apparent Li^+ diffusivities were derived, and plotted in Fig. A.1-15.

As shown in Fig. A.1-15(a), the charge-transfer resistance (R_{ct}) of both the $LiFePO_4$/G and the *c*-$LiFePO_4$/G progressively increased with the depth of charge (delithiation), as reported by Delacourt *et al* [37]. The differences in values of R_{ct} were noticeable between the two which are prepared by different wrapping methods. Provided that electrolyte/electrode interfaces of the two electrodes are assumed to be the same (electrolyte/graphene), the enhanced charge transfer of $LiFePO_4$/G can be attributed to the well-established electronic percolation of the electrode by the *in situ* confinement of $LiFePO_4$ within graphene. On the contrary, the possible contact resistance between *c*-$LiFePO_4$/G particles, as already described in Fig. A.1-2, impedes the transport of electrons, the result of which is reflected in the greater R_{ct} value. Upon lithiation, the charge transfer resistance of $LiFePO_4$/G decreases down to R_{ct} value at the pristine state, while that of the *c*-$LiFePO_4$/G could not recover to its original R_{ct} value (Tables A.1-2 and A.1-3). It is possible that some of the *c*-$LiFePO_4$/G loses contact with graphene when the volume of the $LiFePO_4$ lattice shrinks by ~6.8% on delithiation [2]. Obviously, the reversibility of R_{ct} for $LiFePO_4$/G might come from the well-defined 3D graphene network that tightly

encloses each nanoparticle.

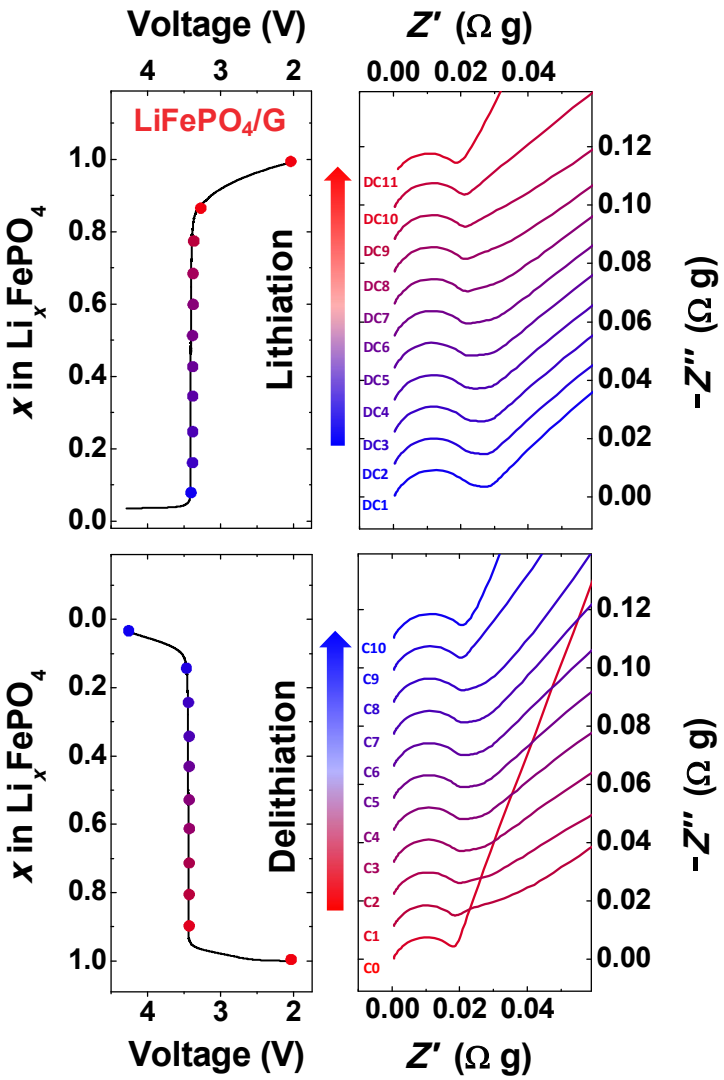

Fig. A.1-13. (Color) The *in situ* impedance analysis results of graphene-wrapped $LiFePO_4$ at different state of charge (delithiation) and discharge (lithiation). It should be noted that different scales are used on both axes of the Nyquist plots for graphene-wrapped $LiFePO_4$ and graphene-wrapped commercial $LiFePO_4$. The circles in the voltage profiles indicate the intervals of impedance analysis.

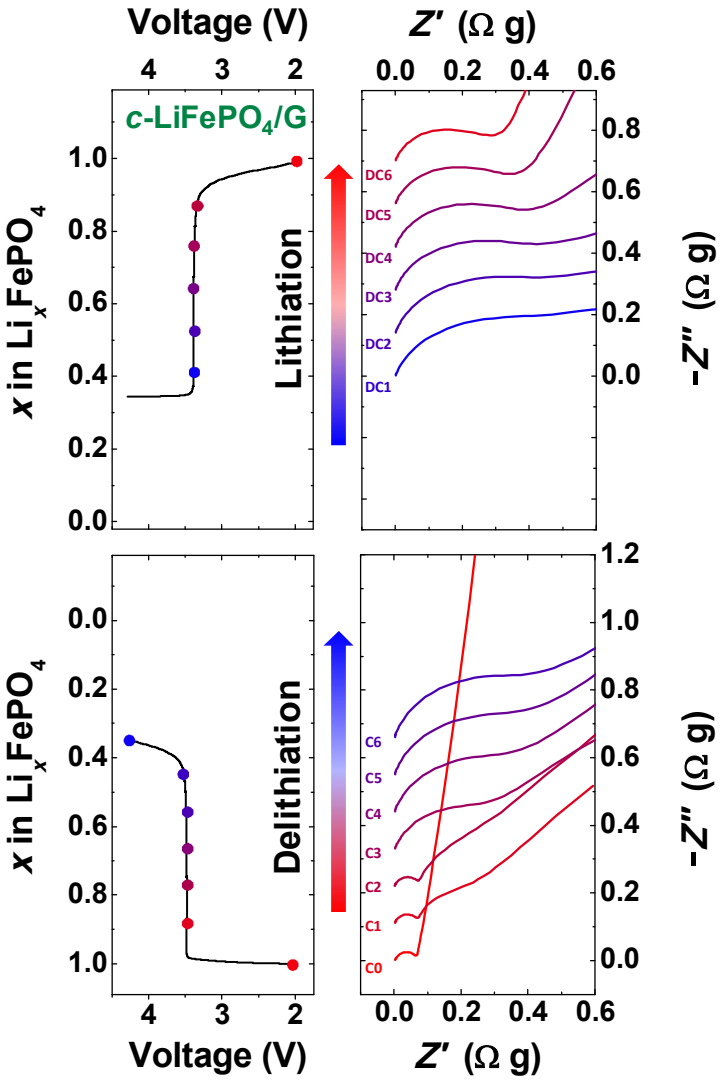

Fig. A.1-14. (Color) The *in situ* impedance analysis results of graphene-wrapped commercial $LiFePO_4$ at different state of charge (delithiation) and discharge (lithiation). It should be noted that different scales are used on both axes of the Nyquist plots for graphene-wrapped $LiFePO_4$ and graphene-wrapped commercial $LiFePO_4$. The circles in the voltage profiles indicate the intervals of impedance analysis.

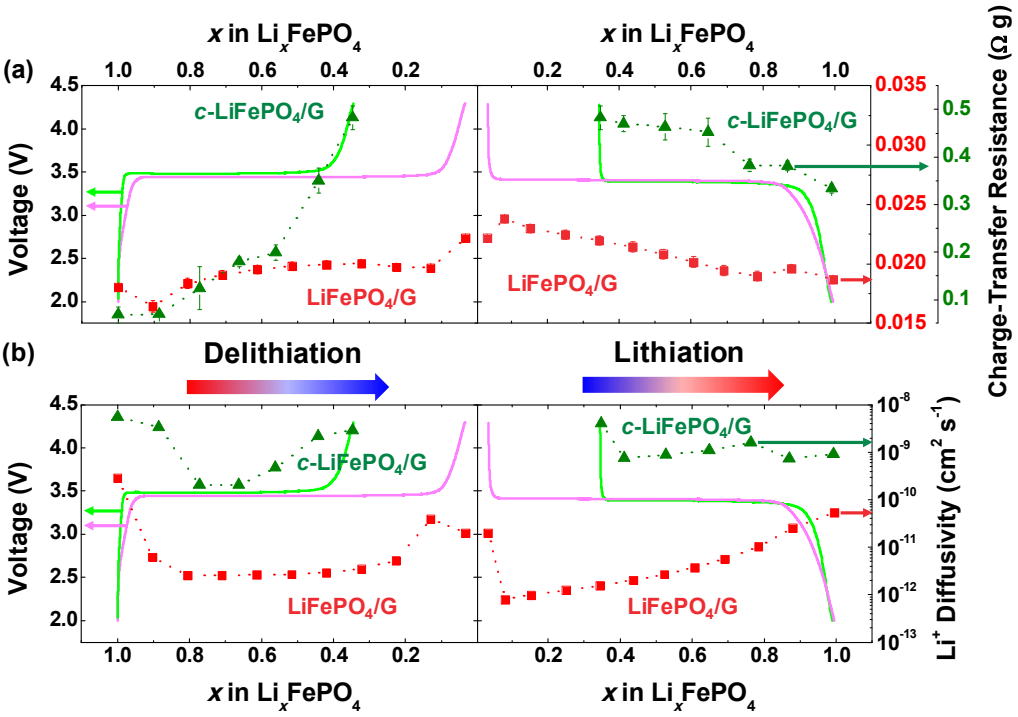

Fig. A.1-15. (Color) (a) Charge-transfer resistance and (b) apparent Li^+ diffusivity of graphene-wrapped $LiFePO_4$ and graphene-wrapped commercial $LiFePO_4$ at different state of charge (delithiation) and discharge (lithiation). Different scales on the axis should be noted for charge-transfer resistance. The red and green solid lines represent the voltage profiles of the graphene-wrapped $LiFePO_4$ and graphene-wrapped commercial $LiFePO_4$, respectively.

In order to identify whether enhanced electronic conductance was the main contributor to the superior electrochemical properties of $LiFePO_4$/G, the Li^+ diffusivity (D_{EIS}) within the olivine structure of the $LiFePO_4$/G and *c*-$LiFePO_4$/G was estimated according to the Warburg equation (Eq. A.1-1) [38]:

$$D_{Li} = \left(\frac{R^2 T^2}{2A^2 n^4 F^4 C_{Li}{}^2 \sigma^2} \right), \quad (1)$$

where D_{Li} is the diffusion coefficient ($cm^2\ s^{-1}$) of Li in the low-frequency ($\leq 10^1$ Hz) region, A is the surface area of the electrode ($cm^2\ g^{-1}$), n is the number of electrons, F is the Faraday constant (96485 C mol^{-1}), C_{Li} is the concentration of Li^+ (mol cm^{-3}), and σ is the Warburg factor obtained from the slope of the lines between the real axis Z' and the reciprocal square root of the lower angular frequencies $\omega^{-1/2}$ ($Z' = R_s + R_{ct} + \sigma\ \omega^{-1/2}$).

As seen in Fig. A.1-15(b), a trend was apparent in the D_{EIS} value profile along the delithiation depth for both $LiFePO_4$/G and *c*-$LiFePO_4$/G: the trend shows that the D_{EIS} value initially decreases, but rises back at the last stage of delithiation [39]. Since the diffusion of Li in $LiFePO_4$, which occurs through the <010> direction, is hindered when the volume of $LiFePO_4$ shrinks by ~6.8% upon delithiation, the changes over the state of charge could be attributed to the coupling of the Li^+ diffusion and the movement of two-phase boundary [40]. In addition, the last stage of (de)lithiation that occurs through the solid solution reaction accounts for the abrupt increase in Li^+ diffusivity at deep (dis)charged state [2,40].

The absolute D_{EIS} values are approximately two orders of magnitude higher for *c*-$LiFePO_4$/G than that for $LiFePO_4$/G. Even though the $LiFePO_4$/G has a shorter Li^+

diffusion path because of its relatively-small grain size (Table A.1-1), overall higher Li^+ diffusivity of *c*-$LiFePO_4$/G shall be rooted from the higher crystallinity of the commercial $LiFePO_4$. Since the solid state of Li^+ diffusion in $LiFePO_4$ lattice is governed by $t = L^2 D^{-1}$, crystallinity of the commercial $LiFePO_4$ compromises the Li diffusion time to be comparable to that of the $LiFePO_4$/G. Hence, this comparative study indicates that the influence of solid-state diffusion of Li^+ on the rate capabilities of the two samples is less significant. Instead, it can be concluded that the superior electrochemical performance of $LiFePO_4$/G to *c*-$LiFePO_4$/G mainly results from the boosted charge (especially electron) transfer that is rendered by the well-percolated conductive graphene network.

Parameters	R_{ct} [Ω g]	Warburg factor σ	D_{Li} [$\times 10^{-10}$ cm^2 s^{-1}]
***c*-LiFePO$_4$/G (C0)**	0.068 ± 0.017	0.289 ± 0.005	55.3
***c*-LiFePO$_4$/G (C1)**	0.069 ± 0.001	0.226 ± 0.003	33.9
***c*-LiFePO$_4$/G (C2)**	0.124 ± 0.045	0.055 ± 0.001	2.0
***c*-LiFePO$_4$/G (C3)**	0.179 ± 0.009	0.056 ± 0.002	2.0
***c*-LiFePO$_4$/G (C4)**	0.199 ± 0.016	0.008 ± 0.001	4.7
***c*-LiFePO$_4$/G (C5)**	0.349 ± 0.026	0.182 ± 0.007	21.8
***c*-LiFePO$_4$/G (C6)**	0.483 ± 0.003	0.211 ± 0.003	29.1
***c*-LiFePO$_4$/G (D1)**	0.483 ± 0.003	0.211 ± 0.003	29.1
***c*-LiFePO$_4$/G (D2)**	0.471 ± 0.016	0.107 ± 0.008	7.6
***c*-LiFePO$_4$/G (D3)**	0.464 ± 0.027	0.116 ± 0.007	8.9
***c*-LiFePO$_4$/G (D4)**	0.453 ± 0.029	0.129 ± 0.005	10.9
***c*-LiFePO$_4$/G (D5)**	0.383 ± 0.012	0.137 ± 0.001	12.3
***c*-LiFePO$_4$/G (D6)**	0.382 ± 0.011	0.136 ± 0.001	12.1
***c*-LiFePO$_4$/G (D7)**	0.334 ± 0.009	0.152 ± 0.005	15.2

Table A.1-2 Impedance parameters extracted using a modified Randles' equivalent circuit for the *c*-LiFePO$_4$/G. In Randles' circuit, R_s (series resistance) represents the high-frequency resistance of the electrolyte. CPE_{dl} (constant phase element) reflects imperfect capacitance of the electrochemical double layer between the electrolyte and electrode. R_{ct} (charge-transfer resistance) is associated with the ion injection and the electron transfer from the electrolyte into the electrode. Z_w is the Warburg impedance.

Parameters	R_{ct} [Ω g]	Warburg factor σ	D_{Li} [$\times 10^{-10}$ cm^2 s^{-1}]
$LiFePO_4$/G (C0)	0.0181 ± 0.0001	0.04652 ± 0.00133	143
$LiFePO_4$/G (C1)	0.0164 ± 0.0005	0.00687 ± 0.00014	3.1
$LiFePO_4$/G (C2)	0.0184 ± 0.0003	0.00621 ± 0.00058	2.5
$LiFePO_4$/G (C3)	0.0191 ± 0.0003	0.00625 ± 0.00014	2.6
$LiFePO_4$/G (C4)	0.0195 ± 0.0003	0.00629 ± 0.00035	2.6
$LiFePO_4$/G (C5)	0.0198 ± 0.0003	0.00638 ± 0.00052	2.7
$LiFePO_4$/G (C6)	0.0199 ± 0.0003	0.00665 ± 0.00072	2.9
$LiFePO_4$/G (C7)	0.0201 ± 0.0003	0.00731 ± 0.00079	3.5
$LiFePO_4$/G (C8)	0.0197 ± 0.0003	0.00892 ± 0.00093	5.2
$LiFePO_4$/G (C9)	0.0197 ± 0.0002	0.02432 ± 0.00023	38.5
$LiFePO_4$/G (C10)	0.0222 ± 0.0002	0.01744 ± 0.00141	20.1
$LiFePO_4$/G (D1)	0.0222 ± 0.0002	0.01744 ± 0.00141	20.1
$LiFePO_4$/G (D2)	0.0181 ± 0.0001	0.00348 ± 0.00003	0.8
$LiFePO_4$/G (D3)	0.0164 ± 0.0005	0.00388 ± 0.00004	0.9
$LiFePO_4$/G (D4)	0.0184 ± 0.0003	0.00433 ± 0.00004	1.2
$LiFePO_4$/G (D5)	0.0191 ± 0.0003	0.00487 ± 0.00003	1.6
$LiFePO_4$/G (D6)	0.0195 ± 0.0003	0.00554 ± 0.00002	2.1
$LiFePO_4$/G (D7)	0.0198 ± 0.0003	0.00637 ± 0.00002	2.7
$LiFePO_4$/G (D8)	0.0199 ± 0.0003	0.00753 ± 0.00003	3.7
$LiFePO_4$/G (D9)	0.0201 ± 0.0003	0.00931 ± 0.00006	5.7
$LiFePO_4$/G (D10)	0.0197 ± 0.0003	0.01248 ± 0.00009	10.3
$LiFePO_4$/G (D11)	0.0197 ± 0.0002	0.01965 ± 0.00003	25.4

Table A.1-3 Impedance parameters extracted using a modified Randles' equivalent circuit for the $LiFePO_4$/G.

A.1.4. Conclusions

The graphene-wrapped $LiFePO_4$ ($LiFePO_4$/G) composites were synthesized by a simple solid-state reaction from graphene-wrapped $FePO_4$ and lithium acetate. The $LiFePO_4$/G had a specific capacity of ~100 mAh g^{-1} even at a rate of 10 C. The enhanced electrochemical performance arose from the graphene sheets' well-established framework, percolating through all of the $LiFePO_4$ nanoparticles, which is confirmed by the reduced charge-transfer resistance. This effective cathode design could also be extended to other electrode materials, which promises to promote the development of next-generation Li-ion batteries.

A.1.5. References

1. A. K. Padhi, K. S. Nanjundaswamy and J. B. Goodenough, Phospho-Olivines as Positive-Electrode Materials for Rechargeable Lithium Batteries. *J. Electrochem. Soc.* **1997**, 144, 1188-1194.
2. Y. S. Yu, C. Kim, D. A. Shapiro, M. Farmand, D. Qian, T. Tyliszczak, A. L. D. Kilcoyne, R. Celestre, S. Marchesini, J. Joseph, P. Denes, T. Warwick, F. C. Strobridge, C. P. Grey, H. Padmore, Y. S. Meng, R. Kostecki and J. Cabana, Dependence on Crystal Size of the Nanoscale Chemical Phase Distribution and Fracture in Li_xFePO_4. *Nano Lett.* **2015,** 15, 4282-4288.
3. M. S. Whittingham, Lithium Batteries and Cathode Materials. *Chem. Rev.* **2004**, 104, 4271-4302.
4. J.-M. Tarascon and M. Armand, Issues and Challenges Facing Rechargeable Lithium Batteries. *Nature* **2001**, 414, 359-367.
5. M. Armand and J.-M. Tarascon, Building Better Batteries. *Nature* **2008**, 451, 652-657.
6. B. Ellis, W. H. Kan, W. R. M. Makahnouk and L. F. Nazar, Synthesis of Nanocrystals and Morphology Control of Hydrothermally Prepared LiFePO4. *J. Mater. Chem.* **2007**, 17, 3248-3254.
7. L. Cheng, J. Yan, G. N. Zhu, J. Y. Luo, C. X. Wang and Y. Y. Xia, General Synthesis of Carbon-Coated Nanostructure $Li_4Ti_5O_{12}$ as a High Rate Electrode Material for Li-Ion Intercalation. *J. Mater. Chem.* **2010**, 20, 595-602.
8. J. Cho, J. G. Lee, B. Kim and B. Park, Effect of P_2O_5 and $AlPO_4$ Coating on $LiCoO_2$ Cathode Material. *Chem. Mater*. **2003**, 15, 3190-3193.

9. S. Wi, J. Kim, S. Lee, J. Kang, K. H. Kim, K. Park, K. Kim, S. Nam, C. Kim, and B. Park, Synthesis of $LiMn_{0.8}Fe_{0.2}PO_4$ Mesocrystals for High-Performance Li-Ion Cathode Materials. *Electrochim. Acta* **2016**, 216, 203.
10. E. Lee, A. Murthy and A. Manthiram, Carbon-Supported Pt Nanoparticles Prepared by a Modified Borohydride Reduction Method: Effect on the Particle Morphology and Catalytic Activity for CO_{ad} and Methanol Electro-Oxidation. *Electrochem. Commun.* **2011**, 13, 480-483.
11. S. Wi, S. Nam, Y. Oh, J. Kim, H. Choi, S. Hong, S. Byun, S. Kang, D. J. Choi, K. Ahn, Y.-H. Kim and B. Park, Facile Synthesis of Porous-Carbon/$LiFePO_4$ Nanocomposites. *J. Nanopart. Res.* **2012**, 14, 1327.
12. H. H. Park, R. Heasley, L. Sun, V. Steinmann, R. Jaramillo, K. Hartman, R. Chakraborty, P. Sinsermsuksakul, D. Chua, T. Buonassisi and R. G. Gordon, Co-Optimization of SnS Absorber and Zn(O,S) Buffer Materials for Improved Solar cells. *Prog. Photovolt.* **2015**, 23, 901-908.
13. T. Hwang, D. Cho, J. Kim, J. Kim, S. Lee, B. Lee, K. H. Kim, S. Hong, C. Kim and B. Park, Investigation of Chlorine-Mediated Microstructural Evolution of $CH_3NH_3PbI_3(Cl)$ Grains for High Optoelectronic Responses, *Nano Energy*, **2016**, 25, 91-99.
14. J. S. Park, X. Meng, J. W. Elam, S. Hao, C. Wolverton, C. Kim and J. Cabana, Ultrathin Lithium-Ion Conducting Coatings for Increased Interfacial Stability in High Voltage Lithium-Ion Batteries, *Chem. Mater.*, **2014**, 26, 3128-3134
15. S. Nam, S. Kim, S. Wi, H. Choi, S. Byun, S.-M. Choi, S.-L. Yoo, K. T. Lee and B. Park, The Role of Carbon Incorporation in SnO_2 Nanoparticles for Li Rechargeable Batteries. *J. Power. Sources* **2012**, 211, 154-160.

16. B. L. Ellis, W. R. Makahnouk, Y. Makimura, K. Toghill and L. F. Nazar, A Multifunctional 3.5 V Iron-Based Phosphate Cathode for Rechargeable Batteries**.** *Nat. Mater.* **2007**, 6, 749-753**.**
17. S. Y. Chung, J. T. Bloking and Y.-M. Chiang, Electronically Conductive Phospho-Olivines as Lithium Storage Electrodes. *Nat. Mater*. **2002**, 1, 123-128.
18. Y. Oh, S. Nam, S. Wi, J. Kang, T. Hwang, S. Lee, H. H. Park, J. Cabana, C. Kim and B. Park, Effective Wrapping of Graphene on Individual $Li_4Ti_5O_{12}$ Grains for High-Rate Li-Ion Batteries. *J. Mater. Chem. A* **2014**, 2, 2023-2027.
19. Y. Hwa, J. Zhao and E. J. Cairns, Lithium Sulfide (Li_2S)/Graphene Oxide Nanospheres with Conformal Carbon Coating as a High-Rate, Long-Life Cathode for Li/S Cells. *Nano Lett.* **2015**, 15, 34793-486.
20. S. Nam, S. J. Yang, S. Lee, J. Kim, J. Kang, J. Y. Oh, C. R. Park, T. Moon, K. T. Lee and B. Park, Wrapping SnO_2 with Porosity-Tuned Graphene as a Strategy for High-Rate Performance in Lithium Battery Anodes. *Carbon* **2015**, 85, 289-298.
21. C. Su, X. Bu, L. Xu, J. Liu and C. Zhang, A Novel $LiFePO_4$/Graphene/Carbon Composite as a Performance-Improved Cathode material for Lithium Ion Batteries. *Electrochim. Acta* **2012**, 64, 190-195.
22. J. Wang, Y. Xu, J. Zhu and P. Ren, Electrochemical in situ Polymerization of Reduced Graphene Oxide/Polypyrrole Composite with High Power Density. *J. Power Sources* **2012**, 208, 138-143.
23. J. Yang, J. Wang, Y. Tang, D. Wang, X. Li, Y. Hu, R. Li, G. Liang, T.-K. Sham and X. Sun, $LiFePO_4$-Graphene as a Superior Cathode Material for Rechargeable Lithium Batteries: Impact of Stacked Graphene and Unfolded Graphene. *Energy*

Environ. Sci. **2013**, 6, 1521-1528.

24. W.-B. Luo, S.-L. Chou, Y.-C. Zhai, H.-K. Liu, Self-Assembled Graphene and $LiFePO_4$ Composites with Superior High Rate Capability for Lithium Ion Batteries. *J. Mater. Chem. A* **2014**, 2, 4927-4931.
25. W. K. Kim, W. H. Ryu, D. W. Han, S. J. Lim, J. Y. Eom and H. S. Kwon, Fabrication of Graphene Embedded $LiFePO_4$ Using a Catalyst Assisted Self Assembly Method as a Cathode Material for High Power Lithium-Ion Batteries. *ACS Appl. Mater. Inter.* **2014**, 6, 4731-4736.
26. J. Ha, S.-K. Park, S.-H. Yu, A. Jin, B. Jang, S. Bong, I. Kim, Y.-E. Sung and Y. A. Piao, Chemically Activated Graphene-Encapsulated $LiFePO_4$ Composite for High Performance Lithium Ion Batteries. *Nanoscale* **2013**, 5, 8647-8655.
27. Y. Shi, S.-L. Chou, J.-Z. Wang, D. Wexler, H.-J. Li, H.-K. Liu and Y. Wu, Graphene Wrapped $LiFePO_4$/C Composites as Cathode Materials for Li-ion Batteries with Enhanced Rate Capability. *J. Mater. Chem.* **2012**, 22, 16465-16470.
28. W. S. Hummers and R. E. Offeman, Preparation of Graphitic Oxide. *J. Am. Chem. Soc.* **1958**, 80, 1339.
29. D. Wang, H. Li, Z. Wang, X. Wu, Y. Sun, X. Huang and L. Chen, New Solid-State Synthesis Routine and Mechanism for $LiFePO_4$ using LiF as Lithium Precursor. *Solid State Chem.*, 2004, **177**, 4582.
30. Y. Lin, M. X. Gao, D. Zhu, Y. F. Liu and H. G. Pan, Effects of Carbon Coating and Iron Phosphides on the Electrochemical Properties of $LiFePO_4$/C. *J. Power Sources*, 2008, **184**, 444.
31. J.-K. Kim, G. Cheruvally, J.-W. Choi, J.-U. Kim, J.-H. Ahn, G.-B. Cho, K.-W.

Kim and H.-J. Ahn, Effect of Mechanical Activation Process Parameters on the Properties of $LiFePO_4$ Cathode Material. *J. Power Sources*, 2007, **166**, 211.

32. Y. Zhang, F. Gao, B. Wanjala, Z. Li, G. Cernigliaro and Z. Gu, High Efficiency Reductive Degradation of a Wide Range of Azo Dyes by SiO_2-Co Core-Shell Nanoparticles. *Appl. Catal. B.*, 2016, **199**, 504.
33. S. Wang, Q. Cai, M. Du, J. Xue and H. Xu, Synthesis of 1D Silica Nanostructures with Controllable Sizes Based on Short Anionic Peptide Self-Assembly. *J. Phys. Chem. B*, 2015, **119**, 12059.
34. J. S. Chen, Z. Wang, X. S. Dong, P. Chen and X. W. Lou, Graphene-Wrapped TiO_2 Hollow Structures with Enhanced Lithium Storage Capabilities. *Nanoscale*, 2011, **3**, 2158.
35. Y.-T. Xu, Y. Guo, C. Li, X.-Y. Zhou, M. C. Tucker, X.-Z. Fu, R. Sun and C.-P. Wong, Graphene Oxide Nano-Sheets Wrapped Cu_2O Microspheres as Improved Performance Anode Materials for Lithium Ion Batteries. *Nano Energy*, 2015, **11**, 38.
36. H. Zhu, X. Wu, L. Zan and Y. Zhang, Three-Dimensional Macroporous Graphene-Li_2FeSiO_4 Composite as Cathode Material for Lithium-Ion Batteries with Superior Electrochemical Performances. *ACS Appl. Mater. Interfaces*, 2014, **6**, 11724.
37. C. Delacourt, L. Laffont, R. Bouchet, C. Wurm, J.-B. Lefiche, M. Morcrette, J.-M. Tarascon and C. Masquelier, Toward Understanding of Electrical Limitations (Electronic, Ionic) in $LiMPO_4$ (M = Fe, Mn) Electrode Materials. *J. Electrochem. Soc.* **2005**, 152, A913-A921.
38. D. D. Lecce and J. Hassoun, Lithium Transport Properties in $LiMn_{1-\alpha}Fe_{\alpha}PO_4$

Olivine Cathodes. *J. Phys. Chem. C* **2015**, 119, 20855-20863.

39. D. Li, X. Liu and H. Zhou, The Size-Dependent Phase Transition of $LiFePO_4$ Particles during Charging and Discharging in Lithium-Ion Batteries. *Energy Technol*. **2014**, 2, 542-574.
40. C. Delmas, M. Maccario, L. Croguennec, F. L. Cras and F. Weill, Lithium Deintercalation in $LiFePO_4$ Nanoparticles via a Domino-Cascade Model. *Nat. Mater.* **2008**, 7, 665-671.

A.2. List of Publications and Presentations

A.2.1. Publications (International):

1. **Sungun Wi**,[+] Jungjin Park,[+] Sangheon Lee, Joonhyeon Kang, Taehyun Hwang, Kug-Seung Lee, Han-Koo Lee, Seunghoon Nam, Chunjoong Kim,* Yung-Eun Sung,* and Byungwoo Park,* "Synchrotron-Based X-Ray Absorption Spectroscopy for the Electronic Structure of $Li_xMn_{0.8}Fe_{0.2}PO_4$ Mesocrystal in Li^+ Batteries,"
   Nano Energy **31**, 495 (2017)

2. **Sungun Wi**,[+] Jungjin Park,[+] Sangheon Lee, Jaewon Kim, Bumjin Gil, Jiwan Yun, Yung-Eun Sung,* and Byungwoo Park,* Chunjoong Kim,* " Insights on the Delithiation/Lithiation Reactions of $Li_xMn_{0.8}Fe_{0.2}PO_4$ Mesocrystal in Li-Ion Batteries by *In Situ* Techniques,"
   In Preperation for Nano Energy

3. **Sungun Wi**,[+] Kimin Park,[+] Sangheon Lee, Joonhyeon Kang, Joon-Phil Choi, Seunghoon Nam,* Chunjoong Kim,* and Byungwoo Park,* "Morphology Evolution of $LiMn_{0.8}Fe_{0.2}PO_4$ Mesocrystals for Advanced Cathode Materials in Lithium-Ion Batteries,"
   In Preperation for J. Mater. Chem. A

4. **Sungun Wi**,[+] Jaewon Kim,[+] Kimin Park,[+] Sangheon Lee, Joonhyeon Kang, Kyung Hwan Kim, Seunghoon Nam,* Chunjoong Kim* and Byungwoo Park,* "Evaluation of Graphene-Wrapped $LiFePO_4$ as Novel Cathode Materials for Li-Ion Batteries,"
RSC Adv. **6**, 105081 (2016)

5. **Sungun Wi**, Jaewon Kim, Sangheon Lee, Joonhyeon Kang, Kyung Hwan Kim, Kimin Park, Kunsu Kim, Seunghoon Nam,* Chunjoong Kim,* and Byungwoo Park,* "Synthesis of $LiMn_{0.8}Fe_{0.2}PO_4$ Mesocrystals for High-Performance Li-Ion Cathode Materials,"
Electrochim. Acta **216**, 203 (2016).

6. **Sungun Wi**,[+] Hyungsub Woo,[+] Sangheon Lee, Joonhyeon Kang, Jaewon Kim, Subin An, Chohui Kim, Seunghoon Nam, Chunjoong Kim, and Byungwoo Park,* "Reduced Graphene Oxide/Carbon Double-Coated 3-D Porous ZnO Aggregates as High-Performance Li-Ion Anode Materials."
Nanoscale Res. Lett. **10**, 204 (2015).

7. **Sungun Wi**, Jaewon Kim, Seunghoon Nam, Joonhyeon Kang, Sangheon Lee, Hyungsub Woo, Moosang Lee, Chong Ho Sonu, Taeho Moon,* and Byungwoo Park,* "Enhanced Rate Capability of $LiMn_{0.9}Mg_{0.1}PO_4$ Nanoplates by Reduced Graphene Oxide/Carbon Double Coating for Li-Ion Batteries."
Curr. Appl. Phys. **14**, 725 (2014).

8. **Sungun Wi**, Seunghoon Nam, Yuhong Oh, Jongmin Kim, Hongsik Choi, Saeromi Hong, Sujin Byun, Suji Kang, Dong Joo Choi, Key-one Ahn, Young-Ho Kim,* and Byungwoo Park,* "Facile Synthesis of Porous-Carbon/$LiFePO_4$ Nanocomposites,"
J. Nanopart. Res. **14**, 1327 (2012).

9. Jaewon Kim,[+] Kyung Eun Lee,[+] Kyung Hwan Kim, **Sungun Wi**, Sangheon Lee, Seunghoon Nam, Chunjoong Kim,* Sang Ouk Kim,* and Byungwoo Park,* "Single-Layer Graphene-Wrapped $Li_4Ti_5O_{12}$ Anode with Superior Lithium Storage Capability,"
Carbon **114**, 275 (2017).

10. Yuhong Oh,[+] Seunghoon Nam,[+] **Sungun Wi**, Joonhyeon Kang, Taehyun Hwang, Sangheon Lee, Helen Hejin Park, Jordi Cabana, Chunjoong Kim,[*] and Byungwoo Park,[*] "Effective Wrapping of Graphene on Individual $Li_4Ti_5O_{12}$ Grains for High-Rate Li-Ion Batteries,"
J. Mater. Chem. A **2**, 2023 (2013).

11. Joonhyeon Kang, Seunghoon Nam, Yuhong Oh, Hongsik Choi, **Sungun Wi**, Byungho Lee, Taehyun Hwang, Saeromi Hong, and Byungwoo Park,[*] "Electronic Effect in Methanol Dehydrogenation on Pt Surfaces: Potential Control during Methanol Electrooxidation,"
J. Phys. Chem. Lett. **4**, 2931 (2013).

12. Seung Jae Yang, Seunghoon Nam, Taehoon Kim, Ji Hyuk Im, Haesol Jung, Jong Hun Kang, **Sungun Wi**, Byungwoo Park, and Chong Rae Park,* "Preparation and Exceptional Lithium Anodic Performance of Porous Carbon-Coated ZnO Quantum Dots Derived from a Metal Organic Framework,"
J. Am. Chem. Soc. **135**, 7394 (2013).

13. Seunghoon Nam,+ Sungsoo Kim,+ **Sungun Wi**, Hongsik Choi, Sujin Byun, Soon-Mi Choi, Sang-Im Yoo, Kyu Tae Lee,* and Byungwoo Park,* "The Role of Carbon Incorporation in SnO_2 Nanoparticles for Li Rechargeable Batteries,"
J. Power Sources **211**, 154 (2012).

14. Seunghoon Nam, **Sungun Wi**, Changwoo Nahm, Hongsik Choi, and Byungwoo Park,* "Challenges in Synthesizing Carbon-Coated $LiFePO_4$ Nanoparticles from Hydrous $FePO_4$ and Their Electrochemical Properties,"
Mater. Res. Bull. **47**, 3495 (2012).

15. Yuhong Oh,* Seunghoon Nam, **Sungun Wi**, Saeromi Hong, and Byungwoo Park,* "Review Paper: Nanoscale Interface Control for High-Performance Li-Ion Batteries,"
Electron. Mater. Lett. **8**, 91 (2012).

A.2.2. Presentations (International):

1. **Sungun Wi**, Joonhyeon Kang, Jaewon Kim, Hyungsub Woo, Sangheon Lee, and Byungwoo Park, " Reduced Graphene Oxide/Carbon Double-Coated 3-D Porous $LiMn_{0.8}Fe_{0.2}PO_4$ Aggregates as High-Rate Cathode Materials for Li-Ion Battery,"
   Materials Research Society (MRS) Spring Meeting, San Francisco, CA, April 2015.
   [**Poster by S. Wi**]

2. **Sungun Wi**, Seunghoon Nam, Joonhyeon Kang, Jaewon Kim, Hyungsub Woo, and Byungwoo Park, " Reduced Graphene Oxide/Carbon Double-Coated 3-D Porous $LiMn_{0.8}Fe_{0.2}PO_4$ Aggregates as High-Rate Cathode Materials for Li-Ion Battery,"
   International Conference on Electronic Materials and Nanotechnology for Green Environment (ENGE2014), Jeju, Korea, November 16-19, 2014.
   [**Oral by S. Wi**]

3. Yuhong Oh, Seunghoon Nam, **Sungun Wi**, Joonhyeon Kang, Taehyun Hwang, Sangheon Lee, and Byungwoo Park, "Inexpensive Wrapping of Graphene on Individual $Li_4Ti_5O_{12}$ Grains for Superior-Rate Li-Ion Batteries,"
   The 9th Tsinghua University - University of Tokyo - Seoul National University Student Workshop, Seoul, Korea, October 9-12, 2013.
   [**Oral by S. Wi**]

4. **Sungun Wi**, Seunghoon Nam, Yuhong Oh, Chohui Kim, Saeromi Hong, and Byungwoo Park, "Graphene/Carbon Double-Coated ZnO Aggregates as High-Rate Electrode Material for Li-Ion Battery,"
Materials Research Society (MRS) Fall Meeting, Boston, MA, November 2012.
[**Poster by S. Wi**]

5. **Sungun Wi**, Seunghoon Nam, Yuhong Oh, Chohui Kim, Saeromi Hong, Suji Kang, and Byungwoo Park, "Graphene/Carbon Double-Coated ZnO Aggregates as High-Rate Electrode Material for Li-Ion Battery,"
The 13th Korea - Japan Student Symposium (Seoul National University - Tohoku University), Seoul, Korea, November 2012.
[**Oral by S. Wi**]

6. Yuhong Oh, Seunghoon Nam, **Sungun Wi**, Saeromi Hong, and Byungwoo Park, "Graphene-Wrapped $Li_4Ti_5O_{12}$ Anode Materials with High-Rate Capability for Li-Ion Batteries,"
Materials Research Society (MRS) Fall Meeting, Boston, MA, November 2012.
[**Poster by S. Wi**]

7. Seunghoon Nam, Sungsoo Kim, **Sungun Wi**, Hongsik Choi, Sujin Byun, and Byungwoo Park, "The Role of Carbon Incorporation in SnO_2 Nanoparticles for Li Rechargeable Batteries,"

Materials Research Society (MRS) Fall Meeting, Boston, MA, November 2012. [**Poster by S. Wi**]

8. Seunghoon Nam, **Sungun Wi**, Yuhong Oh, Saeromi Hong, Hyungsub Woo, Jaewon Kim, Sangheon Lee, Taehyun Hwang, Hongsik Choi, and Byungwoo Park, "Porous Graphene as a Smart Strategy for Wrapping SnO_2," *Materials Research Society (MRS) Fall Meeting*, Boston, MA, December 2013.

9. Yuhong Oh, Seunghoon Nam, **Sungun Wi**, Joonhyeon Kang, Taehyun Hwang, Sangheon Lee, Jordi Cabana, Chunjoong Kim, and Byungwoo Park, "Inexpensive Wrapping of Graphene on Individual $Li_4Ti_5O_{12}$ Grains for Superior-Rate Li-Ion Batteries," *Materials Research Society (MRS) Fall Meeting*, Boston, MA, December 2013.

10. Byungwoo Park, Hongsik Choi, Jae Ik Kim, Seunghoon Nam, Woojin Lee, **Sungun Wi**, Chohui Kim, and Joonhyeon Kang, "Nanoscale Interface Control for Photoluminescence and Solar-Cell Applications," *The 9th Tsinghua University - University of Tokyo - Seoul National University Student Workshop*, Seoul, Korea, October 9-12, 2013.

11. Yuhong Oh, Seunghoon Nam, **Sungun Wi**, Saeromi Hong, and Byungwoo Park, "Graphene-Wrapped $Li_4Ti_5O_{12}$ Anode Materials with High-Rate Capability for Li-Ion Batteries,"

The 13th Korea - Japan Student Symposium (Seoul National University - Tohoku University), Seoul, Korea, November 2012.

12. Seunghoon Nam, Sungsoo Kim, **Sungun Wi**, Hongsik Choi, Sujin Byun, and Byungwoo Park, "The Role of Carbon Incorporation in SnO_2 Nanoparticles for Li Rechargeable Batteries,"
The 13th Korea - Japan Student Symposium (Seoul National University - Tohoku University), Seoul, Korea, November 2012.

13. Saeromi Hong, Seunghoon Nam, Yuhong Oh, **Sungun Wi**, and Byungwoo Park, "Mass Producible Echino-like Porous Silicon for Lithium Rechargeable Battery Anode,"
The 13th Korea - Japan Student Symposium (Seoul National University - Tohoku University), Seoul, Korea, November 2012.

국문 초록

현대사회에서의 삶의 방식을 위해서는 에너지 원이 중요하지만, 현재 에너지 수요의 대부분은 핵 및 화석 연료의 힘에 의존한다. 이는 결국 지구 온난화를 가속화 시키며 천연 자원을 심각하게 고갈시킬 것이다. 결과적으로 연료 전지 및 태양 전지와 같은 효율적이고 친환경적이며 안전한 에너지 원을 개발하는 것이 중요하며, 이러한 친환경 에너지 원을 저장하기 위한 효율적인 에저지 저장 시스템의 개발 또한 중요한 문제로 떠오르고 있다. 다양한 에너지 저장 시스템 중 리튬 이온 배터리는 높은 에너지 밀도 및 수명성을 가지고 있다는 매력을 가지고 있기 때문에 가장 현실적인 에너지 원으로써 관심을 받고 있다. 배터리의 성능은 대개 전극 재료에 의해 결정되므로 많은 연구자들은 전극 물질의 한계를 극복하기위한 획기적인 방법을 모색하고 있다. 리튬 전이 금속 산화물 ($LiMO_2$, M = 전이 금속)과 같은 기존의 양극 물질은 과충전 상태에서 본질적인 화학적 불안정성을 갖는다. 이들은 결정 구조로부터 산소를 방출하거나 높아진 온도에서 비가역적인 상변태를 겪게되고, 결과적으로 작동 중에 안전 문제를 일으킨다. 이와 관련하여 안전하고 안정한 양극 재료를 찾기 위해 많은 연구가 수행되고있다. 많은 후보 물질 중 인산염 물질은 강한 P-O 공유 결합으로 인한 높은 구조 안정성 및 안전성, 낮은 가격, 높은 에너지 밀도 및 우수한 수명특성으로 인해 중대형 에너지 저장 시스템의

가장 좋은 후보로 간주되어왔다. 올리빈 구조의 리튬 인산 철 ($LiFePO_4$)은 높은 이론 용량, 구조 안정성, 환경 친화력 및 저비용으로 차세대 리튬 이온 배터리의 양극 재료 후보 물질로 광범위하게 연구되어왔다. 그러나, $LiFePO_4$는 상대적으로 낮은 산화 환원 전위 (3.4V vs. Li^+/Li)로 인한 낮은 에너지 밀도 때문에 더 폭넓은 시장으로의 적용을 제한한다. 이러한 이유로 보다 높은 산화 환원 전위 (4.1V vs. Li^+/Li)를 갖는 같은 올리빈 구조의 $LiMnPO_4$가 $LiFePO_4$의 대체 물질로 떠오르고 있다.

따라서 본 논문에서는 진기화학적으로 우수한 Mn 기반 올리빈 양극 재료 ($LiMn_{0.8}Fe_{0.2}PO_4$)의 설계와 $LiMn_{0.8}Fe_{0.2}PO_4$ 전극물질에서의 전기화학 반응 중의 Mn과 Fe의 반응 메커니즘에 대한 포괄적 인 분석과 해석에 중점을 두었다.

1 장에서는 올리빈 양극 재료의 실용화에 대한 한계를 극복하기 위한 Mn 기반 올리빈 양극 재료에 대하여 소개를 하였다.

2 장에서는 합성 인자를 제어하여 전기 화학적으로 효율적인 마이크로/나노 구조의 $LiMn_{0.8}Fe_{0.2}PO_4$ 전극을 설계했다. 합성 경로를 디자인 함으로써 $LiMn_{0.8}Fe_{0.2}PO_4$ 결정의 크기와 모양뿐만 아니라 입자의 방향성 응집 (mesocrystal) 경향에 대한 제어가 가능함을 입증했다. 또한, $LiMn_{0.8}Fe_{0.2}PO_4$의 성능 향상은 타원형 (dellipsoidal) 모양의 mesocrystal에서 판편 (flake) 모양의 mesocrystal으로 형태를 맞춤으로써 실현되었다. 향상된 전기 화학적 성능의 원인은 1 차 입자 크기, 다공성, 결함 농도 및 2 차 입자 형상의 관점에서 설명이 된다. 본 저자는 이 연구가 전기 화학적으로 유리한 마이크로/나노

구조를 디자인하는 경로 중 하나를 제공할 수 있다고 믿는다.

전극 물질의 전자 구조는 배터리 작동 중 전극의 전기 화학적인 반응성 및 구조적 안정성에 영향을 미치기 때문에, $LiMn_{0.8}Fe_{0.2}PO_4$의 전자 구조에 대한 깊이 있는 이해는 고성능 다중 전이 금속 올리빈 물질을 설계하는 가이드를 제공 할 수 있다. 따라서 제 3 장에서는 전기 화학적 성능에 대한 전이 금속 (Mn과 Fe)의 전자 구조 효과를 연구하기 위해 싱크로트론 기반의 soft- 및 hard-X 선 흡수 분광기 (sXAS와 XAS)를 정량적으로 수행하였으며, 전기 화학 반응 동안 $LiMn_{0.8}Fe_{0.2}PO_4$ 전극에서 전이 금속 산화/환원 상태의 변화를 분석했다. 저자는 *ex situ* sXAS와 *in situ* XAS를 이용한 깊이 있는 분석 및 해석이 배터리 작동 중 $LiMn_{0.8}Fe_{0.2}PO_4$ 전극의 반응 메커니즘에 대한 명확한 실험적 증거를 제공 할 수 있다고 믿는다.

4 장에서는 $Li_xMn_{0.8}Fe_{0.2}PO_4$의 리튬 삽입/탈리 반응을 *in situ* X 선 회절 (XRD)과 GITT 기법을 활용한 *in situ* 전기 화학적 임피던스 분광법 (EIS)을 통해 분석 하였다. $LiMn_{0.8}Fe_{0.2}PO_4$ (LMFP) 양극 재료의 상변화 거동과 느린 반응 원인에 대한 분석 및 해석을 실시하였다. 이러한 분석을 통하여 LMFP mesocrystal 물질에서 리튬의 삽입 및 탈리 과정시 반응경로가 다르다는 것을 확인하였다.

마지막으로, 부록 1에서는 우수한 성능을 가진 리튬 이온 배터리의 양극 재료로 그래핀으로 싸인 $LiFePO_4$ ($LiFePO_4$/G) 합성에 대하여 기술하였다. 그래핀 산화물로 감싸진 $FePO_4$와 리튬 전구체 사이의 고상 반응은 전기적 전도성이 우수한 $LiFePO_4$/G 복합체를

만들었다. 이 독특한 형태는 모든 $LiFePO_4$ 입자가 배터리 작동 중에 전자가 쉽게 접근 할 수있게 해 주어 현저하게 향상된 속도 능력을 제공하게된다. *In situ* EIS 분석으로 충전 및 방전 반응 전반에 걸쳐 향상된 전기적 전도성이 $LiFePO_4$/G에서 우수한 성능의 원인임을 입증하였다.

주요어: 리튬 이온 전지, $LiMnPO_4$, $LiMn_{0.8}Fe_{0.2}PO_4$, Li^+ 확산속도, 전기 전도성, mesocrystal, 속도 특성, 형태 제어, 전자 구조, X-선 흡수 분광법, 전기 화학적 임피던스 분광법 (EIS), Galvanostatic intermittent titration technique (GITT), X-선 회절, 상 전이 메커니즘, 탄소 코팅, 그래핀 코팅.

학번: 2010-22761